Nonlinear thermomechanical modeling of refractory masonry linings

Mahmoud Mahmoud Alaa Ali

UNIVERSITÉ D'ORLÉANS

ÉCOLE DOCTORALE - Energie, Matériaux, Sciences de la Terre et de l'Univers - EMSTU

Laboratoire de Mécanique Gabriel Lamé (LaMé)

THESIS presented by :

Mahmoud Alaaeldeen Ahmed **ALI**

Defense date : **17 / December / 2021**

Thesis submitted for the degree of :

Doctor of Philosophy of University of Orléans

Discipline/ Specialty : Mechanical Engineering and Production

---

Nonlinear thermomechanical modeling of refractory masonry linings

(In the framework EU Horizon 2020 Marie Skłodowska-Curie ATHOR project)

Thesis supervisors :

M. GASSER Alain, M. SAYET Thomas, M. BLOND Eric
Université d'Orléans - France

JURY :

M. HUGER Marc	Professor, Université de Limoges - France	President
M. FOREST Samuel	Research Director, MINES ParisTech - France	Reviewer
M. LEBON Frédéric	Professor, Université Aix Marseille - France	Reviewer
M. LOURENÇO Paulo	Professor, University of Minho - Portugal	Examiner
M. MARSCHALL Ulrich	Doctor Engineer, RHI Magnesita - Austria	Examiner
M. GASSER Alain	Professor, Université d'Orléans - France	Thesis director
M. BLOND Eric	Professor, Université d'Orléans - France	Thesis co-director
M. SAYET Thomas	Associate Professor, Université d'Orléans - France	Thesis supervisor

Acknowledgments

This work was supported by the funding scheme of the European Commission, Marie Skłodowska-Curie Actions Innovative Training Networks in the frame of the H2020 European project ATHOR - Advanced THermomechanical multiscale mOdelling of Refractory linings [grant number 764987]. I would like to thank all the people who contributed to the realization of this amazing project. It gave me the opportunity to work in an international team with valuable friends and colleagues. It has been an amazing journey, which has unfortunately arrived to the end.

I would like to Thank my supervisors, all the members of the jury, office mates, friends, colleagues, technicians, professors, all people working in the LaMé laboratory at University of Orleans - France. They all contributed to create wonderful work conditions. Without their help and support, all the achievements in my thesis would not have been possible.

Part of this work was carried out at RHI Magnesita technology center - (Leoben, Austria) and at University of Coimbra (Portugal). A great thanks to my secondment mentors and technicians for their help and support during and after the two secondments.

I would like to thank my family in Egypt, my mother, my father, my sisters and brothers, for their continuous support during my entire life.

Finally, I would like to thank my beloved wife, Yasmin, my daughter, Lojain, and my son, Adam, for being with my during my PhD journey and being in my life in general.

To my beloved wife, Yasmin

My daughter, Lojain
and my son, Adam

Introduction

ATHOR project

The present PhD thesis is a part of a European funded Marie Curie research project dedicated to Advanced THermomechanical multi scale mOdelling of Refractory linings (ATHOR) [1]. The ATHOR network is composed of 7 academic institutions and 8 industrial partners (see Fig. 1). They are dedicated to train 15 Early Stage Researchers (ESR) in different fields for better understanding of the thermomechanical behavior of refractories.

Figure 1: ATHOR network: academic and industrial partners [1].

The main objectives of ATHOR project were defined through individual work packages (WPs, see Fig. 2). The four scientific work packages (WP1 to WP4) of ATHOR are well connected and were established to promote innovation in both modeling approaches and experimental methodologies. The project covers all the main features of thermomechanical analysis of refractory linings such as nonlinear thermomechanical modeling at different scales (from the micro structure to the structure scales and the reverse loop from the structure to the micro structure scales), materials characterization, impacts of corrosion on thermomechanical properties, testing large scale refractory masonry and measurement in operation conditions.

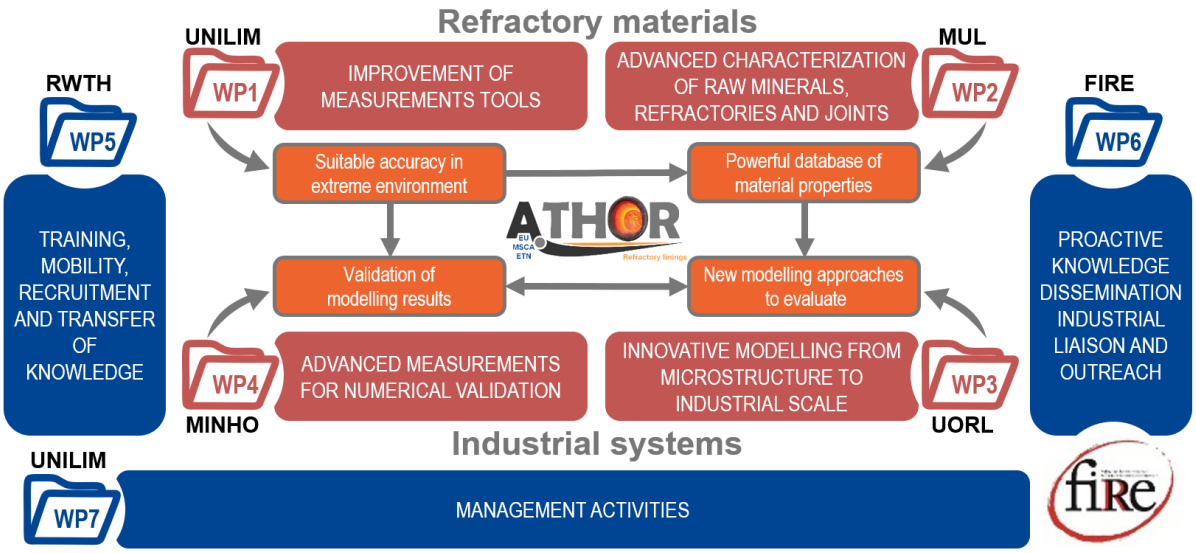

Figure 2: ATHOR PERT diagram [1].

Motivations and objectives

Owing to their high thermomechanical, thermal and chemical stability, refractories are known as unique ceramic materials. They are able to withstand severe working conditions including: high operating temperature (above 1000 °C), thermal shock, high thermomechanical stresses, erosion and corrosion which are identified as the main ageing factors of the materials [2–6]. Being the only low cost material able to withstand complex combinations of these extreme working conditions, refractories are identified as advanced ceramics. These materials are widely used for the linings of many high temperature components, such as steel ladles, furnaces and rotary kilns, used in several high temperature industries as glass production, cement, iron and steel making. The iron and steel making industry is the major consumer of refractories, accounting for around 60% of the refractory materials market [7].

The steel ladle is a key component in the steel making industry, and is the primary refractory user, representing around 25% of all refractory consumption [8]. The design of the steel ladle linings can significantly be different between steel plants and regions. The linings could be castables or masonry with or without mortar. The present work is focused on refractory linings with dry or mortar joints. The design and optimization of these linings is still an engineering challenge due to the complex interaction between the thermal fields, the chemistry and the nonlinear thermomechanical behavior of refractories at high temperature [2, 9, 10]. Therefore, a constant research and development on refractory linings are required to meet with existing and new demanding requirements in the iron and steel industry.

As a part of ATHOR project, this PhD aims at characterizing the mechanical and thermomechanical behavior of refractory masonry with dry joints under a wide range of thermomechanical loading conditions. In addition, developing rigorous and computationally efficient numerical

models for modeling the nonlinear orthotropic thermomechanical behavior of refractory masonry with dry or mortar joints and optimize their thermomechanical performance. The main objectives of the present thesis are summarised as following:

- Experimental characterization of the mechanical and thermomechanical behaviors of refractory masonry walls subjected to a wide range of loading conditions at room and high temperatures. The experimental tests shall help in understanding the complex behavior of refractory masonry at room and high temperatures.
- Performing computational nonlinear homogenization of elastic viscoplastic refractory masonry structures with mortar and dry joints and developing multi scale numerical models for their simulation. The developed models should be efficient in terms of computational cost to enable full scale structural modeling of large scale industrial applications. The validation of the developed models will be carried out by comparing the experimental and numerical results of refractory masonry walls subjected to a wide range of loading conditions at room and high temperatures.
- Performing 3D transient thermomechanical analysis of a simplified steel ladle and investigate it's thermomechanical response during complete thermal cycles of the steel-making process. The influence of temperature fluctuations on the transient thermomechanical response of the steel ladle will be studied. The impacts of joints thickness, joints behavior and the material models used for describing the behavior of the different layers in the ladle on the transient thermomechanical response of the lade will be investigated.

Organization of the thesis

The present PhD dissertation is organized as follows:

- **Chapter 1** is dedicated to review the state of the art of mechanical homogenization of heterogeneous solids as well as experimental and numerical studies of masonry with dry and mortar joints. This state of the art is essential for pointing out possible directions of investigation for the present work. The capabilities and limitations of the different modeling techniques of masonry with dry and mortar joints are discussed. The previous experimental studies on masonry with dry and mortar joints are introduced. A review of existing numerical models of steel ladles is presented.
- **Chapter 2** is devoted to experimental characterization of refractory masonry walls subjected to uniaxial and biaxial compression loads at room and high temperature. This chapter gathers a considerable database on the mechanical and thermomechanical characterization of refractory masonry with dry joints. The two large scale experimental campaigns performed within the framework of ATHOR project are presented. The studied materials, their mechanical and thermo physical properties are introduced. Detailed descriptions of the uniaxial compression test setup at university of Coimbra, displacement and temperature measurement techniques, specimens, results and discussions of masonry

subjected to uniaxial compression at room and high temperatures are given. Detailed descriptions of the biaxial compression test setup at RHI Magnesita, measurement techniques, tested specimens, results and discussions of masonry subjected to a wide range of thermomechanical loading conditions are presented.

- **Chapter 3** is dedicated to the description of the proposed multi scale numerical models of masonry with mortar and dry joints. These models are based on defining possible joint patterns. The nonlinear homogenization technique and the determination of the effective elastic viscoplastic behaviors of masonry with dry and mortar joints are presented. The macroscopic orthotropic constitutive laws used to describe the homogenized elastic viscoplastic behavior of the different joint patterns are presented. Joints closure and/or opening, caused by cyclic loading and unloading, are considered in the models. Details about closure and/or opening criteria of the joints are provided. Finally, some comparisons between the numerical results of detailed micro modeling approach with that of multi scale modeling are presented.
- **Chapter 4** is dedicated to the validation of the developed multi scale models of masonry with dry and mortar joints. For masonry with dry joints, the models were validated by comparing the experimental results (presented in chapter 2) and numerical results of masonry subjected to a wide range of thermomechanical loading conditions. Regarding masonry with mortar joints, comparative studies with numerical and experimental results of masonry subjected to in-plane shear [11] and masonry subjected to bending load [12] are presented.
- **Chapter 5** is devoted to describe the three-dimensional coupled sequential thermomechanical models of a simplified steel ladle. Details about the thermal analysis used to compute the temperature distribution of the steel ladle during three full thermal cycles of the steel making process are given. These temperature distribution has been, in turn, used as thermal load for the thermomechanical analysis. The working lining, the bottom and the safety lining of the ladle have been replaced by equivalent material models that have been developed in chapter 3 and validated in chapter 4. The impacts of temperature fluctuations, joint thickness, joint behavior, constitutive material models of the different linings of the ladle and the steel shell on the transient thermomechanical response of the ladle are investigated.

Finally, this thesis will be closed by some concluding remarks, key results and the proposition of potential future work, based on the gained experience and results.

Contents

List of Tables

List of Figures

CHAPTER 1

LITERATURE SURVEY

This chapter is devoted to review the state of the art of mechanical homogenization of heterogeneous solids as well as experimental and numerical studies of masonry with dry and mortar joints. This state of the art is essential for pointing out possible directions of investigation for the present work. The different modeling techniques of discrete and continuum medium as well as multi scale modeling are introduced in section 1.1. As in multi scale modeling of materials the so called "Representative Volume Element (RVE)" is extensively used, more details about the term RVE and important points to consider when selecting a RVE are discussed in section 1.2. Then, different analytical and computational homogenization techniques of heterogeneous materials are presented in section 1.3. Previous experimental studies on masonry with dry and mortar joints as well as the different modeling approaches are discussed in detail in sections 1.4 and 1.5. Section 1.6 provides a review of existing numerical models of steel ladles. Finally, some concluding remarks about experimental and numerical studies of masonry with dry and mortar joints and numerical modeling of steel ladles are given in section 1.7.

1.1 Modeling techniques

Modeling techniques of refractories, and materials in general, can be classified into two main techniques depending on the length scale spectrum of the material: a) discrete and b) continuum modeling techniques (see Fig. 1.1). The two techniques are very different, and they are used for modeling discrete and continuum media. The difference between the two techniques is caused by how the material is represented at the nano scale (represented as discrete medium) and at the micro to macro scales (represented as continuum medium). A discrete medium is usually represented by a finite number of points (atoms, nodes in a lattice structure), separated by finite distances and connected together by individual elements (i.e. bonds) that drive the interactions between them. On the other hand, a continuum medium is represented by infinite number of zero dimensional points that form continuous lines, surfaces and volumes. Of course

the latter representation diverges from the physical structure of materials (at the nano scale), but it's a prerequisite for practical description of materials behavior at large scales. Moreover, the engineering fields of solids mechanics are based on continuum assumption (including the present work).

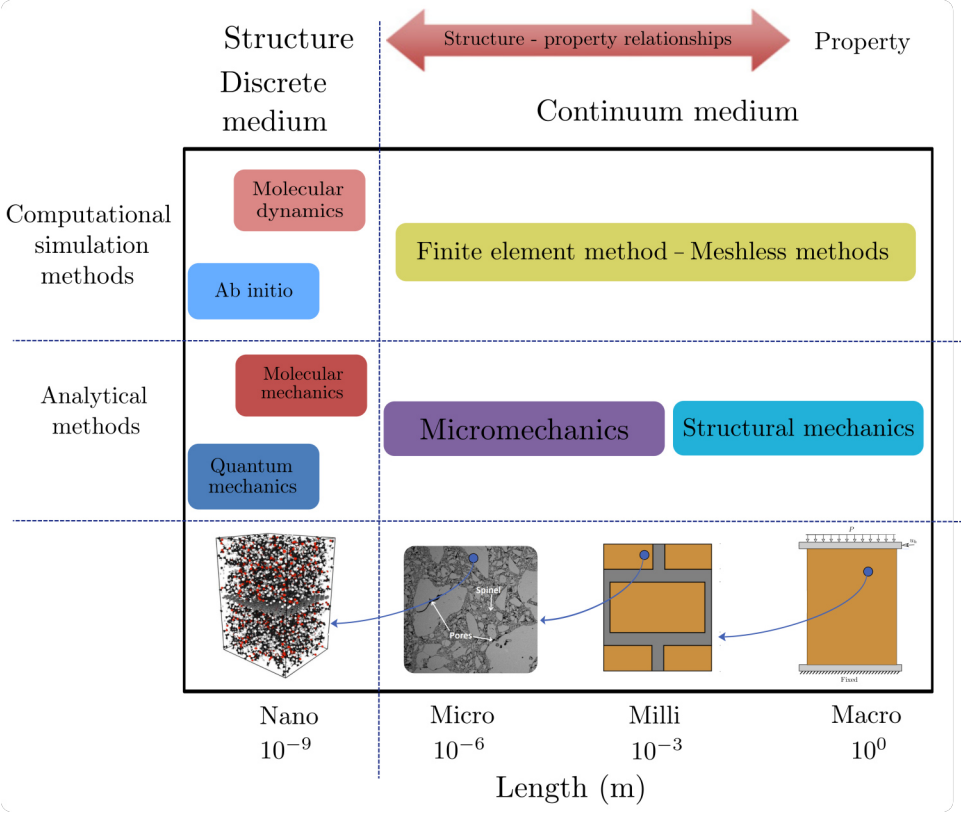

Figure 1.1: Length scale spectrum associated with multi-scale modeling of materials.

The major challenge is to employ efficient methodologies to link the discrete and continuum modeling techniques. Several analytical and computational methods for modeling discrete and continuum media are available (see Fig. 1.1). As the present work is focused on modeling continuum medium, full description of continuum modeling approaches are given in section 1.3. Some well-known analytical and computational discrete modeling approaches are briefly introduced below.

Quantum mechanics: explains the behavior of matter at atomic scale and its interactions with energy. Energies related to the position of atoms drive the properties and equilibrium of materials [13, 14].

Molecular mechanics: In the framework of molecular mechanics, atoms are represented as rigid particles who can only translate in three dimensions (do not have rotational degrees of freedom). These rigid particles interact with each other through different inter atomic force fields such as bond stretching, torsion bond angle bending and Van der Waals interactions [15, 16]. The elastic properties of materials can be estimated from the force fields.

AB initio: is a computational method that builds on quantum mechanics principles [17]. It is used to predict a range of properties such as atomic interactions, band gaps, electrical

conductivity, molecular structure and elastic constants. The results are predicted by knowing the system structure and elemental composition of the material.

Molecular dynamics: is a computer simulation method that builds on molecular mechanics framework. As compared to molecular mechanics, molecular dynamics can predict the time dependent evolution (resulting from atomic motion) of inter atomic forces. Time dependent evolution of inter atomic forces are captured by tracking the motion of atoms due to temperature, pressure, etc [18, 19].

1.2 Representative volume element

In the field of multi scale modeling of materials, both discrete and continuum (especially from μm to mm) modeling techniques are using a carefully chosen volume of the material at the small scale (for example nano scale, see Fig. 1.1) to determine the effective properties of the material at a bigger scale (for example micro scale, see Fig. 1.1). The chosen volume is very small as compared to the larger scale and it's behavior should be representative to that of the material at the bigger scale. The carefully chosen volume of the material is called Representative Volume Element (RVE). The RVE concept is important in the field of computational multi scale modeling of materials as it allows to move from smaller to larger scales and to build relationships between materials' structure and properties.

The term RVE was coined by Hill [20] and further explained by Hashin [21]. The RVE is a volume of material whose properties are representative to the bulk material. In the case of fictions homogeneous materials, the RVE is finitely small. However, at some scale, all materials are heterogeneous. The RVE is a valuable limit (in terms of size) to choose between microscopic and continuum theories. As in the case of scales above the RVE, continuum theories can be used. On the other hand, for scales smaller than the RVE one should use microscopic theories and consider the detailed structure of the material. Several points should be considered when choosing the size of the RVE such as:

- The volume of the RVE must be large enough (as compared to micro structure of the material) to capture all the information about the material from a statistical point of view.
- The RVE volume should be large enough to allow the heterogeneous nature of the materials to be averaged.
- If uniform displacement or force are applied to the boundaries of the RVE, similar response should be obtained [20].
- As shown in Fig. 1.2, uniform force or displacement boundary conditions require larger RVE as compared to periodic boundary conditions (PBC) [22–24]. Further details about different types of boundary conditions are given later.

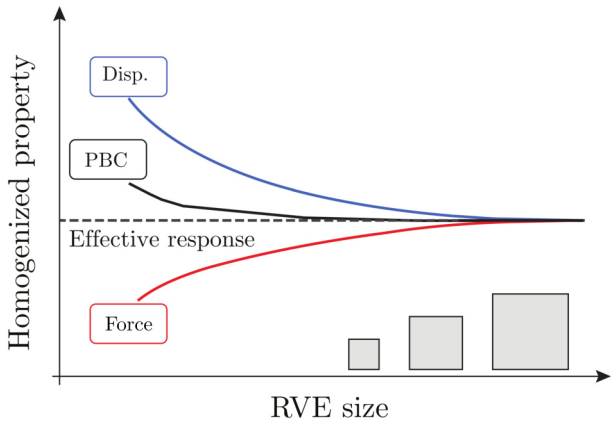

Figure 1.2: Convergence of the homogenized property as a function of the RVE size using different types of boundary conditions.

1.3 Homogenization techniques

The major objective of homogenization is to determine the effective properties (mechanical, thermo-physical, etc.) of a heterogeneous material from the knowledge of geometrical configurations and properties of its constituents. This allows to replace a heterogeneous material, at the microscopic scale, with an equivalent homogeneous material at the macroscopic scale, see Fig 1.3.

Several analytical and numerical homogenization techniques were developed in the past decades. They can be classified into two main categories: (a) mean field techniques (also known as average field techniques) and (b) full field techniques. Generally speaking, these techniques are physics and mathematics based approaches [25]. The most common mean field and full field homogenization techniques are reviewed in sections 1.3.1 and 1.3.2.

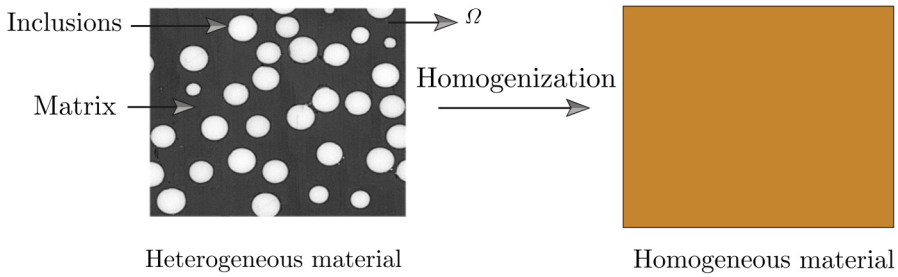

Figure 1.3: Principle of the homogenization technique [26].

1.3.1 Mean field techniques

The mean field techniques (MFTs) are analytical or semi-analytical approaches based on Eshelby's equivalent inclusion method [27,28]. They are well-developed in the framework of linear elasticity. The extension of MFTs to rate dependent or independent elasto-plasticity is a challenging task as they usually require linearization procedures such as secant formulations [29–31].

MFTs are fast and efficient from the computational point of view. Many approximations were developed over the past decades such as classic bounds approaches [32–35], Mori–Tanaka [36] and self-consistent schemes [37, 38]. The main drawback of MFTs is that they are restricted to small volume fractions of inclusions with ellipsoidal or spherical shapes.

Before introducing the MFTs, some important theoretical formulations and scale transition between the microscopic and macroscopic fields are firstly introduced. Consider a RVE (Ω) with volume V_Ω of heterogeneous material composed of an elastic matrix (m) with volume V_m and randomly distributed inclusions (i) with volume V_i, ($V_\Omega = V_m + V_i$) and boundary Γ; see Fig. 1.3. The elastic properties of i and m are known. The volume fractions v_i and v_m, in the absence of voids, are expressed as:

$$v_m = \frac{V_m}{V_\Omega} \tag{1.1}$$

$$v_i = \frac{V_i}{V_\Omega} = 1 - v_m \tag{1.2}$$

When the RVE boundaries are subjected to stress or strain, the macroscopic or average stress ($\overline{\overline{\Sigma}}$) and strain ($\overline{\overline{E}}$) tensors can be obtained from those of the matrix ($\overline{\overline{\Sigma}}_m,\ \overline{\overline{E}}_m$,) and inclusions ($\overline{\overline{\Sigma}}_i,\ \overline{\overline{E}}_i$,) using the role of mixtures according to [39, 40]:

$$\overline{\overline{\Sigma}} = v_m\overline{\overline{\Sigma}}_m + v_i\overline{\overline{\Sigma}}_i \tag{1.3}$$

$$\overline{\overline{E}} = v_m\overline{\overline{E}}_m + v_i\overline{\overline{E}}_i \tag{1.4}$$

with

$$\overline{\overline{\Sigma}}_m = \overline{\overline{\overline{\overline{C}}}}_m : \overline{\overline{E}}_m \tag{1.5}$$

$$\overline{\overline{\Sigma}}_i = \overline{\overline{\overline{\overline{C}}}}_i : \overline{\overline{E}}_i \tag{1.6}$$

and the inverses are:

$$\overline{\overline{E}}_m = \overline{\overline{\overline{\overline{S}}}}_m : \overline{\overline{\Sigma}}_m \tag{1.7}$$

$$\overline{\overline{E}}_i = \overline{\overline{\overline{\overline{S}}}}_i : \overline{\overline{\Sigma}}_i \tag{1.8}$$

Where $\overline{\overline{\overline{\overline{C}}}}_i$ and $\overline{\overline{\overline{\overline{C}}}}_m$ are the 4^{th} order stiffness tensor of the inclusions and the matrix, respectively. $\overline{\overline{\overline{\overline{S}}}}_i$ and $\overline{\overline{\overline{\overline{S}}}}_m$ are the 4^{th} order compliance tensor of the inclusions and the matrix, respectively. Using Eq. 1.5 and 1.6, Eq. 1.3 can be written as:

$$\overline{\overline{\Sigma}} = v_m\overline{\overline{\overline{\overline{C}}}}_m : \overline{\overline{E}}_m + v_i\overline{\overline{\overline{\overline{C}}}}_i : \overline{\overline{E}}_i \tag{1.9}$$

Combining Eq. 1.7 and 1.8 with Eq. 1.4 yields:

$$\overline{\overline{E}} = v_m\overline{\overline{\overline{\overline{S}}}}_m : \overline{\overline{\Sigma}}_m + v_i\overline{\overline{\overline{\overline{S}}}}_i : \overline{\overline{\Sigma}}_i \tag{1.10}$$

The macroscopic strains of the matrix and inclusions can be written in terms of the macroscopic strains of the RVE using 4^{th} order strain concentration tensors $\overline{\overline{\overline{\overline{A}}}}$ as :

$$\overline{\overline{E}}_i = \overline{\overline{\overline{\overline{A}}}}_i : \overline{\overline{E}} \tag{1.11}$$

$$\overline{\overline{E}}_m = \overline{\overline{\overline{\overline{A}}}}_m : \overline{\overline{E}} \tag{1.12}$$

and

$$v_m \overline{\overline{\overline{\overline{A}}}}_m + v_i \overline{\overline{\overline{\overline{A}}}}_i = \overline{\overline{\overline{I}}} \tag{1.13}$$

Where, $\overline{\overline{\overline{I}}}$ is the 4^{th} order symmetric identity tensor. Similarly, the macroscopic stresses of the matrix and inclusions can be written in terms of the macroscopic stress of the RVE using 4^{th} order stress concentration tensors $\overline{\overline{\overline{\overline{B}}}}$ as :

$$\overline{\overline{\Sigma}}_i = \overline{\overline{\overline{\overline{B}}}}_i : \overline{\overline{\Sigma}} \tag{1.14}$$

$$\overline{\overline{\Sigma}}_m = \overline{\overline{\overline{\overline{B}}}}_m : \overline{\overline{\Sigma}} \tag{1.15}$$

and

$$v_m \overline{\overline{\overline{\overline{B}}}}_m + v_i \overline{\overline{\overline{\overline{B}}}}_i = \overline{\overline{\overline{I}}} \tag{1.16}$$

Combining Eq. 1.11 and 1.12 with 1.9 yields:

$$\overline{\overline{\Sigma}} = \overline{\overline{\overline{\overline{C}}}} : \overline{\overline{E}} \tag{1.17}$$

Where $\overline{\overline{\overline{\overline{C}}}}$ denotes the homogeneous stiffness tensor of the heterogeneous material. Now, it can be written as:

$$\overline{\overline{\overline{\overline{C}}}} = v_m \overline{\overline{\overline{\overline{C}}}}_m : \overline{\overline{\overline{\overline{A}}}}_m + v_i \overline{\overline{\overline{\overline{C}}}}_i : \overline{\overline{\overline{\overline{A}}}}_i \tag{1.18}$$

Using Eq. 1.14 and 1.15 in Eq. 1.10 yields:

$$\overline{\overline{E}} = \overline{\overline{\overline{\overline{S}}}} : \overline{\overline{\Sigma}} \tag{1.19}$$

Where $\overline{\overline{\overline{\overline{S}}}}$ denotes the homogeneous compliance tensor of the heterogeneous material. Now, it can be written as:

$$\overline{\overline{\overline{\overline{S}}}} = v_m \overline{\overline{\overline{\overline{S}}}}_m : \overline{\overline{\overline{\overline{B}}}}_m + v_i \overline{\overline{\overline{\overline{S}}}}_i : \overline{\overline{\overline{\overline{B}}}}_i \tag{1.20}$$

1.3.1.1 The classic bounds

Voigt and Reuss bounds

The simple bounds of Voigt and Reuss can be used to calculate the elastic properties of linear elastic heterogeneous materials composed of two phases [32, 33]. The Voigt homogenization scheme assumes a uniform strain within the material, while the Reuss homogenization scheme assumes a uniform stress in the material.

Under the uniform strain assumption, it follows from Eq. 1.11 and 1.12 that $\overline{\overline{\overline{\overline{A}}}}_i = \overline{\overline{\overline{\overline{A}}}}_m = \overline{\overline{\overline{I}}}$. The effective stiffness tensor of the material is expressed as:

$$\overline{\overline{\overline{\overline{C}}}} = v_m \overline{\overline{\overline{\overline{C}}}}_m + v_i \overline{\overline{\overline{\overline{C}}}}_i \tag{1.21}$$

Eq. 1.21 is known as Voigt bound. Under the uniform stress assumption, it follows from Eq. 1.14 and 1.15 that $\overline{\overline{\overline{B}}}_i = \overline{\overline{\overline{B}}}_m = \overline{\overline{\overline{I}}}$. The effective compliance of the material is expressed as:

$$\overline{\overline{\overline{S}}} = v_m \overline{\overline{\overline{S}}}_m + v_i \overline{\overline{\overline{S}}}_i \tag{1.22}$$

Eq. 1.22 is known as Reuss bound.

Similarly, the upper bound ($+$, or Voigt bound) of the effective bulk (k) and shear (G) modulus can be written as:

$$k^+ = v_i k_i + v_m k_m \tag{1.23}$$

$$G^+ = v_i G_i + v_m G_m \tag{1.24}$$

The lower bound ($-$, or Reuss bound) of the effective bulk (k) and shear (G) modulus can be written as:

$$\frac{1}{k^-} = \frac{v_i}{k_i} + \frac{v_m}{k_m} \tag{1.25}$$

$$\frac{1}{G^-} = \frac{v_i}{G_i} + \frac{v_m}{G_m} \tag{1.26}$$

It should be noted that the gap between the Voigt and Reuss bounds is usually large. Moreover, neither uniform strain (Voigt) nor uniform stress (Reuss) assumption are correct. Because the first assumption is such that the tension at phase boundaries is not in equilibrium. The second assumption is such that i and m cannot remain bonded [40].

Hashin-Shtrikman bounds

Hashin and Shtrikman proposed a more efficient homogenization scheme to predict the homogenized properties of multi phase materials. The method used in this technique is based on solving a problem of inclusions embedded in an infinite homogeneous matrix [34, 35]. As compared to the Voigt and Reuss bounds, the Hashin-Shtrikman bounds are narrower and give more accurate results in the case of particulate composites with perfect bonding. Assuming a particulate material made up of two phases, i and m, and phase i is harder than m, the upper bounds of the effective k and G are given as:

$$k^+ = k_i + \frac{v_m}{\frac{1}{k_m - k_i} + \frac{3v_i}{3k_i + 4G_i}} \tag{1.27}$$

$$G^+ = G_i + \frac{v_m}{\frac{1}{G_m - G_i} + \frac{6v_i(k_i + 2G_i)}{5G_i(3k_i + 4G_i)}} \tag{1.28}$$

And the lower bounds of the effective k and G are expressed as:

$$k^- = k_m + \frac{v_i}{\frac{1}{k_i - k_m} + \frac{3v_m}{3k_m + 4G_m}} \tag{1.29}$$

$$G^- = G_m + \frac{v_i}{\frac{1}{G_i - G_m} + \frac{6v_m(k_m + 2G_m)}{5G_m(3k_m + 4G_m)}} \tag{1.30}$$

1.3.1.2 Mori-Tanaka scheme

Mori and Tanaka [36] proposed an approach for calculating the average stress in the matrix of a composite material containing misfitting reinforcements. This approach was further developed by several authors to estimate the effective stiffness of multi phase composites from the volume fractions, shapes and elastic moduli of the phases [41–44]. The approach is based on Eshelby's solution of an inclusion in infinite matrix. Each phase of the composite is treated as homogeneous. The macroscopic behavior of the composite material is estimated from the average strain and stress fields of each phase. Assuming a composite material made up of N homogeneous phases, the strain of the s$^{\text{th}}$ phase ($\overline{\overline{E}}_s$) can be written in terms of the average macroscopic strain ($\overline{\overline{E}}$) by using a localization tensor ($\overline{\overline{\overline{\overline{A}}}}_s$) as:

$$\overline{\overline{E}}_s = \overline{\overline{\overline{\overline{A}}}}_s : \overline{\overline{E}} \tag{1.31}$$

The strain localization tensor is given by:

$$\overline{\overline{\overline{\overline{A}}}}_s = \overline{\overline{\overline{\overline{T}}}}_s : \left[\sum_{n=0}^{N} v_n \overline{\overline{\overline{\overline{T}}}}_n\right]^{-1} \tag{1.32}$$

Where v_n is the volume fraction of phase n and $\overline{\overline{T}}_s$ denotes the interaction tensor of s$^{\text{th}}$ phase. It is expressed as:

$$\overline{\overline{\overline{\overline{T}}}}_s = \left[\overline{\overline{\overline{\overline{I}}}} + \overline{\overline{\overline{\overline{S}}}}\left(\overline{\overline{\overline{\overline{C}}}}_m\right) : \overline{\overline{\overline{\overline{C}}}}_m{}^{-1} : \left[\overline{\overline{\overline{\overline{C}}}}_s - \overline{\overline{\overline{\overline{C}}}}_m\right]\right]^{-1} \tag{1.33}$$

Where $\overline{\overline{\overline{\overline{I}}}}$ and $\overline{\overline{\overline{\overline{S}}}}\left(\overline{\overline{\overline{\overline{C}}}}_m\right)$ denote the 4th order symmetric identity tensor and Eshelby tensor that depends on the matrix stiffness tensor ($\overline{\overline{\overline{\overline{C}}}}_m$), respectively. The macroscopic elastic stiffness tensor of the composite material is expressed as:

$$\overline{\overline{\overline{\overline{C}}}} = \sum_{s=0}^{N} v_s \overline{\overline{\overline{\overline{C}}}}_s : \overline{\overline{\overline{\overline{A}}}}_s = \overline{\overline{\overline{\overline{C}}}}_m + \sum_{s=1}^{N} v_s \left(\overline{\overline{\overline{\overline{C}}}}_s - \overline{\overline{\overline{\overline{C}}}}_m\right) : \overline{\overline{\overline{\overline{A}}}}_s \tag{1.34}$$

The elastic tensors of the matrix and phases are known, equation 1.34 is explicit. In the case of inelastic phases, the elastic tensors of the matrix and phases are replaced with a tangent tensor using incremental methods [45].

1.3.1.3 Self-consistent scheme

The self-consistent method assumes that each inclusion in the composite material is isolated and placed in a fictitious homogeneous matrix which has the unknown macroscopic stiffness that is being searched [37, 38]. Therefore, the homogenization problem can be reduced to the solution of an inclusion (with spherical or ellipsoidal shape) embedded in an infinite effective medium. Under this assumption, the strain concentration tensor of the s$^{\text{th}}$ phase ($\overline{\overline{\overline{\overline{A}}}}_s$) is written as [46]:

$$\overline{\overline{\overline{\overline{A}}}}_s = \left[\overline{\overline{\overline{\overline{I}}}} + \overline{\overline{\overline{\overline{S}}}}_s \left(\overline{\overline{\overline{\overline{C}}}}\right)^{-1} : \left(\overline{\overline{\overline{\overline{C}}}}_s - \overline{\overline{\overline{\overline{C}}}}\right)\right]^{-1} \tag{1.35}$$

The macroscopic elastic tensor ($\overline{\overline{\overline{\overline{C}}}}$) of the composite material is expressed as:

$$\begin{aligned}\overline{\overline{\overline{\overline{C}}}} &= \overline{\overline{\overline{\overline{C}}}}_m + \sum_{s=1}^{n} v_s \left(\overline{\overline{\overline{\overline{C}}}}_s - \overline{\overline{\overline{\overline{C}}}}_m\right) : \overline{\overline{\overline{\overline{A}}}}_s \\ &= \overline{\overline{\overline{\overline{C}}}}_m + \sum_{s=1}^{n} v_s \left(\overline{\overline{\overline{\overline{C}}}}_s - \overline{\overline{\overline{\overline{C}}}}_m\right) : \left[\overline{\overline{\overline{\overline{I}}}} + \overline{\overline{\overline{\overline{S}}}}_s \left(\overline{\overline{\overline{\overline{C}}}}\right)^{-1} : \left(\overline{\overline{\overline{\overline{C}}}}_s - \overline{\overline{\overline{\overline{C}}}}\right)\right]^{-1}\end{aligned} \tag{1.36}$$

Equation 1.36 is implicit. A well-known method to determine $\overline{\overline{\overline{\overline{C}}}}$ is to use an iterative approach by initializing ($\overline{\overline{\overline{\overline{C}}}}$) through Mori and Tanaka method or Voigt and Reuss bounds [46].

1.3.2 Full field techniques

Although MFTs are easy to solve, they are limited to specific shapes of inclusions (cylindrical and spherical) with low volume fractions. Moreover, they are not able to predict the micro stress and strain fields. Better predictions of the effective properties can be obtained using fully computational approaches. Several computational approaches (such as finite difference, boundary element and finite element analysis) were developed in the last decades, they are able to predict both the effective properties of heterogeneous materials and the micro stress and strain fields. These methods are based on the simulation of a RVE.

Consider a RVE (Ω) with volume V_Ω and boundary surface Γ. Let Γ subjected to surface tension T_i with normal n_j. The equilibrium of Ω can be expressed in terms of the microscopic Cauchy stress tensor as [47]:

$$\begin{aligned}\sigma_{ij,j} + F_i = 0 \qquad on \qquad V_\Omega \\ T_i = \sigma_{ij} n_j \qquad on \qquad \Gamma\end{aligned} \tag{1.37}$$

Where F_i are the body forces and σ_{ij} are the components of local Cauchy stress tensor. The macroscopic or volume average 2^{nd} order stress tensors ($\overline{\overline{\Sigma}}$) is obtained by integrating the microscopic stress ($\overline{\overline{\sigma}}$) tensor over the volume of the RVE as [48–50]:

$$\overline{\overline{\Sigma}} = \frac{1}{V_\Omega} \int_{V_\Omega} \overline{\overline{\sigma}} dV \tag{1.38}$$

In previous studies, two main approaches have been used to calculate the macroscopic strain fields [25, 48, 49, 51–54]. The first approach is based on calculating the 2^{nd} order macroscopic strain tensor, $\overline{\overline{E}}$, by integrating the local strain, $\overline{\overline{\varepsilon}}$, over the volume of the RVE according to [25, 48, 51, 52]:

$$\overline{\overline{E}} = \langle \overline{\overline{\varepsilon}} \rangle = \frac{1}{V_\Omega} \int_{V_\Omega} \overline{\overline{\varepsilon}} dV \tag{1.39}$$

In the second approach, the macroscopic elastic strains are calculated from the average change in the displacements of the RVE's corners (i.e. by dividing the change in displacements of the corners by the initial dimensions of the RVE) [49, 53, 54]. If there are neither gaps nor

cracks in the RVE, as in Fig. 1.4-a , both techniques converge to the same value. However, in the presence of gaps or cracks, the macroscopic elastic strains cannot be computed by integrating the micro (or local) strains over the volume of the RVE (first approach). The presence of gaps within the RVE leads to discontinuous displacement fields (see Fig. 1.4-b), because there is neither viscosity nor rigidity in the volume of the gaps (i.e. local strains within the gaps are unknown) [48, 49].

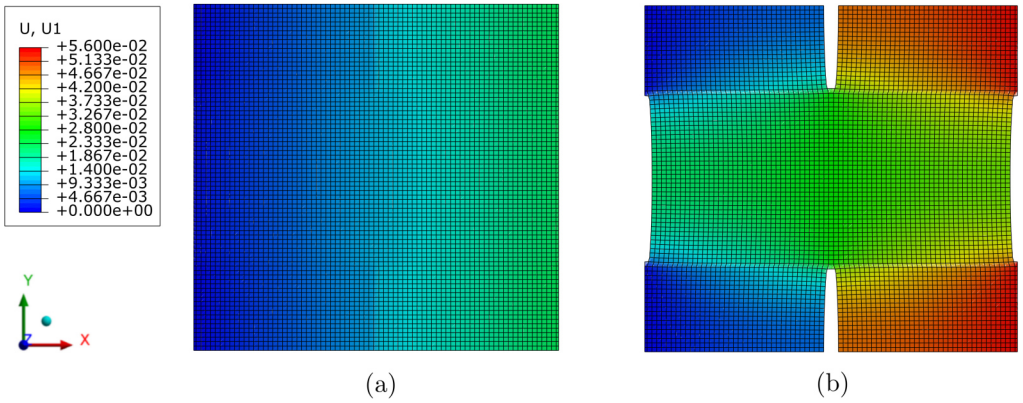

Figure 1.4: Horizontal displacement contours (in mm) in a RVE (a) without gaps and (b) with gaps.

According to Hill-Mandell principle, the strain energy density at the microscopic scale must be equal to that at the macroscopic scale [20]. In the absence of body forces, Hill-Mandell principle is expressed as [20, 22]:

$$\oint_{\Gamma} (T_i - \Sigma_{ij} n_j)\,(u_i - E_{ij} X_k)\,dS = 0 \tag{1.40}$$

Where Σ_{ij}, $\overline{X}$, and E_{ij} are the components of the macroscopic stress tensor, the position vector and components of macroscopic strain tensor, respectively. u_i is the displacement of point i at the microscopic level. The contour integration integral emphasizes that the integration is over a closed surface, S. The microscopic displacement can be decomposed into a macroscopic part (U_i, due to macroscopic deformation) and a micro fluctuation part $\tilde{u_i}$, $u_i = U_i + \tilde{u_i}$ [23, 55]. For periodic structures $\tilde{u_i}$ should be periodic at the opposite boundaries, see Fig. 1.5, [22, 56].

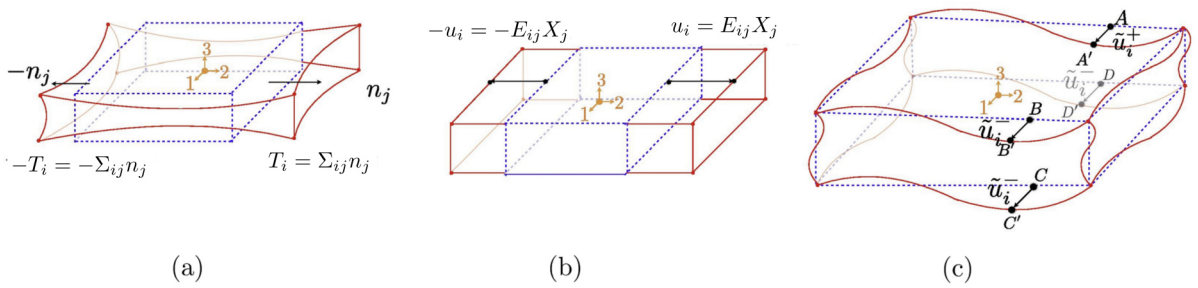

Figure 1.5: Schematics of reference and deformed RVE subjected to a) uniform tension, (b) uniform displacement and (c) periodic boundary conditions [22].

To satisfy the Hill-Mandell principle (Eq. 1.40), one of the following boundary conditions can be applied to Γ:

- Uniform tension boundary conditions, see Fig. 1.5-a:

$$T_i = \Sigma_{ij} n_j \qquad on \qquad \Gamma \tag{1.41}$$

- Uniform displacement boundary conditions, see Fig. 1.5-b:

$$u_i = E_{ij} X_j \qquad on \qquad \Gamma \tag{1.42}$$

- Periodic boundary conditions, see Fig. 1.5-c:

$$\begin{aligned} u_i^+ &= E_{ij} X_j^+ + \tilde{u_i} \qquad on \qquad \Gamma^+ \\ u_i^- &= E_{ij} X_j^- + \tilde{u_i} \qquad on \qquad \Gamma^- \end{aligned} \tag{1.43}$$

  The $+$ and $-$ signs denote the opposite surfaces of Γ.

In contrast to uniform displacement and tension boundary conditions, periodic boundary conditions satisfy both boundary displacement periodicity and boundary force periodicity. Moreover, homogeneous boundary conditions are over constrained conditions, violate stress periodicity of the boundaries and, therefore, are not recommended to be used for periodic RVE subjected to shear loading conditions [23, 56].

1.4 Experimental and numerical studies of masonry with dry joints

Masonry systems with dry joints (without mortar) are composed of bricks and dry joints. They can be classified into two main categories according to their operating temperature: a) civil structural masonry that normally operates at room temperature or, sometimes, under fire situations, and b) refractory masonry for high temperature industrial applications (> 1000 °C). The main difference between the two categories is the constitutive material of the bricks. In the first category, the bricks are usually made of stones, cooked clay, concrete, etc., while in the second category, bricks are made of refractory ceramics.

In a typical masonry structure with dry joints, bricks with height h_b, length l_b and depth d_b are periodically arranged in running bond texture. Dry joints with initial thickness ($g_0 << h_b,\ l_b,\ d_b$) are separating the bricks from each other, see Fig. 1.6. Often, these joints are resulting from the surface unevenness, shape and dimensions errors of the bricks during production. However, sometimes, for instance rotary kiln and blast furnace, the joints are designed by attaching cardboard spacers to the bricks during installation to compensate for thermal expansion effects. Two types of joints are defined on the basis of their orientation: bed joints (horizontal joints) and head joints (vertical joints), see Fig. 1.6-b.

Most of previous experimental and numerical studies on mortarless masonry typically focused on civil structural masonry [57–65]. The most important findings of these studies are reviewed in sections 1.4.1 and 1.4.2.

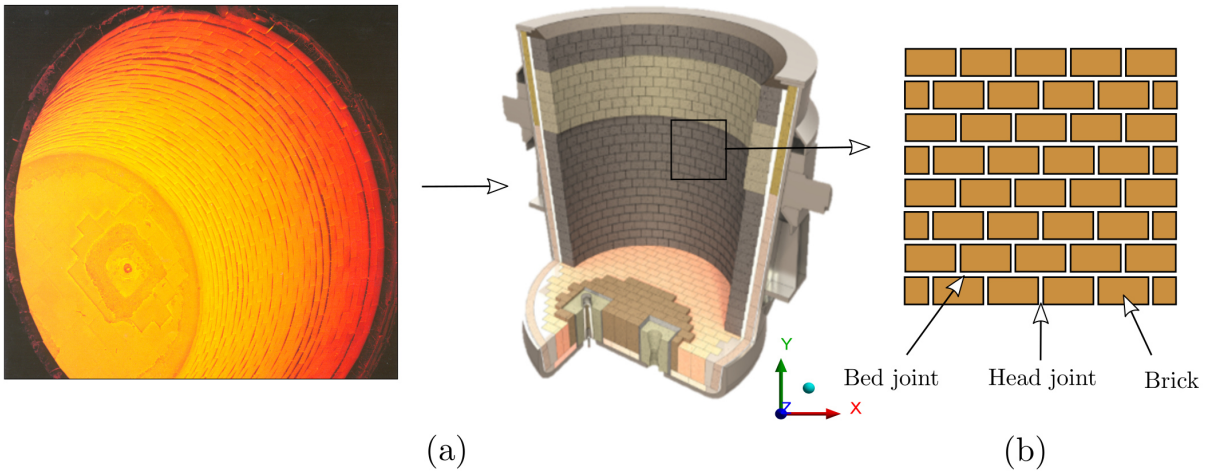

Figure 1.6: (a) Steel ladle lined with mortarless refractory masonry. (b) Schematic of mortarless masonry wall showing the periodically arranged bricks and the gaps between them.

1.4.1 Experimental work

Roughly speaking, previous experimental studies on mortarless masonry can be classified into two main categories depending on the size of specimen and number of bricks used:

- Small scale tests: usually few bricks are used, to measure dry joints thickness and contact area between the adjacent surfaces of the bricks. In addition, to understand the impact of joints, dimensional errors of the bricks and actual contact area on the ultimate compressive strength of a small assembly of bricks.
- Full scale tests: wall scale tests, to investigate the impacts of joints, joints closure and reopening on the global behavior of the structure.

1.4.1.1 Small scale tests

The presence of joints greatly impacts the behavior of mortarless masonry. To investigate this point, Andreev et al. [66] performed uniaxial compression tests at room temperature of two types of magnesia carbon cylindrical samples namely: samples with one dry joint and samples without joint, see Fig. 1.7. The height and diameter of the samples without joint were 100 and 50 mm, respectively. The samples with joint were composed of two cylindrical parts, the diameter and height of each part were 50 mm. In both cases, the samples were drilled from $700 \times 100 \times 120$ mm^3 bricks. For the samples with joint, the joints were maintained as the outer surfaces of the brick. As can be seen from Fig. 1.7, the samples with joint showed nonlinear behavior with progressive strain stiffening as compared to samples without joints. The gradual closure of the joint is responsible for the non linearity in the stress-strain curve. It vanishes when joints close (i.e. the two cylindrical parts reach perfect contact).

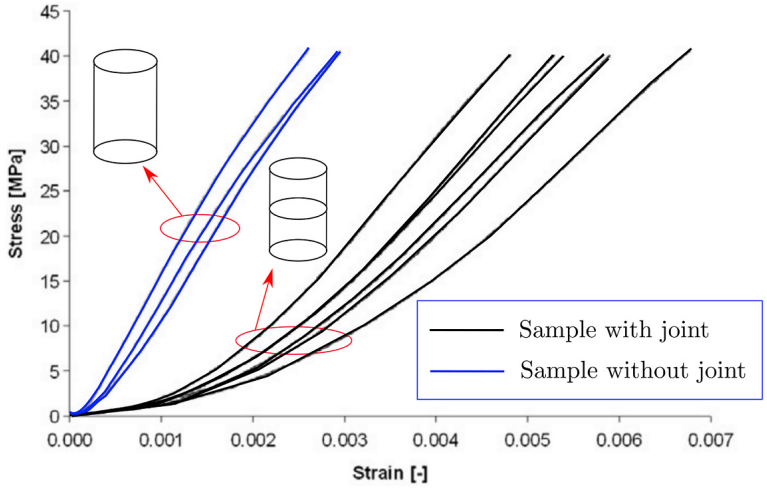

Figure 1.7: Comparisons between stress strain curves of magnesia carbon cylindrical samples without and with dry joints [66].

Understanding joints closure behavior can be deepened by using full field measurement techniques such as digital image correlation (DIC) [67]. To investigate the local and global behavior of dry joints, Allaoui et al. [68] performed uniaxial compression tests, at room temperature, of stack of two magnesia chromite bricks. The dimensions of each brick were $50\times50\times120$ mm^3. There were cut from a bigger bricks with dimension errors of ±1 mm, a common value for refractory bricks. DIC was also used to gather more details about the local and global joints behavior, see Fig. 1.8. Their results clearly demonstrated that joints' behavior is heterogeneous, nonlinear and orthotropic. Local joint opening was noticed (during compression) due to rigid body rotation of the upper brick, see Fig. 1.8. In addition, dimension errors of the bricks determine the joint thickness, while surface roughness is a complement.

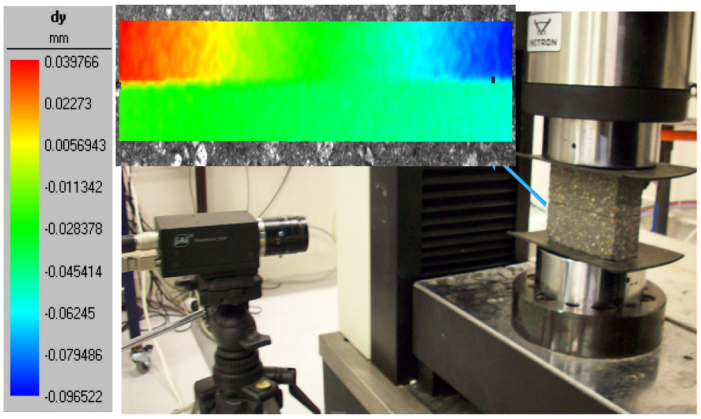

Figure 1.8: Test setup of measuring local and global joints closure behavior using digital image correlation [68].

The dimensional errors and surface roughness of the bricks lead to limited contact between the adjacent surfaces of the joints. This, in turn, leads to stress concentration and a decrease in the

ultimate compressive strength of mortarless masonry. Several experimental studies were carried out to investigate the relationship between actual contact area and load bearing capacity of stack and running bond mortarless masonry systems and to test different strategies for mitigating dimensional errors and surface roughness of the bricks [57, 59, 66, 69]. Usually the contact area is measured using carbon paper [70], pressure based sensors [57] or contact sensors [59].

Chewe Ngapeya and Waldmann [59, 69] performed uniaxial compression tests of a small masonry assembly built up from three civil structural bricks with $500 \times 200 \times 200$ mm^3 size, see Fig. 1.9, to study the impact of contact area on the ultimate compressive strength of the masonry. Different contact layers are applied to the bed joint surfaces. Also, received masonry without contact layers were tested as a reference. Summary of the contact layers and resulting contact areas are given in table 1.1. The contact area was measured using contact sensors. From table 1.1, it can be noticed that increasing the contact area from 23 to 98 % resulted in an improvement factor of 1.97 in terms of maximum failure load. Similar results were obtained by Zahra and Dhanasekar [57]. As reported by Andreev et al. [66] and later by Zahra [71], grinding the surfaces of joints is another efficient solution, as it leads to decrease surface unevenness, helping to attain perfect contact and, thus, increases the contact area and load bearing capacity of the structure.

Table 1.1: Summary of the four masonry assemblies tested by Chewe Ngapeya and Waldmann [59].

Series	Contact layer	Contact area (%)	Failure load (kN)	Improvement
1	Without	23	320	–
2	10 mm - mortar	50	366	1.14
3	10 mm - mortar	55	439	1.37
4	10 mm - Auxetic materials	98	631	1.97

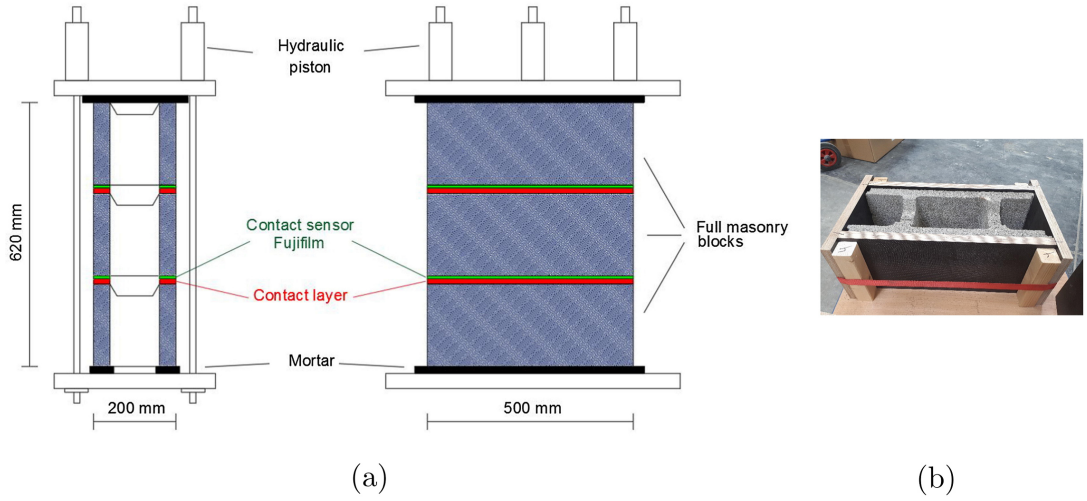

Figure 1.9: a) Schematic of test setup used to investigate the impact of contact area on loading bearing capacity of mortarless masonry assemblages and (b) mold used for contact layer application [59].

1.4.1.2 Large scale tests

The mechanical behavior of mortarless stone masonry subjected to pre-compression load and in-plane shear has been studied by Lourenço et al. [61] and Silva et al. [72]. An example of the in-plane combined loading test setup is shown in Fig. 1.10. The test procedures were as following: first, a pre-compression vertical load was applied to the top stiff beam. Next, the top beam was maintained under force control. Finally, a monotonically increased horizontal displacement was applied to the top beam. The horizontal reaction force and horizontal displacement were recorded.

The main findings of previous combined in-plane loading tests can be summarized as following: [61, 72]:

- The shear capacity of the wall increases with the increase of the pre-compression vertical load.
- Under low pre-compression loads, the failure mode is usually rocking. On the other hand, under high vertical compression loads, diagonal cracking failure mode was observed.
- With the increase of pre-compression load, the horizontal force required to start sliding increases (Coulomb law).
- Surface roughness and bricks imperfections impact the normal and shear behaviors of the walls.

From the reported results, it can be observed that dry joints impact the shear resistance and failure mode of mortarless masonry. Under low compression loads, joints closure and, therefore, contact areas are small. This promotes low values of the horizontal force required to start sliding.

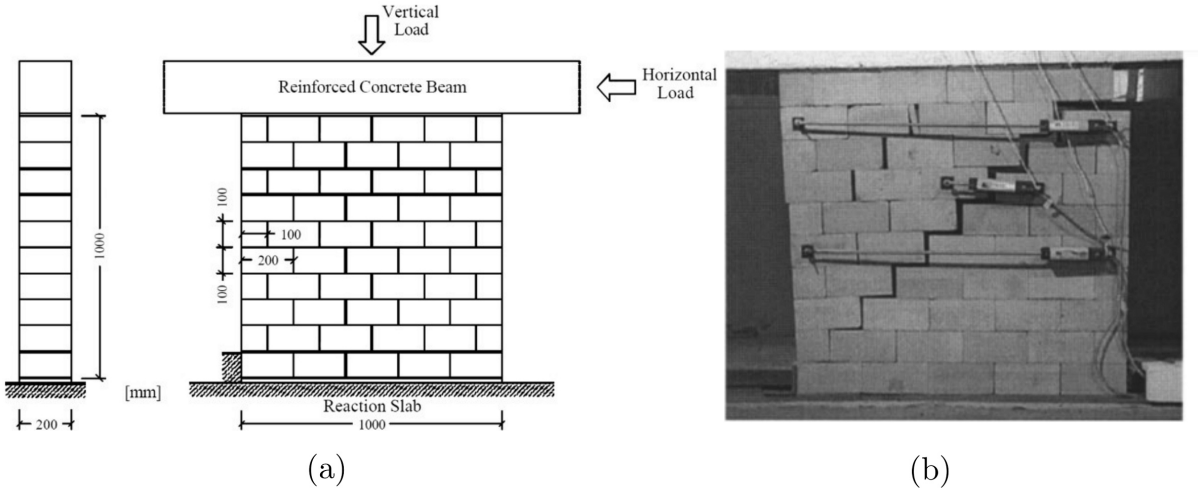

Figure 1.10: Dry joins masonry subjected to a pre-compression and in-plane shear loads: a) schematic representation and b) failure pattern of the wall [61].

The mechanical behavior of magnesia chromite mortarless refractory masonry subjected to biaxial compression load has been studied by Prietl et al. [73–76]. The biaxial compression test setups at room temperature and 1200 °C are shown in Fig. 1.11. The testing procedures were as

following: first a pre-compression load was applied to the two moving ceramic plates at the same time and then, it was stopped in the direction for which the LVDTs detected a displacement while continuing in the second direction until the LVDTs, in the corresponding direction, detected a displacement. Finally, monotonically increasing loads were applied to both directions at the same time. For the high temperature test, the test field was covered by a heating hood. The temperatures of the top face (hot face) and bottom face (cold face) were measured. During heating, the masonry wall was free to expand. Once the wall reached the thermal steady state, the in-plane biaxial compression load was applied similar to the room temperature test. The temperatures of the hot and cold faces during load application were around 1200 °C and 800 °C, respectively.

The main findings of previous biaxial compression tests are summarized as following:

- The macroscopic mechanical behavior of the wall is orthotropic.
- Under the same applied load and for both room and high temperature tests, the resulting strains in the direction perpendicular to the surfaces of bed joints are higher than that in the direction perpendicular to the surfaces of head joints.
- The macroscopic mechanical behavior of the wall is nonlinear due to gradual closure of joints and the increase of the effective stiffness with joints closure.
- As compared to the room temperature test and under the same applied load, the strains (and displacements), in the two directions are higher due to the decrease of the material stiffness with increasing the temperature and the viscoplastic behavior of refractories at high temperature.

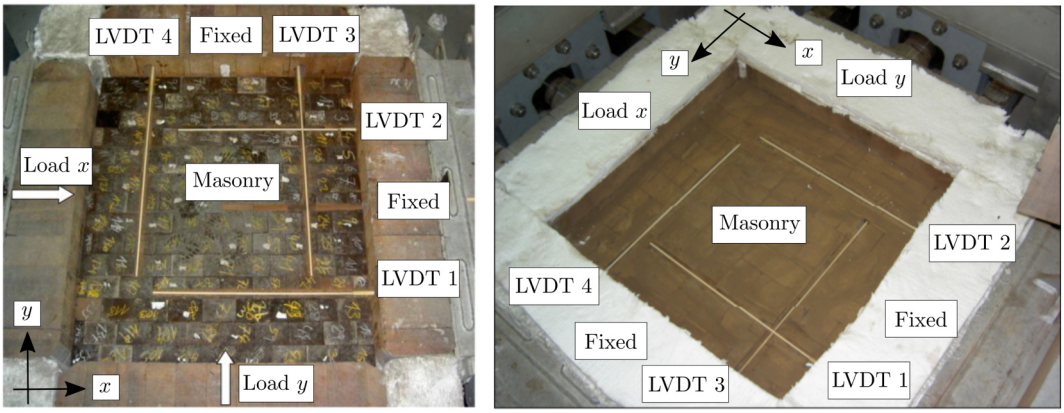

(a) (b)

Figure 1.11: Setup of the biaxial compression tests a) at room temperature and b) 1200 °C of magnesia chromite refractory masonry walls [73–76].

1.4.2 Numerical work

Numerical models represent an efficient way to study the mechanical behavior of small and large scale mortarless masonry structures. Several Finite Element (FE) numerical models are available in the literature [57, 61, 66, 76–79]. The majority of them are based on the micro

modeling approach [57, 61, 66, 77–79]. Only one multi scale model of mortarless masonry [76] can be found in the literature. Also, limit analysis and discrete element modeling of the collapse mechanism of masonry walls subjected to in-plane and out-of-plane loading conditions can be found in the literature [58, 60, 80–83]. FE based models are reviewed below.

1.4.2.1 Micro modeling

Micro modeling approach provides accurate results as the detailed geometry of the bricks and the joints are separately modeled and, almost, all the information about the masonry components are taken into account. Within the framework of micro modeling, different models were developed. They differ by the constitutive laws used to describe the behavior of dry joints and the physical models of joints. The majority of these models assumed rigid or purely elastic bricks and all material non-linearity is concentrated in the joints.

To investigate the impact of bed joint unevenness on the mechanical behavior of hollow stack concrete bricks, Zahra and Dhanasekar [57] developed a 3D-FE model of two hollow concrete bricks. The locations and elevations of the randomly distributed high points were determined experimentally using pressure based sensors, and later implemented in the physical FE model by modifying the mesh (increasing the elevation of some nodes), see Fig. 1.12. It should be noted that the predetermined locations and elevations of the high points is valid only for the current bricks configuration. Changing one of the bricks (or even rotating one brick) would require another experiment.

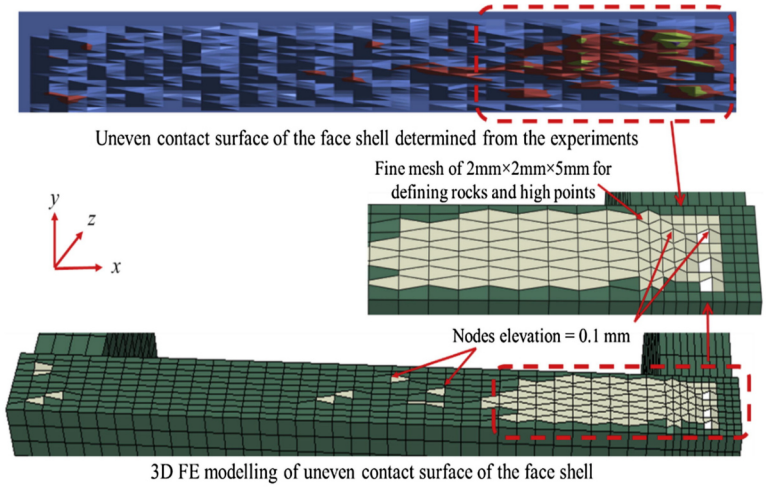

Figure 1.12: Detailed micro model developed by Zahra et al. [57].

To investigate the impact of initial contact area and initial joint thickness on the mechanical behavior of two stacks of refractory bricks, Andreev et al. [66] developed a FE axi-symmetric model shown in Fig. 1.13. The initial contact area and joint thickness (i.e. before loading) were controlled by changing two geometrical parameters in the physical model, R_1 and D, see Fig. 1.13. The authors assumed that joints closure starts from the center to the sides of the bricks. It

has been shown that a nonlinear joint closure behavior can be obtained by controlling the initial contact area and initial joint thickness.

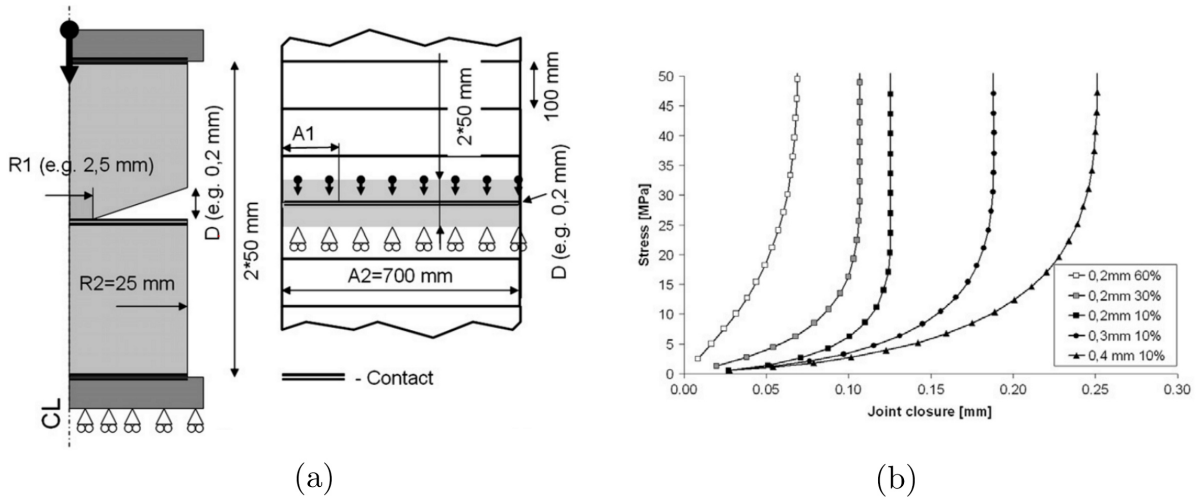

Figure 1.13: (a) Micro model developed by Andreev et al. [66] to investigate the impacts of joints thickness and initial contact area on the mechanical response of two stacks of refractory bricks. (b) Impacts of initial contact area and initial joint thickness on the mechanical behavior.

As mentioned in section 1.4.1.1, the local behavior of joints is heterogeneous and complex, due to local joints opening and the aforementioned imperfections. Therefore, the detailed micro models presented above are not efficient (especially from computational point of view due to the level of details). For this reason, recent studies focused on describing the global (or average) behavior of the joints instead of the local behavior. The joints were considered as either an interface with zero thickness [61, 77, 78] or a thin layer perfectly bonded to the bricks [84], see Fig. 1.14.

In the case of zero thickness interface, the normal $k_{n,\,\text{joint}}$ and shear $k_{s,\,\text{joint}}$ stiffnesses of the joint are expressed as [61]:

$$k_{n,\,\text{joint}} = \frac{1}{h_b\left(\frac{1}{E_{\text{wall}}} - \frac{1}{E_{\text{brick}}}\right)} \tag{1.44}$$

$$k_{s,\,\text{joint}} = \frac{k_{n,\,\text{joint}}}{2(1+\nu)} \tag{1.45}$$

Where h_b, E_{wall} and E_{brick} are the bricks height, Young's modulus of the wall and the bricks, respectively. ν is the Poisson's ratio of the bricks. Equations 1.44 and, therefore, 1.45 requires Young's modulus of the wall (in the loading direction that varies with load level) and does not take into account the strain stiffening behavior due to gradual joints closure.

Another equation of k_n was introduced by Thanoon et al. [77, 78] which is similar to pressure-over closure soft contact model in Abaqus [85]:

$$k_{n,\,\text{joint}} = k_{ni,\,\text{joint}} + Ag^B \tag{1.46}$$

Where $k_{ni,\,\text{joint}}$ and g are the initial stiffness of joints due to initial contact and instantaneous joint thickness (i.e. over-closure in Abaqus), respectively. A and B are constants determined

form experiments. Using this equation, accurate predictions of the mechanical behavior of small scale masonry subjected to uniaxial compression were obtained.

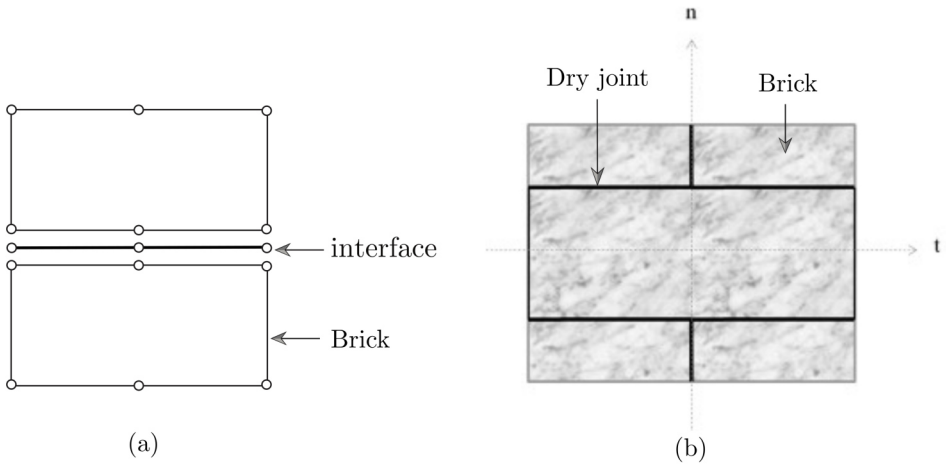

Figure 1.14: Simplified micro models of mortarless masonry (a) joints reduced to an interface with zero thickness [61,77,78] and (b) joints considered as a thin layer bonded to the bricks [84].

In the second case, joints are considered as a thin layer perfectly bonded to the bricks, see Fig. 1.14-b [84]. The global behavior of the joint is determined using the DIC setup presented in Fig. 1.8. It is expressed as:

$$\sigma_{nn}\left(\varepsilon_{nn}\right) = E_e^j \varepsilon_{nn} + \sigma_0 \varepsilon_{nn}^{m_0} \tag{1.47}$$

Where σ_{nn} and ε_{nn} denote the normal stress and strain respectively. E_e^j, σ_0 and m_0 are constants determined form the experiment. The homogenized mechanical behavior of the RVE was determined using the mechanical homogenization approach described before.

Up to now, the presented micro models considered few bricks and focused on modeling the impact of surface unevenness. Recently, Chewe Ngapeya et al. [69, 79] developed a FE micro model to investigate the impact of dimensional errors of the bricks on the load bearing capacity of concrete masonry, see Fig. 1.15. As can be seen from the figure, bricks with ± 2 mm dimension errors are arranged in a running bond texture. Their results indicated that dimensional errors (Δ) lead to stress concentrations near head joints and decrease the load bearing capacity of the wall.

The micro FEM approach is only suitable for modeling few bricks and joints. Because considering all the bricks and joints of a wall (hundreds of bricks) leads rapidly to high computational costs and many solution convergence problems.

1.4.2.2 Multi scale modeling

Multi scale modeling splits the structural problem into two scales: a homogeneous equivalent medium studied at the macroscopic scale with homogeneous properties determined by homogenizing the microscopic stress and strain fields in a carefully selected RVE (microscopic scale).

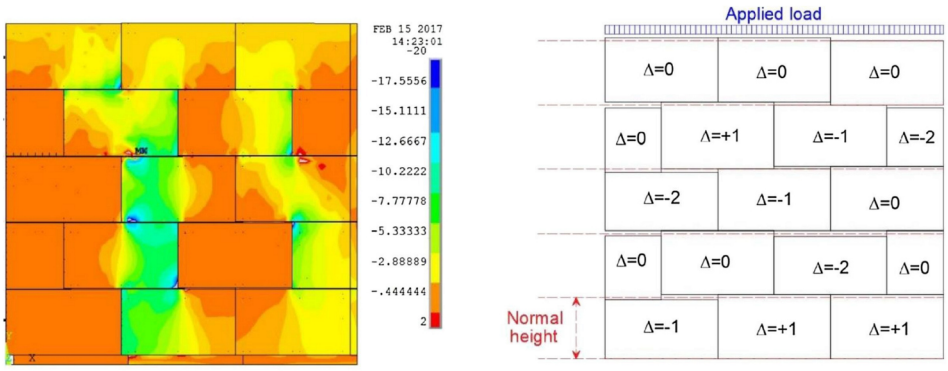

(a) (b)

Figure 1.15: Micro FE model developed by Ngapeya et al, to study the impact of dimension errors (Δ) of the brick on the loading bearing capacity of a running bond concrete masonry [69, 79].

The homogenized properties are usually obtained using mechanical homogenization technique described before.

Nguyen et al. [76] developed and validated a homogeneous equivalent material model for the simulation of mortarless refractory masonry structures. The bricks are considered to obey isotropic linear elasticity with zero dimensional errors. Also, perfect joints with two states (open or closed, progressive closure of joints was neglected) were considered. Four joint states are predefined based on the states of bed and head joints, see Fig 1.16. The transition criteria from one joint state to another are written in terms of macroscopic strains. The effective elastic behavior of the different joint states was determined using FE-based linear homogenization technique. The developed model was validated by comparing the numerical and experimental results of refractory masonry wall subjected to biaxial compression at room temperature, presented in Fig 1.11a. Their results indicated that the macroscopic behavior of the masonry structure is orthotropic and nonlinear due to the change from one joint state to another during loading and the difference between the number of bed and head joints in the studied wall. The multi scale model developed by Nguyen et al. [76] can be used to simulate large scale structures, such as steel ladles and furnaces, with reasonable computational costs.

1.5 Experimental and numerical studies of masonry with mortar joints

Masonry systems with mortar joints are composed of units, mortar joints and unit/mortar interface. The latter represents the interaction behavior between the units and the mortar joints. They can be classified into two main categories according to their operating temperature: a) civil structural masonry that normally operates at room temperature or sometimes under fire situations and b) refractory masonry for high temperature industrial applications (> 1000 °C). The main differences between the two categories are the constitutive material of the units and the mortar.

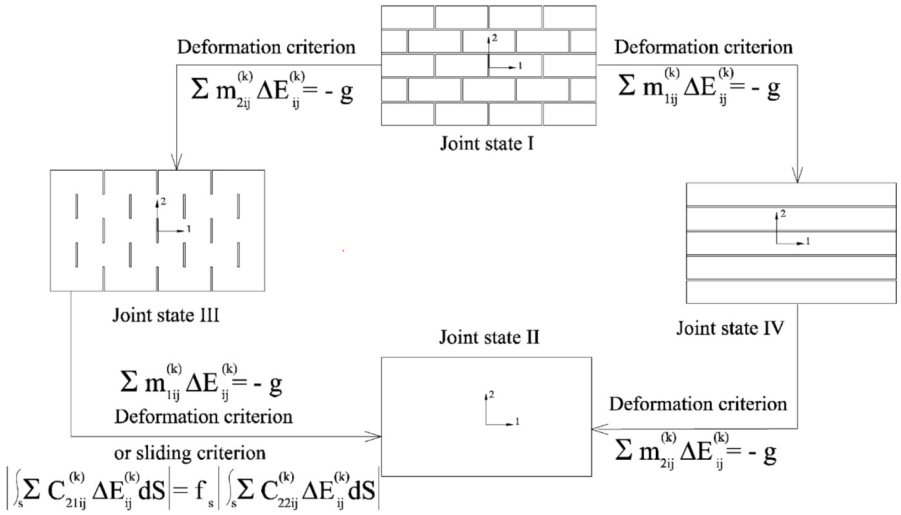

Figure 1.16: Multi scale model of mortarless refractory masonry developed by Nguyen et al. [76].

In the first category, units can be blocks, irregular stones, bricks, adobes, ashlars and others. Mortar can be bitumen, clay, chalk, cement-based, lime, glue, or others.

Several arrangements of the units and joints can be found depending on the stretcher and header arrangements, see Fig. 1.17. In the second category, units and mortar are made of refractory based materials and, usually, arranged in running bond texture, see Figs. 1.17. Most of previous experimental and numerical studies on masonry with mortar joints focused on the civil structural category. The most important findings of these studies are reviewed in sections 1.5.1 and 1.5.2

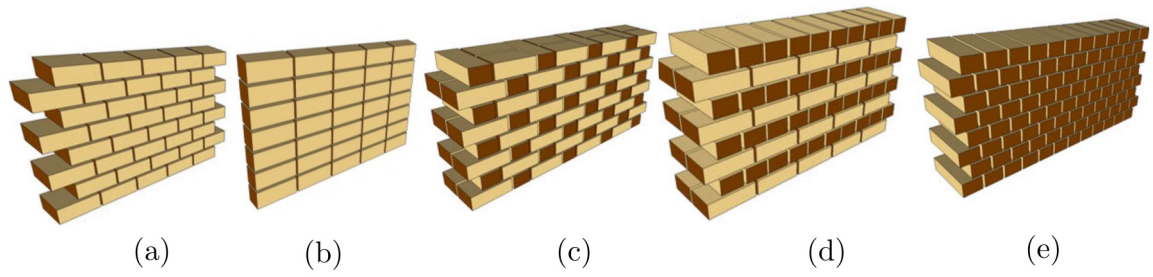

Figure 1.17: Schematic representations of different textures of masonry with mortar joints: (a) running bond, (b) stack bond, (c) Flemish bond, (d) English bond and (e) header bond.

1.5.1 Experimental work

1.5.1.1 Brick-mortar interface

The brick-mortar interface is considered as the weakest link in the structure and it can fail under tensile or shear loads. Therefore, its behavior is widely investigated to obtain its failure criteria in terms of ultimate tensile strength, cohesion, friction angle and others.

Tensile failure of the brick-mortar interface is one of the major reasons of collapse of masonry structures. Usually, the tensile strength of masonry is considered as that of the interface. Different test setups were developed to characterize the ultimate tensile strength of the brick/mortar interface such as direct tensile, wedge splitting and bending tests. A schematic of room temperature direct tensile tests, on calcium silicate and solid clay small masonry units in combination with different types of mortars, carried out by Van der Pluijm is shown in Fig. 1.18-a [86, 87]. Brulin et al. [88] developed a test setup to characterize the strength of brick-mortar interface at high temperature. The specimens of these tests are shown in Fig. 1.19-a. These specimens were placed inside a furnace to be heated up to the required temperature and, then, tested.

Shear failure of brick-mortar interface is another major collapse mechanism of masonry systems. Usually, shear loads are combined with compression or tensile loads. Therefore, in experimental investigations, pure shear modes were changed either to shear-tension or shear-compression modes. The main challenge in performing shear tests is to maintain a uniform stress state in the mortar joints. Several studies were carried out to develop test setups and to characterize the shear behavior of brick mortar interface at room and high temperatures [86–93]. Van der Pluijm [87] introduced the compression-shear test setup presented in Fig. 1.18-b. It has been further improved to perform tension-shear tests, see Fig. 1.18-c. Brulin et al. [88] developed the slanted shear test setup shown in Fig. 1.19-b to characterize the shear behavior of refractory brick-mortar interface at high temperature.

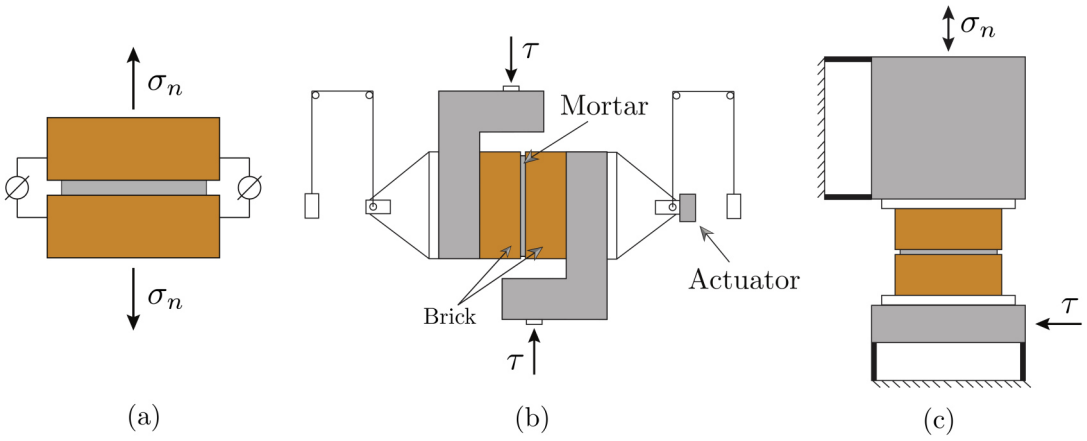

Figure 1.18: Schematics of test setup for the characterization of brick mortar interface: (a) direct tensile test (b and c) shear tests [86, 87].

1.5.1.2 Small scale tests

Several tests were carried out on small assembly of civil structural masonry to characterize its mechanical behavior and/or failure patterns [94–99]. These tests include uniaxial tensile tests, uniaxial compression tests and biaxial compression tests.

The tensile strength of masonry depends on the mechanical properties of the bricks, mortar and brick-mortar interface and on the applied load orientation with respect to bed joints. Previous

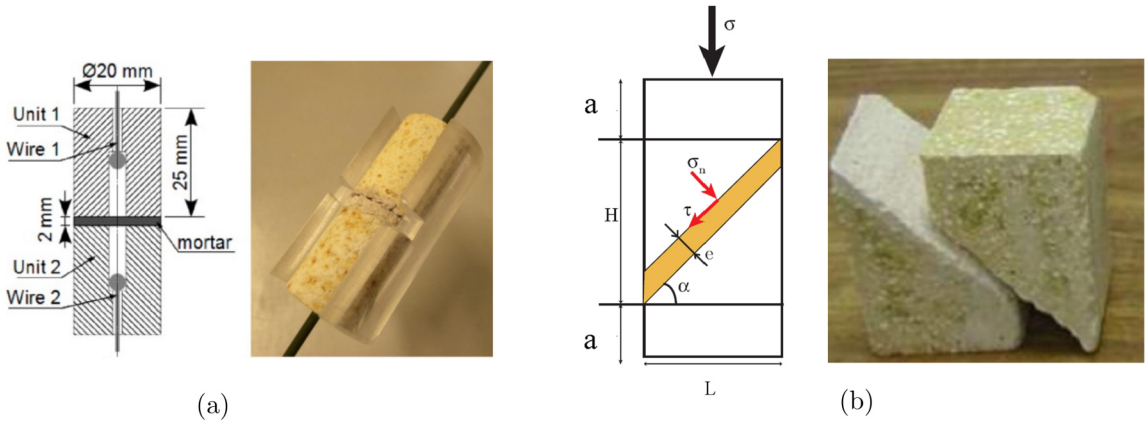

(a) (b)

Figure 1.19: Characterization of brick/mortar interface at high temperature: samples of (a) direct tensile tests and (b) slanted shear tests [88].

experimental studies reported that:

- For strong bricks, weak interface, and tensile loads normal to bed joints, the tensile strength of the masonry is considered as that of the interface and cracks pass through bed joints or bed interface [94].
- For weak bricks, strong interface, and tensile loads normal to bed joints, separate experimental tests are required as cracks initiation and propagation are noticed in the bricks [94].
- For strong bricks, weak interface, and tensile loads normal to head joints, cracks initiation and propagation are in head joints [95].
- For weak bricks, strong interface, and tensile loads normal to head joints, cracks initiation and propagation are noticed in head joints and the center of the bricks [95].

Page [96] performed experimental tests of small assembly of solid clay masonry subjected to uniaxial tensile loads with different angles θ from the bed joint surface, see Fig. 1.20. It can be seen that the experimental crack pattern depends on the angle of the applied tensile load. For angles between 0° and 22.5° separation along head joints can be observed. For angles between 67.5° and 90° debonding along bed joints appeared. Finally for tensile loads oriented 45°, combination of bed and head interface failure was noticed, see Fig. 1.20.

The compressive strength of masonry in the direction normal to bed joints is considered as one of the most relevant properties. It depends on the mechanical properties of the bricks and the mortar. Previous experimental studies showed that for strong bricks and weak mortar, the compressive strength of the masonry is in between that of the mortar and the brick [99], see Fig. 1.21-a. On the other hand, for strong brick and mortar, the compressive strength of the masonry is below that of the mortar and the brick [98], see Fig. 1.21-b.

Page [96, 97] performed experimental tests of small assemblage solid clay masonry subjected to uniaxial compression loads with different angles θ from the bed joint surface, see Fig. 1.22. It can be seen that the experimental crack pattern depends on the angle of the applied compression load. For angles between 0° and 22.5° separation along head joints can be observed. For angles between 45° and 67° debonding along bed and head joints as well as cracks through the bricks

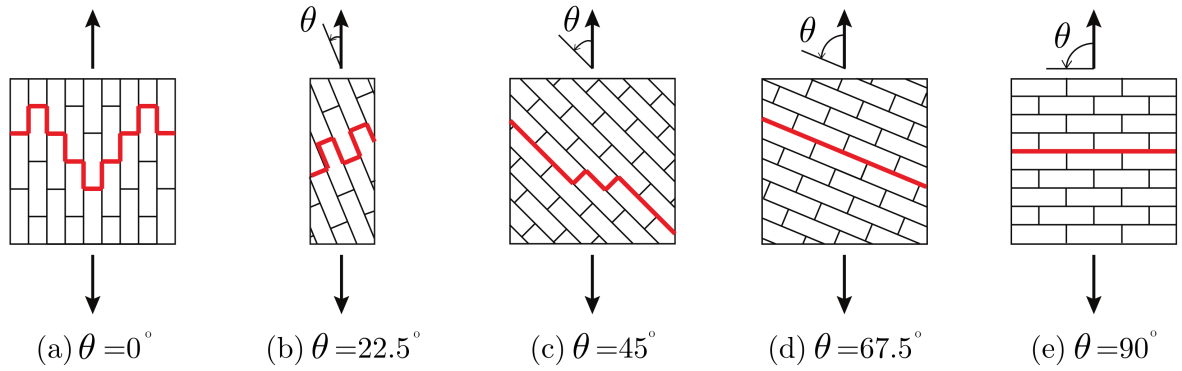

Figure 1.20: Failure patterns of masonry assemblages subjected to uniaxial tensile loads with different angles θ from the bed joint surface [96].

appeared. Finally, for compressive loads normal to bed joints (90°), cracks in head joints and bricks were noticed, see Fig. 1.22.

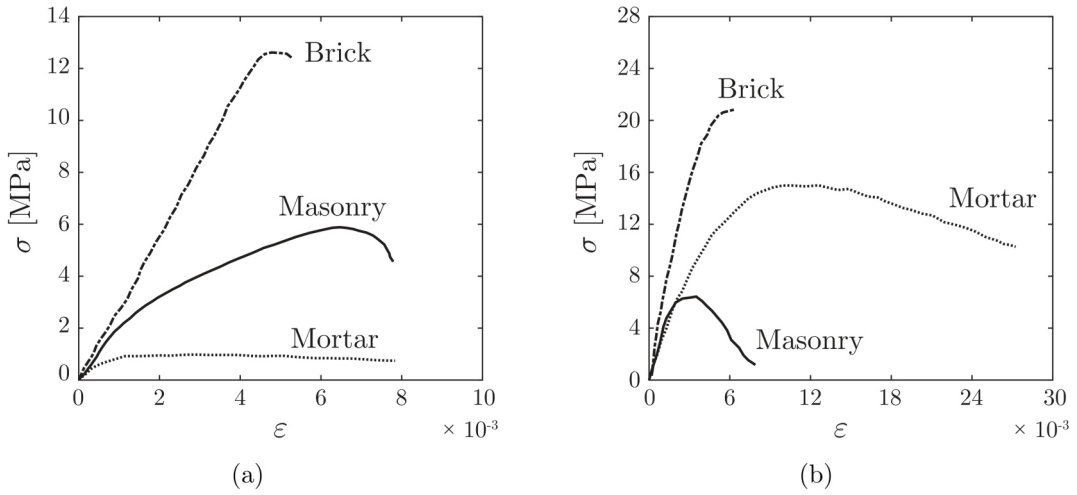

Figure 1.21: Stress-strain curves for mortar, brick, and masonry: (a) weak mortar [99] and (b) strong mortar [98].

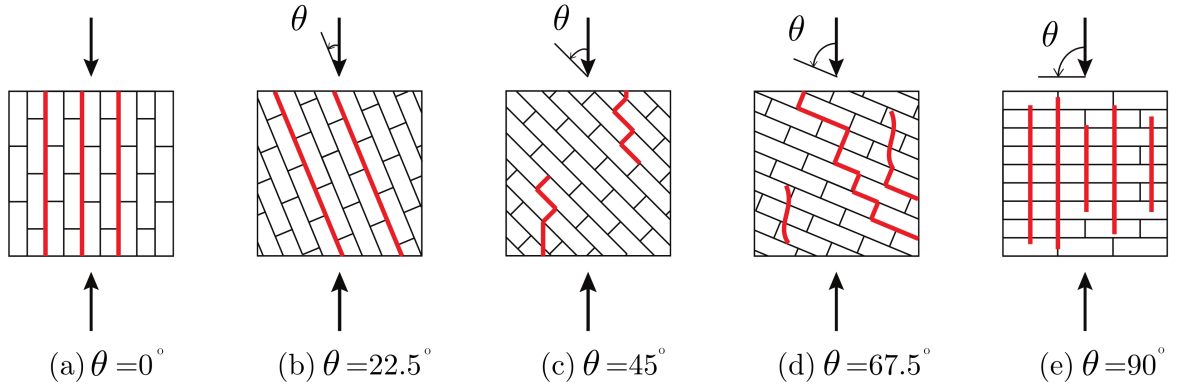

Figure 1.22: Failure patterns of masonry assemblages subjected to uniaxial compression loads with different angles θ from the bed joint surface [96].

To fully characterize the mechanical behavior and failure envelope of solid clay masonry, Page [96, 97] carried out 360 biaxial compression tests of a square small assembly of solid clay masonry. The schematic of the test setup and an example of the failure envelope are shown in Fig. 1.23. The biaxial load orientations with respect to bed joints were varied (as in uniaxial tests). There results clearly indicated that the masonry has orthotropic behavior with higher strength in the direction normal to bed joints (higher as compared to direction parallel to bed joints). Moreover, the highest resistance was observed for biaxial compression loads.

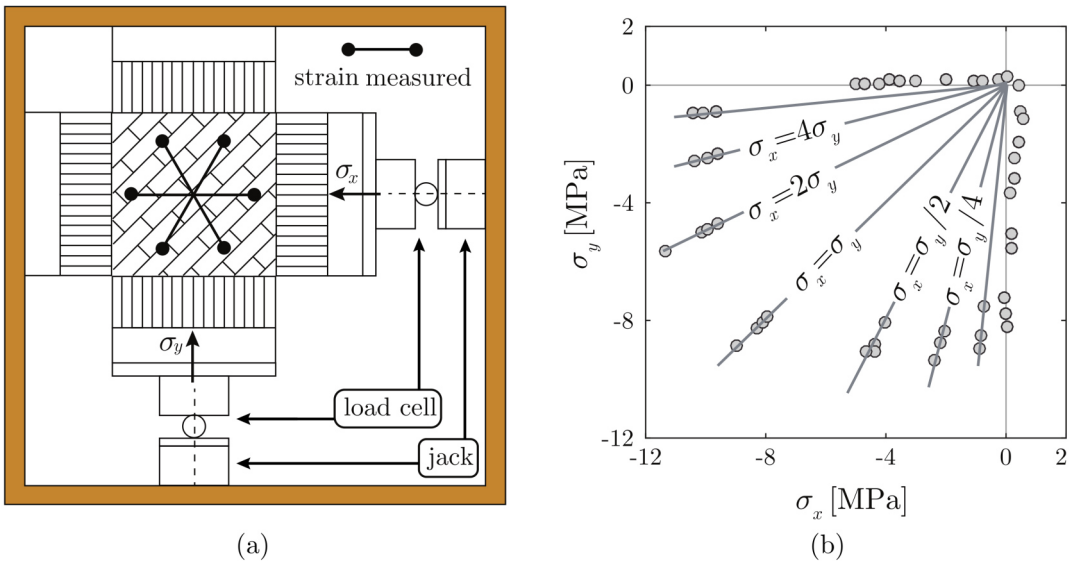

Figure 1.23: (a) Schematic of biaxial compression test setup for the characterization of biaxial strength of masonry performed by Page and (b) biaxial strength envelope of masonry [96, 97].

1.5.1.3 Large scale tests

Traditionally, experimental results of two large scale tests of masonry walls are widely used by the masonry community for the calibration of numerical models. The two tests are: pre-compression load and in-plane shear tests of masonry walls performed by Raijmakers and Vermeltfoort [11] and bending tests (also called deep beam tests) carried out by Page [12]. Both experimental tests are carried at room temperature.

Schematic of the masonry wall with mortar joints subjected to uniaxial pre-compression and in-plane shear loading are depicted in Fig. 1.24 [11]. Solid clay bricks with length of 210 mm, height of 100 mm and depth of 52 mm are periodically arranged in a running bond texture. The thickness of the mortar joints is 10 mm. The size of the wall is $1000 \times 990 \times 52$ mm^3 and it is made up of 18 courses, 16 of them are active and 2 are fixed to the stiff steel beams (the 2 courses in contact with the steel beams, the top and bottom ones, see Fig. 1.24). The testing procedures were as following: first, a pre-compression vertical load was applied to the steel beam. Then, the top steel beam has been kept under displacement control and no vertical movements were allowed. Finally, a monotonically increasing horizontal load was applied to the top right surface

of the steel beam. The force-displacement relationship and the crack pattern were recorded. The results of these tests are presented later in chapter 4.

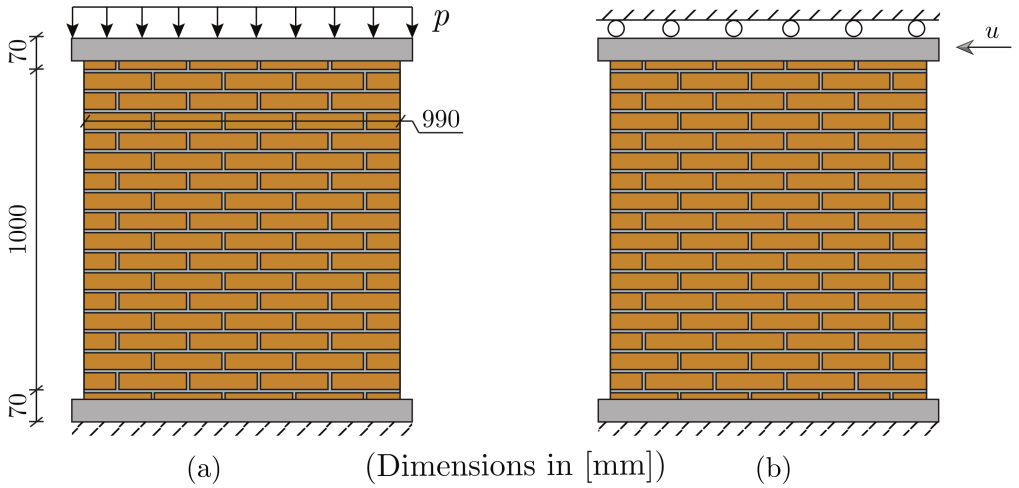

Figure 1.24: Test procedures for Raijmakers-Vermeltfoort panels: (a) application of vertical pre-compression load and (b) horizontal loading under displacement control [11].

In 1978, Page [12] performed bending tests of masonry walls with mortar joints as described in Fig. 4.34. Pressed solid clay bricks with length of 122 mm, height of 37 mm and depth of 54 mm are periodically arranged in a running bond texture. A vertical force, P, was applied to the top stiff beam and the resulting vertical stresses were determined at some points near mid height of the wall. Tests with different values of P were performed. The results of these tests are presented later in chapter 4.

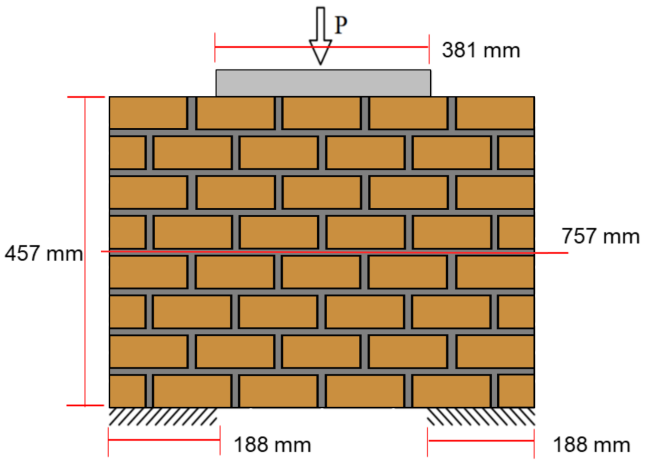

Figure 1.25: Schematic of masonry wall with mortar joints subjected to bending [12, 100].

1.5.2 Numerical work

1.5.2.1 Micro modeling

In the micro modeling approach, the bricks, mortar joints and interface are modeled separately. Therefore, the computational size of the problem is high. This represents the main drawback of the micro modeling approach. In previous studies, different constitutive laws were proposed for modeling masonry constitutes [92, 101–107]. They can be summarized as:

- Constitutive laws for the brick:
  1. Rigid.
  2. Deformable with linear response.
  3. Deformable with nonlinear response (damage).
- Constitutive laws for the mortar:
  1. Continuum material or interface with linear response.
  2. Continuum material or interface with nonlinear response.

The most two common micro modeling techniques are detailed micro modeling and simplified micro modeling, see Fig. 1.26. In the detailed micro modeling, both the bricks and joints are represented by continuum medium (continuum finite elements), while the interface is considered as discontinuous elements (Fig. 1.26-a). In the simplified micro modeling the mortar joint and brick-mortar interface are reduced to an interface with no thickness (Fig. 1.26-b).

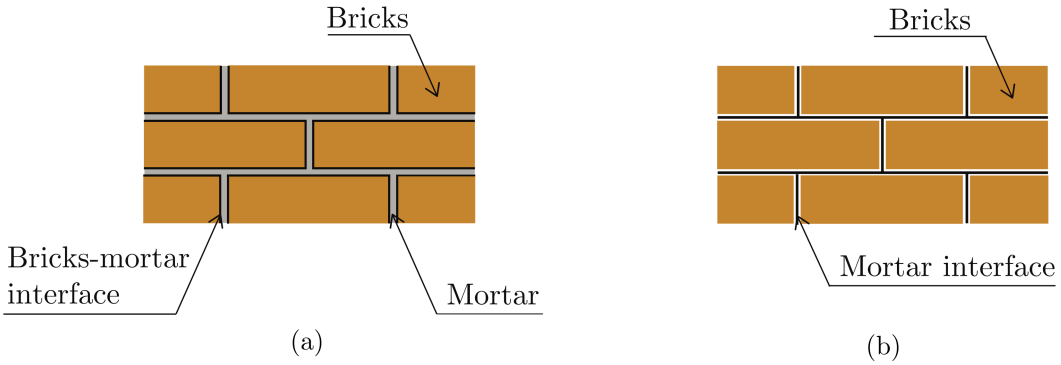

Figure 1.26: Micro-modeling approaches of masonry with mortar joints. (a) detailed micro modeling and (b) simplified micro modeling.

The most widely used interface constitutive model is the so called "multi-surface plasticity", proposed by Lourenço and Rots [102], see Fig. 1.27-a. They assumed that the out of plane normal stress and shear strain components are negligible. Also, the out of plane displacement is constant through the thickness of the masonry following a plane-stress condition. Under these assumptions, the authors proposed a composite yield surface to simulate the tensile and shear failure of mortar joints and crushing of units under high compression stresses. The 3D version of this interface model is shown in Fig. 1.27-b [108, 109]. It takes into account the impacts of 3D stresses and the presence of vertical joints in the depth of the wall, in the case of Flemish and English bond masonry, see Fig. 1.17.

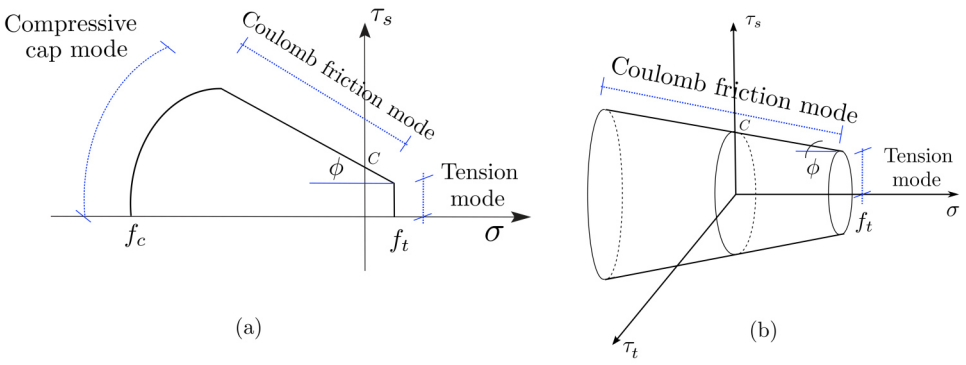

Figure 1.27: Multi-surface plasticity model used for modeling (a) line interface [100, 102] and (b) surface interface [108, 109].

1.5.2.2 Macro modeling

To reduce the computational burden and be able to model large scale structures, several macro models were developed in the literature [102, 110–114]. In the macro modeling approach, the masonry is represented as either isotropic or orthotropic continuum medium. Therefore, the constituent materials of the bricks and joints are no longer distinguishable. The major benefit of macro models is the acceptable computational time. The mechanical properties of the continuum medium is usually determined by experimental tests on small assemblage or wall scales as described in section 1.5.1.2. The main drawback of this approach is the high number of tests required to characterize the masonry structure.

Several material models have been used to predict the mechanical behavior of large scale masonry structures using macro modeling approach [102, 110–114]. For example, Valente and Milani [115] employed the Concrete Damage Plasticity (CDP) model to investigate the mechanical behavior of historical masonry towers. The CDP model was originally developed by Lubliner et al. [116] for concrete structures, but it gives satisfactory results for masonry as well. As the tensile strength of masonry is far below the compression strength, Lee and Fenves [117], proposed an asymmetric damage model to take into account the asymmetric damage of the material. The compression and tension damage responses are combined by using a weighting factor. Based on the theory of plasticity, Lourenço et al. [102] proposed a constitutive macro model for the masonry. Rankine and Hill criteria were used to simulate the compressive and tensile behavior.

1.5.2.3 Models based on the state of joints

As the brick-mortar interface is generally the weakest link in the structure and it can be damaged or undamaged, some authors developed numerical models based on the damage state of bed and head joints. The first model was proposed by Luciano and Sacco [118, 119], see Fig. 1.28. The authors defined 8 joint states of the masonry based on weather the vertical and horizontal mortar joint is damaged or not. Then, the equivalent homogeneous elastic properties of each joint state

was determined using FE-based homogenization approach.

Using the periodic unit cell symmetry of Luciano and Sacco model, Landreau [120], and later Brulin [121], proposed to reduce the number of joint states from 8 to 4. As can be seen in Figs. 1.28 and 1.29, states S3, S4, S5 and S7 of Luciano and Sacco model are deleted. The effective elastic behavior of each state is determined using FE-based homogenization. The joints opening and transition criteria from one state to another were written in terms of Mohr-Coulomb friction (for shear failure) and tension cut off (for tensile failure). The developed model was used to simulate large scale industrial structures such as coke ovens and blast furnaces [120, 121].

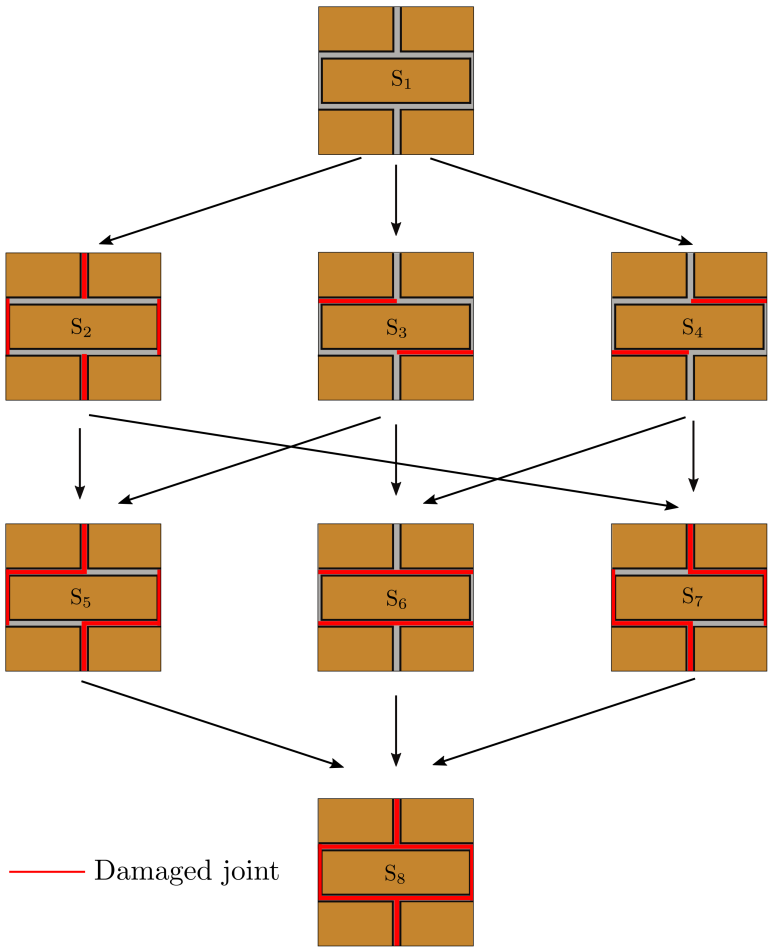

Figure 1.28: Possible joint states and paths of damage in masonry with mortar joints [118, 119].

1.6 Numerical modeling of steel ladle

Steel ladles are industrial vessels that are used in the steel industry for liquid steel transportation and refinement. Normal operating conditions of steel ladles include high operating temperatures (around 1700 °C), high thermal stresses, slag corrosion, and degradation of layers in contact with liquid steel. To withstand these severe operating conditions, the steel ladle design is based on the concept of multi-layer design. Each layer has unique thermal, mechanical, physical, and

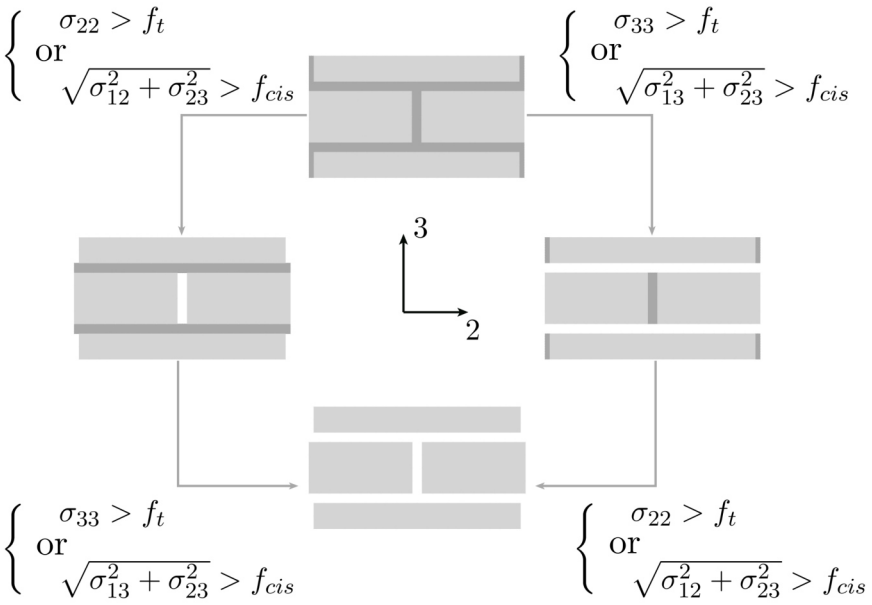

Figure 1.29: Model based on joint states proposed by Landreau [120].

chemical properties. The most critical layer in the steel ladle is the working lining, layer in contact with liquid steel, as its temperature values are the highest within the ladle. In addition, this layer is usually subjected to thermal shock and severe chemical environments, leading to thermomechanical degradation [9, 122–126]. Working linings could be made of refractory masonry with dry joints or castables.

The design and optimization of steel ladles require accurate thermal and mechanical numerical models with proper boundary conditions and solution domains. Most of previous studies typically focused on studying the thermal and heat transfer behavior of steel ladles during the steel making process. For instance, Xia and Ahokainen [127] numerically analyzed the impact of preheating temperature and slag heat losses on thermal stratification in a steel ladle during the holding step. Similarly, Glaser et al. [128] developed a 2D axisymmetric numerical model to investigate heat transfer behavior and heat losses during the liquid steel teeming step. Recently, Santos et al. [129] presented a 2D axisymmetric transient thermal numerical model to investigate the impact of lining design on the transient thermal behavior and energy consumption of a steel ladle during preheating, holding liquid steel, and being empty.

With regard to the thermomechanical modeling of steel ladles, few studies have been carried out. Considering all the bricks and joints of the working lining, as well as the contact between them, leads to an increase in the computational time and cost. Furthermore, a converged solution of the computations is not guaranteed. For these reasons, a number of authors have neglected the presence of joints [130], while others have considered only few bricks and joints between them [131]. For example, Yilmaz [130] used a 2D steady-state axisymmetric finite element simulation to investigate the thermomechanical response of a ladle. The presence of joints within the working lining and bottom has been neglected and all lining layers have been considered isotropic. Aidong et al. [131] investigated the influence of material properties and lining thickness

on the thermomechanical behavior of the slag zone using 2D transient finite element analysis of few bricks in the slag line zone and Taguchi method. Due to the selected 2D solution domain, only one head joint with 0.4 mm thickness has been considered while bed joints have been neglected.

A reasonable approach to consider the presence of joints and their impact on the thermomechanical response of mortarless masonry without increasing computation costs is to replace the bricks and joints by an equivalent material. Gasser et al. [128] used the multi scale model of Nguyen et al. [76] and developed steady-state 3D finite element models of a steel ladle to investigate the influence of bottom design (radial, parallel, and fish bone designs) and joint thickness on the resulting thermomechanical stresses. Joints in the ladle bottom have been considered, whereas joints in the ladle wall have not been taken into account. Their results indicate that using a radial design of the ladle bottom results in lower values of the von Mises stress in the steel shell as compared to parallel and fish bone designs. In addition, von Mises stresses in the steel shell decrease with the increase in joint thickness. Similar model was developed by Gasser et al. [132] to investigate the impact of joint thickness on the resulting steady state thermomechanical stresses. Their results indicated that increasing joint thickness leads to a reduction in resulting thermomechanical stresses.

1.7 Conclusion

In this chapter, the state of the art of mechanical homogenization of heterogeneous solids as well as experimental and numerical studies of masonry with dry and mortar joints are reviewed. Details about the different homogenization techniques of heterogeneous solids were presented. The capabilities and limitations of the different modeling techniques of masonry with dry and mortar joints as well as steel ladles were discussed. The previous experimental studies of masonry with dry and mortar joints were introduced. The above review of experimental and numerical studies of refractory masonry with dry and mortar joints as well as numerical studies of steel ladles shows that:

- Only two large scale tests of refractory masonry walls subjected to biaxial compression at room and high temperature exist. The behavior of refractory masonry walls under different loading conditions at room temperature and their thermomechanical behavior when subjected to different thermomechanical loads are still needed to be investigated experimentally.
- Previous numerical studies on masonry with dry joints focused on civil structure masonry using micro FE approach and considered elastic behavior of the bricks. However, these models are not suitable to model large sized structures such as steel ladles and furnaces due to high computational costs. In addition, only one multi scale numerical model has been developed in the literature and it is suitable to simulate only the elastic or thermo-elastic behavior of the masonry. This multi scale model needs further developments to increase

it's accuracy and to take into account the viscoplastic behavior of refractories at high temperature.

- Previous numerical studies on masonry with mortar joints focused on civil structure masonry and considered elastic bricks and damageable joints. However, these models are not suitable to predict the mechanical behavior of refractory masonry with mortar joints. Because at high temperature, refractory masonry with mortar joints has orthotropic elastic-viscoplastic damageable behavior.
- Previous numerical studies of steel ladles focused on their steady-state thermomechanical behavior and did not show their transient nonlinear thermo-mechanical response during a complete thermal cycle of the steel-making process. In most cases, either a simple 2D cut of few bricks is used as a physical model or the joints were neglected and the linings are represented by isotropic homogeneous material. In all cases, the mechanical behavior of the linings was linear. Therefore, advanced numerical models of steel ladle are still required.

CHAPTER 2

EXPERIMENTAL CHARACTERIZATION OF REFRACTORY MASONRY WITH DRY JOINTS

This chapter is devoted to experimental characterization of refractory masonry walls subjected to uniaxial and biaxial compression loads at room and high temperature. Within the framework of ATHOR project, two large scale experimental campaigns were performed[1]*. The first experimental campaign was performed at University of Coimbra – Portugal and the second experimental campaign was carried out at RHI Magnesita company, Leoben – Austria. In section 2.1 the studied materials, their mechanical and thermo physical properties are introduced. Detailed descriptions of the uniaxial compression test setup at University of Coimbra, displacement and temperature measurement techniques, specimens, results and discussions of masonry walls subjected to uniaxial compression at room and high temperature are given in section 2.2. Detailed descriptions of the biaxial compression test setup at RHI Magnesita, measurement techniques, tested specimens, results and discussions of masonry walls subjected to a wide range of thermomechanical loading conditions are presented in section 2.3. Finally, the conclusions of the present chapter are given in section 2.4.*

2.1 Materials

Refractory masonry walls built up with alumina spinel cuboid bricks are tested in the present work. The working lining of the steel ladle is built up from thousands of tapered shape bricks arranged in a running bond texture. However, for the sake of simplicity, while building the walls, new cuboid bricks are used in the two experimental campaigns. The bricks were produced by RHI Magnesita company. They have been fully characterized within the cooperative framework

[1] All tests presented in this chapter are performed in collaboration with Early Stage Researcher (ESR) 11: Rafael DE OLIVEIRA (University of Coimbra). To perform these tests, ESR 10 Mahmoud ALI did two secondments at University of Coimbra and RHI Magnesita.

of ATHOR project. The chemical composition of the material is 94 wt% alumina, 5 wt% magnesia and 1 wt% other oxides such as iron oxide and silica. The apparent porosity and density of the material are 19% and 3130 kg/m^3, respectively [10]. The thermal conductivity and specific heat of the material are shown in Fig 2.1- a and b [133]. The Young's modulus, measured using acoustic emissions technique [134] and mechanical tests, and the ultimate compressive stress [135] variations with temperature are presented in Fig 2.1- c and d, respectively.

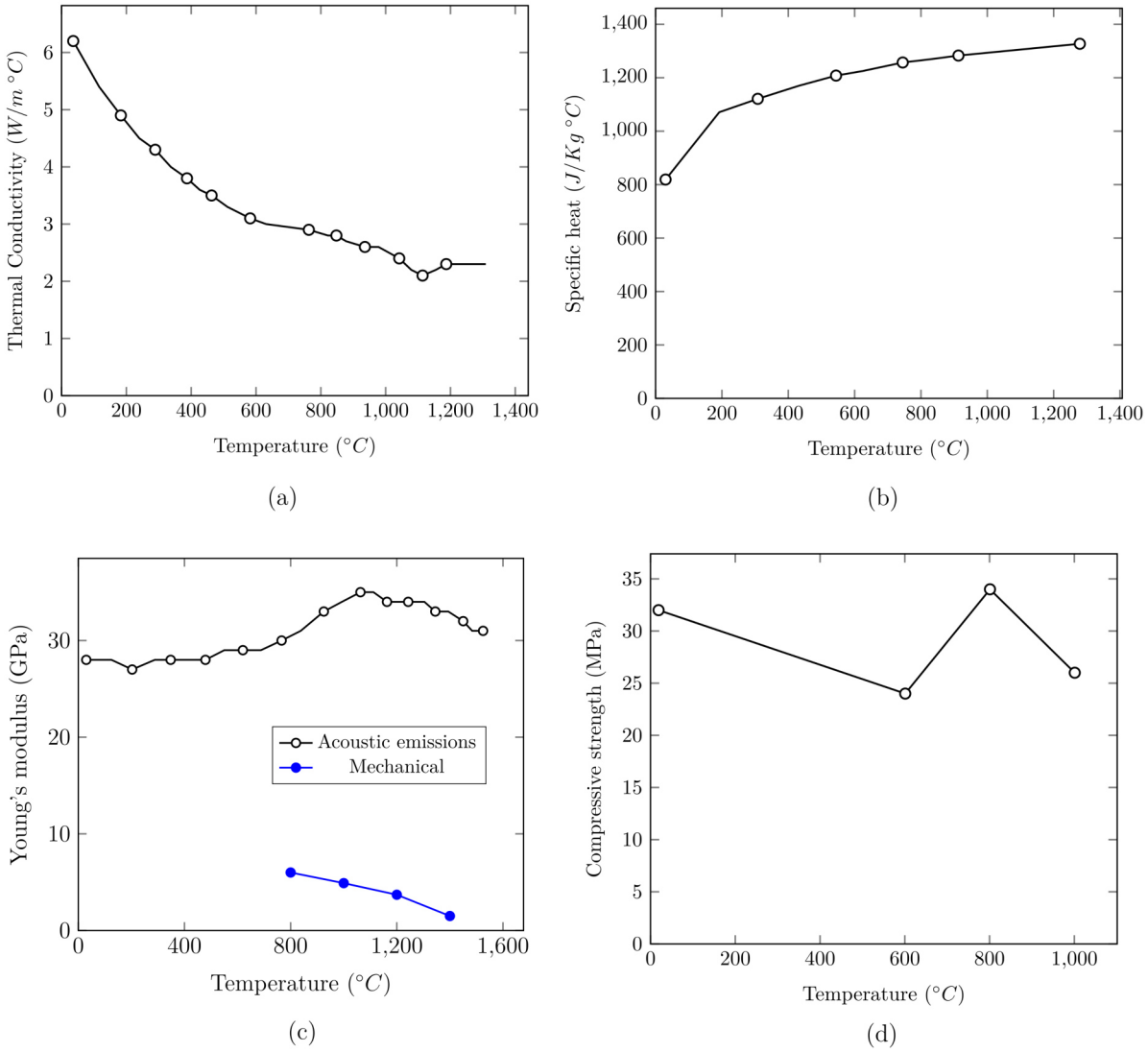

Figure 2.1: Thermal and mechanical properties of alumina spinel bricks tested in the present work: (a) thermal conductivity [133], (b) specific heat [133], (c) Young's modulus [134] and (d) ultimate compressive strength [135].

The values of Young's modulus measured using mechanical tests are preferred and will be used later in the present work while developing the numerical models (for room temperature and due to lack of data, the value measured using acoustic emissions was used). The mechanical tests of Young's modulus were carried out by RHI Magnesita company. The creep behavior of the material was characterized within the framework of ATHOR project. The creep parameters were

identified by Samadi et al. [10] and Teixeira et al. [136] at three different temperatures namely: 1300 °C, 1400 °C and 1500 °C . They are reported in table 2.1 (A, n and m are the constants of power law creep equation [85]). To verify whether creep is significant for temperatures below 1300 °C, four compressive creep tests (at 1200 °C and 1000 °C, each temperature repeated two times) were carried out by RHI Magnesita. The results of these tests are compared with the results of compressive creep tests at higher temperatures [10, 136] in Fig. 2.2. It can be seen that below 1200 °C and for the studied compressive stress level (6 MPa, maximum load used in the large scale creep and relaxation tests reported later in this chapter), the creep of the material is insignificant. However, in the case of steel ladle (as will be presented later in chapter 5), the stress levels are much higher than 6 MPa and the creep impacts could be significant. Therefore, experimental studies to investigate the creep behavior of alumina spinel at lower temperatures and higher stress levels (up to the ultimate compressive stress of the material) are planned to be carried out in the future.

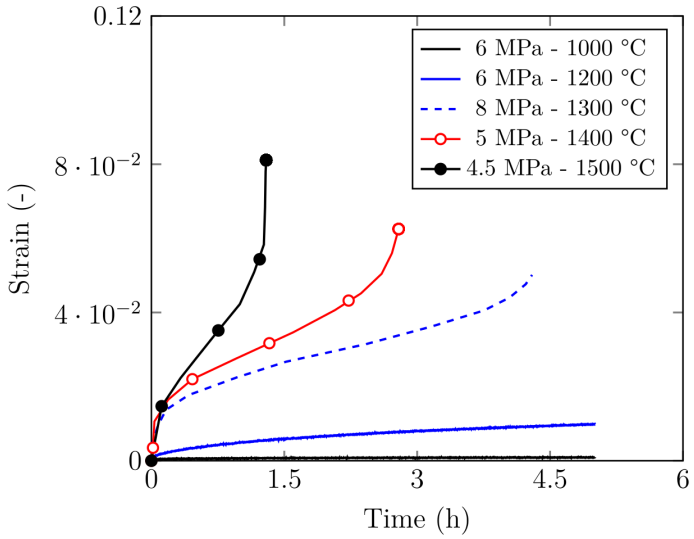

Figure 2.2: Creep behavior of alumina spinel refractory material at different temperatures and compressive stress levels.

Table 2.1: Creep parameters of alumina spinel refractory materials at different temperatures [10, 136].

Temperature (°C)	**Primary**			**Secondary**	
	A (MPa $^{-n}$ s^{-1})	n (-)	m (-)	A (MPa $^{-n}$ s^{-1})	n (-)
1300	3.89×10^{-15}	4.25	-2.73	1.25×10^{-12}	6.45
1400	1.25×10^{-14}	5.8	-2.65	1.62×10^{-12}	9.20
1500	1.62×10^{-10}	2.0	-1.97	1.32×10^{-9}	5.84

The masonry walls are built up with half and full cuboid bricks. The dimensions of the full bricks are $150 \times 100 \times 140$ mm^3 (length, height and depth) and the dimensions of the half bricks are $75 \times 100 \times 140$ mm^3. The dimensional tolerances of the bricks are $\pm$ 2 mm in the pressing

direction (150 ± 2 mm) and ± 1 mm in directions perpendicular to the pressing direction (100 ± 1 mm and 140 ± 1 mm). The former tolerances are higher as they are affected by the amount of powder material injected in the mold and the applied pressure during the pressing step of refractory bricks production process. The dimensional and shape tolerances of the bricks lead to non uniform joint thickness in the wall and limited initial contact. As can be seen in Fig. 2.3, the dry joints are almost closed in some locations while being open in other locations.

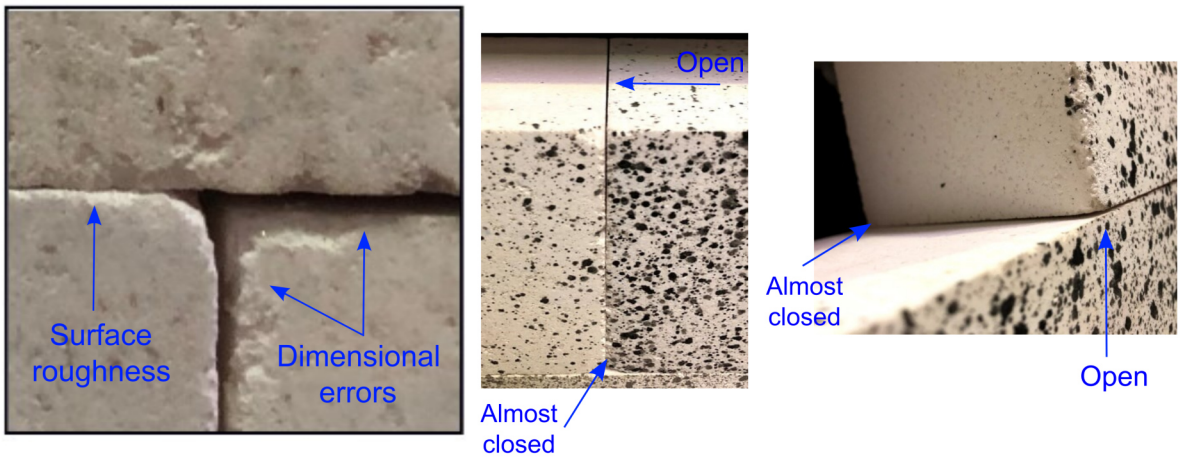

Figure 2.3: Nonuniform dry joints thickness and limited initial contact caused by the dimensional and shape tolerances of the bricks.

2.2 Uniaxial compression tests

2.2.1 Experimental setup

The experimental setup used to perform uniaxial compression tests of refractory masonry walls at room and high temperature is shown in Figs. 2.4 and 2.5. It is composed of the following:

- Reaction frame built up with two HEB-500 and two HEB-600 steel beams. The reaction frame is fixed to a concrete reaction slab.
- Two loading beams, one HEB-240 beam and one composite steel concrete beam.
- Two lateral steel guides to ensure the alignment of the loading beams. They are fixed to the reaction slab.
- One hydraulic jack for load application with 3000 kN capacity. The jack is fixed to the reaction frame and controlled by a servo hydraulic central unit.
- One load cell for measuring the applied load with 5000 kN maximum capacity. It is fixed between the jack head and the top loading beam.
- One 45 KVA electric furnace to heat one face of the masonry wall (high temperature tests only), the other face is exposed to the ambient.
- A data recorder for saving the data of the Linear Variable Deferential Transformers (LVDTs) and the thermocouples.

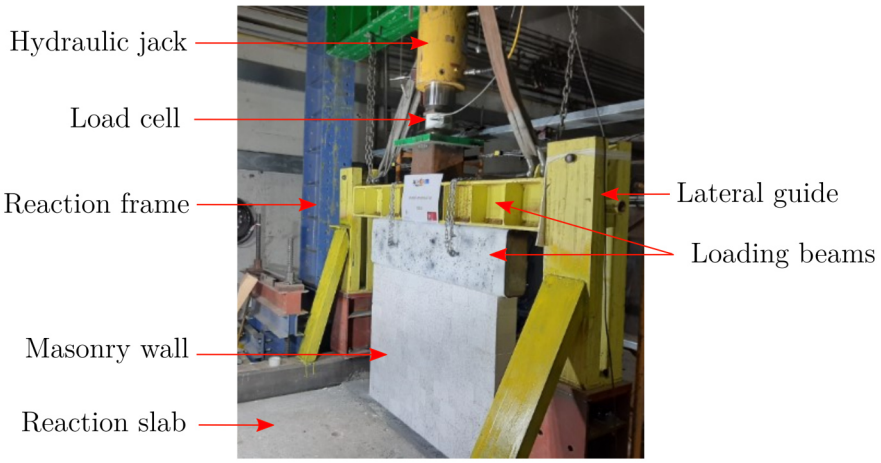

Figure 2.4: Experimental setup used to perform uniaxial compression tests of alumina spinel refractory masonry walls at room temperature.

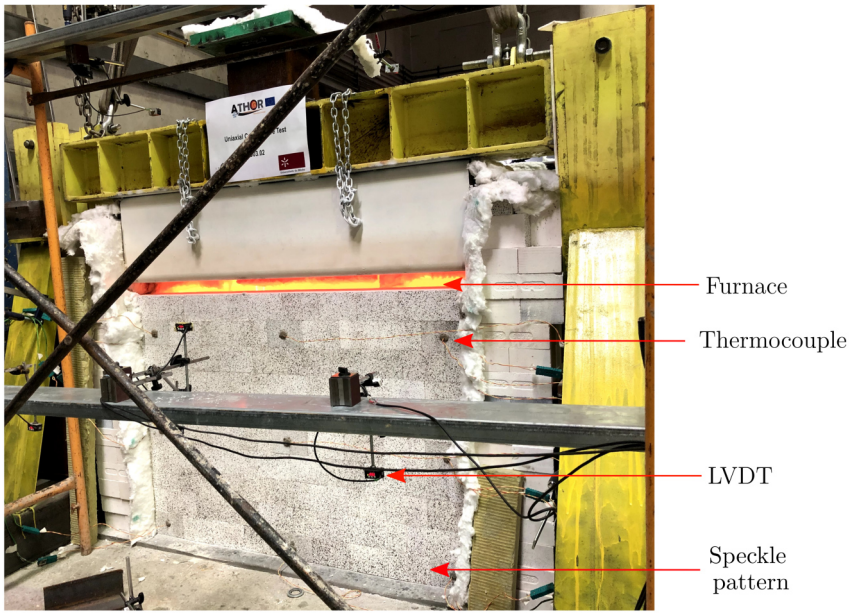

Figure 2.5: Experimental setup used to perform uniaxial compression tests of alumina spinel refractory masonry walls at high temperature.

2.2.2 Displacement measurement

For measuring the in-plane displacement in the direction normal to bed joints, three LVDT were used. The measurement range of the LVDTs is 0 - 500 mm with $\pm$0.001 mm. The arrangements of the LVDTs are shown in Fig. 2.6. In addition to the LVDTs, Digital Image Correlation (DIC) technique was used. One 18 mega pixels (5184$\times$3486) camera was used to take pictures of the wall. Black automotive paint was used to generate the speckle pattern. The bricks were laid on horizontal position on the floor and, then, painted using the black automotive paint and an aerographe. Finally, the bricks were left for 48 h to dry. After the tests, an open source software (Ncorr) was used for the DIC analysis [137].

2.2.3 Temperature measurement

To measure the temperature of the hot and cold faces of the wall during the high temperature tests, 18 type K thermocouples were used (9 installed in each face). The thermocouples are installed inside the bricks, 10 mm in the depth. The installation procedures of the thermocouples were as following: first, 8 mm diameter and 10 mm depth holes are drilled in the bricks. Next, the thermocouples are placed inside the holes. Finally, the holes are closed with cement and left for 48 h to dry. The arrangements and locations of the thermocouples are shown in Fig. 2.6.

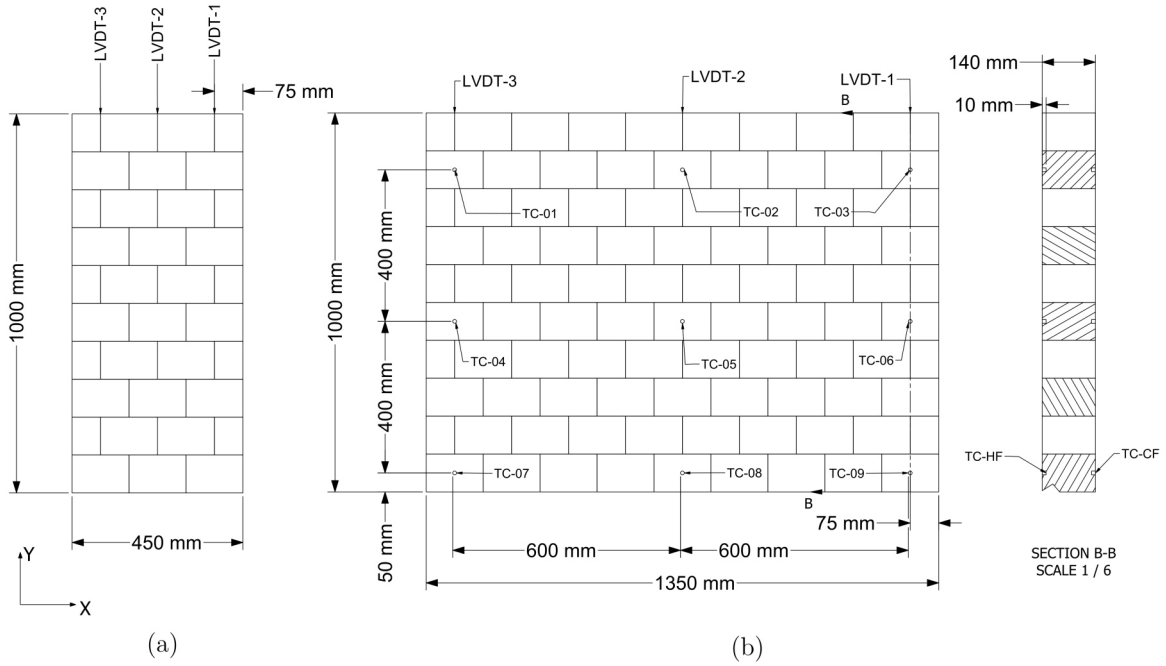

Figure 2.6: Schematics of refractory masonry specimen (a) series S01 and (b) series S02.

2.2.4 Specimens

Summary of the performed uniaxial compression tests (in the direction normal to bed joints) of refractory masonry walls at room and high temperature is given in table 2.2. Schematics of the wall dimensions, brick arrangements, locations of the LVDTs and the thermocouples are presented in Fig. 2.6. The walls are built up with full and half alumina spinel refractory bricks arranged in a running bond texture. For all tests, the height and thickness of the wall were 1000 $\times$ 140 mm^2, respectively. For series S01, the width of the wall was 450 mm while, for series S02 the width of the wall was 1350 mm.

Table 2.2: Summary of the uniaxial compression tests of refractory masonry walls performed at room and high temperature.

Test series	Specimen	Temperature	Maximum load	Wall dimensions (mm)
S01	S01-01 S01-02 S01-03	Room temperature	Up to failure	450×1000×140
S02	S02-01 S02-02 S02-03	High temperature	8 MPa	1350× 1000×140

2.2.5 Test procedures, results and discussions

2.2.5.1 S01 - uniaxial compression up to rupture at room temperature

The main goal of series S01 was to understand the impact of dimension errors of the bricks (major origin of dry joints) on the mechanical response of the wall, its load bearing capacity and ultimate uniaxial compressive strength in the direction normal to bed joints. Therefore, the mechanical load was applied until the failure of the wall. Based on the maximum loading capacity of the hydraulic jack and structural resistance of the reaction frame, a wall with small width (450 mm) was used for this test series. Three specimens were tested at room temperature under the same loading conditions.

The testing procedures of series S01 were as following: *(i)* The speckle pattern was applied to the bricks and then left to dry. *(ii)* The wall was built inside the testing frame and its vertical and horizontal alignment was verified. *(iii)* The loading beam was lowered using a crane till it touched the upper surface of the wall. *(iv)* The LVDTs were connected and calibrated. *(v)* The camera was placed in front of the wall and its correct alignment was verified. Then, several reference images of the wall were taken. *(vi)* The load was applied under displacement control (0.01 mm/sec) up to the failure of the wall. The displacement in the direction normal to bed joints and the reaction forces were recorded during the test.

Figure 2.7 shows specimen S01-01 before testing, during failure and after failure. The displacement fields, in the direction normal to bed joints, in S01-01, obtained using DIC, at different load levels are presented in Fig. 2.8. It can be seen that the displacement fields are non uniform due to the dimension errors of the bricks and non flatness of the surface in contact with the loading beam. The displacement of one brick located at the top course of the wall is higher as compared to other bricks in the same row.

Resulting reaction forces, measured by the load cell, variations with the displacements are given in Fig. 2.9-a. The stress – strain diagrams of the three performed tests are given in Fig. 2.9-b. Good agreements between the three tests can be observed. The resulting force displacement diagrams of the walls are nonlinear. A strain (or displacement) stiffening behavior with brittle failure can be observed. The mechanical stiffness of the wall and effective tangent

Young's modulus increase with the increase of the applied load. This is due to that with the increase of the applied load, dry joints close gradually leading to an increase in the contact area between the bricks and, therefore, an increase in the mechanical stiffness.

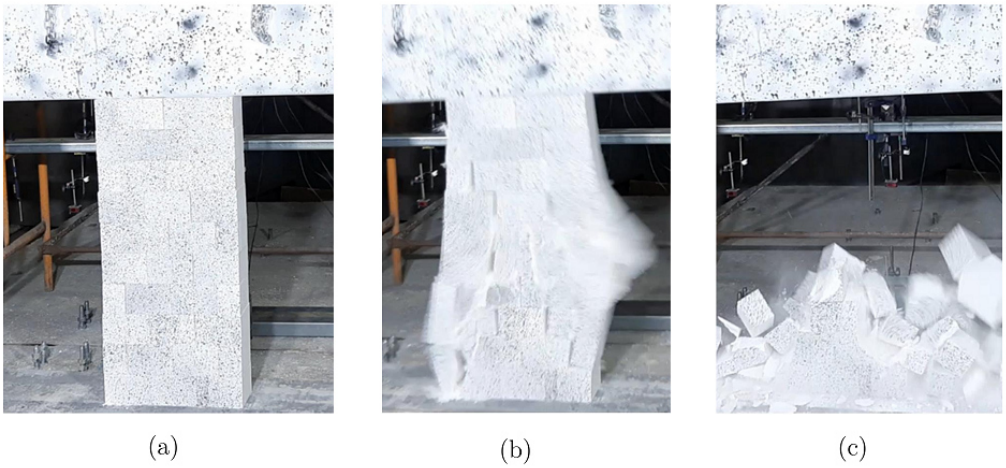

Figure 2.7: Test specimen S01-01 (a) before testing, (b) during failure and (c) after failure.

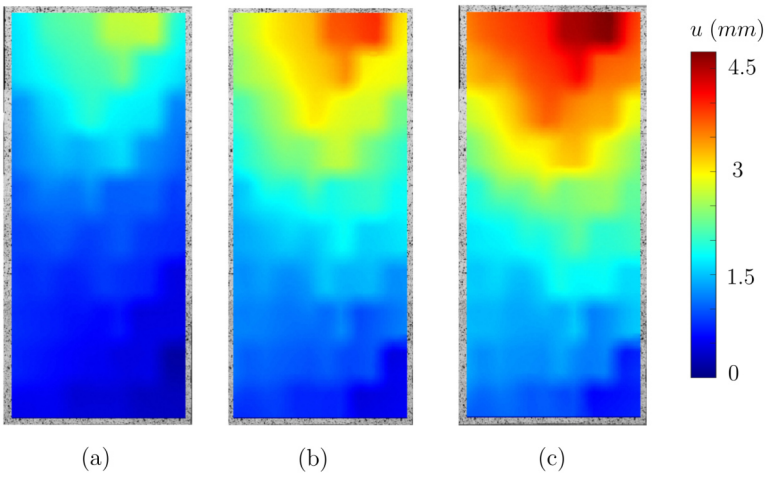

Figure 2.8: Displacement fields in the direction normal to bed joints (vertical direction in this image) in S01-01 at: (a) 25 % (b) 50 % and (c) 99 % of the failure load.

The values of ultimate compressive strength and effective Young's modulus of the wall (in the loading direction) can be determined from the given stress strain diagrams. Among the three performed tests, the maximum values of ultimate compressive strength and tangent Young's modulus of the wall are 22.4 MPa and 4.6 GPa, respectively. These values are small as compared to the ultimate compressive strength (32 MPa) and Young's modulus (28 GPa) of the brick. This can be attributed to that the dimensional errors of the bricks leads to limited contact between the bricks. In addition, they lead to stress concentration at the middle of the brick (near the vertical head joint). Lower values of Young's modulus of the wall, as compared to that of the brick, indicate that perfect closure of joints was not achieved and some joints were still open even when

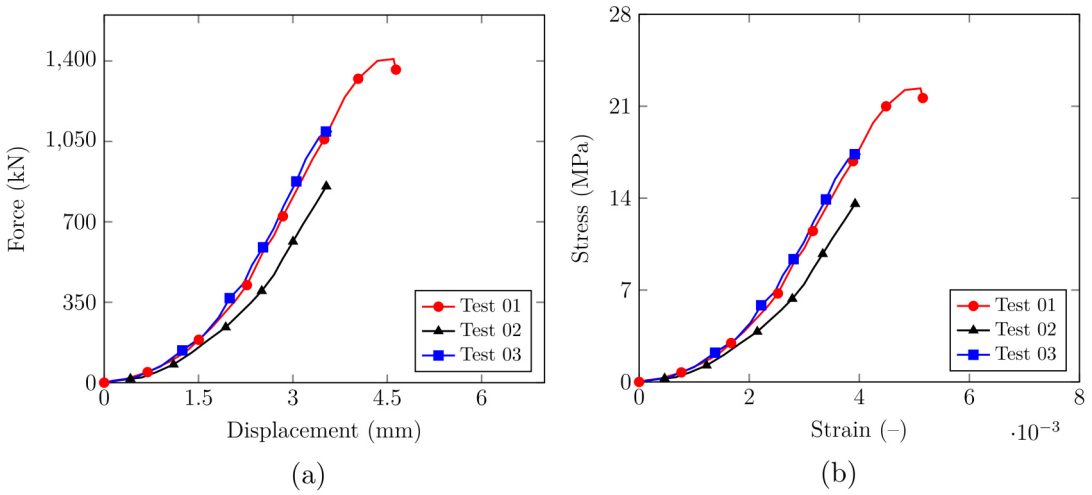

Figure 2.9: S01: (a) measured displacements in the direction normal to bed joints versus vertical reaction forces and (b) stress strain diagrams.

the wall was loaded up to rupture. This conclusion is based on the fact that, as mentioned in chapter 1, in the case of perfect closure of joints, the value of the Young's modulus of the wall is similar to that of the brick.

2.2.5.2 S02 - uniaxial compression at high temperature

The main objective of series S02 was to understand the thermomechanical behavior of the wall under constant applied stress and large thermal gradients. In addition, it was also performed to understand the contribution of thermal expansion to the closure of dry joints. Therefore, a uniaxial mechanical load was applied at room temperature and kept constant then, the wall was heated. Three specimens were tested under the same thermomechanical loading conditions.

The testing procedures of series S02 were as following: the first five steps are similar to S01 then: *(vi)* The load was applied to the wall under displacement control (0.01 mm/sec) up to 8 MPa. Then, the loading beam was kept under force control. *(vii)* The furnace was turned on and the wall was heated. The displacements in the direction normal to bed joints, temperatures of the cold and hot faces and the vertical reaction force were recorded.

Time variations of the hot (HF) and cold (CF) faces temperature of S02 and the furnace temperature are given in Fig. 2.10-a. The solid black lines represent the temperatures measured by the thermocouples in different locations of the HF and CF. The furnace was turned on after mechanical load application (for the first 30 minutes, the temperature was equal to 20 °C, ambient temperature). The furnace was programmed to follow the standard heating curve ISO 834-1, ($T = 20 + \log(8t + 1)$, T is the temperature in °C and t is the time in minutes). However, due to high heat losses from the CF to the ambient and the high heat capacity of the wall, the furnace could not follow the programmed heating curve. From Fig. 2.10-a it can be seen that the temperature of the top and middle portions of the HF and CF are higher as compared to the bottom portions. In addition, high temperature gradients through the thickness of the wall was

observed and the CF temperature started to increase 20 minutes after the furnace was turned on. The reasons for this are that the low thermal conductivity, high thermal capacity of alumina spinel and the heat losses from the CF to the ambient.

Time variations of the displacements, in the direction normal to bed joints, of the loading beam of the three performed tests are given in Fig. 2.10-b. For each test, the vertical displacement is calculated as the average of the three measured displacements by the three LVDTs. Good agreements between the displacements versus time of the three tests can be observed. One can observe that in the first half hour, an average negative displacement of around -3.5 mm was measured by the LVDTs due to uniaxial compression load application (8 MPa). Then, when the furnace was turned on and with the increase of the temperature, the wall started to expand gradually and a steady state increase in the displacement, in the opposite direction, was recorded. At around 4.5 hours, the thermal expansion effects of the wall over passed the impact of mechanical load application and a positive displacement was recorded by the LVDTs.

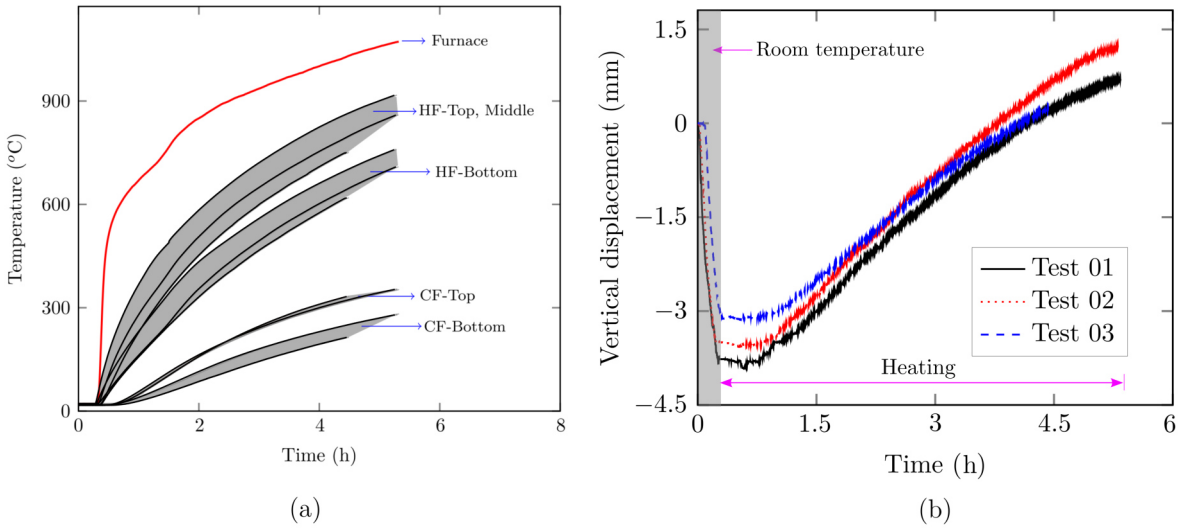

Figure 2.10: Series S02: (a) time variations of the hot face, cold face and furnace temperatures. (b) Time variations of the vertical displacement of the three performed tests.

The displacement field in the direction normal to bed joints obtained using DIC in S02-02 by the end of mechanical load application is shown in Fig. 2.11. After turning on the furnace and with the increase of CF temperature, the speckle pattern disappeared (see Fig. 2.12). The automotive paint used to generate the speckle pattern is designed to operate at room temperature only. So, DIC analysis were performed up to the end of mechanical load application. Nonuniform displacement field with higher values near the left side of the wall can be observed. This nonuniform displacement field is caused by the dimension errors of the bricks.

As can be seen in Fig. 2.12, several vertical cracks are observed near the middle of the bricks. A closer look at Fig. 2.13 can explain this phenomena. This image corresponds to the end of the mechanical load application (i.e. maximum load of 8 MPa). It can be observed that due to brick height imperfections, the majority of bed joints between two bricks are almost closed in some

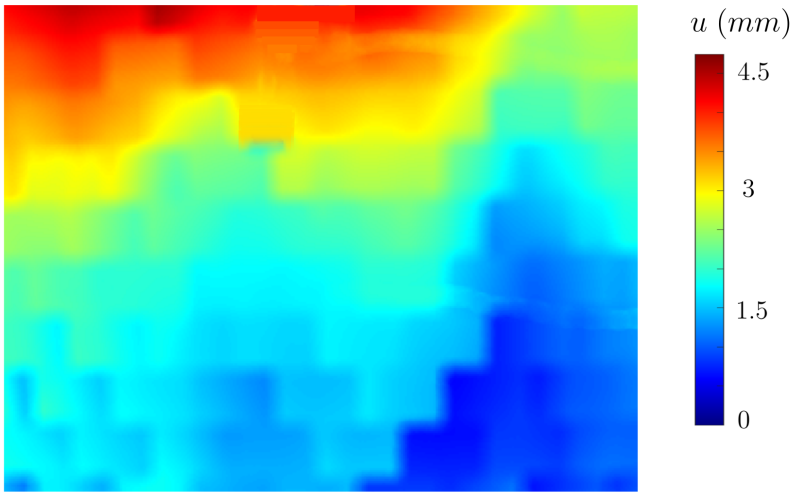

Figure 2.11: Displacement field in the direction normal to bed joints (vertical direction in this image) in S02-02 obtained using DIC by the end of mechanical load application (absolute values).

locations while being open at other locations. This local heterogeneous joint behavior leads to limited contact, non uniform loading conditions and, therefore, stress concentrations near the middle of the bricks.

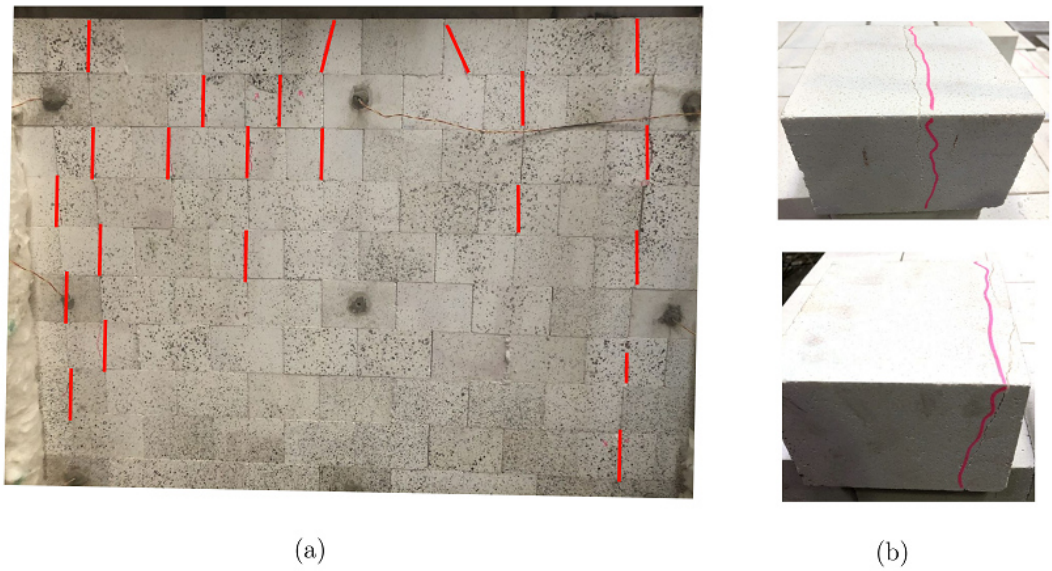

Figure 2.12: Series S02: vertical cracks near the middle of the bricks: (a) global view and (b) cracks in the middle of the brick (top) and near the hot face.

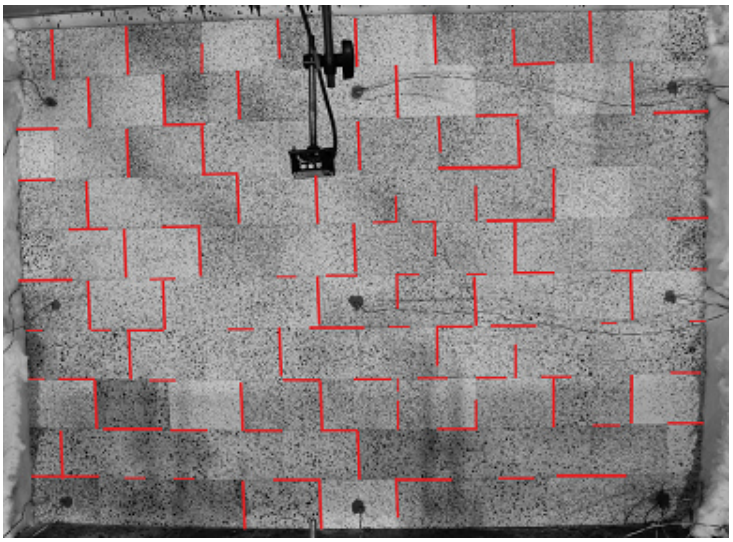

Figure 2.13: Series S02: non uniform contact between the bricks due to presence of open joints (marked in red).

2.3 Biaxial compression tests

2.3.1 Experimental setup

The experimental setup used to perform the biaxial compression tests of refractory masonry walls at room and high temperatures is shown in Fig. 2.14. It is composed of the following:

- The test field where the masonry wall is placed and tested. The size of the test setup is 3 $\times$ 3 $\times$ 1.6 m^3.
- Eurotherm 5180V 48 channels data recorder for storing the data of the thermocouples, LVDTs and hydraulic cylinders.
- Rexroth control unit for controlling the two hydraulic cylinders. Several control programs for the two hydraulic cylinders were written. The control programs were written in NC programming language and compiled thanks to a computer then transferred to the control unit.
- Rexroth hydraulic pump to feed the two hydraulic cylinders.

Detailed views of the 3D model of the test field at room and high temperature are presented in Figs. 2.15 and 2.16. The biaxial compression test field is composed of the following:

- A steel reaction frame with 3$\times$3$\times$1.6 m^3 size. The reaction frame has high stiffness. Therefore, during testing, the displacements in the frame do not impact the measured displacements in the specimen.
- Two hydraulic cylinders with maximum stroke of 90 mm. Each cylinder is equipped with two pressure gauges for measuring the applied forces. The temperatures of the cylinders were monitored during the tests to ensure that their hydraulic oil is operating below the maximum allowable working temperature. The hydraulic cylinders are controlled by the Rexroth control unit.

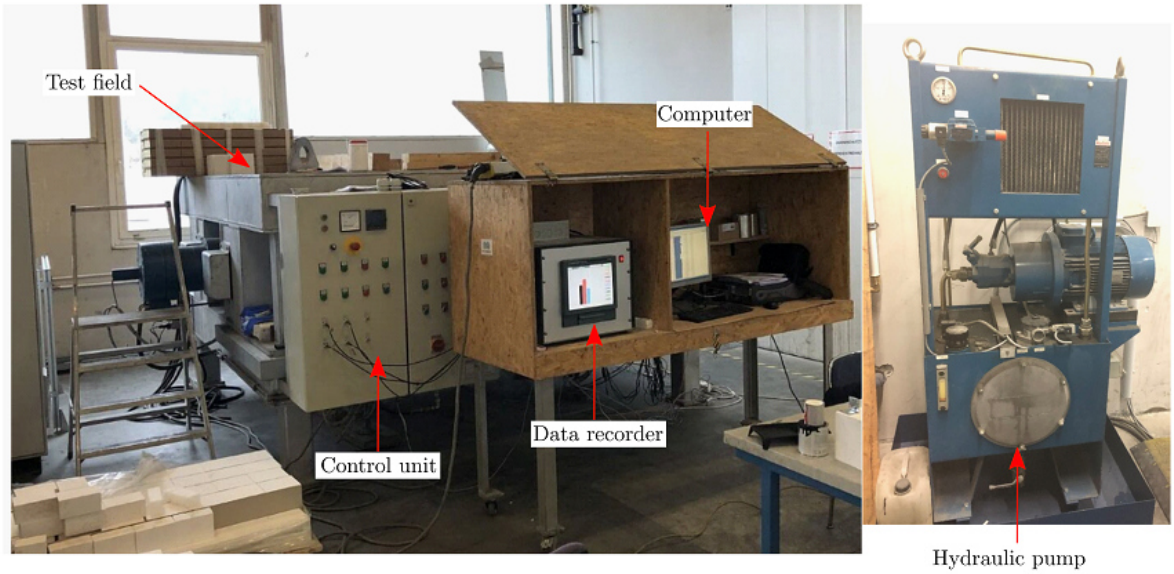

Figure 2.14: Biaxial compression test setup at RHI Magnesita technology center – Leoben.

- Four steel plungers, two of them are fixed and the other two are moving. The two moving plungers are connected to the two hydraulic cylinders and equipped with lateral steel guides to ensure their alignment during load application. The lateral guides were lubricated to reduce the friction. The four plungers are water cooled to avoid overheating of the hydraulic cylinders during tests performed at high temperature. Each fixed plunger has three openings for placing the measurement instrumentation (LVDTs and thermocouples).
- Plunger linings installed inside the steel plungers. The plunger linings were built up with Magnesia Chromite (MCh) bricks with dry joints. MCh bricks were chosen owing to their high elastic stiffness and creep resistance. Dry joints type was chosen to allow free expansion of the MCh bricks during high temperature tests.
- Four insulation refractory masonry layers. The top layer (in contact with the cold face of the specimen) was a masonry with dry joints, while the other three layers were masonries with mortar joints. The number of layers, material and thickness of each layer were chosen based on several heat transfer numerical simulations.
- A steel bottom that carries the four insulation layers and the test specimen. The steel bottom can be lowered or elevated thanks to eight screwed legs.
- A heating hood equipped with 36 KANTHAL SUPER 1900 heating elements. The heating hood was composed of steel frame and 20 cm thickness insulation. The maximum operating temperature of the heating elements was 1850 °C.

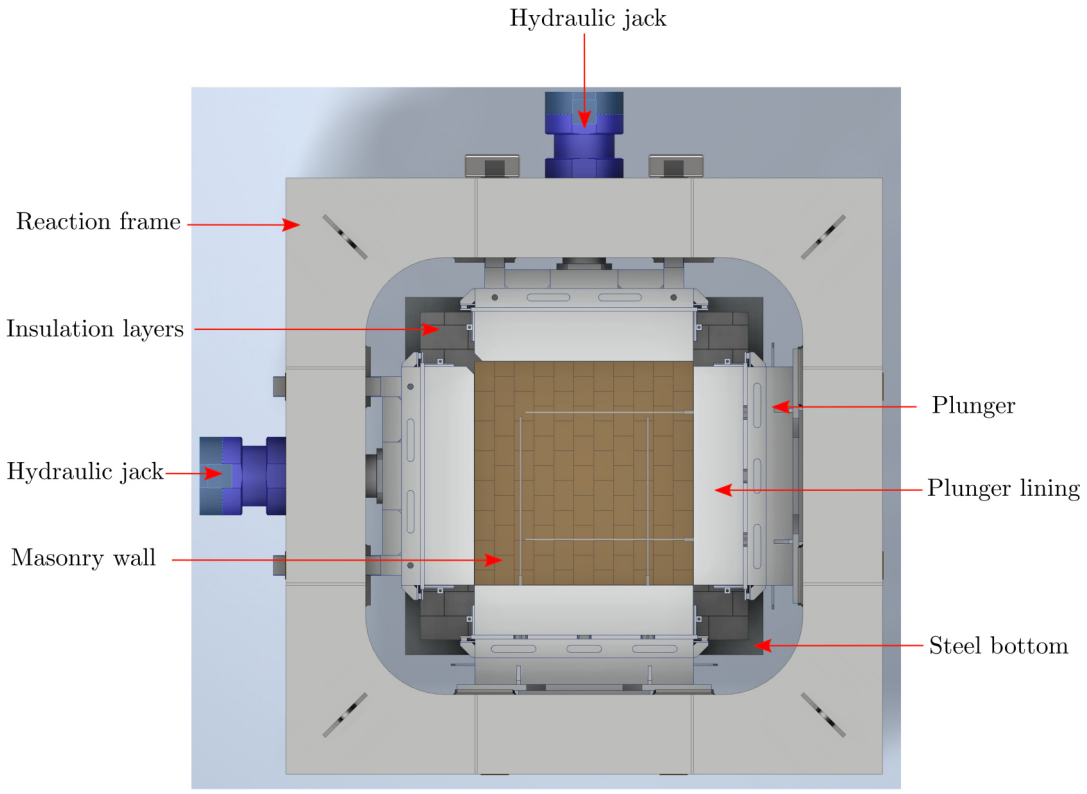

Figure 2.15: Top view of the biaxial compression test field.

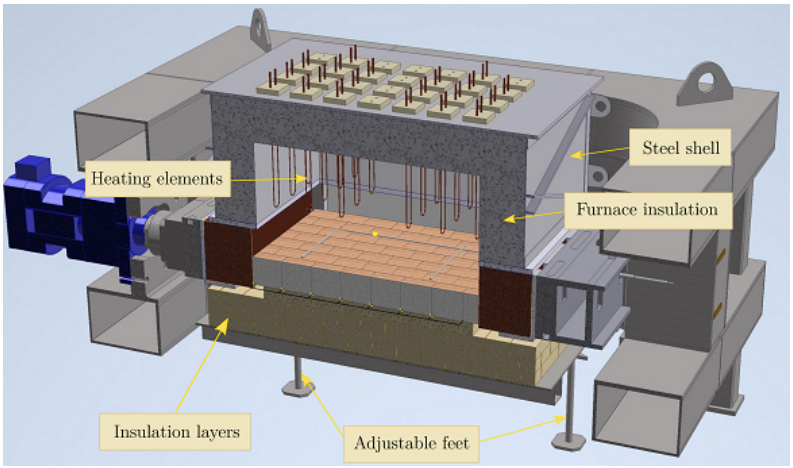

Figure 2.16: Cross section view of the biaxial compression test setup showing the heating chamber, the test specimen, the metallic and ceramic plungers and the insulation layers.

2.3.2 Displacement measurement

For measuring the in-plane displacement of the specimen, four tube in tube and LVDTs devices are used. The tube in tube device is shown in Fig. 2.17 (total length was around 150 cm). It is composed of:

- A LVDT (Fig. 2.17-c) with $\pm$ 50 mm measurement range. The LVDT is placed inside a steel tube.

- A steel tube with two open ends and a grove (Fig. 2.17-b).
- An alumina tube with two open ends (Fig. 2.17-b) glued to the steel tube using high temperature glue.
- A long alumina tube with one open end inserted inside the alumina and steel tubes and touching the LVDT tip (Fig. 2.17-b).
- A thermocouple inserted inside the long alumina tube.

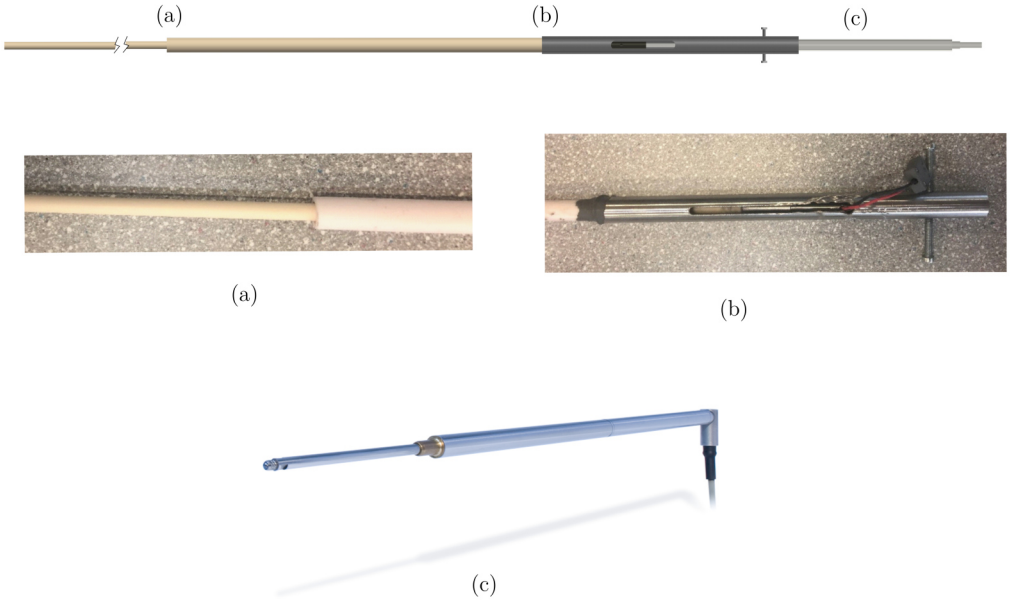

Figure 2.17: Details of the tube in tube device used to measure the displacement and temperature of specific points of the hot face.

The arrangements of the tube in tube devices depend on the test series and will be shown later. In addition to the tube in tube device, digital image correlation technique was used to measure the full experimental displacement fields (for room temperature tests only). As shown in Fig. 2.18, one 18 mega pixels (5184×3486) camera was used to take pictures of the wall. The camera was controlled using a computer. LED lights were used to enlighten the specimen and to improve the contrast of the taken images. Black automotive paint and a brush were used to generate the speckle pattern. The bricks are laid on horizontal position on the floor and, then, painted using the black automotive paint and the brush. Finally, the bricks were left for 48 h to dry. After the test, an open source software (Ncorr) was used for the DIC analysis [137].

2.3.3 Temperature measurement

To measure the temperature of the hot and cold faces of the wall, the heating hood, the hydraulic cylinders, the plungers, the steel bottom, several thermocouples were used. They are summarized as following:

- Five type B thermocouples were used to measure the temperature of the cold face of the specimen. The arrangements of these thermocouples are given in Fig. 2.19.

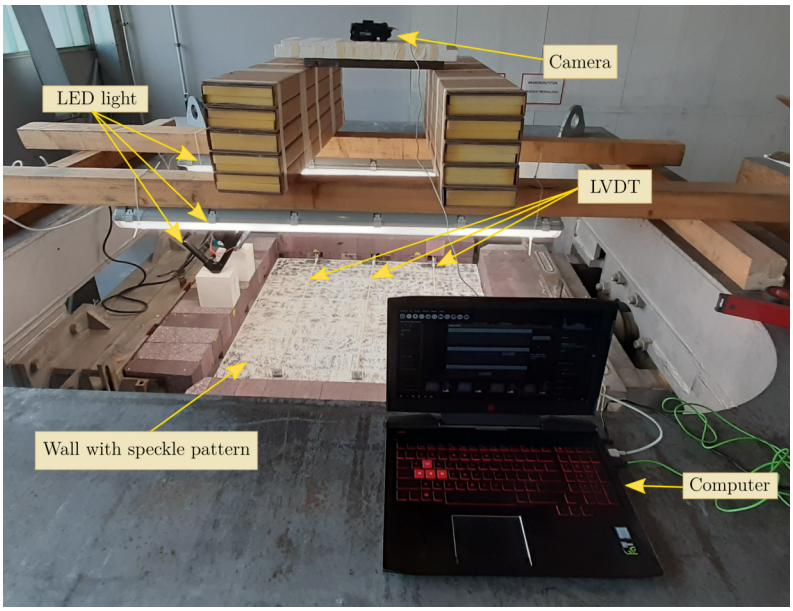

Figure 2.18: Digital image correlation setup used in the biaxial compression tests of masonry walls at room temperature.

- Five type B thermocouples were used to measure the temperature of the hot face of the specimen. Four of them were placed in the tube in tube devices and the other one was in contact with the hot face.
- One type S thermocouple was used to measure the temperature of the air inside the heating hood.
- Eleven type K thermocouples were used to monitor the temperature of the LVDTs, hydraulic cylinders, steel bottom and steel plungers.

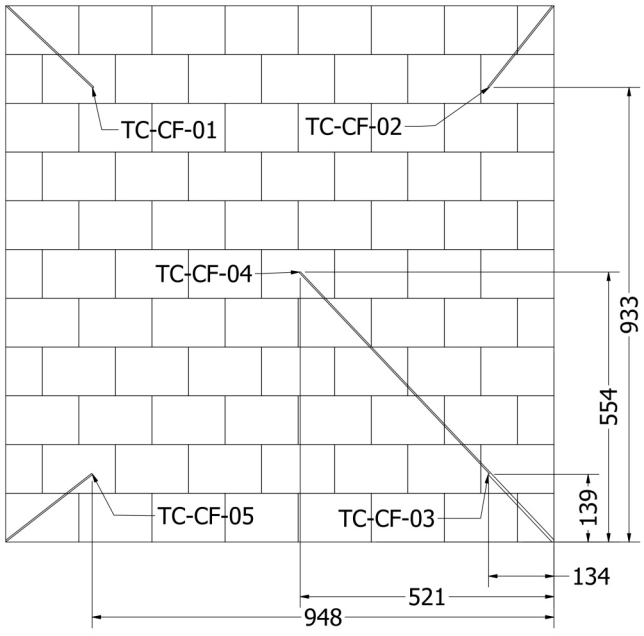

Figure 2.19: Schematic of the last insulation layer showing the locations of the thermocouples used to measure the temperature of the cold face. All dimensions are in mm.

2.3.4 Specimens

Fourteen tests of alumina spinel refractory masonry walls were performed. Six of them were performed at room temperature and the remaining eight tests were carried out at high temperature. The test series names, loading conditions in directions perpendicular to the surfaces of bed and head joints and testing temperatures are given in table 2.3. For all tests, the dimensions of the walls were $1125 \times 1100 \times 140$ mm^3.

Table 2.3: Summary of the biaxial compression tests of refractory masonry walls performed at room and high temperatures.

Series	Specimen	Maximum load		Temperature
		Bed	Head	
S03	S03-01 S03-02	6 MPa	Constrained	Room temperature
S04	S04-01 S04-02	Constrained	6 MPa	
S05	S05-01 S05-02	6 MPa	6 MPa	
S06	S06-01	6 MPa	Constrained	High temperature
S07	S07-01 S07-02	4 MPa		
S08	S08-01	Constrained	4 MPa	
S09	S09-01 S09-02	4 MPa	4 MPa	
S10	S10-01 S10-02	4 – 6 MPa	4 – 6 MPa	

Schematics of the specimens showing their dimensions, bricks arrangements, locations of the LVDTs and arrangements of the tube in tube devices of the eight test series are given in Figs. 2.20 and 2.22. An image of S05 (room temperature test) showing the arrangements of the bricks, speckle pattern, LVDTs, moving and fixed plungers is shown in Fig. 2.21. An image of S09 (high temperature test) showing the arrangements of the bricks, LVDTs, moving and fixed plungers is shown in Fig. 2.23. In all tests, the specimens are built up with full and half bricks arranged in a running bond texture. The walls dimensions were chosen based on the available space between the moving and fixed plungers and the maximum stroke of the hydraulic cylinders.

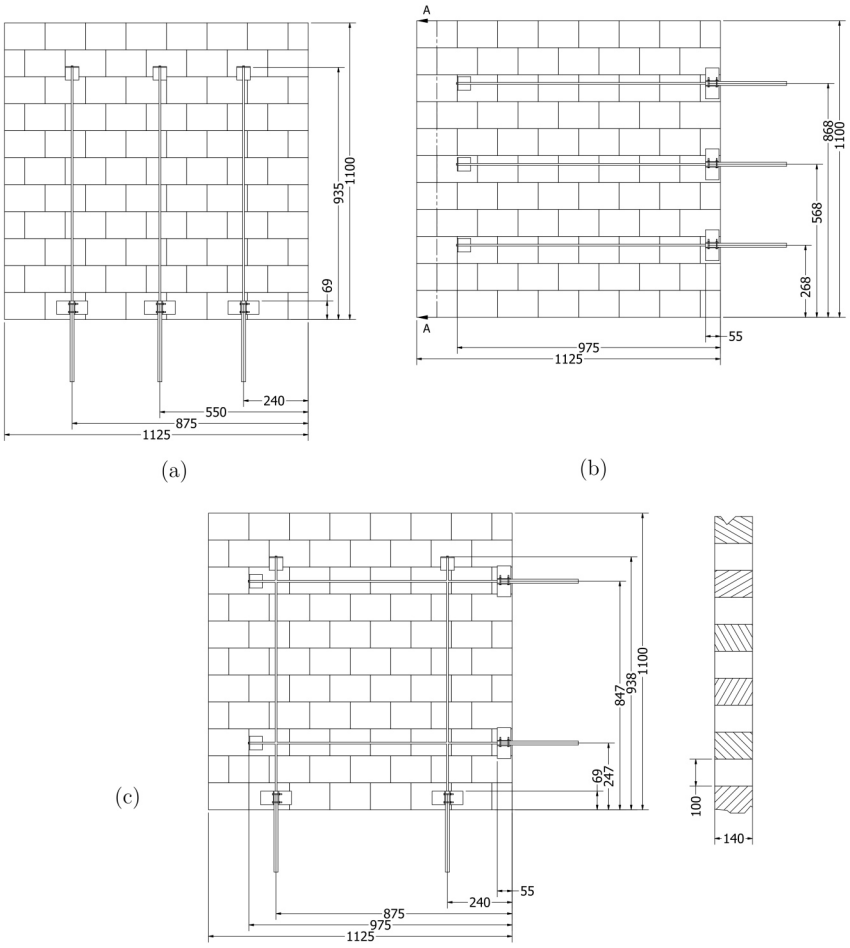

Figure 2.20: Schematics of the specimens tested at room temperature showing the arrangements of the bricks, LVDTs and the dimensions of the walls: (a) S03, (b) S04 and (c) S05. All dimensions are in mm.

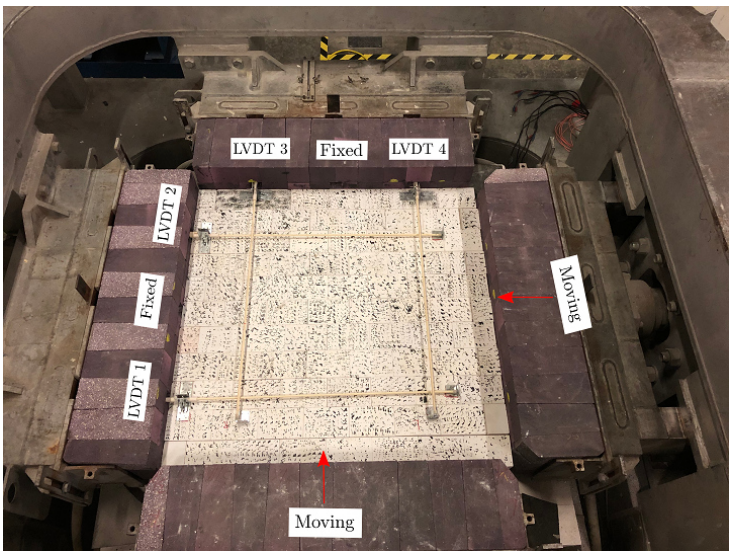

Figure 2.21: An example of refractory masonry wall subjected to biaxial compression at room temperature (S05) showing the arrangements of the LVDTs, wall with speckle pattern, moving and fixed plungers.

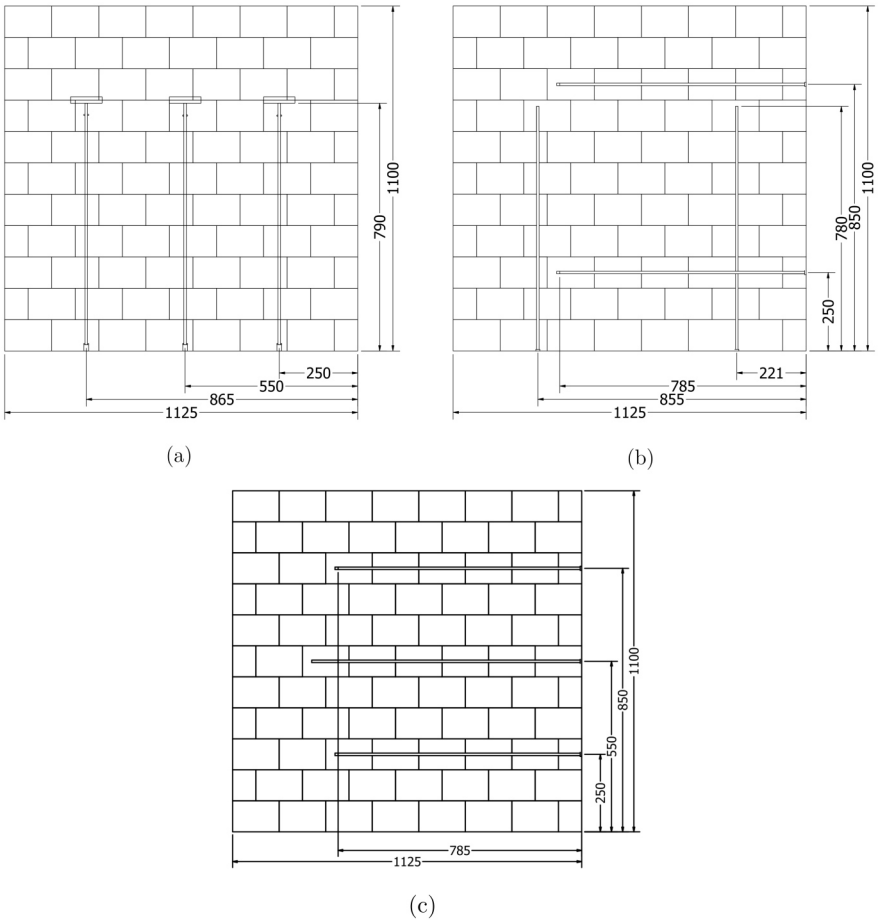

Figure 2.22: Schematics of the specimens tested at high temperature showing the arrangements of the LVDTs, bricks and the dimensions of the walls: (a) S06 and S07, (b) S09 and S10, and (c) S08. All dimensions are in mm.

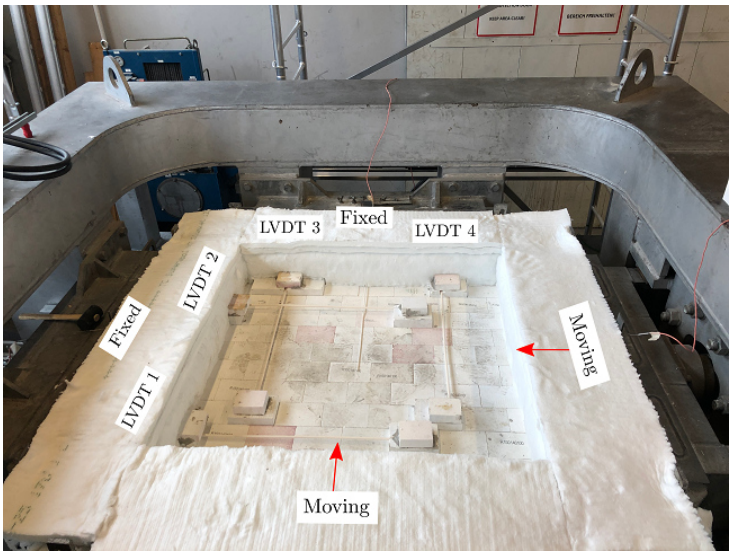

Figure 2.23: An example of refractory masonry wall subjected to biaxial compression at high temperature (S09) showing the arrangements of the LVDTs, moving, and fixed plungers.

2.3.5 Test procedures, results and discussions

2.3.5.1 S03: uniaxial loading and unloading - normal to bed joints at room temperature

The main objective of series S03 was to investigate the impact of joints closure and reopening on the mechanical response of the wall when subjected to cyclic loading and unloading at room temperature in the direction normal to bed joints. In addition, to understand the mechanical behavior of the wall when the direction normal to bed joints is loaded while the direction normal to head joints is constrained by the ceramic plungers (i.e. the positions of the plungers were locked). Therefore, a 6 MPa uniaxial compression load was applied to the direction normal to bed joints and the sides of the walls were constrained. As shown in Fig. 2.20-a, three LVDTs were used to measure the displacement in the direction normal to bed joints (the measurement range was 935 mm covering nine bed joints). Also, the displacement fields are measured using DIC. The reaction forces in directions normal to bed and head joints were recorded.

The testing procedures of series S03 were as following: *(i)* The speckle pattern was applied to the bricks and then left until it dries. *(ii)* The wall was built in the testing field. *(iii)* The LVDTs were connected and calibrated and the camera is placed in front of the wall, its correct alignment was verified. Then, several reference images were taken. *(iv)* The moving plunger (normal to head joints) was moved until it touched the wall sides. *(v)* The load in the direction normal to bed joints was applied to the wall under displacement control (0.01 mm/sec). The displacement (in the direction normal to bed joints) and reaction forces (in both directions) were recorded. *(vi)* After reaching the maximum load (945 kN), a dwell time of around 100 seconds was considered. Then, unloading, under displacement control, was performed.

An example of the resulting reaction forces normal to bed (f_{bed}) and head (f_{head}) joints during loading and unloading are given in Fig. 2.24-a. During loading and for the first 100 seconds, f_{bed} increased slightly. Next, f_{bed} rose gradually to reach the pre programmed maximum value of 945 kN. Then, f_{bed} remained constant during a 100 seconds dwell time. This dwell time was important in order to allow the camera to take several images of the wall corresponding to the maximum load level. Finally, the unloading step started and the measured reaction force dropped gradually. With the rise of f_{bed}, an increase in f_{head} was observed. This increase in f_{head} was caused by the constrained expansion of the wall in the direction normal to head joints.

Force displacement diagrams of the two performed tests are shown in Fig. 2.24-b. The displacements are calculated as the average of the three displacements measured by the three LVDTs. Small scattering between the two tests can be observed. The full displacement fields obtained using DIC, in the direction perpendicular to bed joints, of S03-01 at 25 $\%$, 100 $\%$ of maximum load level and after unloading are presented in Fig. 2.25. In agreement with S01 and S02, non uniform displacement fields can be seen in the figure. Higher values of the displacement at the right side of the wall can be observed. In addition, after unloading, there was a permanent deformation and the wall did not go back to the initial configuration. This can be attributed to the fact that the final joint thickness after unloading is usually smaller as compared to the initial

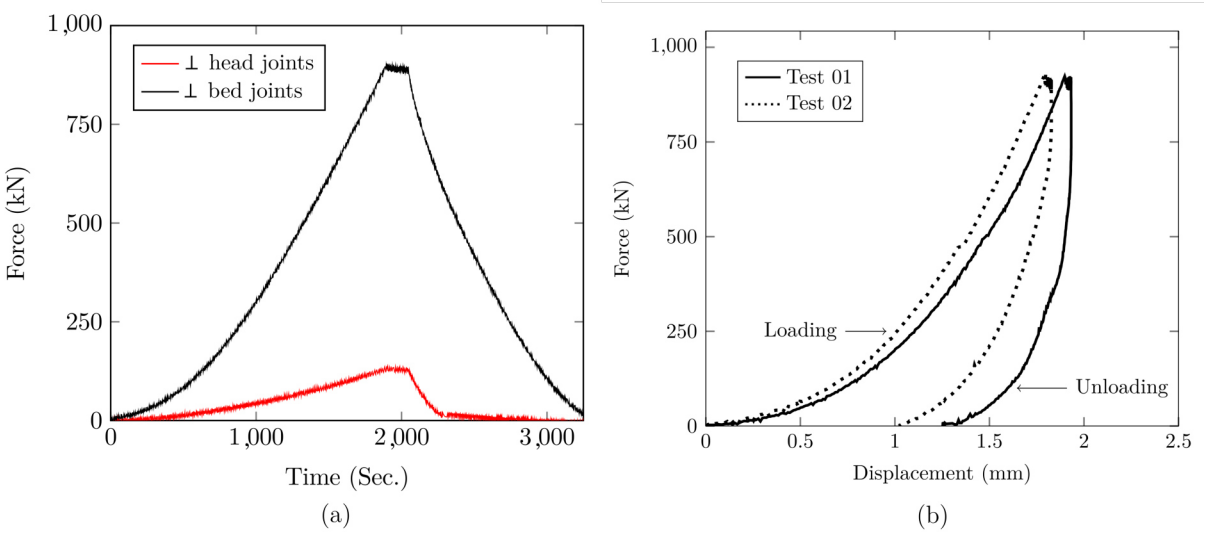

Figure 2.24: Series S03: (a) resulting reaction forces in directions normal to the surfaces of bed and head joints during loading and unloading, (b) force - displacement diagram in the direction normal to bed joints.

one. This behavior was also noticed from cyclic loading and unloading of a stack of two bricks (as reported in chapter 1).

During loading, a nonlinear displacement stiffening behavior can be observed (see Fig. 2.24-b). This behavior is caused by the gradual closure of joints and the increase in stiffness with joints closure. Regarding unloading, in the beginning, a huge drop in the reaction force was noticed without any decrease in the displacement. Then, both the displacement and reaction force decreased. The slope of the line during unloading is steeper as compared to that of loading. This behavior may be explained as that the joint behavior during loading is different from the joint behavior during unloading. This can be attributed to that, during the load application step, the asperities and the surface roughness present on the contact surfaces of the bricks have been crushed and/or deformed. Therefore, the joints (after load application step) are not the same as before load application anymore.

2.3.5.2 S04: uniaxial loading and unloading - normal to head joints at room temperature

With regard to series S04, it was performed to understand the impact of dimension errors of the bricks length on the mechanical response of the wall at room temperature. In addition, to understand the mechanical behavior of the wall when the direction normal to head joints is loaded while the direction normal to bed joints is constrained. Therefore, a 6 MPa uniaxial compression load was applied to the direction normal to head joints and the sides of the walls were constrained. As shown in Fig. 2.20-b, three LVDTs were used to measure the displacement in the direction normal to head joints (the measurement range was 975 mm covering six head joints). Also, the displacement fields were measured using DIC. The reaction forces in directions normal to bed and head joints were recorded.

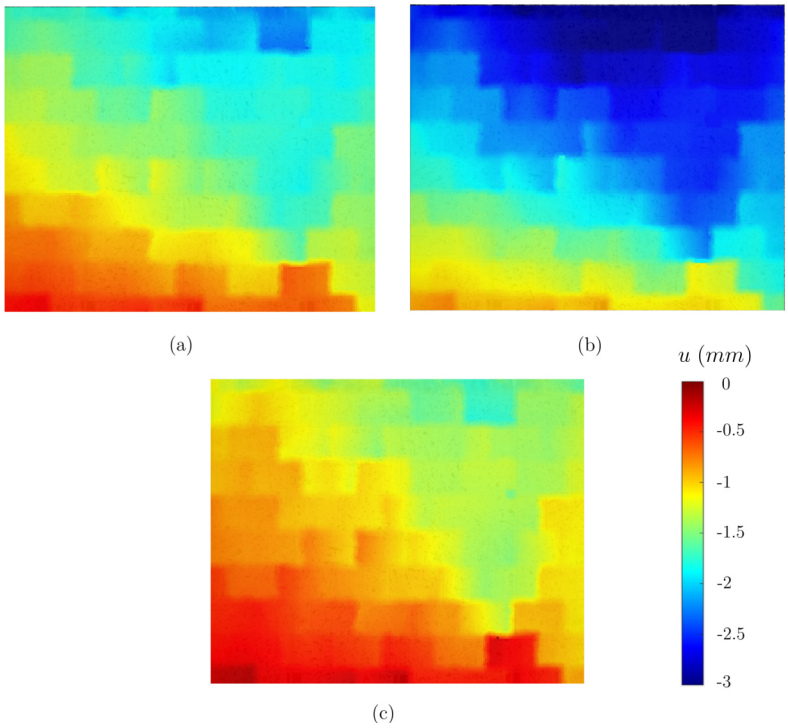

Figure 2.25: Displacement fields in S03-01, in the direction normal to bed joints (vertical direction in this image), at: (a) 25 % of maximum load level, (b) 100 % of maximum load level and (c) after unloading.

The testing procedures of series S04 were as following: the first three steps are similar to that of S03. Then: (iv) The moving plunger (normal to bed joints) was moved until it touched the wall sides. (v) The load in the direction normal to head joints was applied to the wall under displacement control (0.01 mm/sec). The displacement and reaction forces were recorded. (vi) After reaching the maximum loading capacity of the hydraulic cylinder (924 kN), a dwell time of around 100 seconds was considered. Then, unloading, under displacement control, was performed.

Figure 2.26-a shows an example of time evolution of the resulting reaction forces normal to head (f_{head}) and bed (f_{bed}) joints during loading and unloading. As compared to S03, the maximum programmed force (924 kN) was reached in shorter period of time. This can be attributed to that the number of head joints in the wall was smaller than the number of bed joints (7 head joints and 10 bed joints). During the dwell time (around 100 seconds), f_{head} remained constant. This dwell time allowed the camera to take several pictures corresponding to the maximum load level. Finally, the unloading step started and the measured reaction force dropped gradually. With the gradual increase of f_{head}, a rise in f_{bed} was observed due to the constrained expansion of the wall. It should be noted that the value of f_{bed} was smaller as compared to the value of f_{head} in the case of S03. This can be explained by the difference in the number of bed and head joints in the wall. Higher number of joints in the direction normal to the loading directions leads to more space to absorb the lateral expansion of the wall caused by Poisson's effects and, therefore, low values of resulting reaction forces.

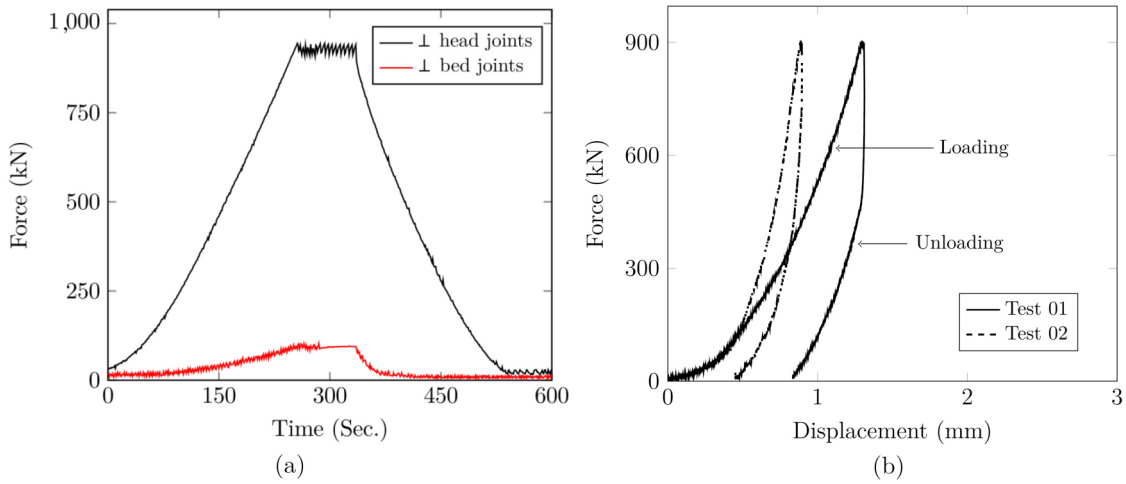

Figure 2.26: Series S04: (a) resulting reaction forces in directions normal to the surfaces of head and bed joints during loading and unloading, (b) force - displacement diagram in the direction normal to head joints.

Figure 2.26-b shows the force displacement diagrams of the two performed tests. The displacements are calculated as the average of the three displacements measured by the three LVDTs. As compared to S03, higher scattering between the two tests can be observed. The high scattering values are caused by the higher dimensional errors in the length of the bricks as compared to the dimensional errors in the height of the bricks (± 2 mm as compared to ± 1 mm). A nonlinear displacement stiffening behavior during load application, due to gradual closure of head joints, can be noticed from the figure. In comparison to S03, the maximum value of the average displacement measured by the LVDTs is smaller (1.3 mm for S04 and 2 mm for S03), because the number of head joints is less than the number of bed joints. This leads to higher stiffness in the direction normal to head joints as compared to the direction normal to bed joints. In the beginning of unloading, a remarkable decrease in the reaction force was noticed without any decrease in the displacement. Then, both the displacement and reaction force decreased. After unloading, the wall did not go back to the initial configuration and there was permanent deformation caused by joints closure and the decrease of joints thickness as compared to the initial one. Due to some technical issues related to the vibration of the camera holding setup and some rigid body motions, DIC analysis were not successful for this test series.

2.3.5.3 S05: biaxial loading and unloading at room temperature

With respect to series S05, it was carried out to investigate the mechanical response of the wall under biaxial compression ($\sigma_{bed}/\sigma_{head} = 1$) at room temperature. Therefore, a 6 MPa biaxial compression load was applied to the directions normal to bed and head joints. As, shown in Figs. 2.20-c and 2.21, two LVDTs were used to measure the displacement in each direction (the measurement in direction normal to bed and head joints were 938 mm and 975 mm, respectively, covering 9 bed joints and 6 head joints). Also, the displacement fields were measured using

DIC. The reaction forces in directions normal to bed and head joints were recorded. As the wall stiffness in directions normal to bed and head joints is different, several trial tests were performed to determine the optimum parameters of the controllers (speed, acceleration, displacement increment, etc) that maintain ($\sigma_{bed}/\sigma_{head} = 1$) at any time during the load application. These optimum parameters were used for the final tests.

The testing procedures of series S05 were as following: the first three steps are similar to that of S03. Then: (iv) The two moving plungers (normal to head and bed joints) were moved manually until they touched the wall sides (i.e. pre-load). (v) The loads in both directions were applied to the wall under displacement control. The displacements and reaction forces were recorded. (vi) After reaching the maximum loads (945 kN and 924 kN, in directions normal to bed and head joints respectively), a dwell time of around 100 seconds was considered. Then, unloading, under displacement control, was performed.

Figure 2.27-a shows an example of the time variations of the resulting reaction forces normal to head (f_{head}) and bed (f_{bed}) joints during loading and unloading. From the previous uniaxial compression tests, it has been shown that the stiffness of the wall in the directions normal to bed and head joints is different. The speed of the two moving plungers was adjusted in order to keep $f_{bed}/f_{head} = 1$. During loading, the maximum programmed forces (945 and 924 kN) were reached almost in the same time. f_{bed} and f_{head} remained constant during the dwell time. Then, the unloading step started and the measured reaction forces dropped gradually.

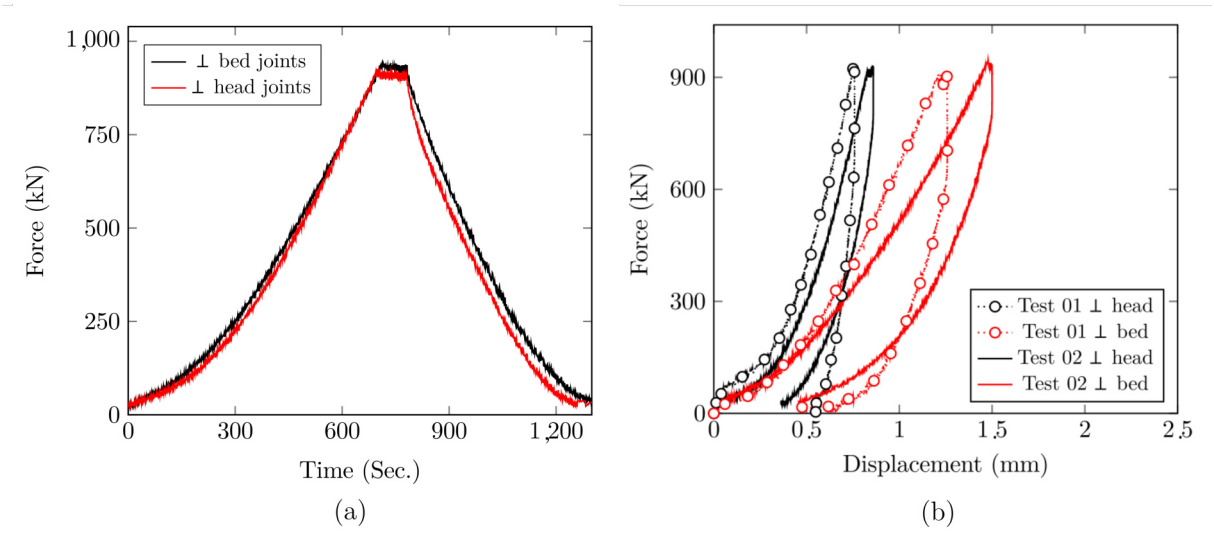

Figure 2.27: Series S05: (a) resulting reaction forces in directions normal to the surfaces of bed and head joints during loading and unloading, (b) force - displacement diagrams in the directions normal to bed and head joints.

Figure 2.27-b shows the force displacement graphs of the two performed tests. The displacements in each direction are calculated as the average of the two displacements measured by the two LVDTs. Good agreement between the two tests can be observed. During load application step and for both directions, a nonlinear displacement stiffening behavior, due to the gradual increase of stiffness with the gradual closure of joints, was observed. The maximum displacement

in the direction normal to head joints is smaller as compared to that in the direction normal to bed joints, because the number of head joints is less than the number of bed joints. Moreover, in comparison with the maximum measured displacements in uniaxial tests (series S03 and S04), the maximum values of the average displacements (in both directions) measured in biaxial tests are smaller. Regarding the unloading, a decrease in the reaction force was observed without any decrease in the displacement. Then, both the displacement and reaction force decreased.

The full displacement fields, in the direction normal to head joints, obtained using DIC of S05-02 at 25 % and 100 % of maximum load level and after unloading are presented in Fig. 2.28. The full displacement fields, in the direction normal to bed joints, obtained using DIC of S05-02 at 25 %, 100 % of maximum load level and after unloading are presented in Fig. 2.29. The noise in the images is caused by the alumina tubes used to measure the displacements. Nonuniform displacement fields can be seen in Figs. 2.28 and 2.29. The negative signs in the color map are due to the coordinate system used in DIC analysis. Absolute values should be considered when comparing the two DIC figures with the force displacement diagrams.

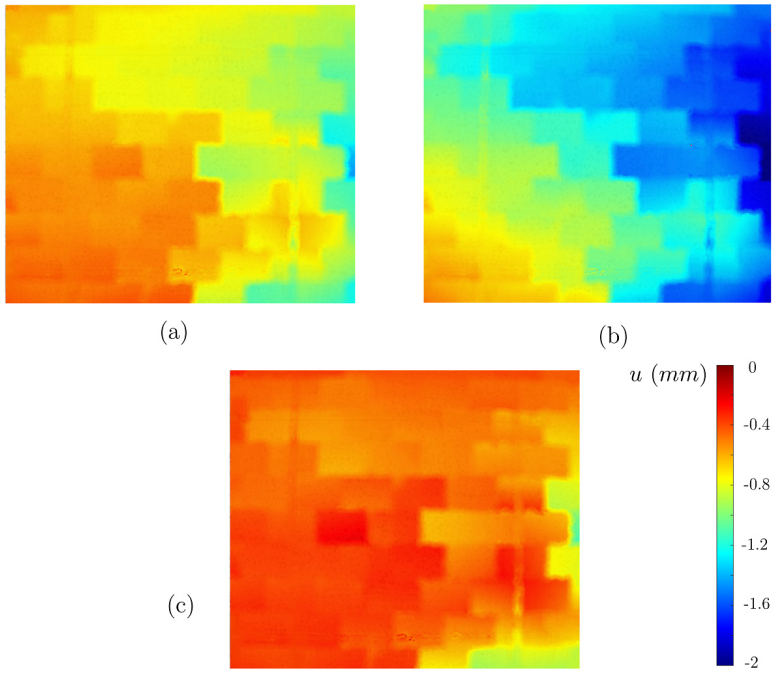

Figure 2.28: Specimen S05-02: displacement fields in the direction normal to head joints (horizontal direction in this image) in S05-02 at: (a) 25 % of maximum load level, (b) 100 % of maximum load level and (c) after unloading.

2.3.5.4 S06: uniaxial creep behavior normal to bed joints - preliminary test

The main goal of series S06, and later S07, was to understand the impact of bed joints (due to dimension errors of the bricks height) and bed joints closure on the nonlinear mechanical response (elastic viscoplastic behavior) of the wall at high temperature. In addition, to understand the creep behavior of the wall when the direction normal to bed joints is loaded (at high temperature)

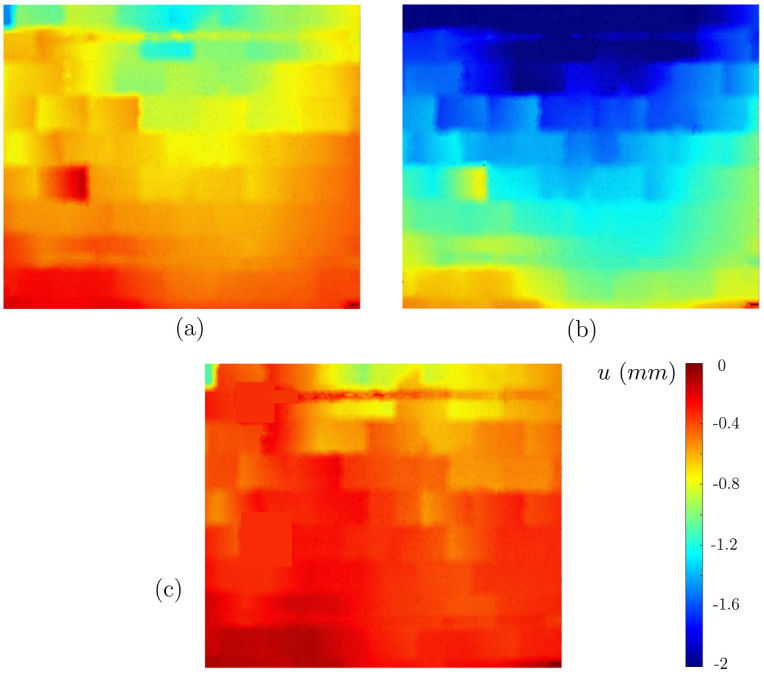

Figure 2.29: Specimen S05-02: displacement fields in the direction perpendicular to bed joints (vertical direction in this image) at: (a) 25 % of maximum load level, (b) 100 % of maximum load level and (c) after unloading.

while the direction normal to head joints is constrained. Therefore, a 6 MPa uniaxial compression load was applied to the direction normal to bed joints and the sides of the walls were constrained by the locked plungers. As shown in Fig. 2.22-a, three LVDTs were used to measure the displacement in the direction normal to bed joints (the measurement range was 790 mm covering seven bed joints). This range is less as compared to room temperature tests. This is due to that the LVDTs had to be moved far from the wall, allowing them to operate within their safe operating temperature range.

The testing procedures of series S06 and S07 were as following: (i) The wall was built in the testing field and soft insulation (superwool) was placed above the moving and fixed plungers. (ii) The LVDTs and thermocouples were connected, calibrated and the water cooled system of the plungers was turned on. (iii) The heating hood was placed on top of the test field and then, heating started. The temperatures of the cold and hot faces were recorded. (iv) After reaching thermal steady state, the moving plunger (normal to head joints) was moved until it touched the wall. (v) The load in the direction normal to bed joints was applied under displacement control (0.01 mm/sec) till reaching 945 kN. Then the hydraulic cylinder controller was switched to force control. The load has been kept constant during the holding time and, finally, unloading. (vi) During load application, holding and unloading, the displacements of the LVDTs and the reaction forces (in both directions) were recorded.

Test series S06 was the first high temperature test and it includes only one test (S06-01). The main goal of this trial series was to test the high temperature test setup, and to answer several questions related to the thermal performance of the test setup such as:

- Is the heating power provided by the heating system sufficient to heat the masonry wall up to 1500 °C?
- Is the insulation of the system good enough and are the thermal losses reasonable?
- Are the LVDTs and the hydraulic jacks operating within the safe temperature range (<40 °C)?

Time variations of the wall's cold (CF) and hot (HF) faces temperatures during heating and testing are presented in Fig. 2.30. The five solid black lines in the figure represent the five temperatures measured by the five thermocouples. The temperature of the CF center was higher as compared to the four thermocouples installed near the corners of the wall. It can be seen that the temperature of the hot face did not reach the desired value (1500 °C) due to low heating power provided by the heating system, high heat capacity of wall and the test setup, and high heat losses (from the heating hood to the ambient and the sides of the wall to the water cooled plungers). After 20 h of heating, several changes in the electrical connections of the heating system were carried out to increase the input electric power. However, all the trials were unsuccessful. The sudden drops in the temperature of the HF (after t = 20 h) occurred during the changes of the electrical connections configuration. After this test, the heating elements and electrical connections configurations were adjusted and the insulation was improved. It was possible to reach the target temperature.

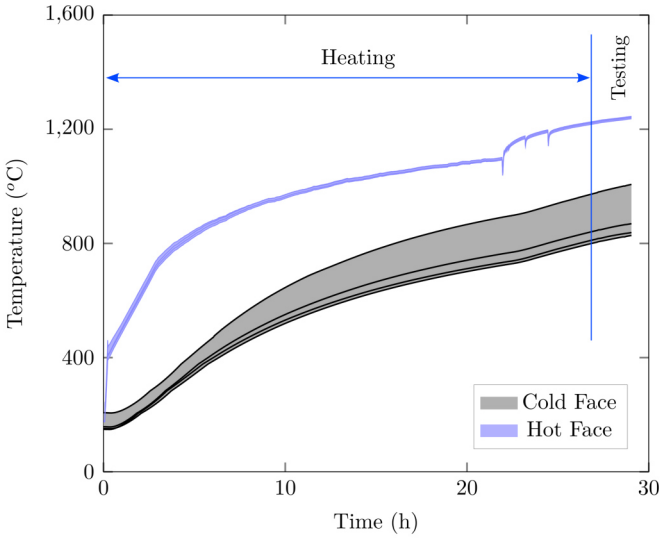

Figure 2.30: Test series S06: time variations of the cold and hot faces temperatures during heating and testing.

During the heating step (first 28 hours), the wall was free to expand. Then a uniaxial compression load of 6 MPa (945 kN) was applied in the direction normal to the bed joints while, the direction normal to head joints was constrained by the ceramic plungers. Time variations of resulting reaction forces normal to bed (f_{bed}) and head (f_{head}) joints of specimen S06-01 during loading and holding stages are given in Fig. 2.31. During loading, f_{bed} increased gradually to reach the pre programmed maximum value of 945 kN. Then, to investigate the uniaxial creep

behavior of the wall in the direction normal to bed joints, f_{bed} was kept almost constant during the holding time. With the rise of f_{bed}, an increase in f_{head} was observed (to around 67 kN). This increase in f_{head} was caused by the constrained expansion of the wall. The value of f_{head} is smaller as compared to that of series S03 due to the decrease of the material stiffness with the temperature increase.

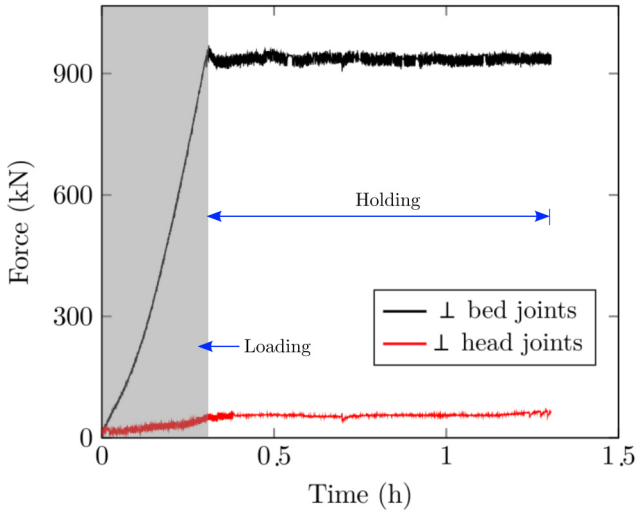

Figure 2.31: Test series S06-01: resulting reaction forces in the directions normal to bed and head joints during mechanical loading and holding stages.

The resulting force – displacement diagram as well as the displacement – time diagram during loading and holding steps are given in Fig. 2.32. The average displacement is calculated as the average of the three displacements measured by the three LVDTs. During loading, a nonlinear displacement stiffening behavior can be observed (see Fig. 2.32-a) due to gradual closure of joints. Then, during the holding step, an increase in the displacement can be observed due to creep. The average total strains (ε_t) in the wall can be calculated from the measured displacement (d) and the LVDTs measurement range (i.e. initial length) (L_0) as: $\varepsilon_t = d/L_0$. It should be noted that the value of ε_t by the end of load application step (0.003) is composed of the strain due to joints closure, elastic and viscoplastic strains of the bricks. This total strain is higher as compared to the total strain of series S03 (0.0024). During the holding step the increase in ε_t from 0.003 to 0.0038 was mainly caused by creep.

2.3.5.5 S07: uniaxial creep behavior normal to bed joints

After adjusting the electrical configurations of the heating system, increasing the input power and improving the insulation of the experimental setup, it was possible to heat the sample to the desired temperature. The defined heating program was as following: from 20 °C to 500 °C in 10 minutes then, from 500 °C to 1500 °C in 10 hours. The fast heating rate in the first 10 minutes was used in order to overcome some electrical technical issues related to the change of electric resistance of the heating elements with temperature. The time variations of cold and

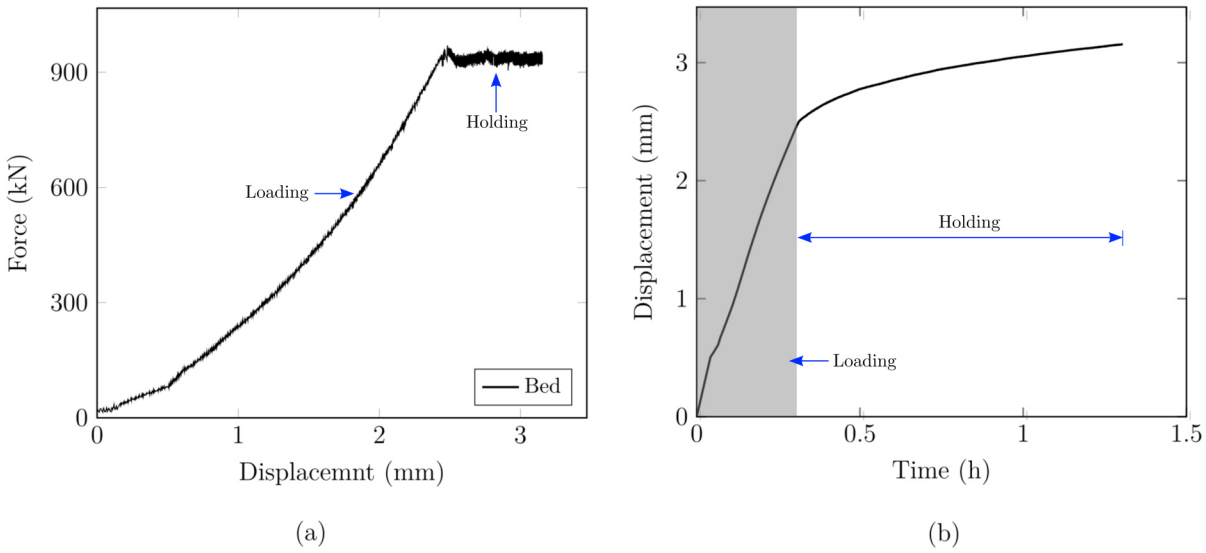

Figure 2.32: Test series S06: (a) resulting force displacement diagram and (b) time variations of average displacement during mechanical loading and holding steps in the direction normal to the surfaces of bed joints.

hot faces temperatures during heating, mechanical load application, holding and unloading are presented in Fig. 2.33. The temperatures of the HF and the CF were measured using ten type B thermocouples, five in each face. In the HF, four thermocouples are inside the alumina tubes (used to measure the displacement) and one was positioned near the center of the HF. Similar values of temperature readings of all five thermocouples on the HF are obtained indicating uniform temperature distribution. In the CF, four thermocouples were installed in the four corners of the wall, and one is installed in the center of the CF. The five solid black lines in the figure represent the five temperatures measured by the five thermocouples. The temperature of the CF center was higher as compared to the four thermocouples installed near the corners of the wall. Due to high heat losses from the outer surface of the heating hood the heating system could not follow the programmed heating curve. It took around 28 h to heat the specimen up to around 1500 °C and reach thermal equilibrium. For all other test series presented below, similar temperature distributions were obtained. Therefore, the time variations of the temperature is presented and discussed only here.

While heating, the wall was free to expand. Then, a uniaxial compression load of 4 MPa (630 kN) was applied in the direction normal to the bed joints while, the direction normal to head joints was restrained by the plungers. Figure 2.34 shows an example of the time variations of f_{bed} and f_{head} during loading, holding and unloading stages. During load application step (lasted around 50 minutes), f_{bed} increased gradually to reach the pre programmed maximum value of 630 kN (4 MPa). Then, to investigate the uniaxial creep behavior of the wall in the direction normal to bed joints, f_{bed} was kept almost constant during the load holding time (16 h). An increase in f_{head} was observed (to around 43 kN) with the increase of f_{bed}. This increase was caused by the lateral restraint provided by the locked plungers. During the holding step and as

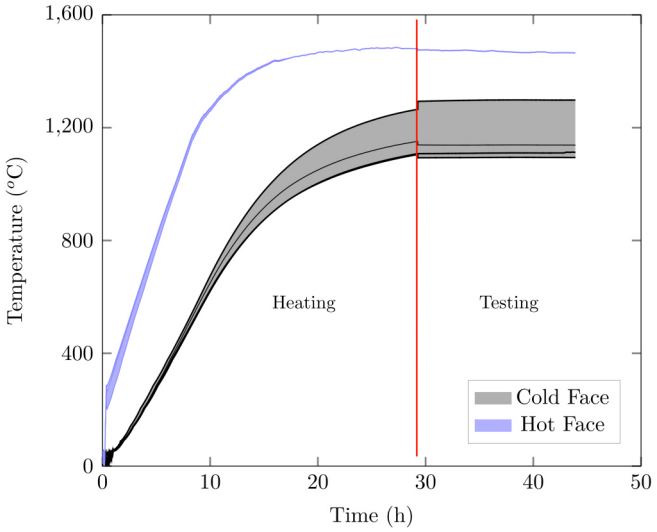

Figure 2.33: Test series S07: time variations of the cold and hot faces temperatures during heating and mechanical testing.

shown in Fig. 2.34-b, f_{head} decreased due to the relaxation behavior in the direction normal to head joints (due to locked positions of the plungers in contact with the sides of the wall). During unloading, f_{bed} and f_{head} decreased gradually to zero.

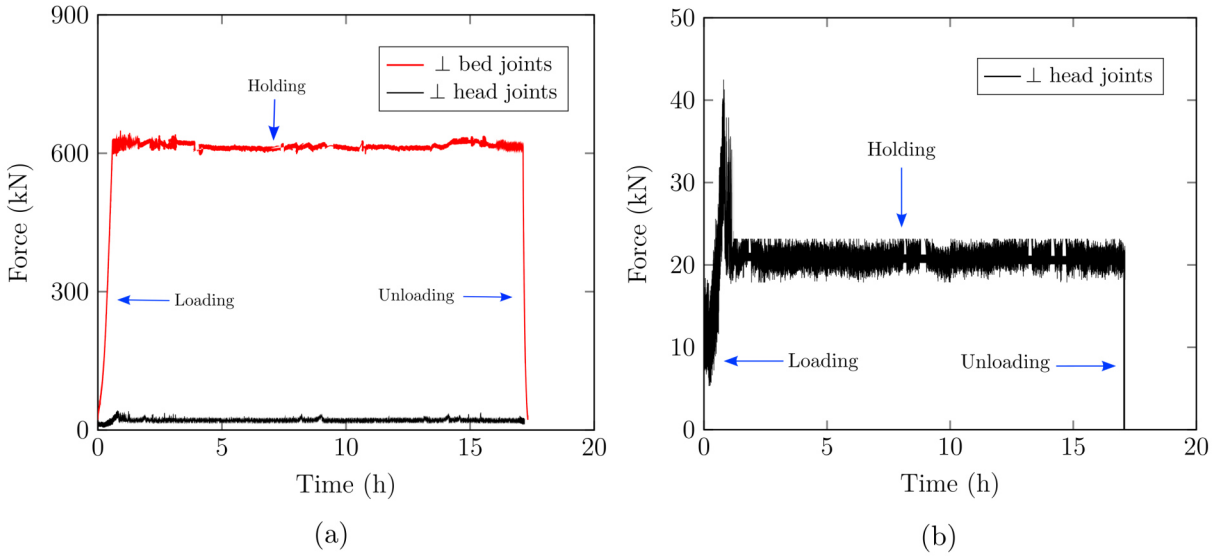

Figure 2.34: Specimen S07-01: (a) resulting reaction forces in the directions normal to the surfaces of bed and head joints during mechanical loading, holding and unloading stages. (b) The decrease in f_{head} during the load holding step.

Figure 2.35 presents the resulting force – displacement diagrams and the displacement – time diagrams of the two performed tests during loading, holding and unloading steps. Good agreement between the two tests was observed. A nonlinear displacement stiffening behavior can be observed during the loading step. During the holding step, an increase in the displacement can be observed due to creep. Then, the displacement decreased slightly due to unloading. In addition, after load removal, the recovered strain is very small as compared to the strain due to

the applied load. This can be attributed to that, first, during unloading, only few joints reopen and their final thickness is very small as compared to the initial joint thickness. More details about this point will be given later in section 2.3.6. Second, the permanent deformation resulting from the viscoplastic behavior of the structure. The noise in the measured force was caused by a problem in the controllers of the hydraulic jacks. By analyzing the displacement – time diagrams, it is possible to observe the primary and secondary creep stages. The ε_t in the wall by the end of load application step was around 0.005. This value reached 0.015 by the end of load holding step. The values of ε_t are higher as compared to series S06 due to higher bulk temperature of the specimen and, therefore, higher creep rates.

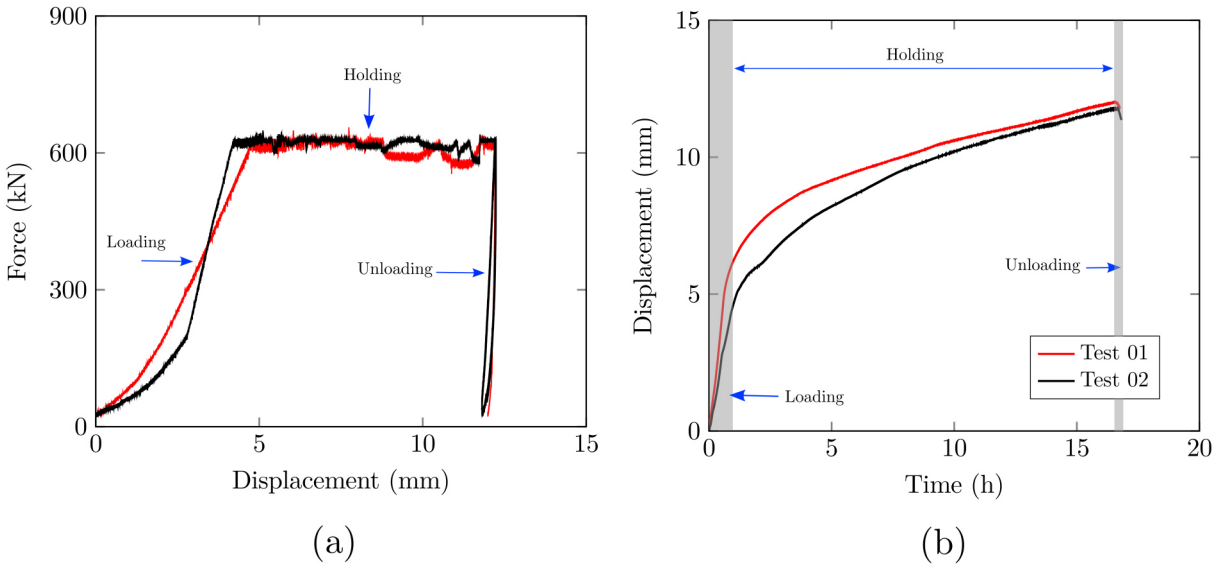

Figure 2.35: Test series S07: (a) resulting force–displacement diagrams and (b) time variations of the average displacements during mechanical loading, holding and unloading steps in the direction normal to bed joints.

2.3.5.6 S08: uniaxial creep behavior normal to head joints

The main goal of series S08 was to understand the impact of head joints and head joints closure on the nonlinear mechanical response (elastic viscoplastic behavior) of the wall at high temperature. In addition, to understand the creep behavior of the wall when the direction normal to head joints is loaded (at high temperature) while the direction normal to bed joints is constrained. Therefore, a 4 MPa uniaxial compression load was applied to the direction normal to head joints and the sides of the walls were constrained by the locked plungers. As shown in Fig. 2.22-c, three LVDTs were used to measure the displacement in the direction normal to head joints (the measurement range was 785 mm covering 5 head joints). The test procedures of series S08 are similar to that of S07. The major difference between S08 and S07 is that the uniaxial compression load was applied to the direction normal to head joints while the other two sides of the wall were constrained by the ceramic plungers (direction normal to bed joints).

The time variations of the HF and CF temperatures are similar to those presented in Fig. 2.33. Figure 2.36 shows the time evolution of f_{head} and f_{bed} of specimen S08-01 during loading, holding and unloading steps. The test was performed one time only due to lack of raw materials (bricks). To study the uniaxial creep behavior of the wall in the direction normal to head joints, f_{head} was kept almost constant during the load holding time. As compared to S07, the maximum programmed force (616 kN) was reached in shorter period of time. This can be attributed to that the number of head joints was smaller than the number of bed joints. With the gradual increase of f_{head}, a rise in f_{bed} was observed due to the constrained expansion of the wall. During the holding step, f_{bed} decreased due to the relaxation behavior in the direction normal to bed joints (see Fig. 2.36-b). After 5 hours of holding, it increased slightly due to a problem in the controller of the hydraulic jack. However, this increase did not greatly impact the results of the test.

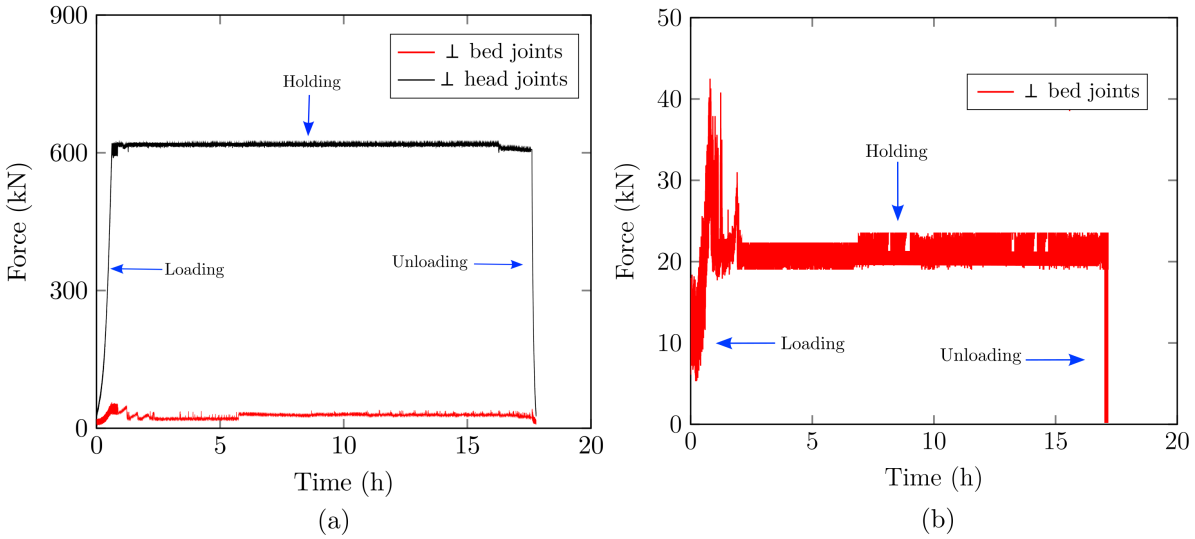

Figure 2.36: Specimen S08-01: (a) resulting reaction forces in the directions normal to the surfaces of bed and head joints during mechanical loading, holding and unloading stages. (b) The decrease in f_{bed} during the load holding step.

The resulting force – displacement diagram and the displacement – time diagram, during loading, holding and unloading steps, of the performed test are shown in Fig. 2.37. During the load application step, a nonlinear displacement stiffening behavior, in the direction normal to head joints, can be observed due to the pre-mentioned reasons. During the holding step, an increase in the average displacement can be observed due to creep. After unloading, a slight decrease in the displacement was observed due to reasons mentioned above. From the displacement – time diagram, it is possible to observe the primary and secondary creep stages. The ε_t in the wall by the end of load application step was around 0.004. This value is slightly smaller as compared to ε_t in the case of S07 (by the end of load application stage) and much higher as compared with series S04. The value of ε_t reached 0.014 by the end of load holding step. It should be noted that in case of test series S07 and test series S08, the increase in ε_t during the holding time is almost equal. The numerical models, presented later in chapters 3 and 4, shall help in understanding the reasons behind this behavior.

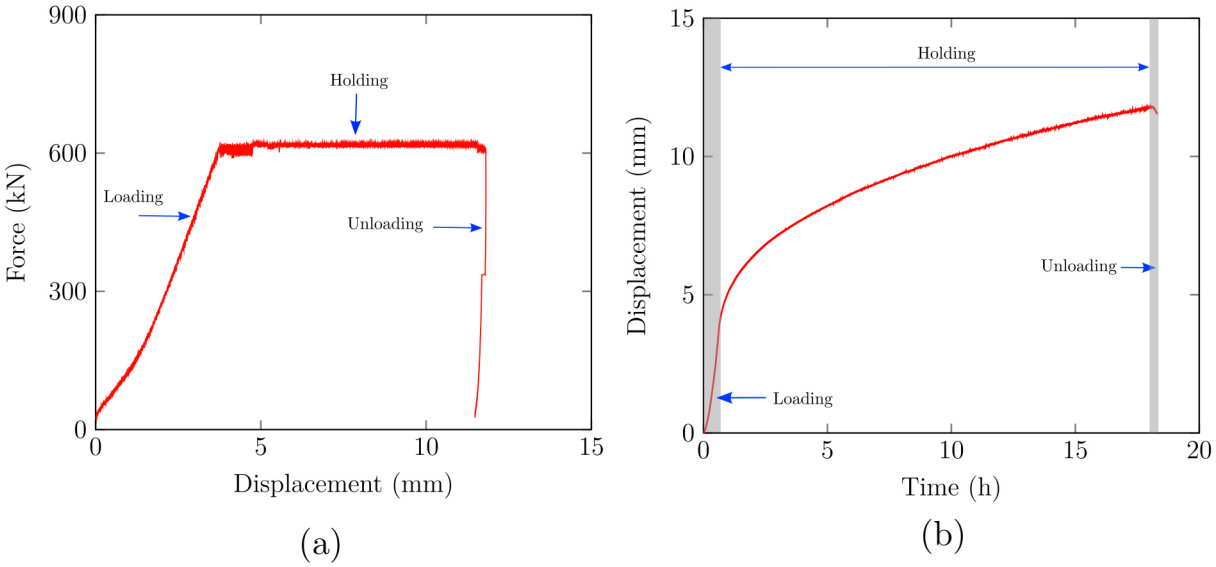

Figure 2.37: Test series S08: (a) resulting force–displacement diagram and (b) time variations of the average displacement during mechanical loading, holding and unloading steps in the direction normal to the surfaces of head joints.

2.3.5.7 S09: biaxial creep behavior

Test series S06, S07 and S08 showed the uniaxial creep behavior of the masonry in the directions normal to bed and head joints. The main objective of test series S09 was to investigate the creep behavior of the wall under in-plane biaxial compression load at high temperature ($\sigma_{bed}/\sigma_{head} \approx 1$). Therefore, a 4 MPa compression load was applied to both directions normal to bed and head joints. As shown in Figs. 2.22-b and 2.23, two LVDTs were used to measure the displacement in each direction (the measurement ranges were 850 and 785 mm in directions normal to bed and head joints, respectively, covering seven bed joints and five head joints).

The testing procedures of series S09 were as following: the first three steps are similar to that of S07 and S08. Then: (iv) After reaching thermal equilibrium, the two moving plungers (normal to head and bed joints) were moved until they touched the wall. (v) The loads in both directions normal to bed and head joints were applied under displacement control (0.01 mm/sec) till reaching 630 kN and 616 kN (4 MPa) in directions normal to bed and head joints, respectively. Then the two hydraulic cylinders were switched to force control. The loads have been kept constant for 16 hours then, unloading. (vi) During load application, holding and unloading, the displacement of the four LVDTs and reaction forces were recorded. The time variations of the HF and CF temperatures are similar to those presented in Fig. 2.33. Figure 2.38 shows the time variations of f_{head} and f_{bed} specimen S09-02 during loading, holding and unloading. The noise in the measured forces are caused by a problem in the controller of the hydraulic jacks.

Figure 2.39 shows the resulting force – displacement diagrams and the displacement – time diagrams in the directions normal to bed and head joints during loading, holding and unloading steps of the two performed tests. The displacement in each direction was calculated as the average of the two displacements measured by the two LVDTs. Good agreement between the

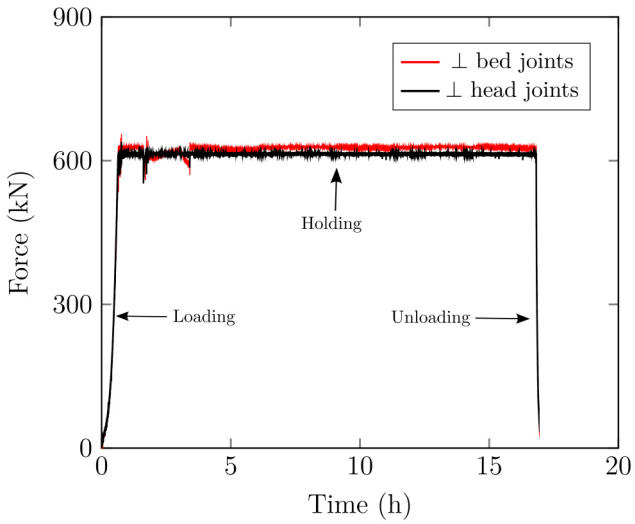

Figure 2.38: Specimen S09-01: resulting reaction forces in the directions normal to the surfaces of bed and head joints during mechanical loading, holding and unloading stages.

two tests can be observed. During load application step and for both directions, a nonlinear displacement stiffening behavior, due to the gradual increase of stiffness with the gradual closure of joints, was observed. The slight drop in f_{bed} and f_{head} of specimen S09-02 during loading was caused by a problem in the controllers of the two hydraulic jacks. The maximum displacement in the direction normal to bed joints is higher as compared to that in the direction normal to head joints due to the difference between the number of bed and head joints in the wall. Again, after load removal, a slight decrease in the displacement was observed.

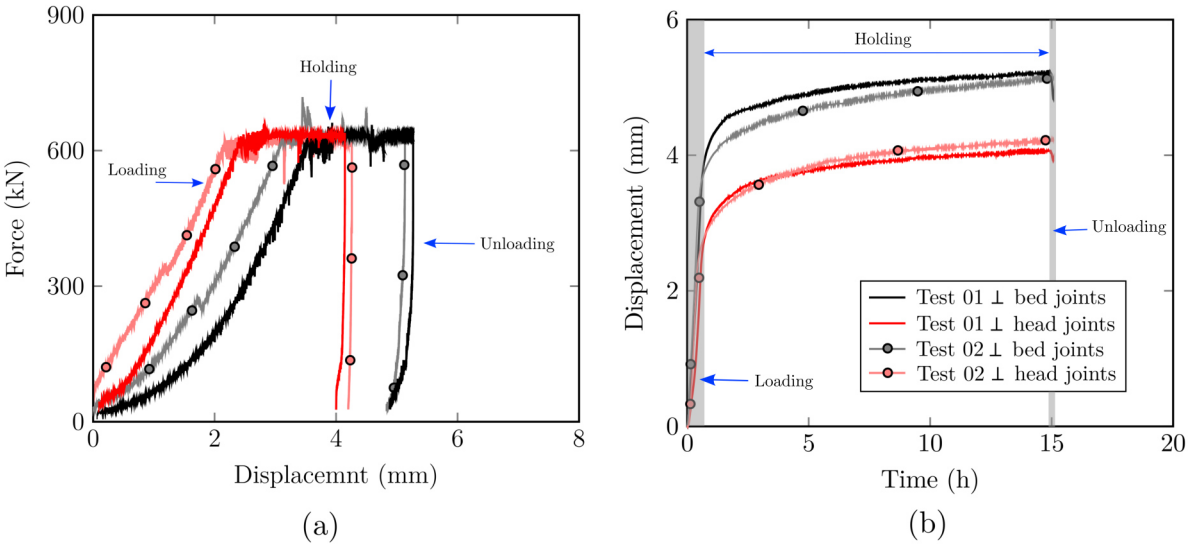

Figure 2.39: Test series S09: (a) resulting force–displacement diagrams and (b) time variations of the average displacements during mechanical loading, holding and unloading steps in the directions normal to the surfaces of bed and head joints.

2.3.5.8 S10: biaxial relaxation behavior

Up to now, all the high temperature uniaxial and biaxial compression tests were performed to investigate the creep behavior of the walls (constant stress loading conditions). The goal of test series S10 was to investigate the relaxation behavior of the wall (constant strain loading conditions). Therefore, at high temperature and after reaching thermal steady state, a biaxial compression load was applied to both directions normal to bed and head joints. Then, the positions of the moving plungers were locked. The arrangements of the LVDTs and the measurement ranges were similar to those of S09. In general, the testing procedures of series S10 are similar to that of S09. The only difference is that the two hydraulic cylinders were kept under displacement control during holding. Only two biaxial relaxation tests were performed due to lack of time and raw materials (bricks). The time variations of the HF and CF temperatures are similar to those presented in Fig. 2.33.

In these tests, two biaxial loading cycles were performed. For the first loading cycle, the wall was loaded up to 4 MPa (in both in-plane directions) and then the ceramic plungers were kept under displacement control for several hours and the resulting reaction forces were measured. Next, the wall was unloaded and loaded directly up to 6 MPa biaxial compression load. Then, the plungers were kept under displacement control for several hours and the reaction forces were recorded. Finally, the wall was unloaded. Figure 2.40 shows the resulting reaction forces in the directions normal to the bed and head joints during the first and second loading cycles. During loading, the resulting reaction forces increased gradually to reach the pre programmed peak load. Then, when the position of the plungers is locked, a decay in the resulting reaction forces was observed due to the relaxation behavior of the wall. In the beginning of the holding stage, a significant decrease in the reaction forces can be observed. Similar behaviors were noticed for both loading cycles.

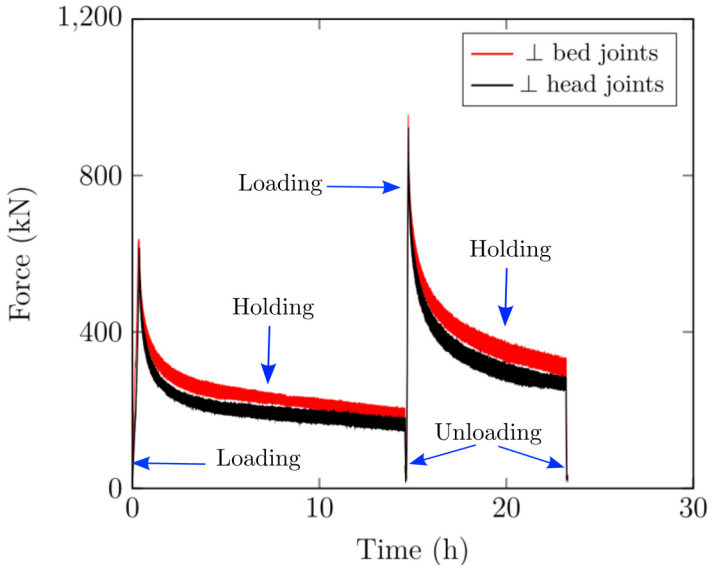

Figure 2.40: Specimen S10-01: resulting reaction forces versus time during loading, holding and unloading steps of the two performed cycles.

It was not possible to keep the same test procedure for the two performed tests due to restrictions imposed by the Austrian authorities (COVID-19 regulations, curfew) when the second test was performed. For the second test, the holding time of first loading cycle was shorter than that of the first test and the holding time of the second loading cycle was longer than that of the first test. Similar trends during loading, holding and unloading were observed. Due to a problem related to bending of the alumina tubes, during the tests, it was not possible to record the displacements of the LVDTs. Only time variations of the resulting reaction forces were recorded. They are reported in Fig. 2.41.

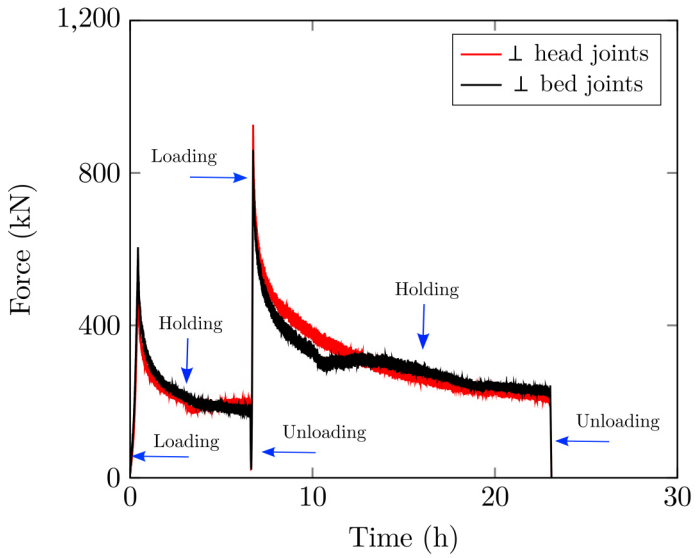

Figure 2.41: Specimen S10-02: resulting reaction force versus time during loading, holding and unloading steps of the two performed cycles.

2.3.6 Remarks

Figure 2.42 presents an example of refractory masonry wall after a creep test at 1500 °C. The zone marked in red indicates the locations of closed joints (after testing) while, the region marked in blue indicates the locations of cracked bricks. The zone in purple indicates the locations of highly deformed bricks. This category of bricks was also found in the red zone. Some examples of perfect closure of head and bed joints are given in Fig. 2.42-b and c. Perfect closure of head joint is depicted in Fig. 2.42-b and perfect closure of both bed and head joints is depicted in Fig. 2.42-c. Due to the high temperature and the thermomechanical load, the bricks were fused together and the joints did not reopen after unloading. The majority of the wall was like this. For this reason, the recovered displacement after unloading was very small. Near the two moving plungers (region in blue) cracks located in the middle of the bricks were observed. Due to the chamfer in the ceramic plungers, Fig. 2.42-e, only half of the brick in contact with the chamfer was loaded. This leads to nonuniform loading conditions and stress concentrations at the middle of the brick. The pink marks in the bricks (near the ceramic plungers) are caused by

the interaction between the superwool soft insulation and the bricks. At high temperature, the soft insulation melted.

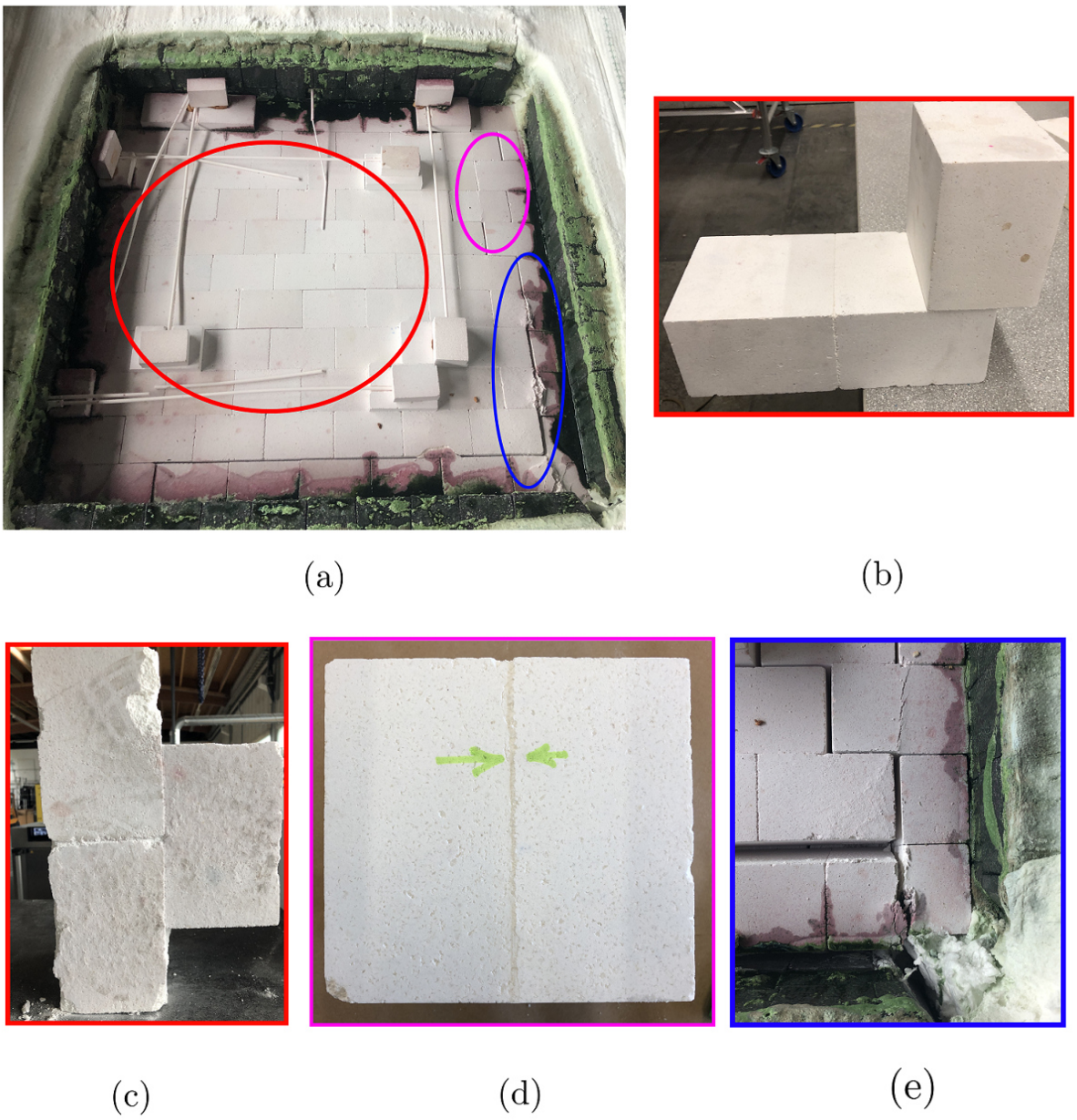

Figure 2.42: An example of refractory masonry wall after creep test at 1500 °C: (a) global view, (b) perfect closure of head joint, two bricks are fused together, (c) perfect closure of bed and head joints, three bricks are fused together, (d) deformation of the bricks, the green arrows highlight the high deformation at the middle of the brick and (e) cracks due to stress concentration.

2.4 Conclusion

This chapter gathers a considerable database on the mechanical and thermomechanical characterization of refractory masonry with dry joints. The test setups, measurement techniques,

specimens, test procedures and results of the two large scale experimental campaigns performed within the framework of ATHOR project were presented. The mechanical and thermomechanical behavior of alumina spinel refractory masonry were investigated for a wide range of loading conditions at room temperature and high temperatures up to 1500 °C. Uniaxial compression tests, in the directions normal to bed and head joints, and biaxial compression tests at room temperature were performed. Uniaxial and biaxial creep tests as well as biaxial relaxation tests were carried out. The results of the tests help in understanding the complex thermomechanical behavior of refractory linings. The impacts of joints, joints closure and reopening, dimensional and shape tolerances of the bricks were investigated. The experimental results clearly demonstrate that the in-plane mechanical behavior of mortarless masonry is orthotropic, highly nonlinear (strain stiffening behavior) and different during loading and unloading. The orthotropic behavior is caused by the difference between the number of bed and head joints. The strain stiffening behavior is caused by the gradual closure of dry joints and the increase of contact area (and effective stiffness with joints closure). The results of these tests are essential for the development, calibration and validation of the multi-scale numerical models presented in chapters 3 and 4.

CHAPTER 3

MULTI-SCALE MODELING OF REFRACTORY MASONRY

In chapter 1, it has been shown that the multi-scale models of masonry appear as a fair compromise between accuracy and computational cost. They can be used to simulate large scale industrial structures such as steel ladles and furnaces. In this chapter, two multi scale numerical models of masonry with mortar and dry joints are proposed. These models are a continuation of previous works carried out at University of Orléans [76, 120, 121]. Several changes are introduced to the existing models then, they have been extended to account for the viscoplasticity of refractories at high temperature. As will be shown in section 3.1, the two models are based on defining the so-called "joint patterns". The homogeneous elastic viscoplastic behavior of each pattern is determined using FE-based nonlinear homogenization technique. Details about the homogenization procedures are given in section 3.2. Suitable transition criteria between the four patterns are defined and discussed in section 3.3. The accuracy of the developed elastic viscoplastic multi scale numerical models was evaluated by comparing the numerical results of the detailed micro modeling approach with that of multi scale modeling. These comparisons are presented in section 3.4. The conclusion of this chapter is given in section 3.5.

3.1 Possible joint patterns

In an industrial scale steel ladle, different refractory layers are used for the construction of the ladle. Each layer has a specific purpose and has unique thermo-physical and mechanical properties. The different layers include a working lining (layer in contact with liquid steel), a safety lining (also called permanent lining), insulation layers, and a steel shell. The working lining is usually made of refractory masonry with dry joints (in some cases it could be castable). While, the safety lining could be built up with refractory masonry with mortar joints (in some cases it could be castable).

3.1.1 Masonry with dry joints

The working lining of the considered steel ladle is built up with refractory masonry with dry joints (see Fig. 1.6). The height and diameter of a typical industrial steel ladle are around 5 and 4.5 m, respectively [138]. The working lining is built up from thousands of tapered shape refractory bricks. However, for the sake of simplicity, cuboid bricks with height (h_b), length (l_b) and depth (d_b) are considered in the present work. The bricks are periodically arranged in running bond texture. Dry joints with initial thickness ($g_0 << h_b,\ l_b,\ d_b$) are separating the bricks from each other. Often, these joints are resulting from the shape, dimensional tolerances and surface unevenness of the bricks. However sometimes, for instance rotary kiln and blast furnace, the joints are designed by attaching cardboard spacers to the bricks during installation to compensate for thermal expansion effects.

Two types of joints are defined on the basis of their orientation: bed joints with initial thickness $g_{0,bed}$ (horizontal joints in Fig. 1.6-b) and head joints with initial thickness $g_{0,head}$ (vertical joints in Fig. 1.6-b). As presented in chapter 2, under cyclic loading and unloading, these joints can close and reopen. The mechanical response of masonry with dry joints varies with the closure and reopening of joints. The experimental results presented in chapter 2 show that the effective stiffness of the masonry walls increases with the closure of joints. This phenomenon should be considered when developing thorough numerical models for the simulation of masonry with dry joints.

For the purpose of considering the impact of joints closure and reopening on the homogenized elastic-viscoplastic behavior of the masonry structures, four possible joint patterns are predefined (see Fig. 3.1). Each pattern is based on the state of both bed and head joints (i.e. open or closed) and represents a different periodic masonry structure with a different equivalent behavior. The four joint patterns are as follows [76]:

1. Pattern AC: head and bed joints are closed (All joints are Closed).
2. Pattern HO: bed joints are closed, while Head joints are Open.
3. Pattern BO: head joints are closed, while Bed joints are Open.
4. Pattern AO: head and bed joints are open (All joints are Open).

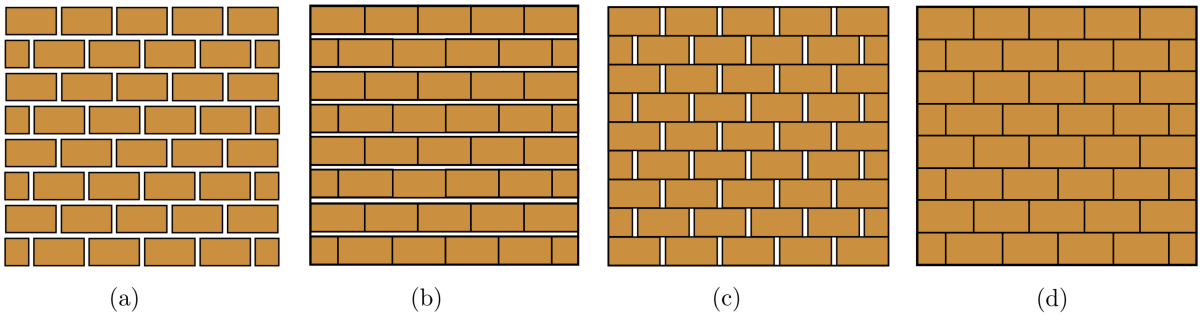

Figure 3.1: Schematics of possible joint patterns of refractory masonry with dry joints (a) pattern AO, (b) pattern BO, (c) pattern HO, and (d) pattern AC.

3.1.2 Masonry with mortar joints

The safety linings of the studied steel ladle are built up with masonry with mortar joints (see Fig. 3.2-a). Bricks with height (h_b), length (l_b) and depth (d_b) are periodically arranged in running bond texture. Mortar joints with thickness (t_m) are separating the bricks from each other. Two types of joints are defined on the basis of their orientation: bed joints with thickness (g_{bed}, horizontal joints in Fig. 3.2-b) and head joints with thickness (g_{head}, vertical joints in Fig. 3.2-b). Usually the thickness of bed and head joints is equal ($g_{bed} = g_{head} = t_m$) and very small (1 to 2 mm) as compared to the dimensions of the bricks ($t_m << h_b,\ l_b,\ d_b$).

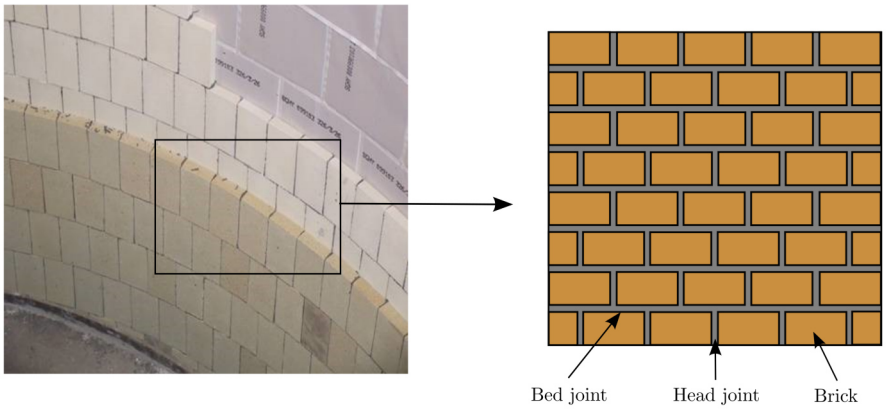

Figure 3.2: (a) The safety lining of a real steel ladle [1]. (b) Schematic of masonry wall with mortar joints showing the bricks and the mortar joints.

Under cyclic thermal or mechanical loading and unloading, the mortar joints can open (damaged) due to either deterioration of internal bonds of the mortar material (cracks through mortar joints) or failure of the brick/mortar interface. It should be noted that the mechanical response of masonry structures varies with the damage evolution of the joints (opening of joints). Previous experimental studies show that the stiffness of masonry structures decreases with the opening of joints [11, 109, 118]. This phenomenon should be considered when developing thorough numerical models for describing the structural behavior of masonry structures. According to Luciano and Sacco [118, 119], the structural behavior of the masonry can be described by considering two states of the brick/mortar interface (open or closed, i.e. damaged or undamaged). For the purpose of considering the impact of joints opening on the homogenized elastic viscoplastic behavior of masonry structures, four possible joint patterns are predefined (see Fig. 3.3). Each pattern is defined based on the state of both bed and head joints (i.e. undamaged or damaged) and represents a different periodic masonry structure with a different equivalent behavior. The four joint patterns are as follows [121]:

1. Pattern AS: All head and bed joints are Safe.
2. Pattern BD: Bed joints are Damaged while, head joints are undamaged.
3. Pattern HD: Head joints are Damaged, while bed joints are undamaged.
4. Pattern AD: All head and bed joints are Damaged.

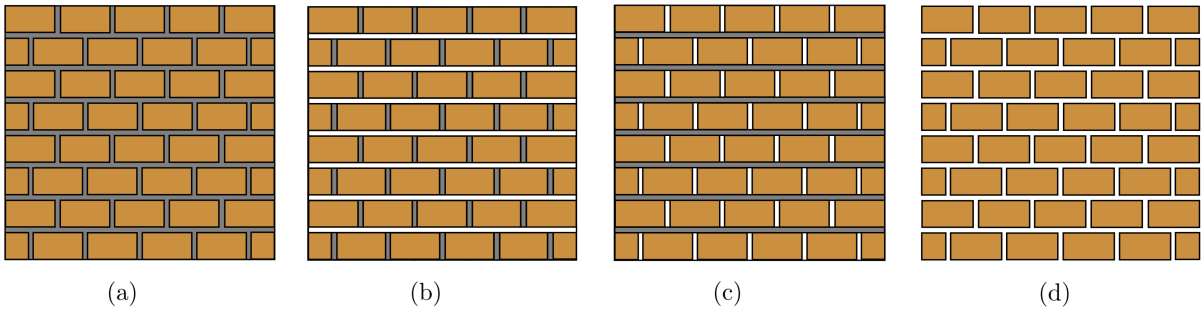

Figure 3.3: Schematics of possible joint patterns of masonry structure with mortar joints (a) pattern AS, (b) pattern BD, (c) pattern HD, and (d) pattern AD.

3.2 Periodic nonlinear homogenization

As presented above, the pre-defined possible joint patterns of masonry with mortar or dry joints are periodic. For the two types of masonry, every joint pattern has a different homogeneous elastic viscoplastic behavior that can be determined using FE – based homogenization technique. At high temperature, the behavior of refractories is elastic-viscoplastic [10, 136, 139]. Therefore, the constitutive materials of the bricks (masonry with dry joints) and mortar (masonry with mortar joints) are assumed to undergo small deformations (i.e. the displacement gradients are small, each component is small as compared to unity), and to exhibit an isotropic linear elasticity as well as an isotropic steady state rate-dependent plasticity (secondary creep). Under these assumptions, the total strain second order tensor ($\overline{\overline{\varepsilon^t}}$) can be described by the symmetric part of the displacement vector ($\overline{u}$) with respect to the position vector ($\overline{X}$) of the material point according to:

$$\overline{\overline{\varepsilon^t}} = \frac{1}{2}\left(\frac{\partial \overline{u}}{\partial \overline{X}} + \left(\frac{\partial \overline{u}}{\partial \overline{X}}\right)^{\mathrm{T}}\right) \tag{3.1}$$

The total strain tensor can be additively decomposed into elastic ($\overline{\overline{\varepsilon^{\mathrm{e}}}}$) and viscoplastic ($\overline{\overline{\varepsilon^{\mathrm{vp}}}}$) second order strain tensors according to:

$$\overline{\overline{\varepsilon^{\mathrm{t}}}} = \overline{\overline{\varepsilon^{\mathrm{e}}}} + \overline{\overline{\varepsilon^{\mathrm{vp}}}} \tag{3.2}$$

The second order linear elastic strain tensor can be determined using Hooke's law for linear elasticity according to:

$$\overline{\overline{\varepsilon^{\mathrm{e}}}} = \frac{1+\nu}{Y}\,\overline{\overline{\sigma}} - \frac{\nu}{Y} tr(\overline{\overline{\sigma}})\overline{\overline{I}} \tag{3.3}$$

where ν is the Poisson's ratio and Y is the Young's modulus of the bulk material of the bricks. $\overline{\overline{\sigma}}$ and $\overline{\overline{I}}$ refer respectively to the second order local stress tensor and the second order identity tensor.

The steady state viscoplastic strain rate second order tensor ($\overline{\overline{\dot{\varepsilon}^{\mathrm{vp}}}}$) is expressed as [140]:

$$\overline{\overline{\dot{\varepsilon}^{\mathrm{vp}}}} = \frac{3}{2} A\ (\sigma_{eq})^{n-1}\ \overline{\overline{\sigma}}_d \tag{3.4}$$

where A and n are the creep parameters of the bulk material of the bricks. σ_{eq} and $\overline{\overline{\sigma}}_d$ denote the von Mises equivalent stress and the second order deviatoric stress tensor, respectively.

The deviatoric stress tensor and von Mises equivalent stress are expressed as [140]:

$$\overline{\overline{\sigma}}_d = \overline{\overline{\sigma}} - \frac{1}{3} tr(\overline{\overline{\sigma}}) \overline{\overline{I}} \tag{3.5}$$

$$\sigma_{eq} = \sqrt{\frac{3}{2}\, \overline{\overline{\sigma}}_{\mathrm{d}} : \overline{\overline{\sigma}}_{\mathrm{d}}} \tag{3.6}$$

The required material parameters of the bricks and the mortar used in this chapter are reported in table 3.1. The dimensions of the brick are: $l_b = 124$ mm, $h_b = 76$ mm, $d_b = 185$ mm. For the sake of simplicity, no strain hardening of the constitutive material of the bricks and the mortar is considered. In addition, symmetric creep behavior is assumed (i.e. creep parameters in tension and compression are equal). Further studies to investigate the impact of creep asymmetry, strain hardening of the material and the creep model (primary or secondary) are planned in the future.

In case of masonry with mortar joints, both the bricks and the mortar are used for the construction of the wall and the creep parameters of the mortar can be different from those of the bricks. However, the thickness of the mortar joints is very small (1 to 2 mm) as compared to the height and length of the bricks. Measuring the creep parameters of the mortar may posses some technical challenges related to sample preparation, testing etc. Therefore, an evaluation of the impact of mortar's creep parameter (A, n) on the homogenized viscoplastic behavior of the structure has been carried out. Three sets of mortar's creep parameters, A and n, are numerically tested namely: (a) $A = 2.77 \times 10^{-8}$ and $n = 2.8$ (equal to those of the brick), (b) $A = 2 \times 10^{-14}$ and $n = 0.2$ and (c) $A = 2 \times 10^{-5}$ and $n = 4$ (parameters in cases b and c are very different from those of the brick). Comparisons between macroscopic total strains in a unit cell (UC), subjected to constant uniaxial tensile stress of 1.5 MPa along the direction normal to head joints, obtained using the three sets of A and n are shown in Fig. 3.4. It can be seen that the impact of mortar's creep parameters on the macroscopic strain is negligible. This can be attributed to that the thickness of the mortar is very small as compared to the dimensions of the brick. Therefore, in the present study, the creep parameters of the bricks and the mortar are assumed to be equal.

Table 3.1: Material parameters of the refractory bricks and the mortar.

Property	Value	
	Brick [139]	Mortar
Y (MPa)	11000	1500
ν (—)	0.2	0.1
n (—)	2.8	2.8, 0.2, 4
A $(s^{-1}\ MPa^{-n})$	2.77×10^{-8}	$2.77 \times 10^{-8},\ 2 \times 10^{-14},\ 2 \times 10^{-5}$

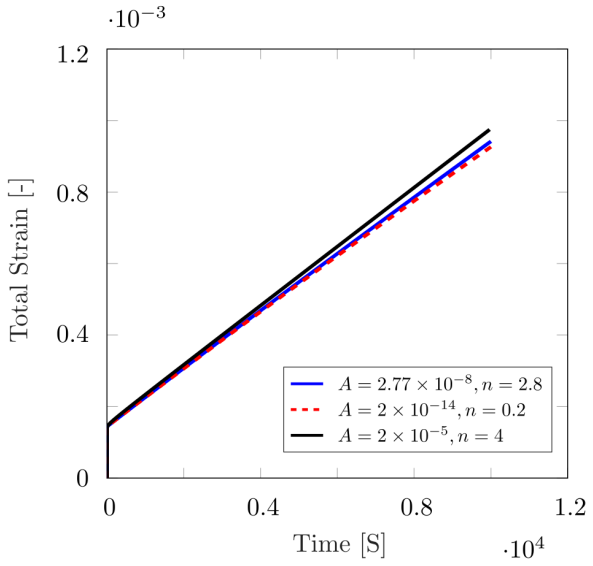

Figure 3.4: Impact of mortar's creep parameters on the homogenized total strain in a UC subjected to uniaxial tensile stress of 1.5 MPa in the direction normal to head joints.

3.2.1 Nonlinear homogenization of masonry with dry joints

3.2.1.1 Pattern AC

As indicated previously in the case of joint pattern AC, head and bed joints are perfectly closed (see Fig. 3.1). Previous experimental studies have shown that when joints are closed, the mechanical behavior of the masonry is similar to the mechanical behavior of the base material of the bricks. Thus, the macroscopic elastic-viscoplastic behavior of pattern AC is isotropic, similar to that of the base material of the bricks and can be described by equations 3.1 to 3.6.

3.2.1.2 Pattern HO

A. Micro modeling

In the case of pattern HO, head joints are open, and bed joints are closed (see Fig. 3.1). The existence of open joints in the masonry results in a reduction in their effective stiffness [76, 138, 141, 142]. Thus, the macroscopic elastic-viscoplastic behavior of pattern HO is different from that of the base material of the bricks. For the purpose of studying the homogenized mechanical behavior of periodic structures, like pattern HO, and computing the effective elastic viscoplastic parameters, the finite element FE – based homogenization technique can be adopted [48, 143–147].

To carry out homogenization of joint pattern HO using FE technique, a periodic unit cell (UC) with volume (V_{UC}) has been selected from the periodic structure as illustrated in Fig. 3.5. Then, 3D – FE simulations have been performed on the UC to characterize its homogenized elastic viscoplastic response. To account for the periodicity of the structure, periodic boundary conditions have been applied to the UC's boundaries [23, 55, 56]. In contrast to homogeneous

boundary conditions, periodic boundary conditions satisfy both boundary displacement periodicity and boundary traction periodicity. Moreover, homogeneous boundary conditions are over constrained conditions, violate stress periodicity of the boundaries and, therefore, are not recommended to be used for periodic UC subjected to shear loading conditions [23, 56].

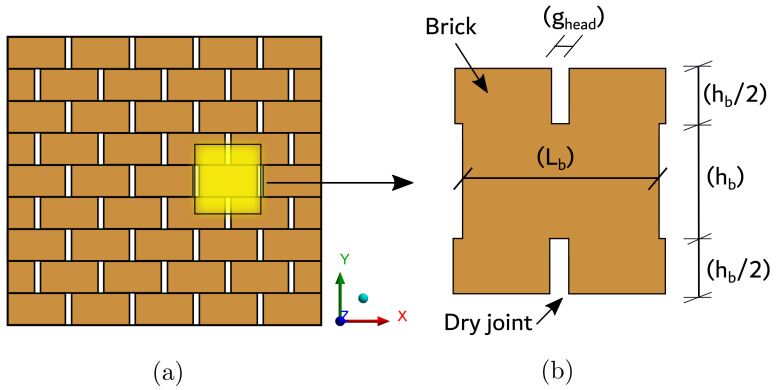

Figure 3.5: (a) Schematic of periodic mortarless masonry structure in pattern HO. (b) Periodic unit cell selected from the structure and used for the nonlinear finite element based homogenization analysis.

Several FE numerical experiments of uniaxial tensile tests along the x, y and z directions and simple shear tests in the xy, xz, and yz planes (see Fig. 3.6) have been performed. The numerical models have been developed using ABAQUS. In all cases, the UC has been subjected to an average or macroscopic stress (Σ, shear or normal) of 1.5 MPa. The base material of the bricks is considered to exhibit an isotropic linear elasticity, an isotropic steady state rate-dependent plasticity (secondary creep) and to obey the elastic and viscoplastic constitutive equations given in section 3.2.

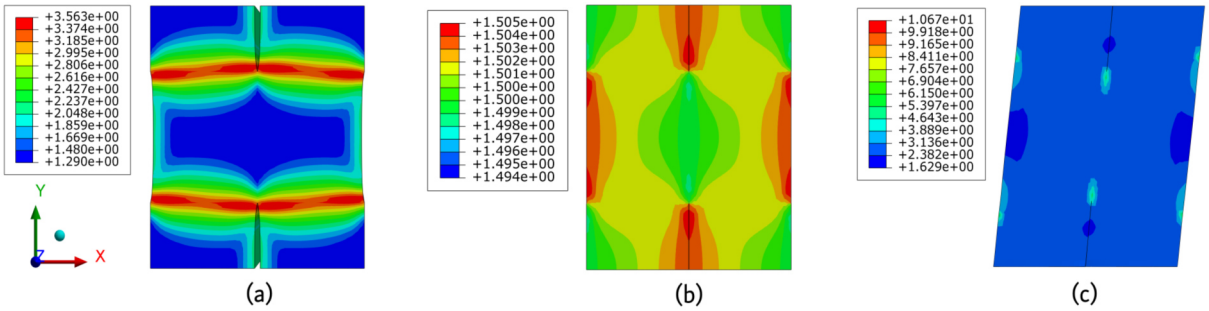

Figure 3.6: Von Mises stress (in MPa) distribution in a periodic unit cell subjected to periodic boundary conditions and (a) uniaxial tension along the x-direction (Σ_{xx}=1.5 MPa), (b) uniaxial tension along the y-direction (Σ_{yy}=1.5 MPa) and (c) simple shear in the xy plane (Σ_{xy}=1.5 MPa).

To characterize the homogenized elastic behavior of the UC and to avoid the contribution of the viscoplastic strain when calculating the effective elastic stiffness of the structure, first, purely elastic numerical simulations have been carried out. Then, viscoplastic numerical analysis have been performed on the UC to characterize its homogenized viscoplastic response. From Fig. 3.6,

it can be seen that the periodicity of boundary displacements and stresses are satisfied due to the applied periodic boundary conditions. From the uniaxial tensile and simple shear numerical tests of the UC subjected to macroscopic normal or shear stress of 1.5 MPa, the macroscopic strain components and the effective material parameters can be found.

B. Macro modeling

B. 1. Macroscopic elastic behavior

The first goal is to define a relation between macroscopic stress tensor and macroscopic elastic strain tensor (i.e. determine the effective elastic stiffness tensor of pattern HO). Due to the existence of open joints, the macroscopic elastic behavior of pattern HO is orthotropic and can be described using equation 3.7. In the case of orthotropic linear elastic materials, the macroscopic stress tensor is related to the macroscopic elastic strain tensor through the macroscopic form of Hooke's law as following [148]:

$$\overline{\overline{\Sigma}} = \overline{\overline{\overline{\overline{C^e}}}} : \overline{\overline{E^{\mathrm{e}}}} \tag{3.7}$$

Where $\overline{\overline{\Sigma}}$ and $\overline{\overline{E^{\mathrm{e}}}}$ are the second order macroscopic stress and elastic strain tensors, while $\overline{\overline{\overline{\overline{C^e}}}}$ is the fourth order macroscopic elastic stiffness tensor.

In equation 3.7, the second and fourth order tensors are symmetric and, therefore, they can be respectively reduced to 6×1 and 6×6 matrices using Voigt notations [145]. The effective elastic fourth order tensor is characterized by 9 nonzero components and can be written in a matrix form, with respect to the principal material coordinate system, using Voigt notations as follows [148]:

$$\overline{\overline{C^{\mathrm{e}}}} = \begin{bmatrix} \frac{1-\widetilde{\nu}_{\mathrm{yz}}\widetilde{\nu}_{\mathrm{zx}}}{\widetilde{E}_{\mathrm{y}}\widetilde{E}_{\mathrm{z}}\triangle} & \frac{\widetilde{\nu}_{\mathrm{yx}}+\widetilde{\nu}_{\mathrm{zx}}\widetilde{\nu}_{\mathrm{yz}}}{\widetilde{E}_{\mathrm{y}}\widetilde{E}_{\mathrm{z}}\triangle} & \frac{\widetilde{\nu}_{\mathrm{zx}}+\widetilde{\nu}_{\mathrm{yx}}\widetilde{\nu}_{\mathrm{zy}}}{\widetilde{E}_{\mathrm{y}}\widetilde{E}_{\mathrm{z}}\triangle} & 0 & 0 & 0 \\ \frac{\widetilde{\nu}_{\mathrm{xy}}+\widetilde{\nu}_{\mathrm{xz}}\widetilde{\nu}_{\mathrm{zy}}}{\widetilde{E}_{\mathrm{x}}\widetilde{E}_{\mathrm{z}}\triangle} & \frac{1-\widetilde{\nu}_{\mathrm{zx}}\widetilde{\nu}_{\mathrm{xz}}}{\widetilde{E}_{\mathrm{x}}\widetilde{E}_{\mathrm{z}}\triangle} & \frac{\widetilde{\nu}_{\mathrm{zy}}+\widetilde{\nu}_{\mathrm{zx}}\widetilde{\nu}_{\mathrm{xy}}}{\widetilde{E}_{\mathrm{x}}\widetilde{E}_{\mathrm{z}}\triangle} & 0 & 0 & 0 \\ \frac{\widetilde{\nu}_{\mathrm{xz}}+\widetilde{\nu}_{\mathrm{xy}}\widetilde{\nu}_{\mathrm{yz}}}{\widetilde{E}_{\mathrm{x}}\widetilde{E}_{\mathrm{y}}\triangle} & \frac{\widetilde{\nu}_{\mathrm{yz}}+\widetilde{\nu}_{\mathrm{xz}}\widetilde{\nu}_{\mathrm{yx}}}{\widetilde{E}_{\mathrm{x}}\widetilde{E}_{\mathrm{y}}\triangle} & \frac{1-\widetilde{\nu}_{\mathrm{xy}}\widetilde{\nu}_{\mathrm{yx}}}{\widetilde{E}_{\mathrm{x}}\widetilde{E}_{\mathrm{y}}\triangle} & 0 & 0 & 0 \\ 0 & 0 & 0 & \widetilde{G}_{\mathrm{xy}} & 0 & 0 \\ 0 & 0 & 0 & 0 & \widetilde{G}_{\mathrm{xz}} & 0 \\ 0 & 0 & 0 & 0 & 0 & \widetilde{G}_{\mathrm{yz}} \end{bmatrix} [MPa], \tag{3.8}$$

With,

$$\triangle = \frac{1 - \widetilde{\nu}_{\mathrm{xy}}\widetilde{\nu}_{\mathrm{yx}} - \widetilde{\nu}_{\mathrm{yz}}\widetilde{\nu}_{\mathrm{zy}} - \widetilde{\nu}_{\mathrm{zx}}\widetilde{\nu}_{\mathrm{xz}} - 2\widetilde{\nu}_{\mathrm{xy}}\widetilde{\nu}_{\mathrm{yz}}\widetilde{\nu}_{\mathrm{zx}}}{\widetilde{E}_{\mathrm{x}}\widetilde{E}_{\mathrm{y}}\widetilde{E}_{\mathrm{z}}} \tag{3.9}$$

In the above equations, $\widetilde{E}$ and $\widetilde{\nu}$ denote respectively the macroscopic or effective Young's modulus and the macroscopic or effective Poisson's ratio. $\widetilde{G}$ is the macroscopic or effective shear modulus.

According to the average theorems, when a uniform stress is applied to the boundary surfaces of the UC, the macroscopic stress is equal to the applied stress (i.e. $\overline{\overline{\sigma}} = \overline{\overline{\Sigma}}$) [145]. Another possible approach for calculating the macroscopic stress is to integrate the local stress fields over

the volume of the UC (V_{UC}) according to Hill's definition as follows [48–50]:

$$\overline{\overline{\Sigma}} = \langle \overline{\overline{\sigma}} \rangle = \frac{1}{V_{\mathrm{UC}}} \int_{V_{\mathrm{UC}}} \overline{\overline{\sigma}} dV \tag{3.10}$$

From the simulated combination of uniaxial tensile and simple shear tests, the local strains can be obtained from solving the boundary value problem of the UC subjected to average normal or shear stress of 1.5 MPa. From the local elastic strains, the macroscopic elastic strains can be calculated. Then, using equations 3.7 - 3.9, the nine nonzero components of $\overline{\overline{\overline{\overline{C^e}}}}$ can be found and the relation between the macroscopic stress tensor and macroscopic elastic strain tensor can be established.

In previous studies, two main approaches have been used to calculate the macroscopic strain fields [25, 48, 49, 51–54]. The first approach is based on calculating the macroscopic total strain by integrating the local total strain ($\overline{\overline{\varepsilon^t}}$) over the volume of the UC according to [25, 48, 51, 52]:

$$\overline{\overline{E^t}} = \langle \overline{\overline{\varepsilon^t}} \rangle = \frac{1}{V_{\mathrm{UC}}} \int_{V_{\mathrm{UC}}} \overline{\overline{\varepsilon^t}} dV \tag{3.11}$$

In the second approach, the macroscopic elastic strains are calculated from the average change in the displacements of the UC's corners (i.e. by dividing the change in displacements of the corners by the initial dimensions of the UC) [49, 53, 54]. If there are neither gaps nor cracks in the UC, both techniques converge to the same value. However, in the case of joint pattern HO, the macroscopic elastic strains cannot be computed by integrating the micro (or local) strains over the volume of the UC (first approach). As, the presence of open joints within the UC leads to discontinuous displacement fields (see Fig. 3.7), because there is neither viscosity nor rigidity in the volume of the gaps (i.e. local strains within the gaps are unknown) [48, 49]. Therefore, in the present study, the second approach has been used to calculate the macroscopic strains. The calculated 9 nonzero components of $\overline{\overline{\overline{\overline{C^e}}}}$ are reported in table 3.2. Now, the relationship between macroscopic stresses and macroscopic elastic strains is established. Further details on defining the macroscopic viscoplastic behavior law are given below.

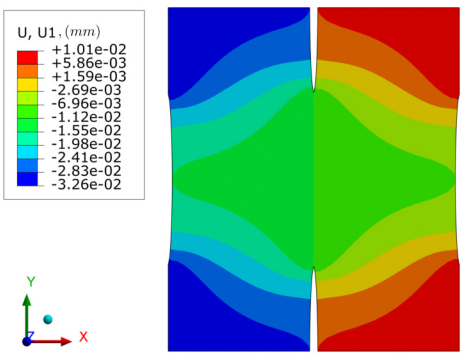

Figure 3.7: Displacement discontinuity in a periodic unit cell subjected to uniaxial tension along the x direction.

B. 2. Macroscopic viscoplastic behavior

The second goal is to define a macroscopic constitutive law to describe the viscoplastic behavior of joint pattern HO. The macroscopic elastic viscoplastic behavior of joint pattern HO is orthotropic due to the presence of open head joints. In order to describe the macroscopic viscoplastic behavior of joint pattern HO, an orthotropic creep equation is required. It should be noted that equation 3.4 is suitable only for describing the local creep behavior of isotropic materials such as joint pattern AC. The orthotropic homogenized steady-state viscoplastic behavior of heterogeneous solids can be described using the macroscopic form of equation 3.4 developed by Tsuda et al. [48, 54, 143, 149]. The main advantage of this constitutive law is that using the same parameters of the base material, the orthotropic homogenized viscoplastic behaviour of heterogeneous solids can be found. The constitutive law is obtained through averaging the local fields ($\overline{\overline{\sigma}}$, $\overline{\overline{\dot{\varepsilon}^{\mathrm{vp}}}}$, and σ_{eq}) over the volume of the UC and using a localization tensor according to:

$$\overline{\overline{\dot{E}^{vp}}} = \frac{1}{2} A \left(\Sigma_{eq}\right)^{n-1} \overline{\overline{\overline{\overline{N}}}} : \overline{\overline{\Sigma}} \tag{3.12}$$

Where A and n are materials parameters of the bricks, reported in table 3.1, Σ_{eq} and $\overline{\overline{\overline{\overline{N}}}}$ are the macroscopic equivalent stress and a fourth order tensor with the same meaning of the localization tensor. Tensor $\overline{\overline{\overline{\overline{N}}}}$ accounts for the orthotropy and compressibility in the x direction of the structure and enables using the creep parameters of the constitutive material (i.e. bridge between the micro and macro scales). Tensor $\overline{\overline{\overline{\overline{N}}}}$ is symmetric and can be represented by 6×6 matrix using Voigt notations. $\overline{\overline{\overline{\overline{N}}}}$ is characterized by 9 nonzero components and can be represented, with respect to the principal material coordinate system, as:

$$\overline{\overline{\overline{\overline{N}}}} = \begin{bmatrix} N_{11} & N_{12} & N_{13} & 0 & 0 & 0 \\ N_{12} & N_{22} & N_{23} & 0 & 0 & 0 \\ N_{13} & N_{23} & N_{33} & 0 & 0 & 0 \\ 0 & 0 & 0 & N_{44} & 0 & 0 \\ 0 & 0 & 0 & 0 & N_{55} & 0 \\ 0 & 0 & 0 & 0 & 0 & N_{66} \end{bmatrix} \tag{3.13}$$

For heterogeneous solids, the macroscopic equivalent stress is written in terms of the macroscopic stress tensor and $\overline{\overline{\overline{\overline{N}}}}$ as [48, 54, 150]:

$$\Sigma_{eq} = \sqrt{\frac{1}{2} \left(\overline{\overline{\Sigma}}\right)^{T} : \overline{\overline{\overline{\overline{N}}}} : \overline{\overline{\Sigma}}} \tag{3.14}$$

Here $\left(\overline{\overline{\Sigma}}\right)^{T}$ is the transpose of the macroscopic stress second order tensor. The macroscopic equivalent viscoplastic strain rate ($\dot{E}^{vp}_{eq}$) is defined in terms of $\overline{\overline{\overline{\overline{N}}}}$ and $\overline{\overline{\dot{E}^{vp}}}$ as follows [48]:

$$\dot{E}^{vp}_{eq} = \sqrt{2 \left(\overline{\overline{\dot{E}}}^{\,vp}\right)^{T} : \left(\overline{\overline{\overline{\overline{N}}}}\right)^{-1} : \overline{\overline{\dot{E}^{vp}}}} \tag{3.15}$$

By combining equations 3.12 - 3.14 and using the combinations of uniaxial and simple shear finite element numerical tests presented before, the 9 non-zero components of tensor $\overline{\overline{\overline{N}}}$ can be calculated and the macroscopic creep law can be defined.

Under uniaxial loading and periodic boundary conditions, the shear components of the macroscopic stress tensor vanish. Therefore, the first 6 components of $\overline{\overline{\overline{N}}}$ can be defined as follows [48]:

- Uniaxial tension along the x-direction

$$N_{11} = 2\left(\frac{1}{\Sigma_{xx}}\right)^2 \left(\frac{\Sigma_{xx}\dot{E}^{vp}_{xx}}{A}\right)^{\frac{2}{n+1}} \tag{3.16}$$

$$N_{12} = \left(\frac{\dot{E}^{vp}_{yy}}{\dot{E}^{vp}_{xx}}\right) N_{11} \tag{3.17}$$

$$N_{13} = \left(\frac{\dot{E}^{vp}_{zz}}{\dot{E}^{vp}_{xx}}\right) N_{11} \tag{3.18}$$

- Uniaxial tension along the y-direction:

$$N_{22} = 2\left(\frac{1}{\Sigma_{yy}}\right)^2 \left(\frac{\Sigma_{yy}\dot{E}^{vp}_{yy}}{A}\right)^{\frac{2}{n+1}} \tag{3.19}$$

$$N_{12} = \left(\frac{\dot{E}^{vp}_{xx}}{\dot{E}^{vp}_{yy}}\right) N_{22} \tag{3.20}$$

$$N_{23} = \left(\frac{\dot{E}^{vp}_{zz}}{\dot{E}^{vp}_{yy}}\right) N_{22} \tag{3.21}$$

- Uniaxial tension along the z-direction:

$$N_{33} = 2\left(\frac{1}{\Sigma_{zz}}\right)^2 \left(\frac{\Sigma_{zz}\dot{E}^{vp}_{zz}}{A}\right)^{\frac{2}{n+1}} \tag{3.22}$$

$$N_{13} = \left(\frac{\dot{E}^{vp}_{xx}}{\dot{E}^{vp}_{zz}}\right) N_{33} \tag{3.23}$$

$$N_{23} = \left(\frac{\dot{E}^{vp}_{yy}}{\dot{E}^{vp}_{zz}}\right) N_{33} \tag{3.24}$$

Under shear loading and periodic boundary conditions, the normal components of $\overline{\overline{\Sigma}}$ vanish and the shear components of $\overline{\overline{\overline{N}}}$ are written as follows:

- Simple shear in the xy-plane:

$$N_{44} = 2\left(\frac{1}{\Sigma_{xy}}\right)^2 \left(\frac{\Sigma_{xy}\dot{E}^{vp}_{xy}}{A}\right)^{\frac{2}{n+1}} \tag{3.25}$$

- Simple shear in the xz-plane:

$$N_{55} = 2\left(\frac{1}{\Sigma_{xz}}\right)^2 \left(\frac{\Sigma_{xz}\dot{E}^{vp}_{xz}}{A}\right)^{\frac{2}{n+1}} \tag{3.26}$$

- Simple shear in the yz-plane:

$$N_{66} = 2\left(\frac{1}{\Sigma_{yz}}\right)^2 \left(\frac{\Sigma_{yz}\dot{E}^{vp}_{yz}}{A}\right)^{\frac{2}{n+1}} \tag{3.27}$$

In the previous equations, the values of macroscopic normal and shear stresses are equal to the applied average stresses. The macroscopic viscoplastic strain rates are determined from the time derivative of the macroscopic viscoplastic strain ($\overline{\overline{E^{\mathrm{vp}}}}$ calculated from the displacement of the corners of the UC as described before). The obtained values of the nine none-zero components of $\overline{\overline{\overline{N}}}$ are reported in table 3.2. It can be observed that y and z components of the tensor are almost the same (due to the absence of joints in the z direction, only one brick in the depth of the wall, and the absence of open joints in the y direction). To compare the components of tensor $\overline{\overline{\overline{N}}}$ of joint pattern HO and those of the constitutive material, the components of tensor $\overline{\overline{\overline{N}}}$ have been identified for joint pattern AC, using the same approach, and reported in table 3.2. It can be seen that, in the case of pattern HO, the y and z components of tensor $\overline{\overline{\overline{N}}}$ are almost equal to those of the constitutive material of the bricks.

3.2.1.3 Pattern AO

As presented earlier, in the case of pattern AO, both head and bed joints are open. It can be seen from Fig. 3.1 that the masonry structure is composed of an array of separated bricks and is disconnected. This pattern usually presents the initial state of the masonry (before loading). When the bricks are machined (i.e. the dimension tolerances of the bricks are negligible) or cardboard spacers are used to generate the joints), one can assume that joints are perfect and they can be considered as either open or closed (the gradual increase of stiffness with the gradual closure of joints can be neglected). This assumption has been used in previous works [76, 138, 141].

To compute the effective mechanical parameters of masonry with perfect joints (elastic and viscoplastic), the finite element-based homogenization approach (micro modeling) presented earlier can not be employed, because the boundary value problem of the UC is not clearly defined. However, the mechanical parameters of the constitutive material of the bricks can be used to define the effective mechanical properties of joint pattern AO [76, 138, 141] as

following. Due to the existence of open joints in the x and y directions, the effective elastic and viscoplastic mechanical parameters of the masonry structure in the x and y directions are very small. Therefore, the effective Young's modulus and the components of $\overline{\overline{\overline{\overline{N}}}}$ in directions x and y can be assumed equal to zero ($\widetilde{E}_{\mathrm{x}} = \widetilde{E}_{\mathrm{y}} = \widetilde{G}_{\mathrm{xy}} = \widetilde{\nu}_{\mathrm{xy}} = 0$, see the coordinate system in Fig. 3.5). On the other hand, the effective Young's modulus and $\overline{\overline{\overline{\overline{N}}}}$ components in z direction are equal to those of the constitutive material of the bricks due to the absence of joints in the z direction (only one brick in the z direction, depth of the wall).

In the case of perfect joints, $\overline{\overline{\overline{\overline{C^e}}}}$ and $\overline{\overline{\overline{\overline{N}}}}$ tensors of joint pattern AO are reported in table 3.2. To facilitate the numerical computations and to avoid numerical singularities and solution divergence, a very small value has been assigned to $\widetilde{E}_{\mathrm{x}},\ \widetilde{E}_{\mathrm{y}}$, and $\widetilde{G}_{\mathrm{xy}}$ instead of zero.

It should be noted that in the case of imperfect joints (natural bricks and dimensions and shape tolerances of the bricks are significant) the effects of progressive closure of joints and the gradual increase of the contact area (and, therefore, effective stiffness) with joints closure are significant. The nonlinear strain stiffening behavior of the masonry with dry joints presented in chapter 2 is resulting from the gradual increase of the contact area between the bricks. To take into account the gradual increase of stiffness with the closure of head and bed joints and cover the real physical behavior of masonry built up with natural bricks, the average (or global) normal and shear behaviors of joints should be considered. The average behavior is chosen in the present work due to the heterogeneity in the local behavior of joints and the different joint thickness in the wall (will be discussed in detail in chapter 4). Two approaches can be employed to take into account the normal and shear behaviors of the joints namely: soft contact approach and cohesive interface approach.

Regarding the first approach (soft contact approach), it is based on modeling the contact between the bricks using FE method. Different constitutive contact laws can be implemented in the contact surfaces of bed and head joints. The tangential contact behavior of the joints is defined by penalty friction formulation with a coefficient of friction (μ). The normal contact behavior is usually modeled using the softened contact model (pressure – over closure) [85, 135, 151]. A slight overlap (penetration) of the contact partners is allowed. This violation of contact conditions can be physically accepted in the case of masonry by considering the deformation and the crushing of the asperities as penetration. The main limitations of this approach are: firstly, it usually requires the contact pressure (at the surfaces of the joints) that is usually unknown and can be determined experimentally using pressure based sensors as presented in chapter 1; secondly, the high computational time and related contact convergence problems.

In the second approach (cohesive interface), which was used in the present work, the joints are reduced to an interface with small thickness (t_i) where the constitutive normal and shear behaviors of the joints are implemented. Different material behavior laws can be employed for the bricks. The behavior law of the interface is expressed in an incremental form as [85]:

$$\Delta\sigma = k(u)\ \Delta u \tag{3.28}$$

or

$$\Delta \begin{Bmatrix} \sigma_n \\ \tau_x \\ \tau_y \end{Bmatrix} = \begin{bmatrix} k_n(u) & 0 & 0 \\ 0 & k_{sx}(u) & 0 \\ 0 & 0 & k_{sy}(u) \end{bmatrix} \Delta \begin{Bmatrix} u_n \\ u_x \\ u_y \end{Bmatrix} \tag{3.29}$$

Where σ_n is the normal stress, τ_x and τ_y are the transverse stress in the x and y directions, respectively (see the coordinate system in Fig. 3.9). k_n, k_{sx} and k_{sy} are the joint stiffnesses in the normal (n) and shear directions (x, y), respectively. u_n is the normal deformation of the joint or joint closure. u_x and u_y are the shear deformations of the joint.

The variations of k_n with the joints closure can be obtained from joints closure tests as reported in references [68, 77, 84], while k_{sx} and k_{sy} are expressed as [61]:

$$k_{sx}(u) = k_{sy}(u) = \frac{k_n(u_n)}{2(1+\nu)} \tag{3.30}$$

Four types of joints with different normal and shear stiffnesses are proposed in this chapter for the demonstration of the methodology and performing some parametric studies. The identification of $k_n(u_n)$ of the masonry walls, presented in chapter 2, will be shown later in chapter 4. However, the joints' behaviors considered here are similar to those observed in experimental works [68, 77, 84] and those reported later in chapter 4. The variations of k_n and k_s ($k_s = k_{sx} = k_{sy}$) with the joints closure u_n of the considered four joints are presented in Fig. 3.8. In the beginning, the stiffness of the joints is very small then, it increases sharply with the closure of joints.

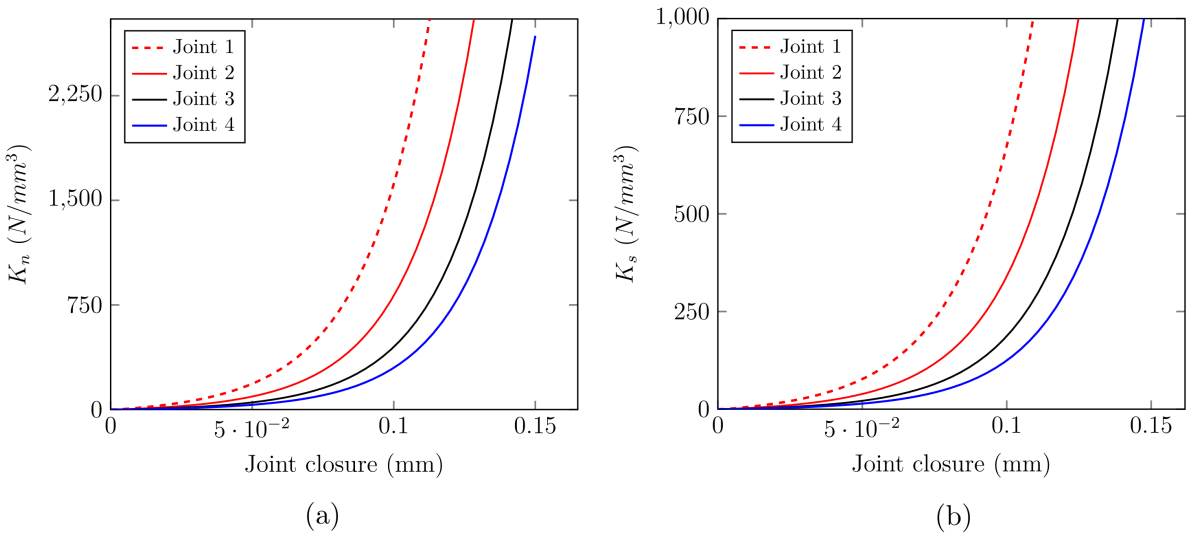

Figure 3.8: Variations of the (a) normal and (b) shear stiffnesses of dry joints with joints closure.

In the proposed 3D FE model, a periodic unit cell (UC) with volume (V_{UC}) has been selected from the periodic structure (see Fig. 3.9). Then, 3D – FE simulations have been performed on the UC to characterize its homogenized response. To account for the periodicity of the structure, periodic boundary conditions have been applied to the UC's boundaries [23, 55, 56]. The bricks

and joints are represented by two types of elements. The FE model was developed using Abaqus using C3D8R solid elements for modeling the bricks and COH3D8 cohesive elements for modeling the interface. The reduced integration was used because it allows obtaining one value per element. The variations of k_n and k_s with the joints closure (presented in Fig. 3.8) were implemented into Abaqus using user subroutine (USDFLD). Several FE numerical experiments of uniaxial compressive tests along the x, y and z directions and simple shear tests in the xy, xz, and yz planes have been performed. For all cases, the UC has been subjected to an average or macroscopic strain (E, shear or normal) and the resulting macroscopic stresses are obtained from solving the boundary value problem.

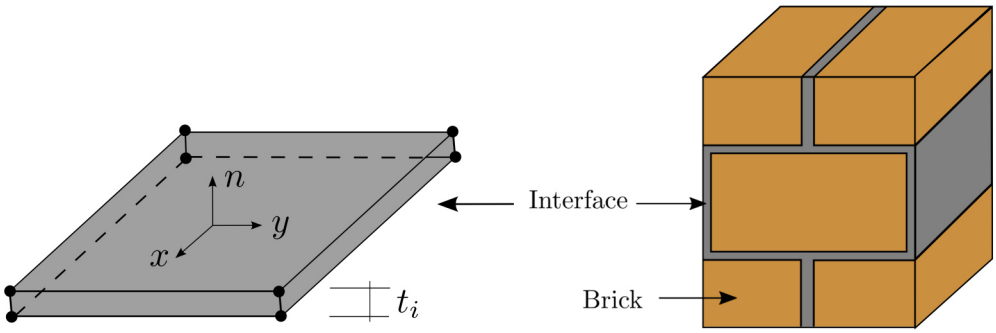

Figure 3.9: Schematic of RVE in pattern AO showing the physical model, brick and interface

The resulting macroscopic stress – strain diagrams in a UC subjected to uniaxial compression in the x (normal to head joints) and y (normal to bed joints) directions as well as simple shear with respect to xy planes are shown in Figs. 3.10-a, 3.11-a and 3.12-a. The macroscopic normal stress – strain ($\Sigma - E$) diagrams in the z direction (depth of the wall) and shear stress – strain diagrams with respect to xz and yz planes are similar to those of the base material of the bricks (indicated as isotropic in the figures). For the four considered joint behaviors, the Young's modulus of the brick was constant and equal to 11 GPa. The variations of the tangent homogenized Young's modulus, determined from $\Sigma - E$ diagrams) in the x ($\widetilde{E}_{xx}$) and y ($\widetilde{E}_{yy}$) directions and shear modulus with respect to xy planes ($\widetilde{G}_{xy}$) are given in Figs. 3.10-b, 3.11-b and 3.12-b. It can be seen from the figures that the numerical models are able to reproduce the nonlinear strain stiffening behavior. In addition, the homogenized Young's (in x, y directions) and shear modulus (with respect to xy plane) and the corresponding resulting normal and shear macroscopic stresses increase with the increase of the joint stiffness. In all cases the resulting normal and shear stresses in x, y directions and with respect to xy plane are less as compared to those in the z direction and with respect to xz and yz planes (indicated as isotropic in the figure). The variations of homogenized Young's and shear modulus with the macroscopic strains can be implemented in the macroscopic FE model to take into account the nonlinear strain stiffening behavior of masonry with dry joints. Since the thickness of the interface is very small as compared to the dimensions of the bricks, the homogenized viscoplastic behavior of pattern AO is considered similar to that of the base material of the bricks.

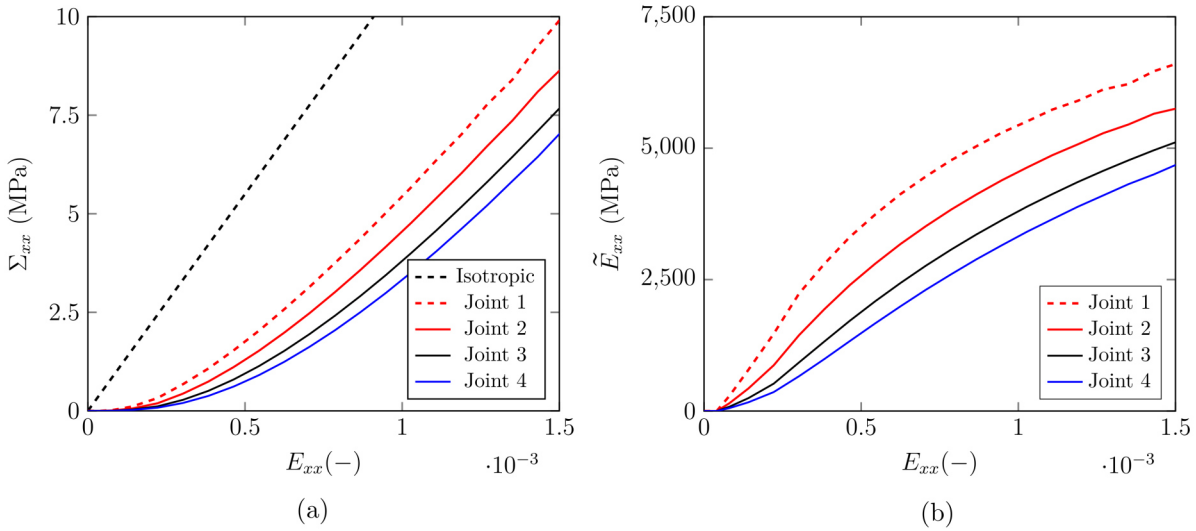

Figure 3.10: (a) Resulting macroscopic normal stress – strain diagrams and (b) variations of homogenized Young's modulus, in the direction normal to head joints, of a UC with different joint behaviors subjected to uniaxial compression.

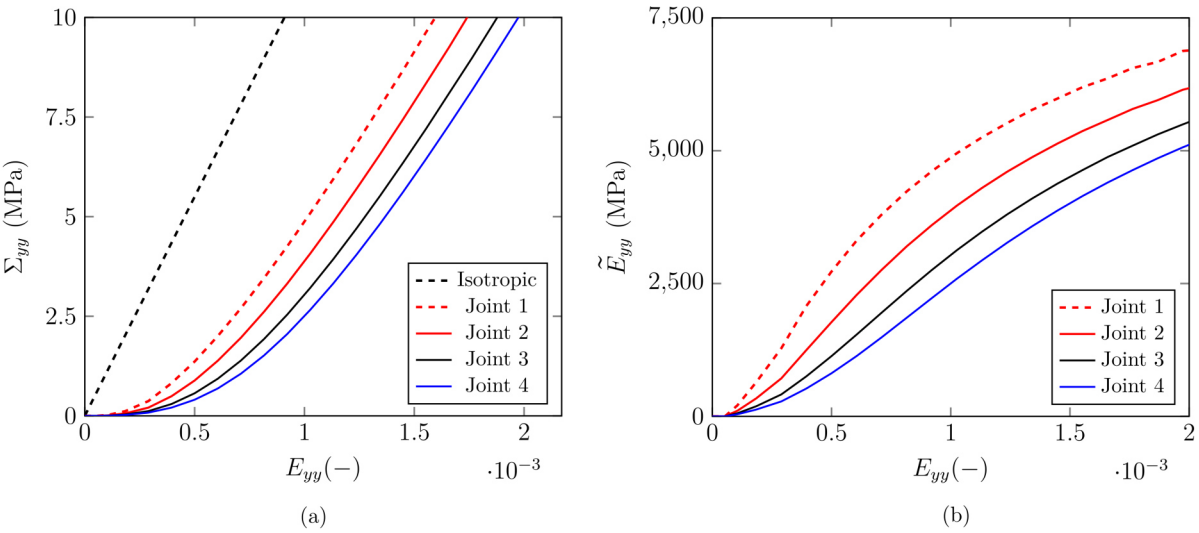

Figure 3.11: (a) Resulting macroscopic normal stress – strain diagrams and (b) variations of homogenized Young's modulus, in the direction normal to bed joints, of a UC with different joint behaviors subjected to uniaxial compression.

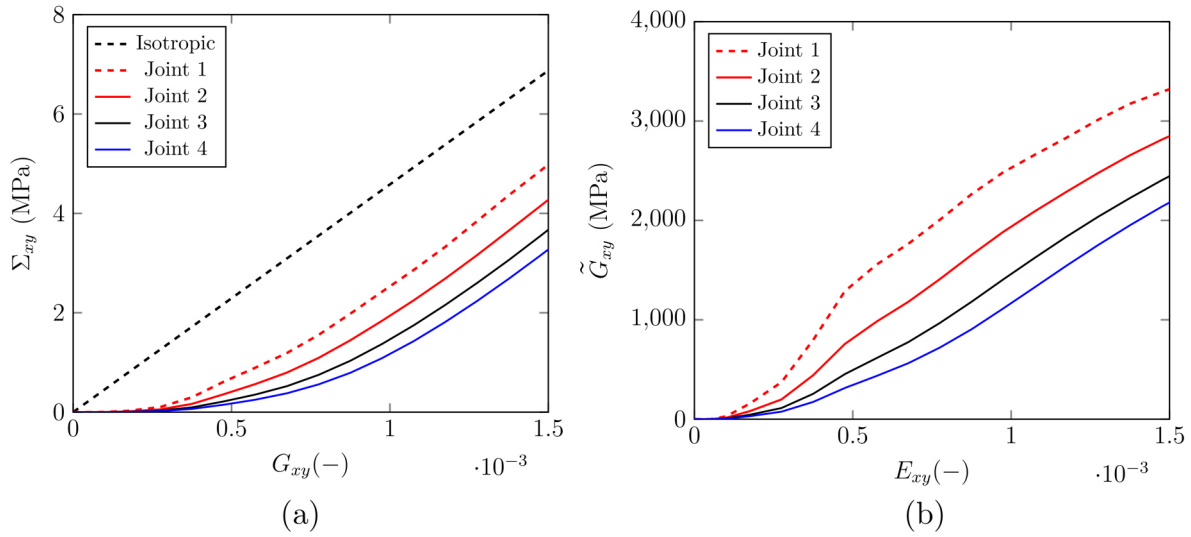

Figure 3.12: (a) Resulting macroscopic shear stress – strain diagrams and (b) variations of homogenized shear modulus, with respect to xy plane, of a UC with different joint behaviors subjected to shear load.

3.2.1.4 Pattern BO

In the case of joint pattern BO, head joints are closed whereas bed joints are open (see Fig. 3.1). The masonry structure is composed of an array of separated courses of bricks (in the y-direction). Under perfect joint assumption, the structure has zero macroscopic stiffness in the y-direction (due to the presence of open joints) while it has stiffness in the x (as all joints are closed in this direction) and z-directions (only one brick in the z direction) [76, 138, 141]. The mechanical parameters of the constitutive material can be used to define the effective mechanical properties of joint pattern BO. Since bed joints are open, the macroscopic stiffness of the structure in direction y is very small and $\widetilde{E}_{\mathrm{y}}$ is zero. Thus, the components of $\overline{\overline{\overline{\overline{N}}}}$ in the y direction are also equal to zero. However, the effective Young's modulus and $\overline{\overline{\overline{\overline{N}}}}$ components in x and z directions are equal to those of the constitutive material due to the absence of joints in the z direction and the absence of open joints in x direction. The $\overline{\overline{\overline{\overline{C^e}}}}$ and $\overline{\overline{\overline{\overline{N}}}}$ tensors of joint pattern BO are reported in table 3.2.

To take into account the impacts of gradual closure of bed joints on the macroscopic mechanical behavior (imperfect joints), the bed joints can be reduced to an interface with small thickness where the constitutive normal and shear behaviors of the bed joints can be implemented. Then homogenized Young's modulus, in the y direction, and shear modulus, with respect to xy plane, can be described as a function of the macroscopic strain (as resented in section 3.2.1.3). $\widetilde{E}_{\mathrm{x}} = \widetilde{E}_{\mathrm{z}} = Y_{brick}$ and $\widetilde{G}_{\mathrm{xz}} = \widetilde{G}_{\mathrm{yz}} = G_{brick}$. Since the thickness of the interface (assumed for bed joints) is very small as compared to the dimensions of the bricks and due to the absence of joints in the depth of the wall (z direction) and absence of open joints in the x direction, the homogenized viscoplastic behavior of pattern BO is considered similar to that of the base material of the bricks.

Table 3.2: Effective elastic and viscoplastic 4$^{\text{th}}$ order tensors of the four joint patterns of masonry with dry joints (perfect joints).

Pattern	$\overline{\overline{\overline{\overline{C^e}}}}$ (MPa)						$\overline{\overline{\overline{\overline{N}}}}$ (-)					
AC	12222	3055	3055	0	0	0	2.01	−0.99	−0.99	0	0	0
		12222	3055	0	0	0		2.01	−0.99	0	0	0
			12222	0	0	0			2.01	0	0	0
				4583	0	0				6.01	0	0
		sym.			4583	0		*sym.*			6.01	0
						4583						6.01
HO	4430	1113	1103	0	0	0	6.25	−1.10	−0.49	0	0	0
		11738	2560	0	0	0		2.01	−0.99	0	0	0
			11733	0	0	0			1.99	0	0	0
				3602	0	0				8.25	0	0
		sym.			4583	0		*sym.*			6.01	0
						4583						6.01
AO	1	0	0	0	0	0	0	0	0	0	0	0
		1	0	0	0	0		0	0	0	0	0
			12222	0	0	0			2.01	0	0	0
				1	0	0				0	0	0
		sym.			4583	0		*sym.*			6.01	0
						4583						6.01
BO	12222	0	3055	0	0	0	2.01	0	−0.99	0	0	0
		1	0	0	0	0		0	0	0	0	0
			12222	0	0	0			2.01	0	0	0
				1	0	0				0	0	0
		sym.			4583	0		*sym.*			6.01	0
						4583						6.01

3.2.2 Nonlinear homogenization of masonry with mortar joints

3.2.2.1 Pattern AS

As indicated previously in the case of joint pattern AS (All Safe), head and bed joints are undamaged (see Fig. 3.13). This pattern presents the initial state of masonry before loading. To compute the homogenized elastic viscoplastic behavior of pattern AS, a UC is selected from the structure then, the homogenized elastic viscoplastic mechanical parameters are determined using FE based nonlinear homogenization approach detailed in section 3.2.1.2. The $\overline{\overline{\overline{\overline{C^e}}}}$ and $\overline{\overline{\overline{\overline{N}}}}$ tensors of joint pattern AS are reported in table 3.3.

3.2.2.2 Pattern HD

In the case of pattern HD (Head Damaged), head joints are damaged and bed joints are undamaged (see Fig. 3.14). The existence of open joints in the masonry with mortar joints results in a reduction in their effective stiffness. Thus, the macroscopic elastic-viscoplastic behavior of pattern HD is different from that of the base materials of the bricks and the mortar. For the purpose of studying the homogenized mechanical behavior of pattern HD, and computing the

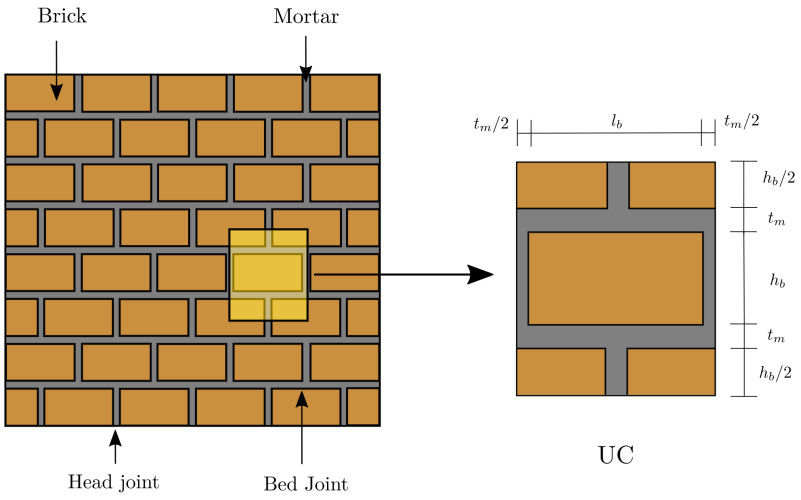

Figure 3.13: Schematic of periodic masonry structure with mortar joints in pattern AS and periodic unit cell selected from the structure and used for the nonlinear finite element based homogenization analysis.

effective elastic viscoplastic parameters, the finite element FE – based homogenization technique described in section 3.2.1.2 has been adopted. The $\overline{\overline{\overline{\overline{C^e}}}}$ and $\overline{\overline{\overline{\overline{N}}}}$ tensors of joint pattern HD are reported in table 3.3.

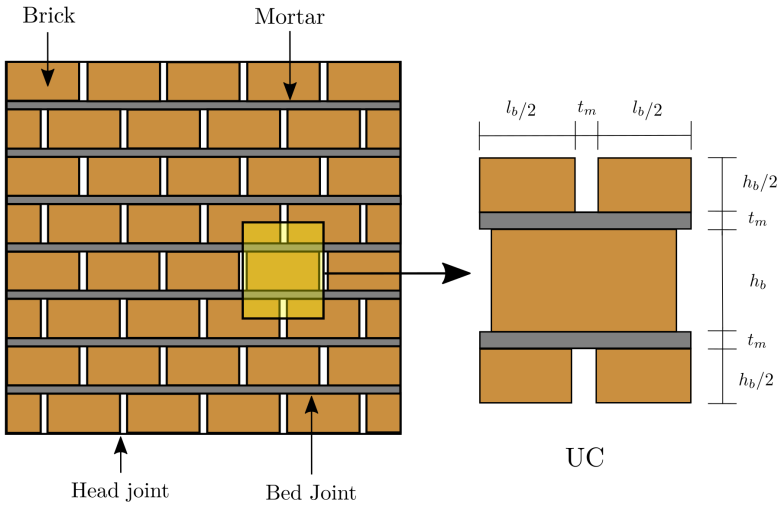

Figure 3.14: Schematic of periodic masonry structure with mortar joints in pattern HD and periodic unit cell selected from the structure and used for the nonlinear finite element based homogenization analysis.

3.2.2.3 Pattern BD

In the case of joint pattern BD (Bed Damaged), head joints are undamaged whereas bed joints are damaged, see Fig. 3.3. The masonry structure is composed of an array of separated courses of bricks (in the y-direction). Thus, the structure has zero macroscopic stiffness in y-direction (due to the presence of open joints) while it has stiffness in x (as all joints are closed in this direction)

and z-directions (only one brick in the z direction). The mechanical parameters of pattern AS can be used to define the effective mechanical properties of joint pattern BD. Since bed joints are open or damaged, the macroscopic stiffness of the structure in direction y is very small and $\widetilde{E}_y$ is zero. Thus, the components of $\overline{\overline{\overline{\overline{N}}}}$ in the y direction are also equal to zero. However, the effective Young's modulus and $\overline{\overline{\overline{\overline{N}}}}$ components in x and z directions are equal to those of the constitutive material due to the absence of joints in the z direction and open joints in x direction. The $\overline{\overline{\overline{\overline{C^e}}}}$ and $\overline{\overline{\overline{\overline{N}}}}$ tensors of joint pattern BD are reported in table 3.3.

3.2.2.4 Pattern AD

As presented earlier, in the case of pattern AD (All Damaged), both head and bed joints are damaged (open). It can be seen from Fig. 3.3 that the masonry structure is composed of an array of separated bricks and the masonry structure is disconnected. For the purpose of computing the effective mechanical parameters of the structure (elastic and viscoplastic), one cannot use finite element-based homogenization approach (micro modeling) presented earlier because the boundary value problem of the UC is not clearly defined. However, the effective mechanical parameters of the undamaged pattern (AS) can be used to define the effective mechanical properties of joint pattern AD. Due to the existence of open joints in the x and y directions, the effective elastic and viscoplastic mechanical parameters of the masonry structure in the x and y directions are very small. Therefore, the effective Young's modulus and the components of $\overline{\overline{\overline{\overline{N}}}}$ in directions x and y are zero ($\widetilde{E}_x = \widetilde{E}_y = \widetilde{G}_{xy} = \widetilde{\nu}_{xy} = 0$). In addition, the effective Young's modulus and $\overline{\overline{\overline{\overline{N}}}}$ components in z direction are equal to those of pattern AS. The $\overline{\overline{\overline{\overline{C^e}}}}$ and $\overline{\overline{\overline{\overline{N}}}}$ tensors of joint pattern AD are reported in table 3.3. To facilitate the numerical computations and to avoid numerical singularities and solution divergence, a very small value has been assigned to $\widetilde{E}_x,\ \widetilde{E}_y$ and $\widetilde{G}_{xy}$ instead of zero.

Table 3.3: Effective elastic and viscoplastic 4^{th} order tensors of the four joint patterns of masonry with mortar joints.

Pattern	$\overline{\overline{\overline{\overline{C^e}}}}$ (GPa)						$\overline{\overline{\overline{\overline{N}}}}$ (-)					
AS	10.9	2.4	2.7	0	0	0	1.91	−0.95	−0.95	0	0	0
		10.3	2.8	0	0	0		2.01	−1.0	0	0	0
			11.6	0	0	0			2.04	0	0	0
				3.7	0	0				6	0	0
		sym.			4.2	0		sym.			6.04	0
						4.2						6.04
BD	10.9	0	2.7	0	0	0	1.91	0	−0.95	0	0	0
		0.001	0	0	0	0		0	0	0	0	0
			11.6	0	0	0			2.04	0	0	0
				0.001	0	0				0	0	0
		sym.			4.2	0		sym.			6.04	0
						4.2						6.04
HD	4.26	1	1	0	0	0	4.59	−1.10	−0.77	0	0	0
		10.0	2.2	0	0	0		2.04	−1.02	0	0	0
			11.6	0	0	0			2.06	0	0	0
				2.7	0	0				7.4	0	0
		sym.			4.2	0		sym.			6.04	0
						4.2						6.04
AD	0.001	0	0	0	0	0	0	0	0	0	0	0
		0.001	0	0	0	0		0	0	0	0	0
			11.6	0	0	0			2.04	0	0	0
				0.001	0	0				0	0	0
		sym.			4.2	0		sym.			6.04	0
						4.2						6.04

3.3 Joints closure and/or opening criteria

3.3.1 Closure and reopening criteria of dry joints

As discussed above, each joint pattern has different homogeneous elastic viscoplastic response. In normal operating conditions, the masonry is subjected to cyclic thermal or mechanical loading and unloading. Thus, head or bed or both joints may close and reopen. Consequently, the masonry structure changes from one joint pattern to another leading to a change in the macroscopic elastic viscoplastic behaviour of the structure. In the present work, this change has been taken into account by using suitable joints closure, reopening and pattern transition criteria.

Before loading, head and bed joints are open and the masonry structure can be fully described by pattern AO. Under compression loads, the thickness of head or bed or both joints decreases gradually from the initial value (g_0) to zero and the structure changes from pattern AO to either pattern BO (when head joints close) or pattern HO (when bed joints close). In addition, the structure may change from pattern AO to pattern AC if both head and bed joints close. Based on the instantaneous thickness of the joints g, head and bed joints are considered to be open as:

$$Joint\ open \qquad if \qquad g_{\text{bed or head}} > 0 \tag{3.31}$$

As the equivalent material properties of the masonry are piece wise constant, the displacement increment at every point in the structure linearly depends on the increment in the macroscopic quantities [76, 138]. Thus, the instantaneous thickness of the head and bed joints can be written in terms of the macroscopic components of total strains in the x ($E^{\mathrm{t}}_{\mathrm{xx}}$) and y ($E^{\mathrm{t}}_{\mathrm{yy}}$) directions as:

$$g_{\mathrm{head}} = g_{0,\ \mathrm{head}} + M_{\mathrm{x}} E^{\mathrm{t}}_{\mathrm{xx}} \tag{3.32}$$

$$g_{\mathrm{bed}} = g_{0,\ \mathrm{bed}} + M_{\mathrm{y}} E^{\mathrm{t}}_{\mathrm{yy}} \tag{3.33}$$

Where g_{bed} and g_{head} are the instantaneous thicknesses of bed and head joints, respectively. $g_{0,\mathrm{bed}}$ and $g_{0,\mathrm{head}}$ denote the initial thickness of bed and head joints, respectively. M_{y} and M_{x} are parameters with the same meaning of the localization tensor, and they depend on the dimensions of the brick ($M_{\mathrm{y}} = h_{\mathrm{b}}$ and $M_{\mathrm{x}} = l_{\mathrm{b}}$). $E^{\mathrm{t}}_{\mathrm{yy}}$ and $E^{\mathrm{t}}_{\mathrm{xx}}$ are the macroscopic total strains (elastic and viscoplastic strains) in the y and x directions. The bed and head joints closure criteria are given in Fig. 3.15.

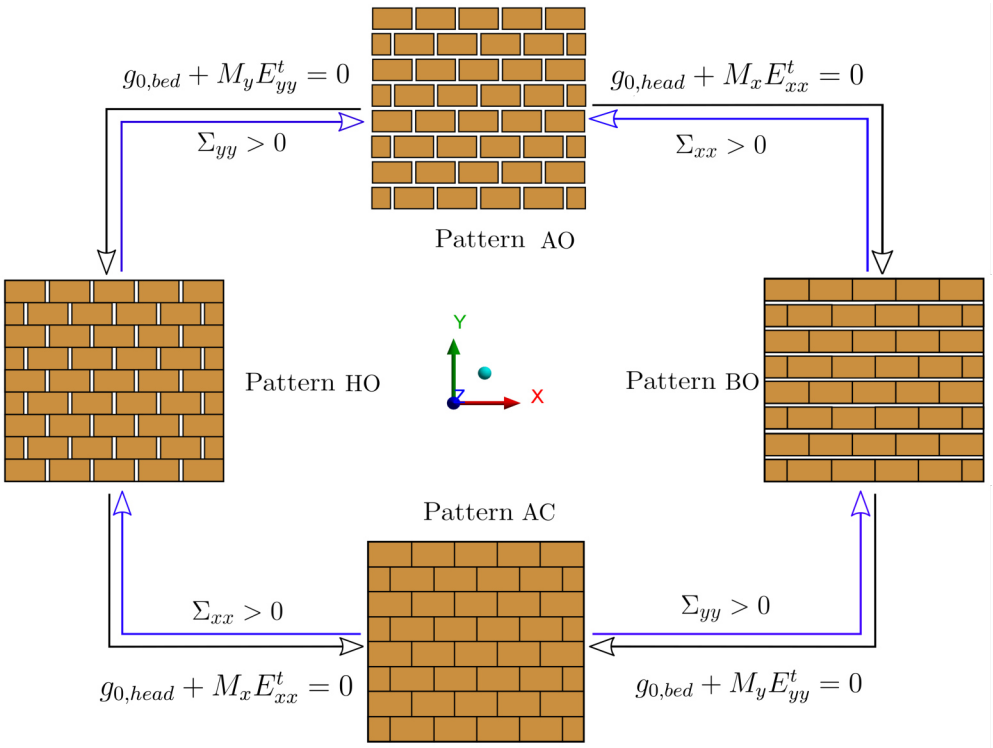

Figure 3.15: Schematics of all possible joint patterns of refractory masonry with dry joints and joints closure and reopening criteria.

With regard to joints reopening criterion, head and bed joints can reopen if the normal stress to the surface of the joint (head or bed) is higher than zero (i.e. tensile stress). In other words, a head joint can reopen if $\sigma_{\mathrm{xx}} > 0$ and a bed joint can reopen if $\sigma_{\mathrm{yy}} > 0$. Joints reopening criterion can be rewritten in terms of macroscopic stresses using localization tensor $\Sigma_{\mathrm{yy}} \longrightarrow \sigma_{\mathrm{yy}}$ and $\Sigma_{\mathrm{xx}} \longrightarrow \sigma_{\mathrm{xx}}$. The approach used to link between the microscopic and macroscopic stress fields is similar to that described in section 3.3.2. The joints closure, reopening and transition criteria

from joint pattern AO to pattern BO, joint pattern BO to pattern HO, joint pattern BO to pattern AC, joint pattern HO to pattern AC, and the opposite are presented in Fig. 3.15.

3.3.2 Opening criteria of mortar joints

The brick-mortar interface is considered as the weakest link in the structure and it can fail under tensile or shear loads. Previous experimental studies have shown that, usually, cracks initiation and propagation occur in the mortar joints [11, 152–154]. Therefore, most of previous numerical studies assumed rigid or purely elastic bricks and all material non-linearity is concentrated in the joints [101, 103, 118, 119, 155–157]. In previous numerical studies [101, 103, 155, 156], three failure mechanisms of masonry are adopted namely: tensile failure of brick/mortar interface, shear failure of brick/mortar interface and compressive failure of the mortar (cap). Experimental studies carried out by Aref and Dolatshahi [109] show that compressive failure of the mortar rarely happens even when the mortar material is very weak. Therefore, tensile and shear failure modes of the brick mortar interface are sufficient to describe the structural behavior of the refractory masonry.

In normal operating conditions, the masonry structure is subjected to cyclic thermal or mechanical loading and unloading. Thus, head or bed or both joints may be damaged. Consequently, the masonry structure changes from one joint pattern to another leading to a change in the macroscopic elastic viscoplastic behavior of the structure. Before loading, head and bed joints are undamaged and the masonry structure can be fully described by pattern AS. Under tensile or shear loads, head or bed or both joints may open and the structure changes from pattern AS to either pattern HD (when head joints are damaged) or BD (when bed joints are damaged). The structure may change from pattern AS to pattern AD if both head and bed joints are damaged. Since crushing of mortar is rarely to happen [109], the yield criterion of the joints can be defined by modified Mohr-Coulomb for shear associated with tension cut off as depicted in Fig. 3.16. The local tensile criterion can be written as:

$$\sigma_{ii} > f_t \tag{3.34}$$

where, σ_{ii} and f_t are respectively the local normal stress at the brick mortar interface and ultimate tensile strength of the brick/mortar interface. i is the direction normal to the interface surface. The local shear criterion reads [120, 121]:

$$\sqrt{\sigma_{ji}^2 + \sigma_{ki}^2} > f_{sh} \tag{3.35}$$

The modified Mohr-Coulomb can be adopted to take into account the hardening of the shear limit in compression as:

$$f_{sh} = C - \frac{1}{2} tan\phi \left(1 - sign(\sigma_{ii})\right) \sigma_{ii} \tag{3.36}$$

with

$$\begin{cases} sign(\sigma_{ii}) = -1 & if \quad \sigma_{ii} < 0 \\ sign(\sigma_{ii}) = \quad 1 & if \quad \sigma_{ii} > 0 \end{cases} \tag{3.37}$$

Here, f_{sh}, C and ϕ are the shear strength of the brick mortar interface, cohesion and internal friction angle, respectively. The joints reopening and transition criteria from joint pattern AS to BD, pattern AS to HD, pattern BD to AD and pattern HD to AD, are written in terms of local shear and normal stresses and presented in Fig. 3.17.

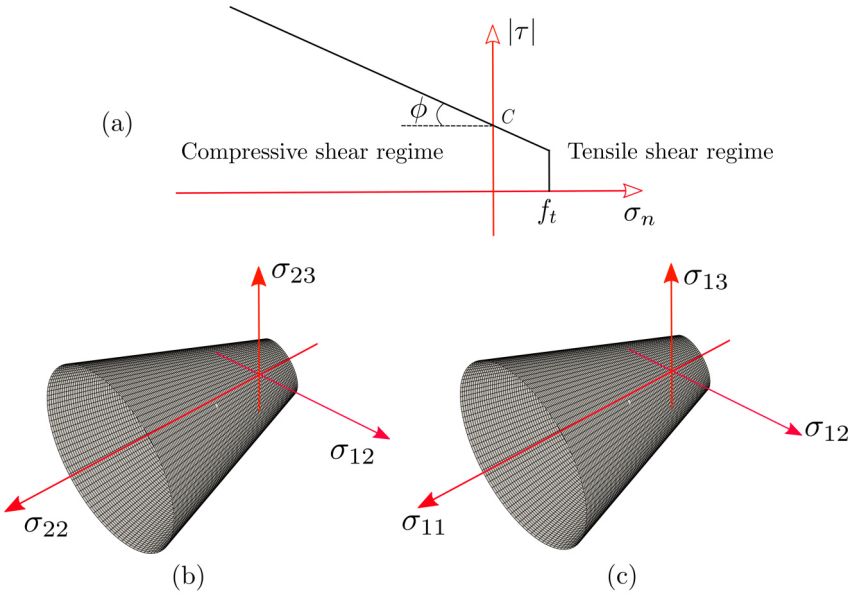

Figure 3.16: Yield surface for the mortar joints: (a) 2D space representation of the yield surface, (b) yield surface for bed joints in 3D space and (c) yield surface for head joints in 3D space.

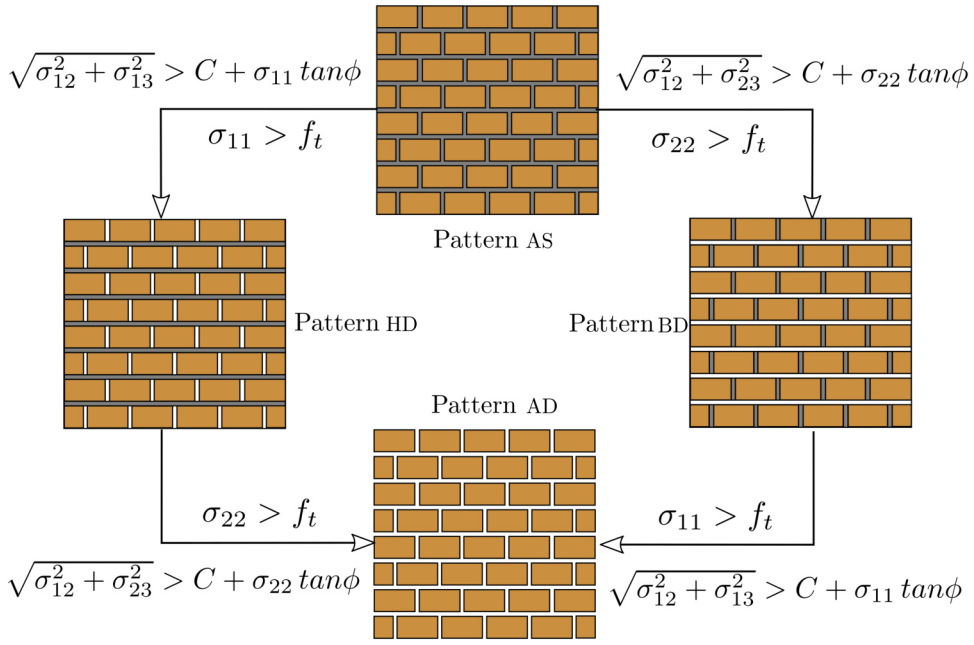

Figure 3.17: Schematics of all possible joint patterns of masonry structure with mortar joints and joints opening criteria.

It should be noted that equation 3.34 and 3.35 are written in terms of local tensile and shear stresses. As the four joint patterns are replaced by a homogeneous continuum medium with an

equivalent macroscopic mechanical behavior, only macroscopic values of stresses and strains are obtained from the FEM solution (at macroscopic level). Therefore, local joints opening criteria should be written in terms of macroscopic stresses and strains. For this purpose, an approach similar to that of Nguyen et al. [76] can be adopted. The increment of the second order micro (or local) stress tensor ($d\overline{\overline{\sigma}}$) can be written in terms of the increment of the mean (or macroscopic) stress tensor ($d\overline{\overline{\Sigma}}$) by using a fourth order stress concentration tensor ($\overline{\overline{\overline{\overline{A}}}}$) as follows:

$$d\overline{\overline{\sigma}} = \overline{\overline{\overline{\overline{A}}}} : d\overline{\overline{\Sigma}} \tag{3.38}$$

Using the macroscopic form of Hooke's law for orthotropic materials, $d\overline{\overline{\Sigma}}$ can be written in terms of the increment of macroscopic elastic strain tensor ($d\overline{\overline{E}}^{\,e}$) and the macroscopic stiffness tensor ($\overline{\overline{\overline{\overline{C^e}}}}$) as:

$$d\overline{\overline{\Sigma}} = \overline{\overline{\overline{\overline{C^e}}}} : d\overline{\overline{E}}^{\,e} \tag{3.39}$$

Substituting equation 3.39 into equation 3.38 gives:

$$d\overline{\overline{\sigma}} = \overline{\overline{\overline{\overline{A}}}} : \overline{\overline{\overline{\overline{C^e}}}} : d\overline{\overline{E}}^{\,e} = \overline{\overline{\overline{\overline{L}}}} : d\overline{\overline{E}}^{\,e} \tag{3.40}$$

It should be mentioned that equations 3.38, 3.39 and 3.40 are written in an incremental form as the mechanical response of the material changes with the change of joint pattern. When the structure changes from an initial pattern to a new pattern (due to joints opening), the local stress tensor can be obtained by integrating equation 3.40 from the initial state to the final state as [76]:

$$\overline{\overline{\sigma}} = \int_{\overline{\overline{E}}^{e}_{ini}}^{\overline{\overline{E}}^{e}_{fin}} \overline{\overline{\overline{\overline{L}}}} : d\overline{\overline{E}}^{\,e} \tag{3.41}$$

As the equivalent material properties of the masonry are piece wise constant (for each joint pattern), equation 3.41 can be written as:

$$\overline{\overline{\sigma}} = \sum_{p=1}^{z} \overline{\overline{\overline{\overline{L}}}}^{\,(p)} : \triangle \overline{\overline{E}}^{\,(p)} + \overline{\overline{\sigma}}_0 \tag{3.42}$$

With $\overline{\overline{\sigma}}_0$, p and z are the initial local stress tensor, pattern and number of pattern changes respectively. $\triangle \overline{\overline{E}}^{\,(p)}$ is the change in the elastic strain tensor during pattern number p. Now, local joints opening criteria (equations 3.34 and 3.35) can be expressed in macroscopic forms as following (for a joint perpendicular to the i direction):
Tensile failure:

$$\sum_{p=1}^{z} L^{(p)}_{iilm} \ \triangle E^{(p)}_{lm} > f_t \tag{3.43}$$

Shear failure:

$$\sqrt{\left(\sum_{p=1}^{z} L^{(p)}_{jilm} \ \triangle E^{p}_{lm}\right)^2 + \left(\sum_{p=1}^{z} L^{(p)}_{kilm} \ \triangle E^{(z)}_{lm}\right)^2} > f_{sh} \tag{3.44}$$

For the four joint patterns, $L^{(p)}_{kilm}$ should be determined.

For joint pattern AS, bed and head joints are undamaged. Therefore, The average normal stresses at the brick mortar interface are similar to the macroscopic or average normal stresses. The joints opening criteria can be written as:

$$\begin{cases} \Sigma_{ii} > f_t \\ \text{or} \\ \sqrt{\Sigma^2_{ji} + \Sigma^2_{ki}} > f_{sh} \end{cases} \tag{3.45}$$

Using the macroscopic form of Hooke's law, $\overline{\overline{\Sigma}} = \overline{\overline{\overline{\overline{C^e}}}} : \overline{\overline{E}}$ [e], the joints opening criteria can be written in terms of macroscopic strains. For example, the tensile failure criterion is expressed as:

$$\Sigma_{ii} = \sum_{j=1}^{3} C_{iijj} E^e_{jj} > f_t \tag{3.46}$$

With,

$$\begin{cases} L^{(AS)}_{iijj} = C_{iijj} \\ L^{(AS)}_{ijij} = C_{ijij} \quad j \neq i \end{cases} \tag{3.47}$$

Regarding joint pattern HD, $L^{(HD)}_{kilm}$ are determined from the FE solution of a UC subjected to different loading conditions. They can be estimated from the average local stresses (σ_{ii}, σ_{ij}) over the surface area (S) at the brick/mortar interface and the applied macroscopic strain (E) according to:

$$\begin{cases} L^{(HD)}_{iijj} = \dfrac{\int_S \sigma_{ii} dS}{S \times E_{ii}} \\ L^{(HD)}_{ijij} = \dfrac{\int_S \sigma_{ij} dS}{S \times E_{ij}} \end{cases} \tag{3.48}$$

In the case of pattern BD, the macroscopic stresses in the direction normal to head joints are almost equal to the local normal stresses at the brick/mortar interface of head joints. Therefore, on can assume that $\sigma_{ii} = \Sigma_{ii}, \sigma_{ij} = \Sigma_{ij}$with $i \neq j$. The tensile and shear failure criteria are expressed as:

$$\begin{cases} \sigma_{ii} = \Sigma_{ii} > f_t \\ \text{or} \\ \sqrt{\Sigma^2_{ji} + \Sigma^2_{ki}} > f_{sh} \end{cases} \tag{3.49}$$

and $L^{(BD)}_{kilm}$ are:

$$\begin{cases} L^{(3)}_{iijj} = C_{iijj} \\ L^{(3)}_{ijij} = C_{ijij} \quad j \neq i \end{cases} \tag{3.50}$$

In the case of joint pattern AD, both bed and head joints are already damaged. Therefore, no constants are required.

Under compressive loads, the damaged mortar joints can re-close and the structure can recover its stiffness. The ultimate tensile strength and the cohesion (of the brick/mortar interface)

of damaged - then - closed joints are equal to zero. The behavior of the damaged mortar joints under compressive stresses needs to be investigated experimentally. Future studies to investigate this phenomena and extension of the numerical model to include re-closure of damaged mortar joints are planned to be carried out in the future. In the present work, the re-closure of mortar joints was neglected.

3.4 Comparisons between the micro and macro modelings

The main aim of this section is to assess the accuracy of the developed macroscopic elastic viscoplastic numerical model. For this purpose, the equivalent material model (hereafter will be called macro model) has been implemented in the finite element code, Abaqus [85], with a user material subroutine UMAT. Then, it has been used to simulate uniaxial, simple shear and biaxial numerical experiments. Two different loading conditions have been considered namely, constant stress (creep) and constant strain loading (stress relaxation). For both loading conditions, comparisons between results from the macro and micro models are performed. In the case of macro modelling, the bricks and the joints are replaced by an equivalent homogeneous medium and the macro constitutive laws (equations 3.7 - 3.27) are used. Whereas, in the case of micro modelling, the bricks and joints are considered and the micro constitutive laws (equations 3.1 - 3.6) are employed.

3.4.1 Masonry with dry joints

For joint pattern HO, comparisons between average total strains (elastic and viscoplastic strains) obtained from the micro and macro models for both constant stress uniaxial tensile load in the x, y and z directions and simple shear load with respect to the xy, xz and yz planes are shown in Fig. 3.18. The comparisons are presented for three constant stress levels in the respective direction. Good agreements between the results obtained from the macro and micro models can be observed. It can be noticed that the macroscopic elastic viscoplastic behavior of pattern HO is orthotropic due to the presence of open joints. In the case of uniaxial loading in the y and z directions, values of the macroscopic total strains ($E^{\mathrm{t}}_{\mathrm{yy}}$ and $E^{\mathrm{t}}_{\mathrm{zz}}$) are almost the same because there are neither open joints in the y direction nor in the z direction. However, $E^{\mathrm{t}}_{\mathrm{yy}}$ and $E^{\mathrm{t}}_{\mathrm{zz}}$ are less than $E^{\mathrm{t}}_{\mathrm{xx}}$, because the presence of open joints in the x direction leads to a decrease in the effective stiffness of the structure and compressibility in the respective direction.

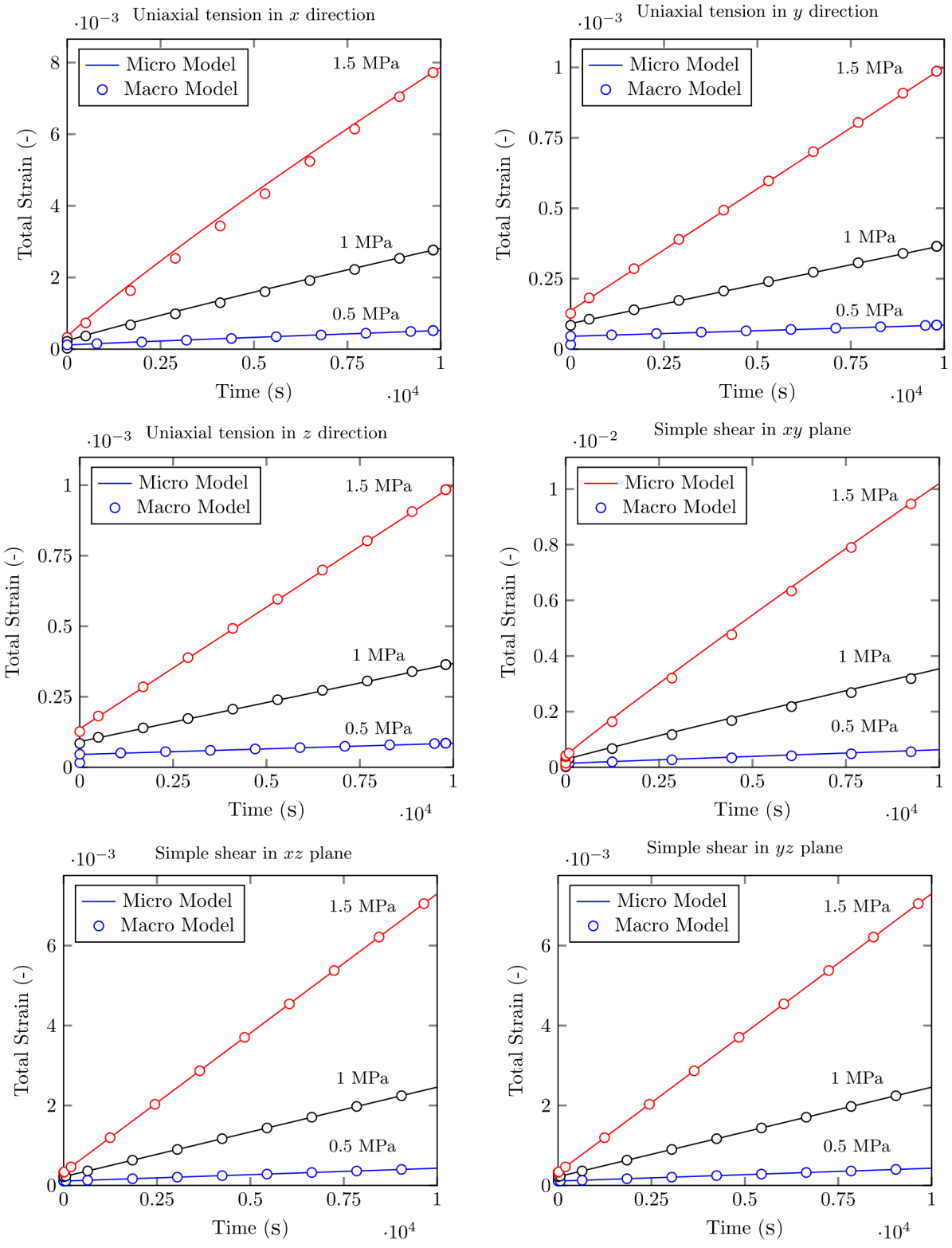

Figure 3.18: Comparisons between average total strains obtained from the detailed micro model (bricks and joints are considered) and macro model (bricks and joints are replaced by equivalent homogeneous medium) for constant stress uniaxial tension (in the x, y and z directions) and simple shear loading conditions (in the xy, xz and yz planes).

It should be noted that the previous constant stress loading conditions (uniaxial and simple shear) are used to identify the elastic viscoplastic parameters of the structure and, therefore, the agreements between the micro and macro models results are predicted. To further examine the macro model and the identification technique, comparisons between the results of the micro and macro models under two different loading conditions (different from those used in the identification) are carried out. The two loading conditions are biaxial constant stress loading and constant strain rate uniaxial loading. In the biaxial constant stress loading case, the following combination of compressive and tensile stresses are considered: compressive stress of 3 MPa in the x direction and tensile stress of 1 MPa in the y direction ($\Sigma_{xx} = -3\ MPa$ and $\Sigma_{yy} = 1\ MPa$). Comparisons between average total strains obtained from the micro and macro models are presented in Fig. 3.19. Good agreements between the micro and macro models are observed.

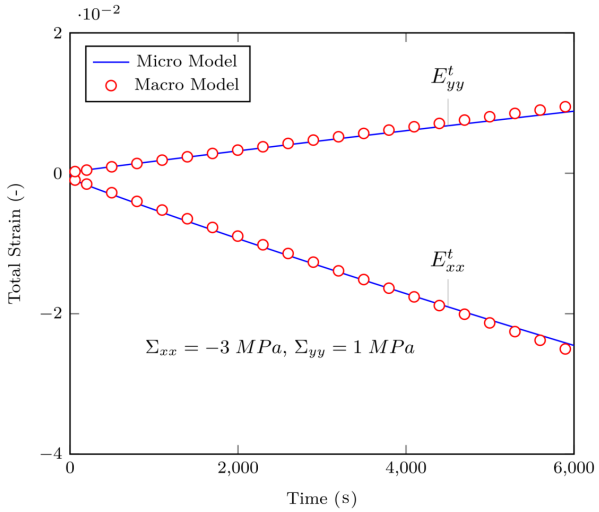

Figure 3.19: Comparisons between average total strains obtained from detailed micro model (bricks and joints are considered) and macro model (bricks and joints are replaced by equivalent homogeneous medium) for constant stress biaxial loading (compression in the x direction and tension in the y direction).

In the second loading case, comparisons between average stresses obtained from the micro and macro models for constant strain rate uniaxial tensile loading followed by holding in the x, y and z directions and simple shear with respect to the xy, xz and yz planes are shown in Fig. 3.20. The comparisons are presented for three constant strain rate levels. Good agreements between the results obtained from the macro and micro models can be observed. Overall, the stresses increase sharply due to load application and then, during holding, there is a decay due to stress relaxation. Again, similar values of macroscopic stresses have been observed in the case of uniaxial loading in the y and z directions. However, Σ_{yy} and Σ_{zz} are higher than Σ_{xx}, because the effective stiffness of the structure in the x direction is lower than that in the y and z directions.

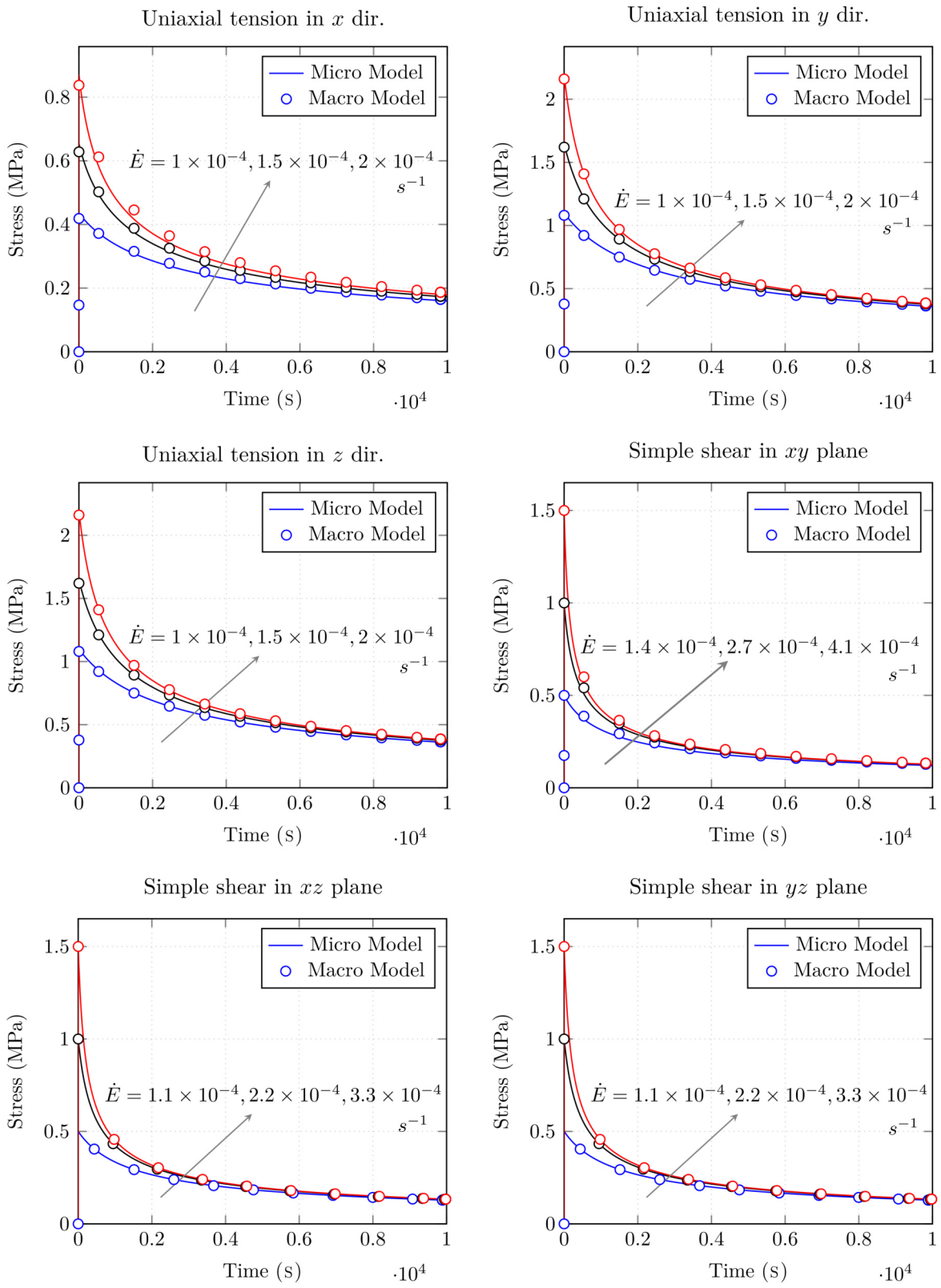

Figure 3.20: Comparisons between average macro stresses obtained from detailed micro model (bricks and joints are considered) and macro model (bricks and joints are replaced by equivalent homogeneous medium) for constant strain rate uniaxial tension (in the x, y and z directions) and simple shear loading (in the xy, xz and yz planes).

3.4.2 Masonry with mortar joints

For joint patterns AS and HD, comparisons between average total strains (elastic and viscoplastic strains) obtained from the micro and macro models for both constant stress uniaxial tensile load in the x, y and z directions and simple shear load with respect to the xy, xz and yz planes are shown in Figs. 3.21 and 3.22. The comparisons are presented for three constant stress levels in the respective direction. Good agreements between the results obtained from the macro and micro models can be observed. From Fig. 3.21, it can be observed that the homogeneous elastic viscoplastic behavior of joint pattern AS is isotropic because the thickness of the mortar joints is very small as compared to the dimensions of the bricks and the creep parameters of the brick and the mortar were considered similar. However, in the case of joint pattern HD, it can be seen from Fig. 3.22 that the macroscopic elastic viscoplastic behavior of pattern HD is orthotropic due to the presence of open joints (damaged head joints). In the case of uniaxial loading in the y and z directions, the values of the macroscopic total strains (E^t_{yy} and E^t_{zz}) are almost the same because there are neither open joints in the y direction nor in the z direction. However, E^t_{yy} and E^t_{zz} are less than E^t_{xx}, because the presence of open joints in the x direction leads to a decrease in the effective stiffness of the structure and compressibility in the respective direction.

It should be noted that the previous constant stress loading conditions (uniaxial and simple shear) are used to identify the elastic viscoplastic parameters of the structure and, therefore, the agreements between the micro and macro models results are predicted. To further examine the macro model and the identification technique, comparisons between the results of the micro and macro models under different loading conditions (different from those used in the identification) are carried out. The different loading conditions are constant stain rate uniaxial tension and simple shear loading followed by holding. For joint patterns AS and HD, comparisons between average stresses obtained from the micro and macro models for constant strain rate uniaxial tensile loading in the x, y and z directions and simple shear with respect to the xy, xz and yz planes are shown in Figs. 3.23 and 3.24. The comparisons are presented for two constant strain rate levels. Good agreements between the results obtained from the macro and micro models can be observed. Overall, the stresses increase sharply due to load application and then, during holding, there is a decay due to stress relaxation. For joint pattern AS, the macroscopic behavior of the structure is isotropic. In contrast, in the case of joint pattern HD, the macroscopic behavior is orthotropic due to the presence of open head joints. Similar values of macroscopic stresses have been observed in the case of uniaxial loading in the y and z directions. However, Σ_{yy} and Σ_{zz} are higher than Σ_{xx}, because the effective stiffness of the structure in the x direction is lower than that in the y and z directions.

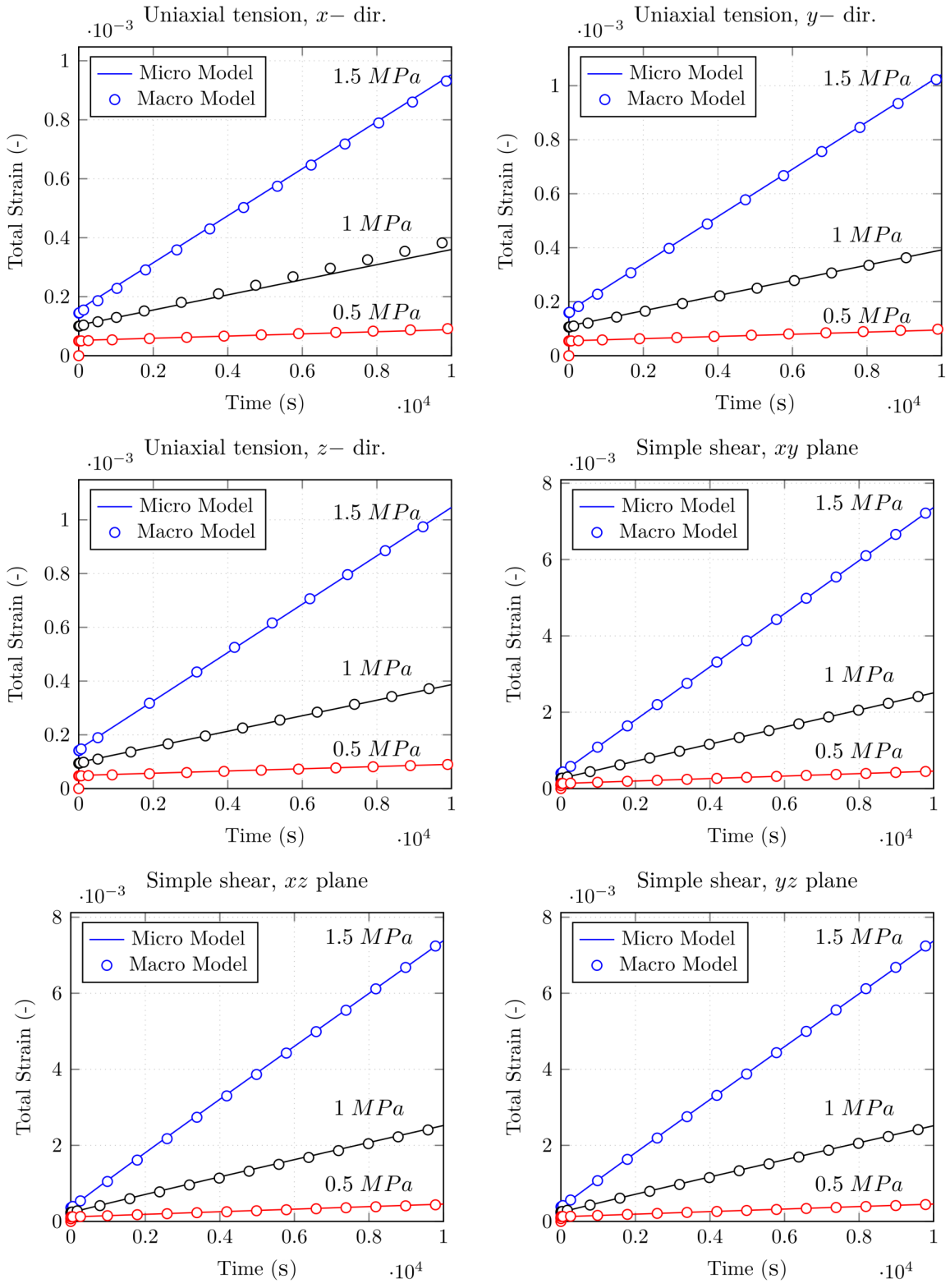

Figure 3.21: Comparisons between average total strains obtained from the detailed micro model (bricks and joints are considered) and macro model (bricks and joints are replaced by equivalent homogeneous medium) of periodic masonry structure in pattern AS subjected to constant stress uniaxial tension (in the x, y and z directions) and simple shear loading (in the xy, xz and yz planes).

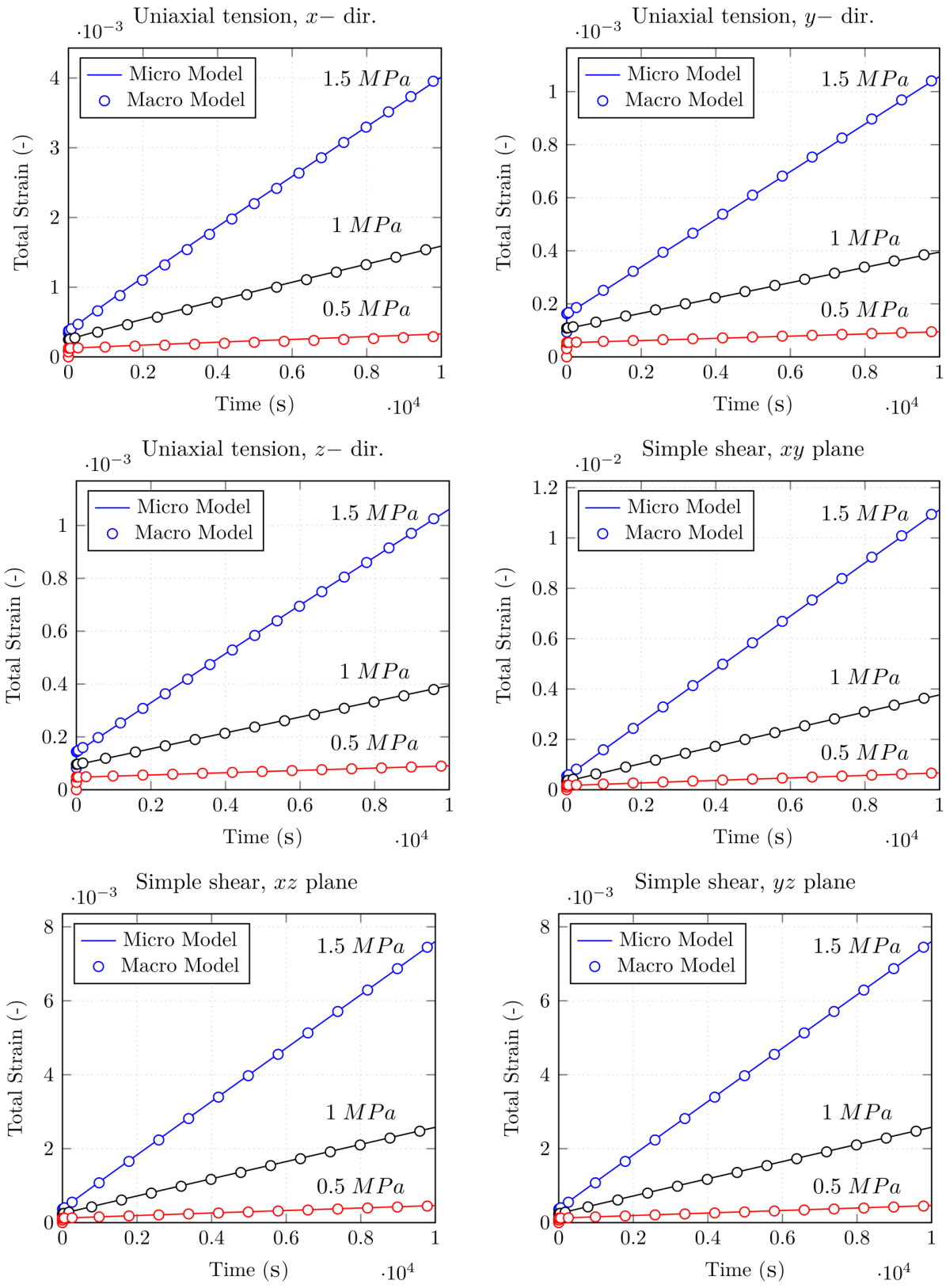

Figure 3.22: Comparisons between average total strains obtained from the detailed micro model (bricks and joints are considered) and macro model (bricks and joints are replaced by equivalent homogeneous medium) of periodic masonry structure in pattern HD subjected to constant stress uniaxial tension (in the x, y and z directions) and simple shear loading (in the xy, xz and yz planes).

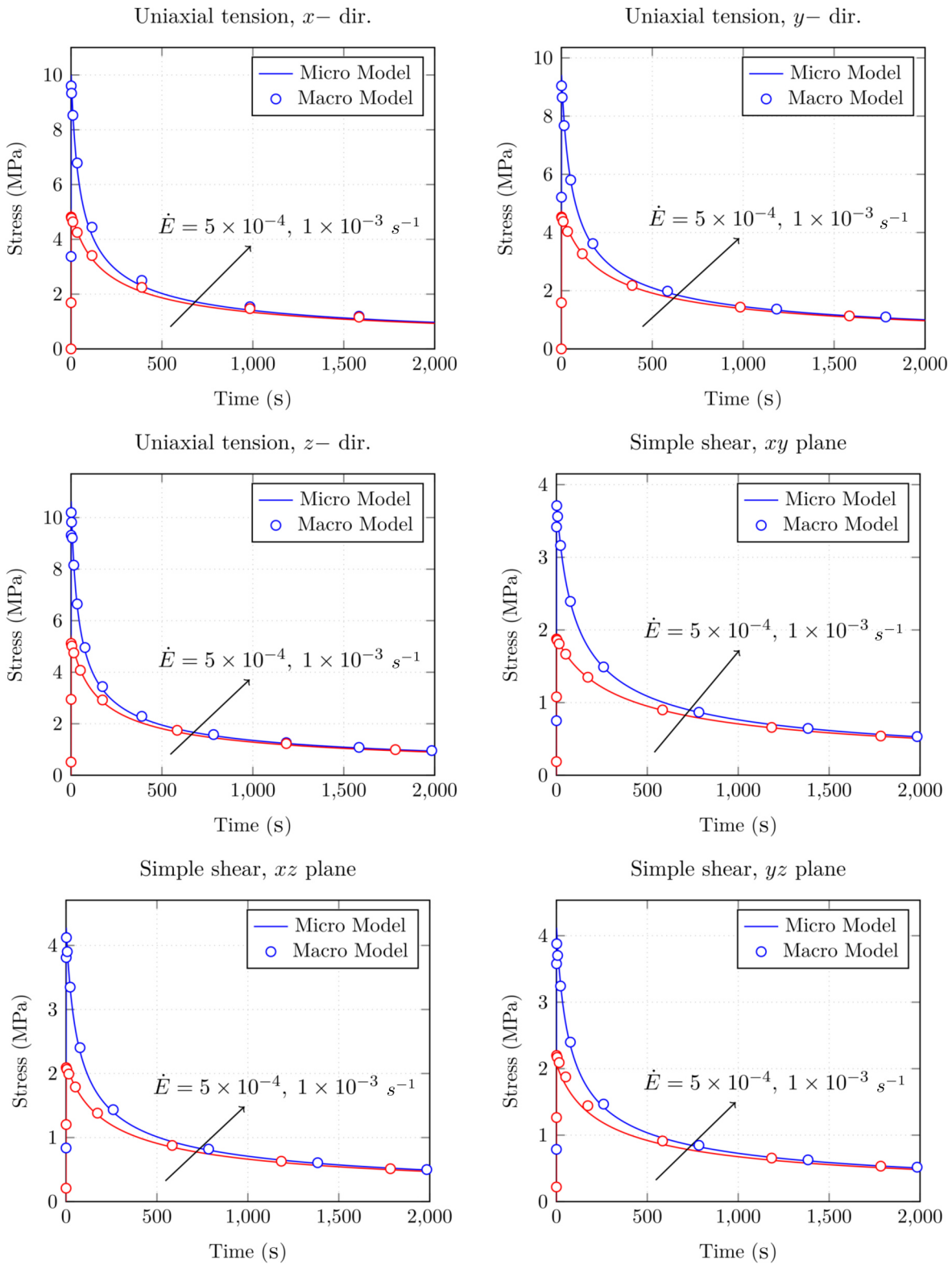

Figure 3.23: Comparisons between average macro stresses obtained from detailed micro model (bricks and joints are considered) and macro model (bricks and joints are replaced by equivalent homogeneous medium) of periodic masonry structure in pattern AS subjected to constant strain rate uniaxial tension (in the x, y and z directions) and simple shear loading (in the xy, xz and yz planes).

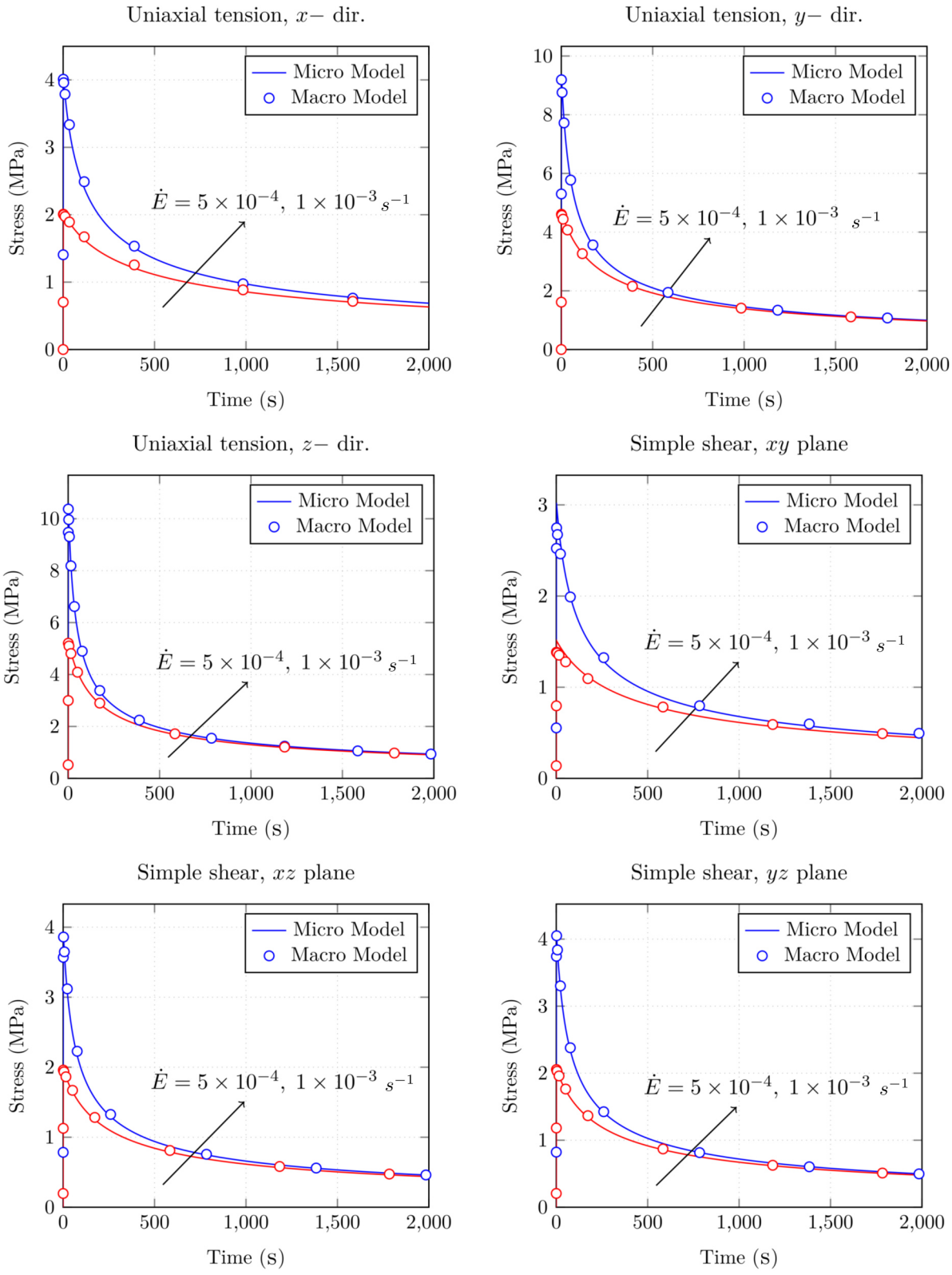

Figure 3.24: Comparisons between average macro stresses obtained from detailed micro model (bricks and joints are considered) and macro model (bricks and joints are replaced by equivalent homogeneous medium) of periodic masonry structure in pattern HD subjected to constant strain rate uniaxial tension (in the x, y and z directions) and simple shear loading (in the xy, xz and yz planes).

3.5 Conclusion

This chapter was devoted to the development of multi scale numerical models of masonry with dry or mortar joints. In the two multi scale models, four periodic joint patterns were defined. Each pattern is associated with a specific state of bed and head joints (open/closed or damaged/undamaged). The homogenized elastic viscoplastic behavior of each pattern was determined using FE based nonlinear homogenization technique. In the case of masonry with dry joints, the gradual increase in the effective stiffness with the gradual closure of joints was taken into account. The joints were reduced to an interface with small thickness (at the RVE level, micro modeling) where the constitutive normal and shear behaviors of the joints have been implemented. Suitable joints closure, reopening and pattern transition criteria were developed and implemented. Regarding masonry with mortar joints, a homogenized elastic-viscoplastic multi scale model was developed. Both the bricks and mortar joints were considered to exhibit linear elasticity as well as rate-dependent plasticity (creep). The transition criterion between the four patterns was defined by tension cut-off associated with Mohr-Coulomb criterion. Verification of the developed multi scale models has been carried out by comparing the numerical results of detailed micro models (brick and joints are considered) with the homogeneous equivalent material models (bricks and joints were replaced by a homogeneous material).

CHAPTER 4

VALIDATION OF THE DEVELOPED MULTI-SCALE MODELS

This chapter is devoted to the validation of the developed multi scale numerical models of masonry with dry or mortar joints presented in chapter 3. The multi scale models of masonry with dry joints are validated by comparing the experimental results, presented in chapter 2, and numerical results of masonry walls subjected to wide range of loading conditions at room and high temperature. Details about the physical models of the masonry with dry joints, boundary conditions as well as comparisons between experimental and numerical results are given in section 4.1. The multi scale models of masonry with mortar joints are validated by comparing some experimental and numerical results of masonry with mortar joints available in the literature with those predicted by the present models. The physical models of the walls, boundary conditions, simulation techniques and comparisons between experimental and numerical results are presented in section 4.2. The two validated models will be employed later in chapter 5 to simulate an industrial scale steel ladle. The conclusion of the present chapter is given in section 4.3.

4.1 Masonry with dry joints

The developed multi scale model of masonry with dry joints has been used to simulate the experimental tests of alumina spinel refractory masonry presented in chapter 2. The thermo-physical and mechanical properties of the alumina spinel bricks that have been used to identify the homogenized mechanical properties of the four joint patterns are given in chapter 2. The average behavior of the dry joints are identified from test series S01. Classical joints closure tests of two small alumina spinel parts were performed by Oliveira et al. [151] (see Fig. 4.1-a). The main limitation of these tests is that they do not consider the dimension and shape tolerances of the bricks, presented in chapter 2, and, therefore, in most cases underestimate joints closure.

The average closure of joints at different stress levels was studied at three different locations in wall S01-01 (top, middle and bottom, see Fig. 4.1-b). The relative displacements between

each set of the horizontal blue lines in the figure (top, middle and bottom, each set compromises two lines, one above and one below the joints) are obtained from the DIC analysis. For each line in each set, the displacements of 30 points were determined. The joints closure was considered as the relative displacement between the two lines in each set. The joints closure variations with the applied stress at different locations in the wall as well as the average of the three studied locations are given in Fig. 4.2-a. Comparisons with the results of the classical joints closure test are reported in the same figure.

The stresses are considered as uniform in the wall. Indeed, in reality, they are nonuniform due to the non flatness of the top raw of the wall and stress concentrations caused by the dimension and shape tolerances of the bricks. From Fig. 4.2-a, it can be noticed that at the same stress level, the classical joints closure tests underestimate the joints closure. The calculated average normal and shear stiffnesses of the dry joints are reported in Fig. 4.2-b. They are calculated as following: the average joints closure of the three locations ($d_{n,\,avg}$) - stress relationship (DIC - Average in Fig. 4.2-a) was fitted. Then, the normal (k_n) and shear (k_s) stiffnesses were calculated using the equations given in chapter 3 ($k_n = \triangle\sigma / \triangle\, d_{n,\,avg}$ and $k_s = k_n/2(1+\nu)$, $\nu = 0.2$).

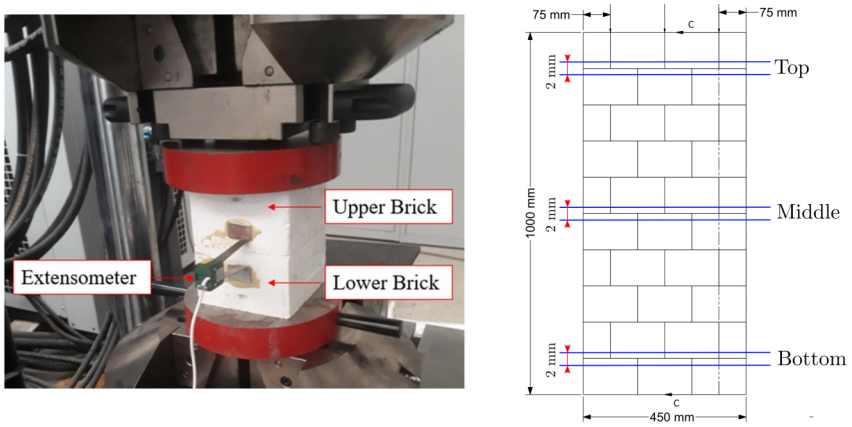

(a) (b)

Figure 4.1: (a) Classical joints closure test of a stack two of alumina spinel parts [151] and (b) schematic showing wall S01-01 and the chosen locations for studying joints closure by DIC.

Due to the lack of experimental data of joints closure at high temperature, it has been assumed that the average stiffness of the joints at higher temperatures is similar to that at room temperature and the difference in the homogenized mechanical behavior, for the same joint pattern, at different temperatures is caused by the change in the mechanical properties of the bricks with temperature. Further experimental studies to investigate the joints closure behavior, with DIC, for a running bond texture dry masonry are required. Examples of the identified homogenized Young's modulus and shear modulus of joint pattern AO at different temperatures are presented in Fig. 4.3. The homogenized elastic and viscoplastic parameters of the four joint patterns at different temperatures are summarized in tables 4.1 and 4.2, respectively. These parameters are used later in this chapter to predict the homogenized behavior of masonry walls subjected to a wide range of thermomechanical loading conditions.

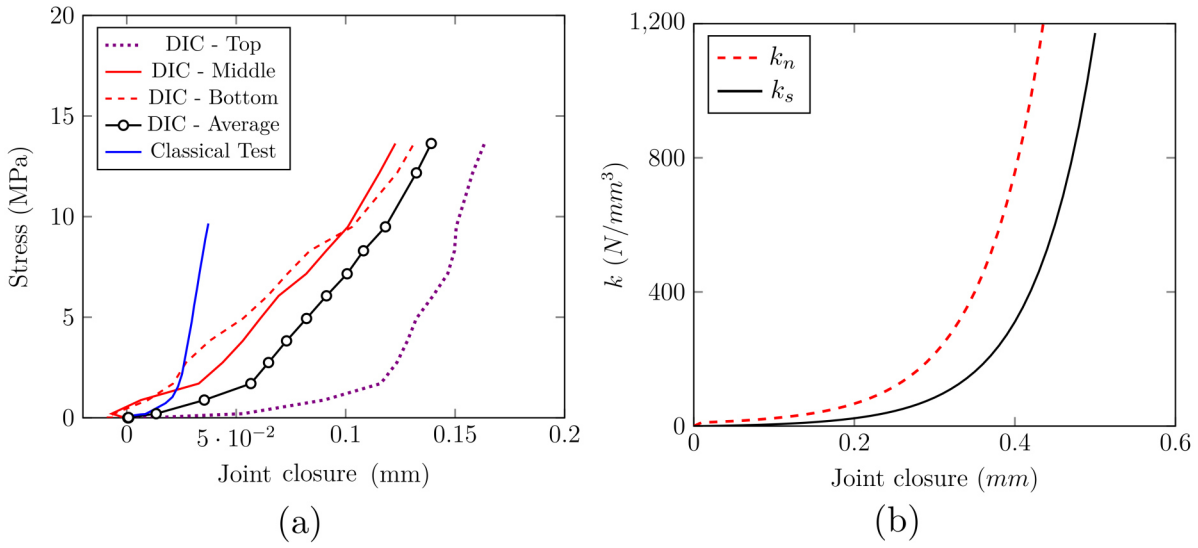

Figure 4.2: (a) Comparisons between stress variations with joints closure at different locations in the wall and results of classical joints closure test and (b) the calculated average normal (k_n) and shear (k_s) stiffnesses of the joints.

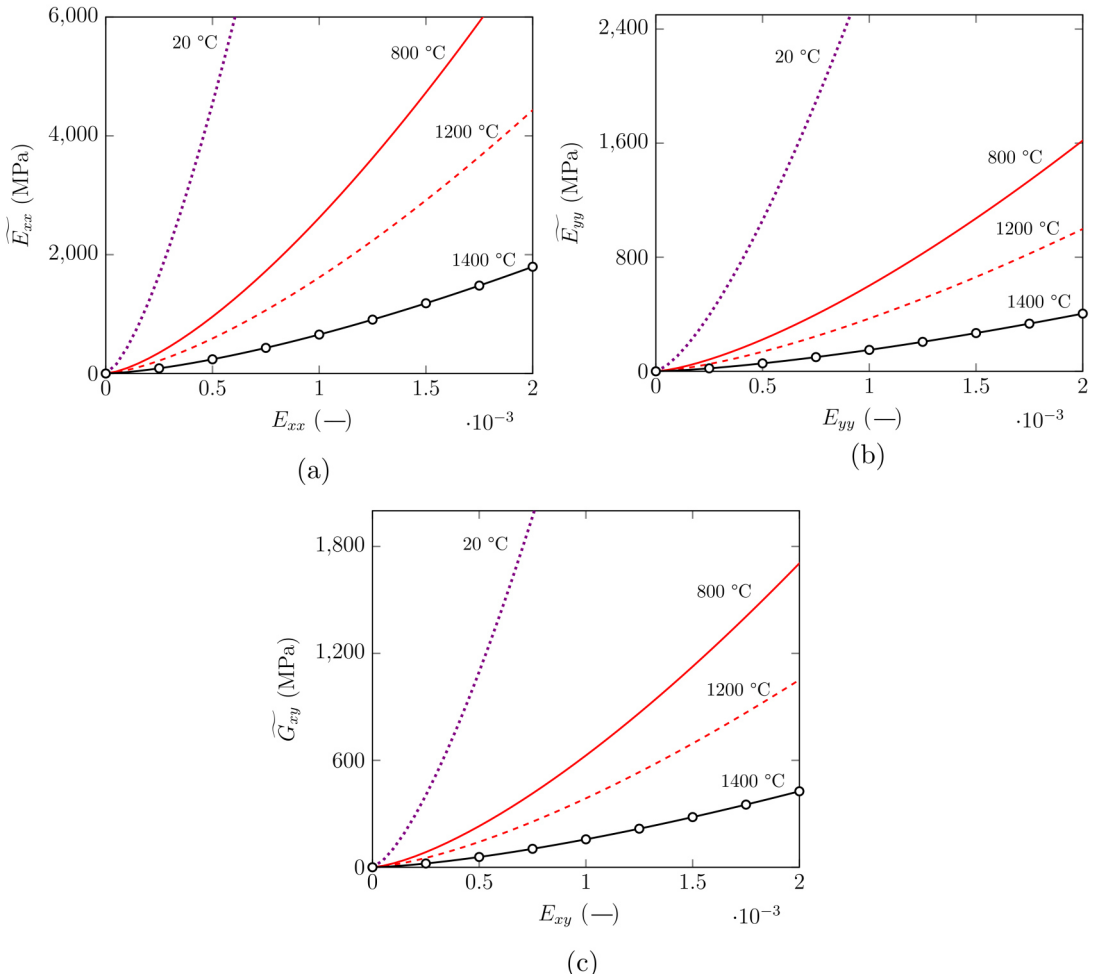

Figure 4.3: Examples of the identified homogenized (a, b) Young's modulus and (c) shear modulus variations with the macroscopic strains of joint pattern AO at different temperatures.

Table 4.1: Effective elastic 4$^{\text{th}}$ order tensor of the four joint patterns of alumina spinel refractory masonry at different temperatures.

Pattern							$\overline{\overline{\overline{\overline{AC}}}}^{\,e}\ (MPa)$																							
Temperature			20 °C							800 °C							1000 °C							1200 °C							1400 °C					
AO	$f(E_{11})$	0	0	0	0	0	$f(E_{11})$	0	0	0	0	0	$f(E_{11})$	0	0	0	0	0	$f(E_{11})$	0	0	0	0	0	$f(E_{11})$	0	0	0	0	0
		$f(E_{22})$	0	0	0	0		$f(E_{22})$	0	0	0	0		$f(E_{22})$	0	0	0	0		$f(E_{22})$	0	0	0	0		$f(E_{22})$	0	0	0	0
			31666	0	0	0			6666	0	0	0			5444	0	0	0			4111	0	0	0			1666	0	0	0
				$f(E_{12})$	0	0				$f(E_{12})$	0	0				$f(E_{12})$	0	0				$f(E_{12})$	0	0				$f(E_{12})$	0	0
					11875	0					2500	0					2041	0					1541	0					625	0
						11875						2500						2041						1541						625
BO	29687	0	5937	0	0	0	6666	0	1666	0	0	0	5444	0	1361	0	0	0	4111	0	1027	0	0	0	1666	0	416	0	0	0
		$f(E_{22})$	0	0	0	0		$f(E_{22})$	0	0	0	0		$f(E_{22})$	0	0	0	0		$f(E_{22})$	0	0	0	0		$f(E_{22})$	0	0	0	0
			30299	0	0	0			6666	0	0	0			5444	0	0	0			4111	0	0	0			1666	0	0	0
				$f(E_{12})$	0	0				$f(E_{12})$	0	0				$f(E_{12})$	0	0				$f(E_{12})$	0	0				$f(E_{12})$	0	0
					11875	0					2500	0					2041	0					1541	0					625	0
						11875						2500						2041						1541						625
HO	10394	2618	2602	0	0	0	2188	551	547	0	0	0	1787	450	447	0	0	0	1349	339	337	0	0	0	547	137	136	0	0	0
		30307	6585	0	0	0		6380	1386	0	0	0		5210	1132	0	0	0		3934	854	0	0	0		1595	346	0	0	0
			30299	0	0	0			6378	0	0	0			5209	0	0	0			3933	0	0	0			1594	0	0	0
				8369	0	0				1762	0	0				1439	0	0				1086	0	0				440	0	0
					11875	0					2500	0					2041	0					1541	0					625	0
						11875						2500						2041						1541						625
AC	31666	7916	7916	0	0	0	6666	1666	1666	0	0	0	5444	1361	1361	0	0	0	4111	1027	1027	0	0	0	1666	416	416	0	0	0
		31666	7916	0	0	0		6666	1666	0	0	0		5444	1361	0	0	0		4111	1027	0	0	0		1666	416	0	0	0
			31666	0	0	0			6666	0	0	0			5444	0	0	0			4111	0	0	0			1666	0	0	0
				11875	0	0				2500	0	0				2041	0	0				1541	0	0				625	0	0
					11875	0					2500	0					2041	0					1541	0					625	0
						11875						2500						2041						1541						625

Table 4.2: Effective viscoplastic 4^{th} order tensor of the four joint patterns of alumina spinel refractory masonry at different temperatures.

Pattern	$\overline{\overline{\overline{\overline{N}}}}\,(-)$																	
Temperature	1300 °C						1400 °C						1500 °C					
AO	2.22	-1.11	-1.11	0	0	0	2.16	-1.08	-1.08	0	0	0	2.25	-1.12	-1.12	0	0	0
		2.22	-1.11	0	0	0		2.16	-1.08	0	0	0		2.25	-1.12	0	0	0
			2.23	0	0	0			2.16	0	0	0			2.25	0	0	0
				9.33	0	0				8.29	0	0				9.71	0	0
					9.33	0					8.29	0					9.71	0
						9.33						8.29						9.71
BO	2.22	-1.11	-1.11	0	0	0	2.16	-1.08	-1.08	0	0	0	2.25	-1.12	-1.12	0	0	0
		2.22	-1.11	0	0	0		2.16	-1.08	0	0	0		2.25	-1.12	0	0	0
			2.23	0	0	0			2.16	0	0	0			2.25	0	0	0
				9.33	0	0				8.29	0	0				9.71	0	0
					9.33	0					8.29	0					9.71	0
						9.33						8.29						9.71
HO	15.07	-1.59	-1.03	0	0	0	11.81	-1.32	-1.08	0	0	0	11.36	-1.50	-1.12	0	0	0
		2.22	-1.11	0	0	0		2.16	-1.08	0	0	0		2.25	-1.12	0	0	0
			2.23	0	0	0			2.16	0	0	0			2.25	0	0	0
				17.06	0	0				12.52	0	0				13.34	0	0
					9.33	0					8.29	0					9.71	0
						9.33						8.29						9.71
AC	2.22	-1.11	-1.11	0	0	0	2.16	-1.08	-1.08	0	0	0	2.25	-1.12	-1.12	0	0	0
		2.22	-1.11	0	0	0		2.16	-1.08	0	0	0		2.25	-1.12	0	0	0
			2.23	0	0	0			2.16	0	0	0			2.25	0	0	0
				9.33	0	0				8.29	0	0				9.71	0	0
					9.33	0					8.29	0					9.71	0
						9.33						8.29						9.71

4.1.1 S01: uniaxial compression up to rupture at room temperature

In this test series, three refractory masonry walls with 450 $\times$ 1000 $\times$ 140 mm^3 dimensions were tested up to rupture. An increasing uniaxial compression load was applied in the direction normal to bed joints up to rupture. The FE model of the wall is presented in Fig. 4.4. The FE model was developed using Abaqus software and the wall was meshed with 3D hexahedron elements. The top loading beam and the reaction slab of the test setup were replaced with rigid plates. The wall (bricks and joints) was represented by a homogeneous material whose mechanical properties vary with the gradual closure and reopening of joints. The interactions between the contact surfaces of reaction slab and the wall and between the loading beam and the wall were modeled using friction contact with a coefficient of friction of 0.5. The boundary conditions of the two rigid plates are given in Fig. 4.4. The sides of the wall were free during load application step. The gravity effects were considered in the FE model.

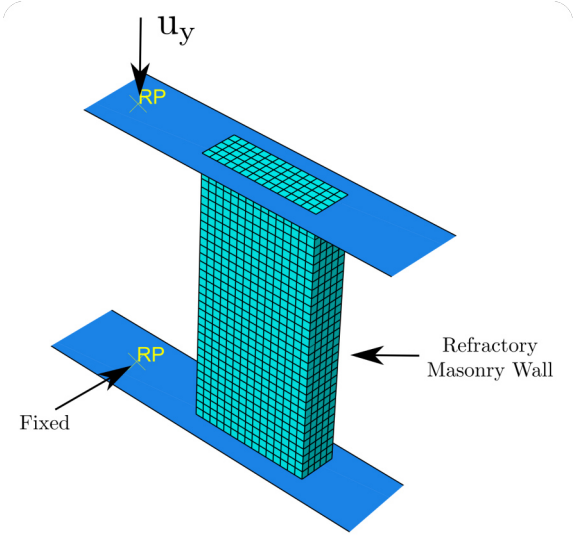

Figure 4.4: Test series S01: FE model of masonry wall subjected to uniaxial compression load in the direction normal to bed joints: geometry and boundary conditions.

The vertical displacement fields predicted by the numerical model (in the direction normal to bed joints - loading direction) on the front surface of the wall at 33 %, 66 % and 99 % of maximum load level are presented in Fig. 4.5. Comparisons between the experimental and the numerical reaction forces variations with the displacements are shown in Fig. 4.6. The displacements of the experimental tests were determined from the DIC analysis (relative displacement between two lines, one in the middle of the top raw of the bricks and another one in the middle of the bottom raw). Good agreements between the experimental and numerical results can be observed. It can be noticed that the present multi scale model can reproduce, with reasonable accuracy, the nonlinear mechanical response of the wall. The resulting force displacement diagram of the wall is nonlinear. The model is able to predict the displacement stiffening behavior of the wall caused by the progressive closure of joints and the gradual increase in the contact area with the increase

of the applied load (increase of effective stiffness and effective tangent Young's modulus of the wall with the increase of the applied load).

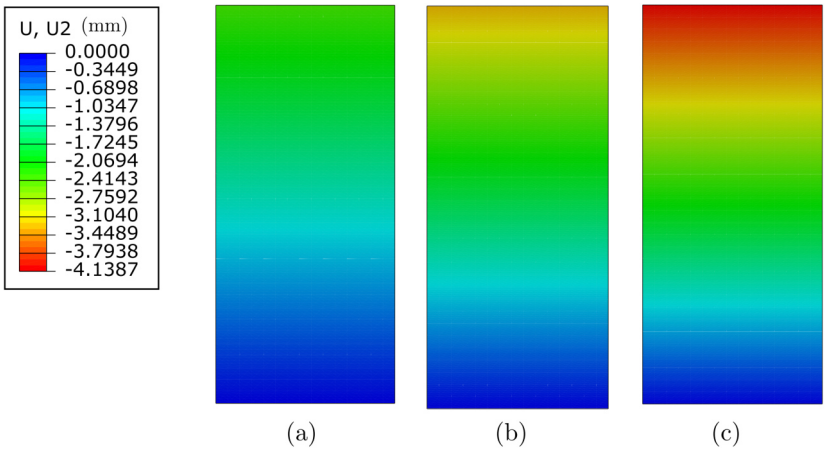

Figure 4.5: Test series S01: vertical displacement fields in masonry wall subjected to uniaxial compression load in the direction normal to bed joints (vertical direction in this image) at (a) 33 %, (b) 66 % and (c) 99 % of maximum load level.

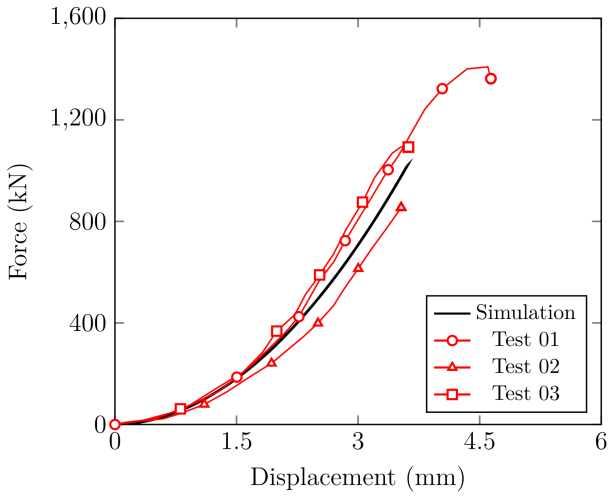

Figure 4.6: Test series S01: reaction forces versus vertical displacements in the direction normal to bed joints in alumina spinel masonry walls subjected to uniaxial compression load, up to failure, at room temperature: experimental and numerical results.

4.1.2 S02: uniaxial compression at high temperature

In this test series, three refractory masonry walls with 1350 $\times$ 1000 $\times$ 140 mm^3 dimensions were tested. A uniaxial mechanical load, normal to bed joints, was applied at room temperature and kept constant then, one face of the wall was heated. The three specimens were tested under the same thermomechanical loading conditions. The FE analysis of the problem compromises two steps: firstly, transient heat transfer analysis to compute the temperature distributions and variations with time; Then, thermomechanical analysis was carried out to compute the

thermomechanical stress and strain fields. The temperature fields calculated in the first step were used as a temperature load in the thermomechanical analysis. The heat transfer and thermomechanical FE models of the wall were developed using Abaqus. The physical model of the wall is similar to that of series S01 with only one difference, which is the width of the wall (1350 mm in the case of series S02). The thermo physical properties of the bricks are reported in chapter 2.

The heat transfer model considers the radiative ($q_{r,\,i}$) and convective ($q_{c,\,i}$) heat exchange between the furnace and the hot face (HF) of the wall, conductive (q_{con}) heat transfer through the wall thickness, convective ($q_{c,\,o}$) and radiative ($q_{r,\,o}$) heat exchange between the cold face (CF) and the ambient (amb). Figure 4.7 shows the thermal resistance diagram used to simulate these phenomena.

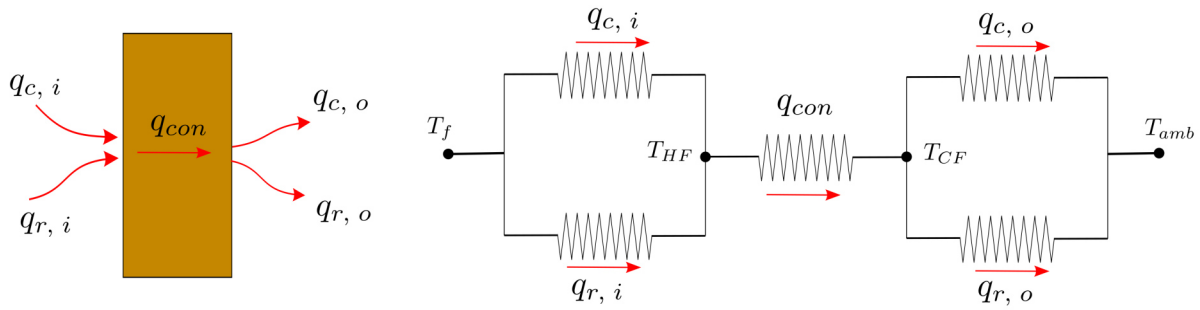

Figure 4.7: Test series S02: schematic of the thermal model of the wall and the thermal resistance circuit equivalence.

The temperature distribution of the wall varies with time (t) and can be obtained by solving the transient form of the energy equation given by [158]:

$$\rho C_p \frac{\partial T}{\partial t} - \mathrm{div}(k\overrightarrow{\mathrm{grad}}(T)) = 0 \tag{4.1}$$

Where ρ, k, T and C_p are the density, thermal conductivity, temperature and specific heat, respectively. Before heating, the initial temperature (T_i) of the wall was assumed to be the same as the ambient temperature. Under this assumption, the initial boundary conditions can be expressed as [158]:

$$T(x, y, z, t = 0) = T_i = 20\ ^{\circ}\mathrm{C} \tag{4.2}$$

The convective heat exchange ($q_{c,\,i}$) between the furnace (f) and the HF of the wall is written as [158]:

$$q_{c,\,i} = h_i \left(T_f - T_{HF}(x, y, z, t)\right) \tag{4.3}$$

$$\frac{\partial T_{HF}}{\partial \vec{n}} = h_i \left(T_f - T_{HF}(x, y, z, t)\right) \overrightarrow{\mathrm{n}} \tag{4.4}$$

Where h_i is the convective heat transfer coefficient (temperature and location dependent to account for the heat losses from the bottom part of the wall to the reaction slab, see Fig. 4.8)

and $\vec{n}$ is the outward normal to the surface. T_{HF} is the hot face temperature. The radiative heat exchange ($q_{r,\,i}$) between the furnace and the HF is expressed as:

$$q_{r,\,i} = \epsilon S \left(T_f^4 - T_{HF}^4(x, y, z, t)\right) \tag{4.5}$$

Where ϵ and S are the emissivity of the wall (taken as 0.8 for alumina spinel) and Stefan–Boltzmann constant, respectively. The convective ($q_{c,\,o}$) and radiative ($q_{r,\,o}$) heat losses from the CF of the wall to the ambient are expressed as [158]:

$$q_{out} = q_{c,\,o} + q_{r,\,o} = h_o \left(T_{CF}(x, y, z, t) - T_{amb}\right) + \epsilon S \left(T_{CF}^4(x, y, z, t) - T_{amb}^4\right) \tag{4.6}$$

Where T_{CF} is the cold face temperature and h_o is the convective heat transfer coefficient between the cold face of the wall and the ambient (location dependent, taken as 9 W/m^2.K for the top and middle portions of the CF and 18 W/m^2.K for the bottom portion of the CF to account for heat losses to the reaction slab).

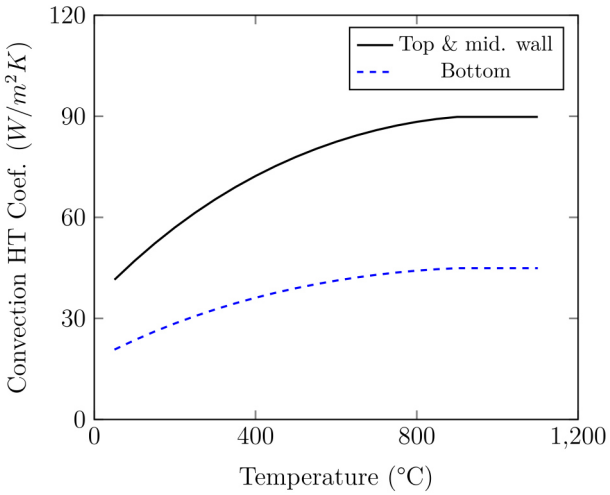

Figure 4.8: Temperature variations of the convection heat transfer coefficient (h_i) used for the top, middle and bottom portions of the HF of the wall.

The experimental and numerical time variations of the temperature of the HF and CF at different locations of the wall during load application and heating steps are shown in Fig. 4.9-a. The shaded areas in the figure present the readings of the thermocouples. Good agreements between the experimental and numerical results can be observed. The temperature distribution at the end of the heating step is presented in Fig. 4.9-b. During load application step (first 0.5 h), the temperature was equal to room temperature. Then, during the heating step, heat is transferred by convection and radiation mechanisms from the furnace to the HF of the wall. As a result, the temperature of the HF increases gradually from room temperature to around 880 °C. The high temperature gradients through the thickness of the wall are caused by the low thermal conductivity, high heat thermal capacity of alumina spinel and high heat losses from the CF to the ambient.

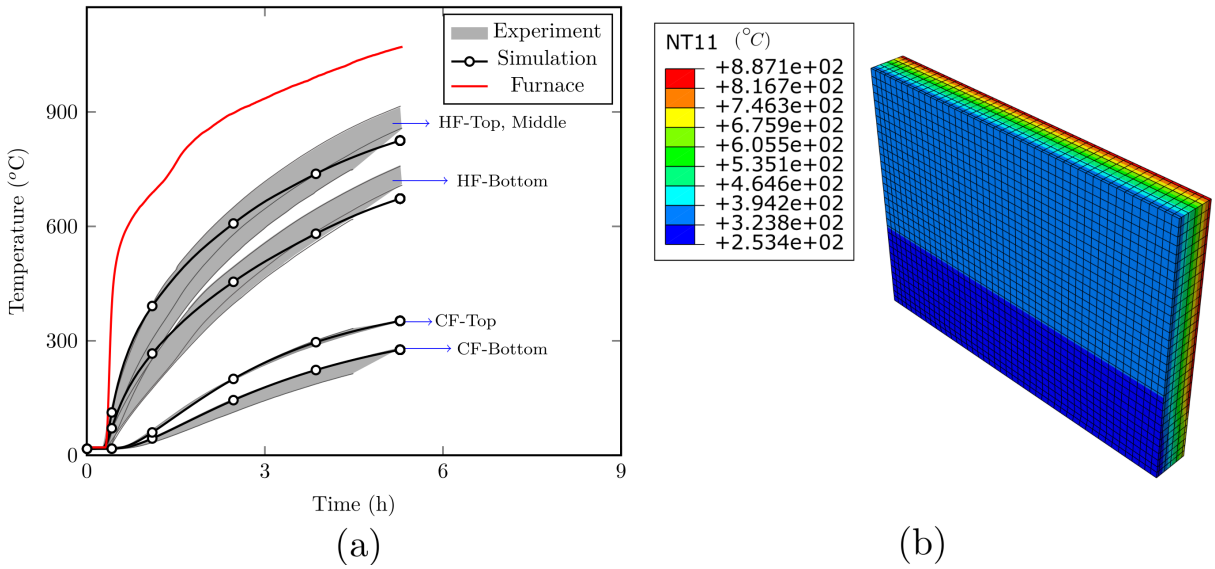

Figure 4.9: Test series S02: (a) time variations of the hot face and cold face temperatures, experimental and numerical results. (b) Temperature distribution at the end of the heating step.

With regard to the thermomechanical analysis, the wall has been replaced by a homogeneous material whose mechanical properties vary with the gradual closure and reopening of joints. The loading beam and the reaction slab were replaced by rigid plates. The frictional interactions between the contact surfaces of the reaction slab and the wall and between the loading beam and the wall were considered (coefficient of friction 0.5). The applied load to top loading beam is that a compressive stress of 8 MPa. The same experimental amplitude was used for load application and load holding steps. The sides of the wall were free to move during load application and holding. The temperature distributions obtained from the heat transfer analysis were employed as a thermal load in the transient thermomechanical analysis.

The experimental and numerical time variations of the displacement in the direction normal to bed joints are given in Fig. 4.10. Good agreements between the experimental and numerical results can be observed. From the figure, one can observe that in the first 0.5 h, an average negative displacement of around -3.5 mm was measured by the LVDTs and predicted by the numerical model due to uniaxial compression load application (8 MPa). Then, when the furnace was turned on and with the increase of the temperature, the wall started to expand gradually and a steady increase in the displacement, in the opposite direction, was recorded. At around 4.5 h, the thermal expansion effects of the wall over passed the impact of mechanical load application and a positive displacement was recorded by the LVDTs and predicted by the present model.

4.1.3 S03: uniaxial loading and unloading - normal to bed joints at room temperature

In this test series, two refractory masonry walls with 1100 $\times$ 1125 $\times$ 140 mm^3 dimensions were tested at room temperature. A uniaxial compression load/unload (up to 6 MPa) was applied in

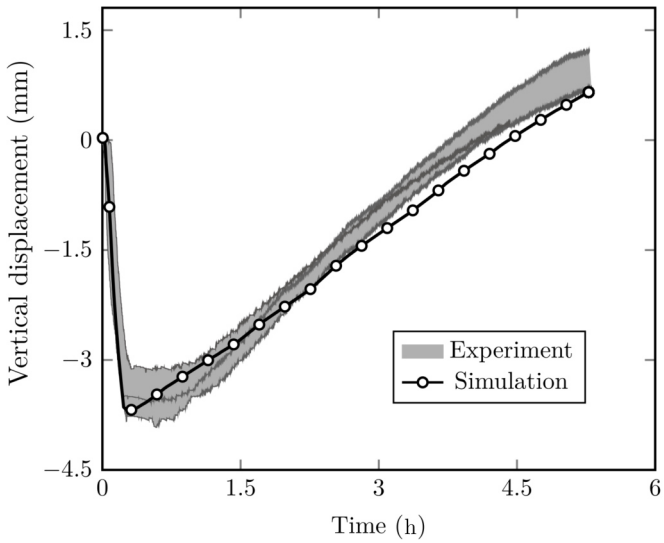

Figure 4.10: Test series S02: experimental and numerical time variations of the vertical displacement.

the direction normal to bed joints and the direction normal to head joints was constrained by the plungers. The FE model of the wall is shown in Fig. 4.11. The x direction (1125 mm) is the direction normal to head joints while, the y direction (1100 mm) is normal to bed joints. The FE model was developed using Abaqus and the wall was meshed with 3D hexahedron elements. The four ceramic plates, as well as the top insulation layer (ground) of the test setup have been modeled as rigid plates. The wall (bricks and joints) was replaced by a homogeneous material whose mechanical properties vary with the gradual closure and reopening of the joints. The homogeneous mechanical behavior of the wall during unloading is different from that during loading, as presented in chapter 2, and was inversely identified (due to lack of data about joints behavior during unloading). The frictional interactions between the contact surfaces of the wall and the fixed, moving rigid plates and the ground were considered (coefficient of friction of 0.5). The boundary conditions of two fixed rigid plates, the moving rigid plate normal to head joints (x direction in Fig. 4.11) and the ground are set to fully fixed.

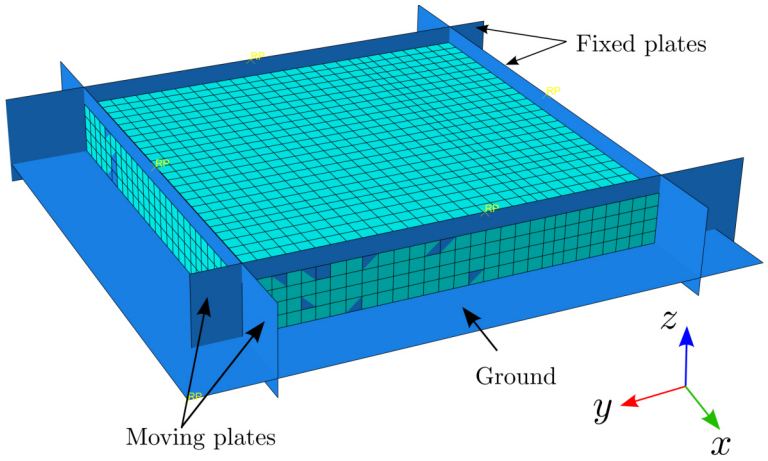

Figure 4.11: Test series S03: FE model of masonry wall subjected to uniaxial compression loading/unloading in the direction normal to bed joints.

Comparisons between the experimental and numerical force - displacement diagrams of a masonry wall subjected to uniaxial compression loading/unloading in the direction normal to bed joints are presented in Fig. 4.12. The bounds of the shaded area represent the results of the two experiments. It can be seen that the present numerical model reproduces with reasonable accuracy the displacement stiffening mechanical behavior of the wall. The reaction force increases with the increase in the applied displacement due to the gradual closure of the joints and the increase in effective stiffness with the gradual closure of joints. The displacement fields in the direction normal to bed joints at maximum load level and after load removal are given in Fig. 4.13. The arrow indicates the location of the moving plunger (in the y direction) and the lines denote the positions of the fixed plunger (in the x direction) and the two fixed rigid plates. After unloading, the wall did not recover to the initial configuration and there was be permanent deformation caused by the closure of joints, the deformation and the crushing of the asperities present at the contact surfaces of bed joints.

4.1.4 S04: uniaxial loading and unloading - normal to head joints at room temperature

With regard to test series S04, two refractory masonry walls with 1100 $\times$ 1125 $\times$ 140 mm^3 dimensions were tested at room temperature. The main difference between S04 and S03 is that the uniaxial compression loading (6 MPa) and unloading was applied to the direction normal to head joints while the other direction (normal to bed joints) was constrained by the ceramic plungers. The FE model of the wall is the same as that presented in Fig. 4.11. The main difference between the two FE models is the boundary conditions of the two moving plungers. The frictional interactions between the contact surfaces of the wall, the plungers and the ground were considered in the FE model. The boundary conditions of two fixed rigid plates, the moving rigid plate normal to bed joints (y direction in Fig. 4.11) and the ground are set to fully fixed.

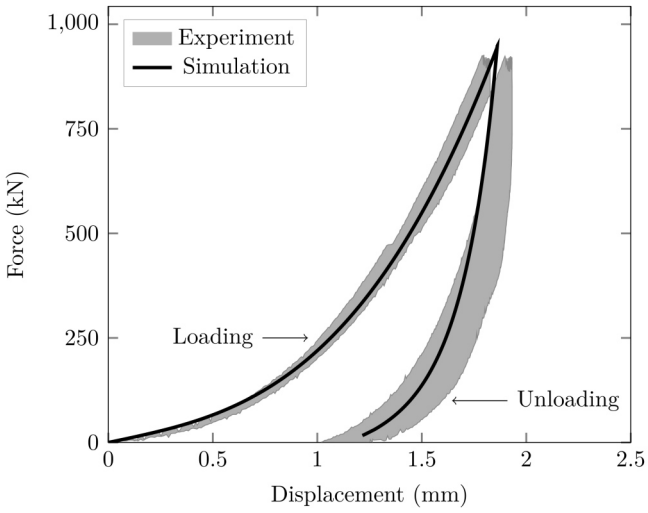

Figure 4.12: Test series S03: comparisons between experimental and numerical force - displacement diagrams of a masonry wall subjected to uniaxial compression loading/unloading in the direction normal to bed joints.

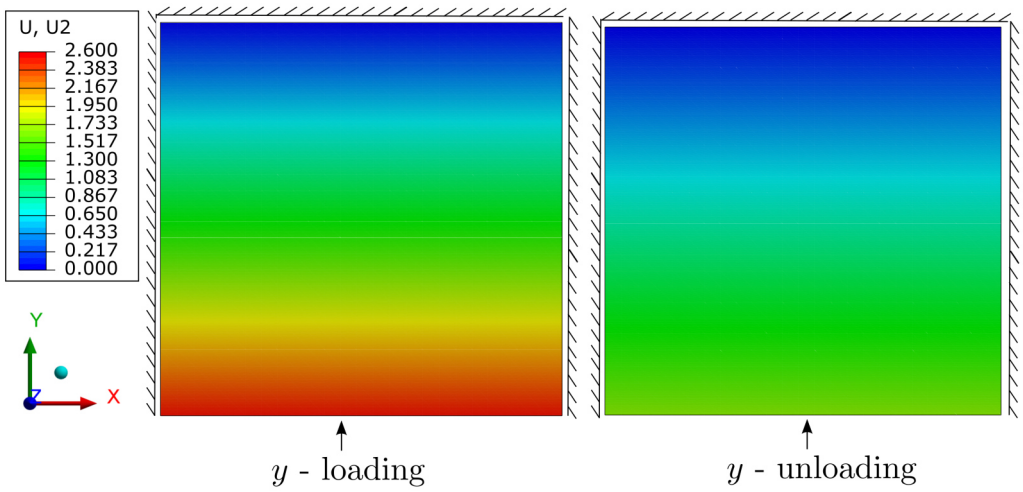

Figure 4.13: Test series S03: displacement fields (in mm), in the direction normal to bed joints, of a masonry wall subjected to uniaxial compression loading/unloading in the direction normal to bed joints (y direction) at maximum load level (left) and after unloading (right).

Figure 4.14 shows comparisons between experimental and numerical force - displacement diagrams of the walls subjected to uniaxial compression loading/unloading in the direction normal to head joints. The numerical model was able to predict the mechanical behavior of the wall with good accuracy. As compared to S03, the value of the displacement at maximum load level is smaller. This can be attributed to that the number of head joints in the wall is less than the number of bed joints. This leads to higher stiffness (and, therefore, less deformation at the same load level) in the direction normal to head joints as compared to the direction normal to bed joints. Fig. 4.15 shows the displacement fields in the direction normal to head joints at maximum load level and after unloading. The arrow indicates the location of the moving plunger (in the x direction) and the lines denote the positions of the fixed plunger (in the y direction) and

the two fixed rigid plates. The wall did not go back to the initial configuration and there was permanent deformation caused by gradual closure of joints, the deformation and the crushing of the asperities present at the contact surfaces of head joints.

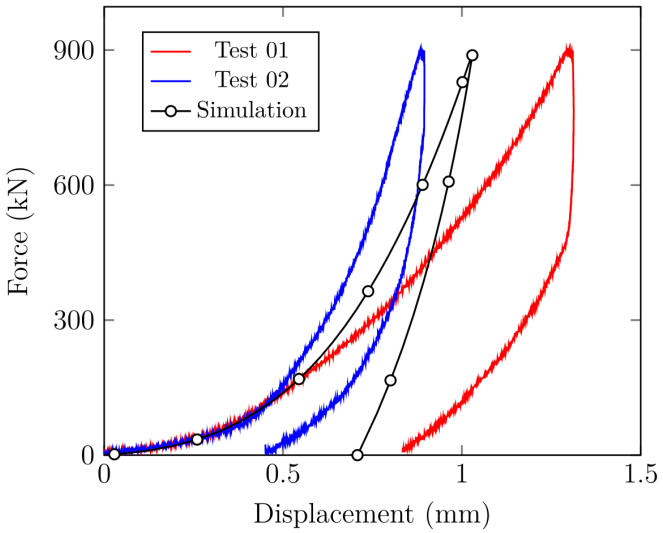

Figure 4.14: Test series S04: comparisons between experimental and numerical force - displacement diagrams of a masonry wall subjected to uniaxial compression loading/unloading in the direction normal to head joints.

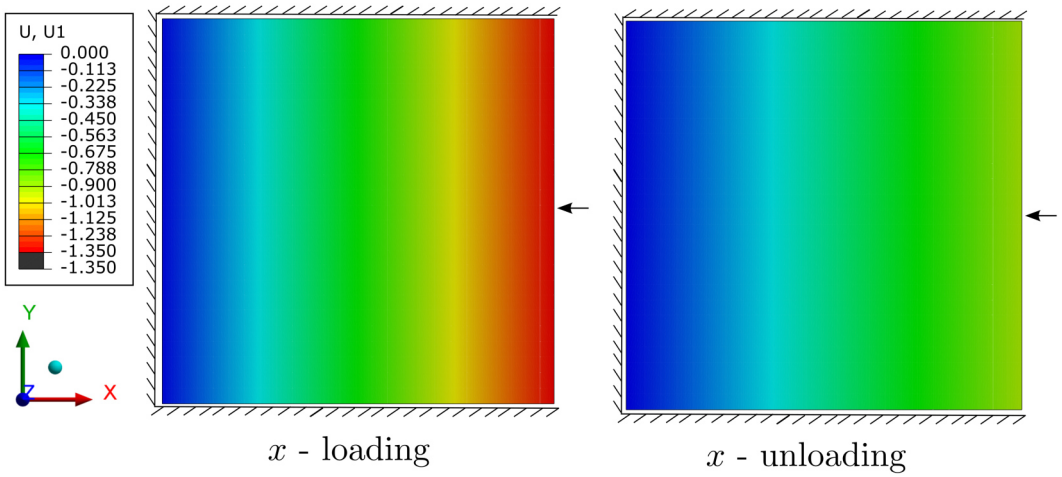

Figure 4.15: Test series S04: displacement fields (in mm), in the direction normal to head joints, of a masonry wall subjected to uniaxial compression loading/unloading in the direction normal to head joints (x direction) at maximum load level (left) and after load removal (right).

4.1.5 S05: biaxial loading and unloading at room temperature

In this test series, two refractory masonry walls with $1100 \times 1125 \times 140$ mm^3 dimensions were tested at room temperature. A 6 MPa biaxial compression load/unload was applied to the directions normal to bed and head joints. The FE model of the wall is similar to that presented in Fig. 4.11. The interactions between the contact surfaces of the wall, the plungers and the ground

were considered in the FE model using frictional contact. The boundary conditions of the ground and the two fixed rigid plates are set to fully fixed.

Comparisons between the experimental and numerical force - displacement diagrams in the directions normal to bed and head joints during loading and unloading are presented in Fig. 4.16. It can be seen that the present numerical model can reproduce with reasonable accuracy the orthotropic displacement stiffening mechanical behavior of the wall. The reaction force increases with the increase in the displacement due to the gradual closure of the joints and the increase in material stiffness with gradual closure of joints. The maximum displacement in the direction normal to head joints is smaller as compared to that in the direction normal to bed joints, because the number of head joints is less than the number of bed joints.

The displacement fields in the direction normal to bed and head joints at maximum load level and after load removal are given in Fig. 4.17. The arrows indicate the locations of the moving plungers (in the x and y directions) and the lines denote the positions of the two fixed rigid plates. After unloading, the wall did not return to the initial configuration and there was permanent deformation in both directions caused by gradual closure of joints, the deformation and the crushing of the asperities present at the contact surfaces of bed and head joints.

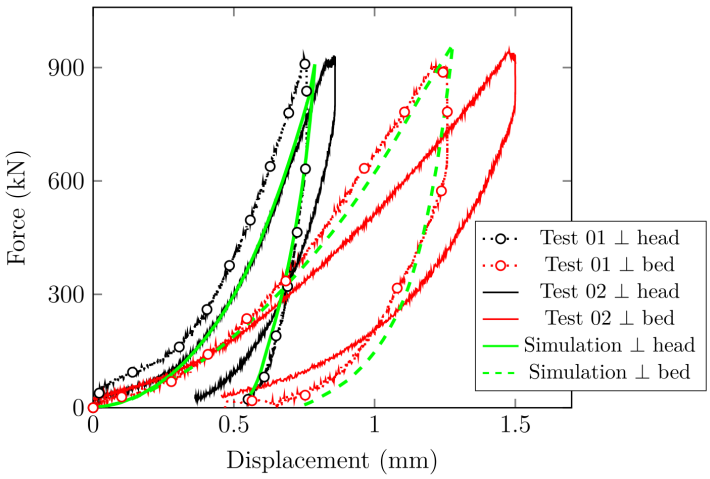

Figure 4.16: Test series S05: comparisons between experimental and numerical force - displacement diagrams of the masonry walls subjected to biaxial compression loading/unloading in the directions normal to bed and head joints.

4.1.6 S06 and S07: uniaxial creep behavior - normal to bed joints

Test series S06 was the first high temperature test and it includes only one test (S06-01). The main goal of this trial series was to test the high temperature test setup. Time variations of the wall's cold (CF) and hot (HF) faces temperatures during heating and testing are presented in Fig. 4.18. It can be seen that the temperature of the HF did not reach the desired value (1500 °C) due to low heating power provided by the heating system, high heat capacity of wall and the test

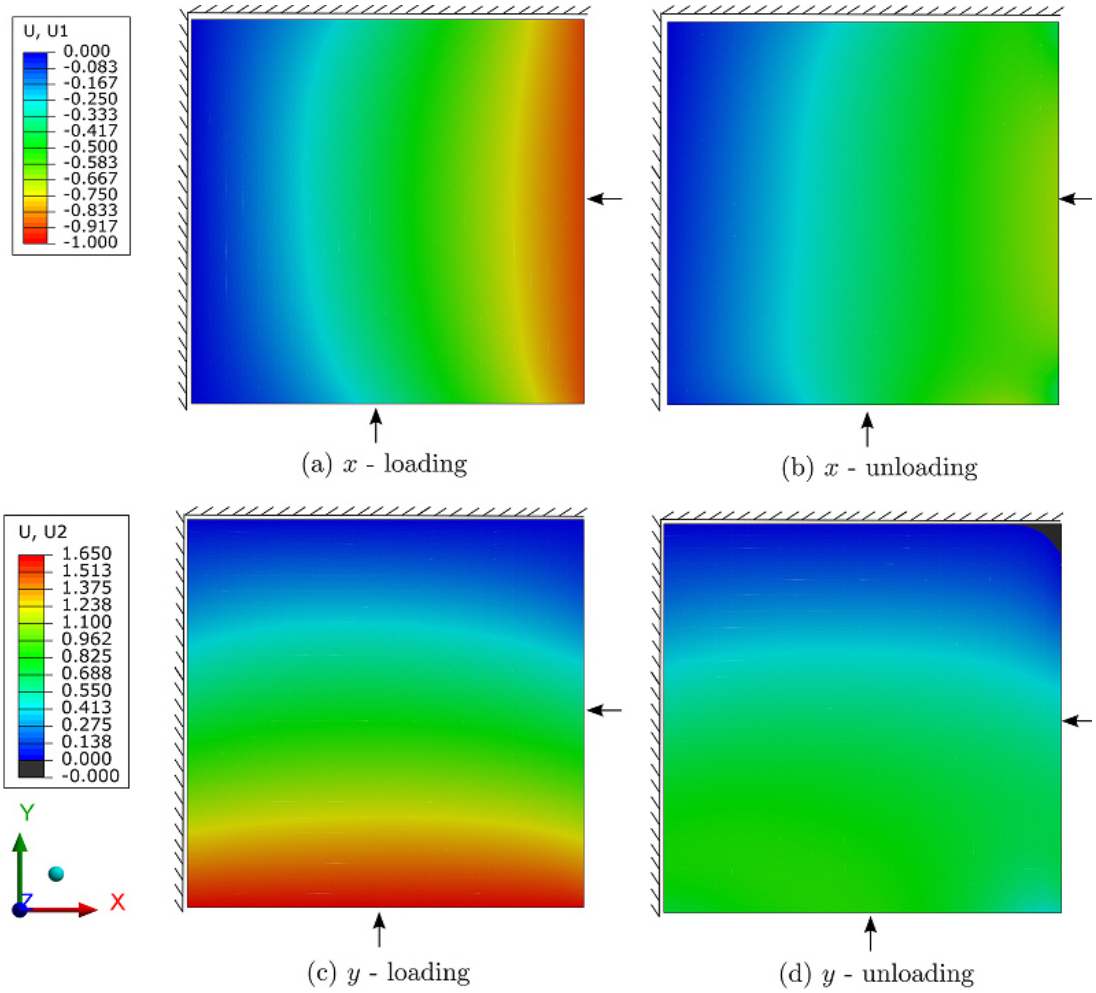

Figure 4.17: Test series S05: displacement fields (in mm) in the direction normal to head joints (x direction, a and b) and in the direction normal to bed joints (y direction, c and d) at maximum load level (left) and after unloading (right) in the masonry walls subjected to biaxial compression loading/unloading.

setup, and high heat losses (from the heating hood to the ambient and the sides of the wall to the water cooled plungers). The solid black lines in the figure represent the values measured by the thermocouples.

The FE analysis of the wall compromises two steps: firstly, transient heat transfer analysis to compute the temperature distributions and variations with time and secondly, transient thermo-mechanical analysis to compute the thermomechanical stress and strain fields. The temperature fields calculated in the first step were used as a temperature load in the thermomechanical analysis. The heat transfer and thermomechanical FE models of the wall were developed using Abaqus. The physical model of the wall is similar to that of S03 (see Fig. 4.11). The average measured temperature variations with time of the HF and CF are applied as thermal boundary conditions in the heat transfer analysis. Therefore, the computed temperatures of the HF and the CF are the same as the applied temperature boundary conditions. The goal was to obtain the temperature fields through the thickness of the wall. The thermo-physical properties of the material used for the heat transfer analysis are reported in chapter 2. Comparisons between the

experimental and numerical CF and HF temperature variations with time are given in Fig. 4.18.

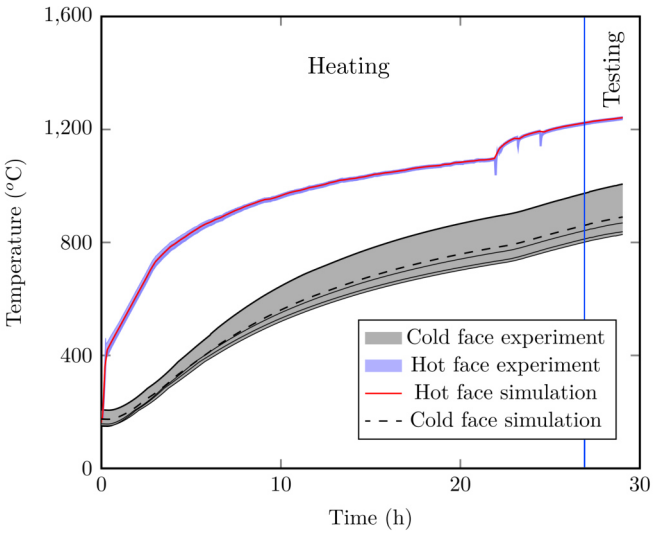

Figure 4.18: Test series S06: time variations of the cold and hot faces temperatures during heating and testing, experimental and numerical results.

Regarding the thermomechanical analysis, the four ceramic plates, as well as the top insulation layer (ground) of the test setup have been modeled as rigid plates. The wall (bricks and joints) was replaced by a homogeneous material whose mechanical properties vary with the gradual closure and reopening of the joints. The frictional interactions between the contact surfaces of the wall and the fixed, moving rigid plates and the ground were considered (coefficient of friction of 0.5). During heating, load application and load holding steps, the boundary conditions of two fixed rigid plates and the ground were set to fully fixed. During heating, the two moving rigid plates were free to move then, during load application and load holding steps, the measured experimental reaction forces were applied as concentrated loads to the moving rigid plates.

Comparisons between the experimental and numerical displacement – time diagrams during the loading and holding steps are given in Fig. 4.19-a. Good agreements between the experimental and numerical results were obtained. During loading, a steady increase in the displacement can be observed. Then, during the holding step, a slight increase in the displacement can be observed due to creep. The measured displacements (in the case of S06) are higher as compared to S03 due to the low values of Young's modulus at high temperature and creep. The joints patterns in the wall by the end of the load holding step are presented in Fig. 4.19-b. The words fixed indicate the locations of the fixed plungers and the arrows denote the moving plungers. Near the HF, all bed joints are closed and all head joints are still open (pattern HO). On the other hand, near the CF, all bed and head joints are open (pattern AO).

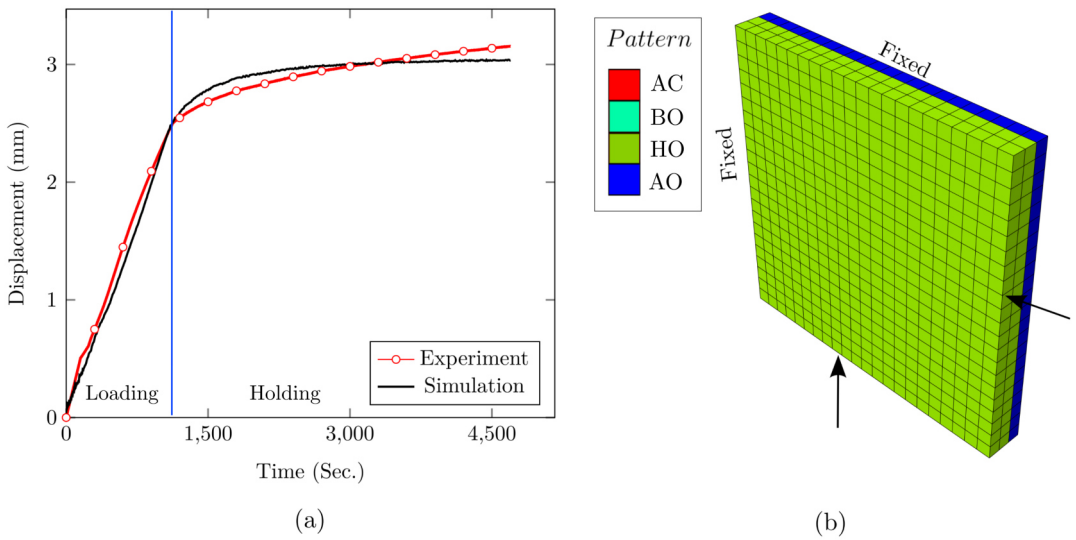

Figure 4.19: Test series S06: (a) experimental and numerical time variations of the displacement in the direction normal to bed joints. (b) Joint patterns in the wall by the end of load holding step.

Regarding test series S07, it was possible to heat the wall to the desired temperature (1500 °C) after adjusting the electrical configurations of the heating system, increasing the input power and improving the insulation of the experimental setup. The modeling technique of S07 is similar to that of S06. In the transient heat transfer analysis, the average measured temperature variations with time of the CF and HF were applied as thermal boundary conditions. Therefore, the computed temperatures of the HF and the CF are the same as the applied temperature boundary conditions. The goal was to obtain the temperature fields through the thickness of the wall during heating, load application, holding and unloading steps. These, in turn, are employed as thermal fields for the thermomechanical analysis. Comparisons between the experimental and numerical HF and CF temperature variations with time are given in Fig. 4.20. The five solid black lines represent the temperatures measured by the thermocouples in contact with the CF.

The solution domain (shown in Fig. 4.11) and the mechanical boundary conditions of the ground, fixed and moving plungers are similar to those of S06. The temperature fields of the wall as well as the deformed shape, by the end of the heating step, due to thermal expansion effects are given in Fig. 4.21. Higher values of thermal expansion near the HF as compared to the CF can be observed from the figure due to the higher temperature of the HF. As a result, the sides of the wall (in contact with the moving and fixed plungers), were not perfectly parallel to the plunger linings (wedged shape, in the depth of the wall) before the load application.

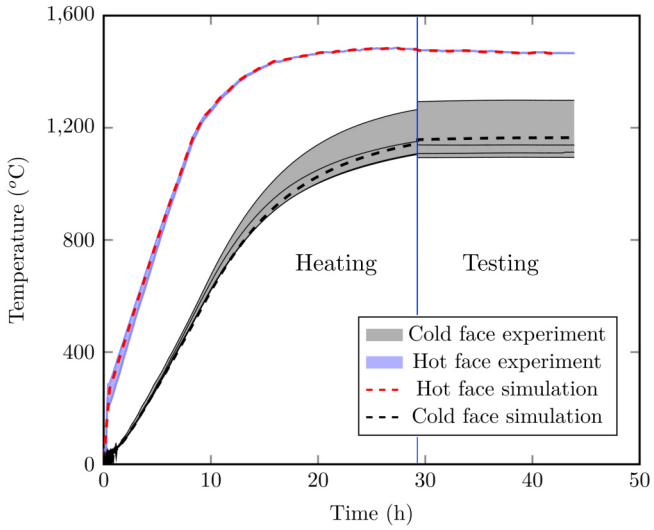

Figure 4.20: Test series S07: time variations of the cold and hot faces temperatures during heating and mechanical testing, experimental and numerical results.

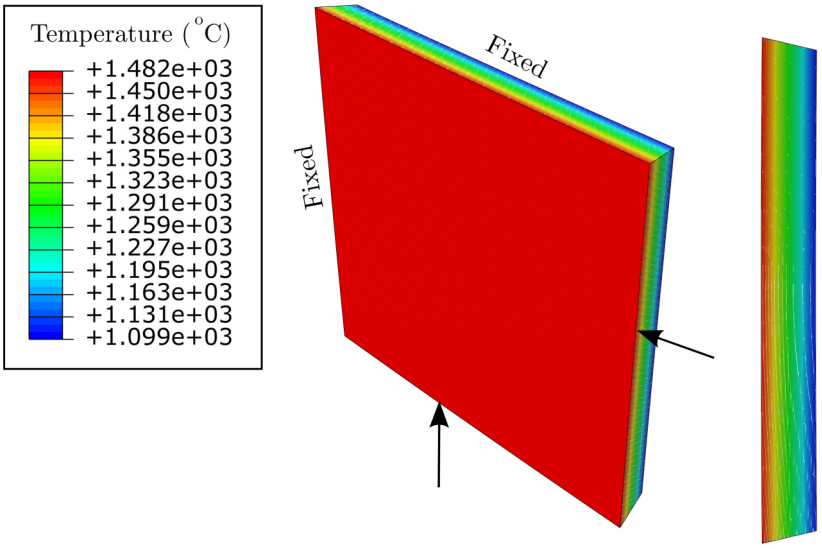

Figure 4.21: Test series S07: temperature distributions of the masonry wall by the end of heating step showing the deformation of the wall due to thermal expansion.

Figure 4.22-a presents comparisons between the experimental and numerical displacement - time diagrams during loading, holding and unloading steps. Good agreements between the numerical and the experimental results (the two performed tests in red) can be observed. During loading, a fast increase in the displacement can be observed due to gradual closure of joints with increasing the applied load. Then, during the holding step, an increase in the displacement can be observed due to creep. Finally, the displacement decreased slightly during the unloading step. After load removal, the recovered displacement was very small as compared to the displacement due to the applied load. This can be attributed to the permanent deformation resulting from the viscoplastic behavior of the structure and joints closure. By the end of the load application step,

the displacement value is higher as compared to series S06 due to the high bulk temperature of the specimen and, therefore, lower values of Young's modulus and higher creep rates as compared to series S06.

Figure 4.22-b shows an example of time variations of the stresses (from the end of heating step to the end of unloading step) in the direction normal to bed joints (σ_{bed}), 15 millimeters from the HF and the CF. By the start of the loading step, the HF carries almost all the applied load due to the wedged deformed shape of the wall (shown in Fig. 4.21) caused by the thermal expansion and the temperature gradient through the thickness of the wall. With the increase of the applied load and the deformation of the zone near the HF, the contact area between the moving plungers and the sides of the wall started to increase and, therefore, the stresses in the CF as well. After reaching the maximum load level and due to the lower creep rate in the CF (due to the lower temperature) as compared to the HF, a decay in σ_{bed} HF was observed due to stress relaxation. On the other hand, an increase in the σ_{bed} CF was observed and, then, remained almost constant during the holding time.

The joints pattern in the wall and the displacement in the loading direction (normal to bed joints) by the end of the holding step are presented in Fig. 4.23. In the HF, almost all bed and head joints are closed (pattern AC). The closure of head joints is caused by the Poisson's effects and the creep (in direction normal to the loading direction). In the CF, almost all bed and head joints were closed while some head joints remained open (patterns AC and HO).

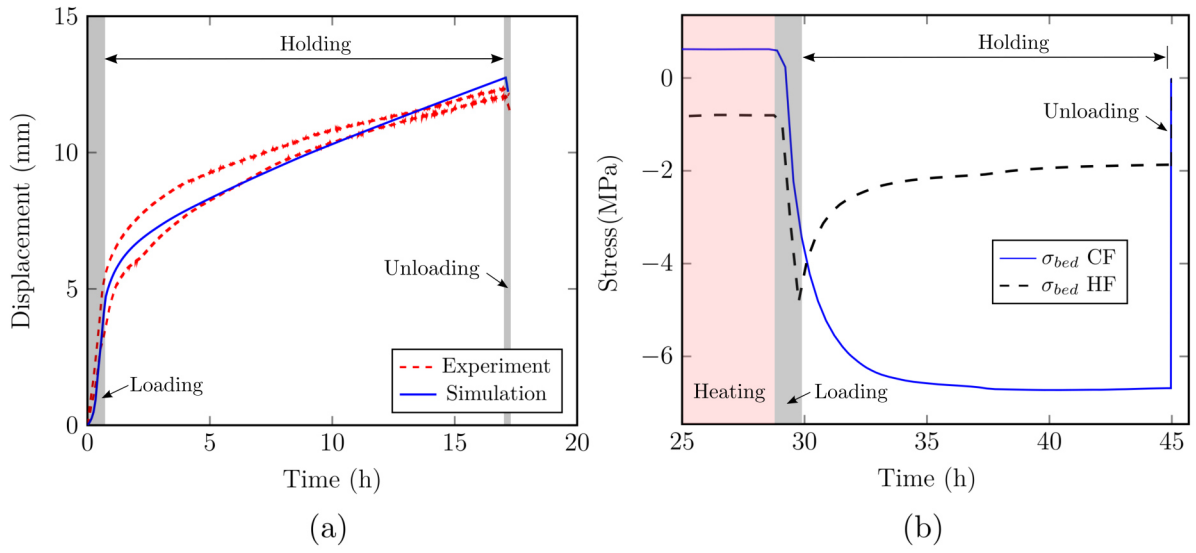

Figure 4.22: Test series S07: time variations of (a) displacements and (b) stresses in the masonry walls subjected to uniaxial creep load at 1500 °C in the direction normal to bed joints.

4.1.7 S08: uniaxial creep behavior - normal to head joints

The major difference between S08 and S07 is that the uniaxial compression load was applied to the direction normal to head joints while the other direction was constrained by the ceramic plungers (direction normal to bed joints). The modeling technique of S08 is similar to that of

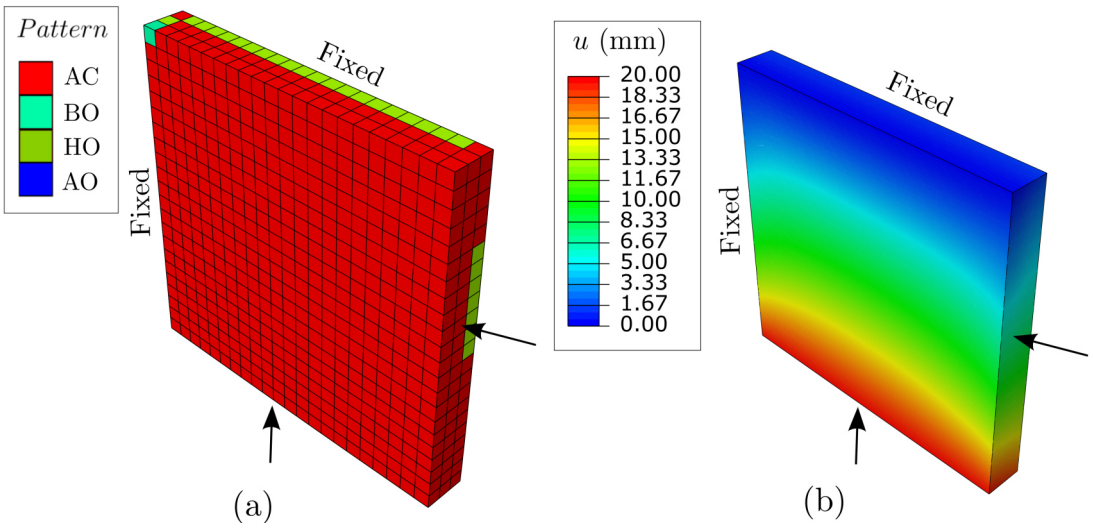

Figure 4.23: Test series S07: (a) joints patterns and (b) displacement fields in the direction normal to bed joints (vertical direction in this image) in a masonry wall subjected to uniaxial compression creep load at 1500 °C by the end of the holding step.

S07. Firstly, transient heat transfer analysis have been carried out to compute the temperature fields of the wall during heating, load application, load holding and unloading. Secondly, the temperature fields are employed as thermal fields for the thermomechanical analysis. The temperature variations with time of the CF and HF are similar to those reported in Fig. 4.20 (also in the case of S09 and S10 reported below, its similar). The temperature fields of the wall as well as the deformed shape, by the end of the heating step, due to thermal expansion effects are similar to those reported in Fig. 4.21 (also in the case of S09 and S10 reported below, its similar).

The physical model of the thermomechanical analysis is the same as that reported in Fig. 4.11. The four ceramic plates, as well as the top insulation layer (ground) of the test setup have been modeled as rigid plates. The frictional interactions between the contact surfaces of the wall and the fixed, moving rigid plates and the ground were considered. During heating, load application and load holding steps, the boundary conditions of two fixed rigid plates and the ground are set to fully fixed. During heating, the two moving rigid plates were free to move then, during load application, load holding and unloading steps, the measured experimental reaction forces were applied as concentrated loads to the moving rigid plates.

Comparisons between the experimental and numerical displacement - time diagrams during loading, holding and unloading steps are given in Fig. 4.24-a. As the test was performed once, the displacements measured by the three LVDTs are given (three red lines). Good agreements between the numerical and the experimental results can be observed. During loading, a fast increase in the displacement can be seen due to the gradual closure of joints with increasing the applied load. Then, during the holding step, an increase in the displacement can be observed due to creep. Finally, the displacement decreased slightly due to unloading. After load removal, the recovered displacement is very small as compared to the displacement measured during load

application step. This is caused by the viscoplastic deformation and closure of joints.

As compared to S04, higher values of the displacement can be observed due to the lower values of Young's modulus at high temperature and viscoplasticity. It should be noted that in case of test series S07 and test series S08, the increase in the displacement during the holding time is almost equal. This can be attributed to that, in both cases, after load application the joints in the loading directions (bed joints in the case of S07 and head joints in the case of S08) are almost closed and, as explained in chapter 3, when joints are closed the behavior of the wall is similar to that of the bricks (i.e. similar behavior in both cases).

An example of the time variations of the stresses (from the end of the heating step to the end of the unloading step) in the CF and HF in the direction normal to head joints (σ_{head}) are reported in Fig. 4.24-b. As compared to S08, similar trends of σ_{head} CF and σ_{head} HF can be observed. These trends can be explained in a similar way to that of series S07 (more details are reported above, section 4.1.6). The joints patterns in the wall and the displacement in the loading direction (normal to head joints) by the end of the holding step are presented in Fig. 4.25. In the HF and CF, almost all head joints are closed (pattern BO). Some bed joints near the moving plunger (perpendicular to the loading direction) are closed (pattern AC). These joints closed due to the applied reaction force (that was measured in the experiment) in the direction normal to bed joints.

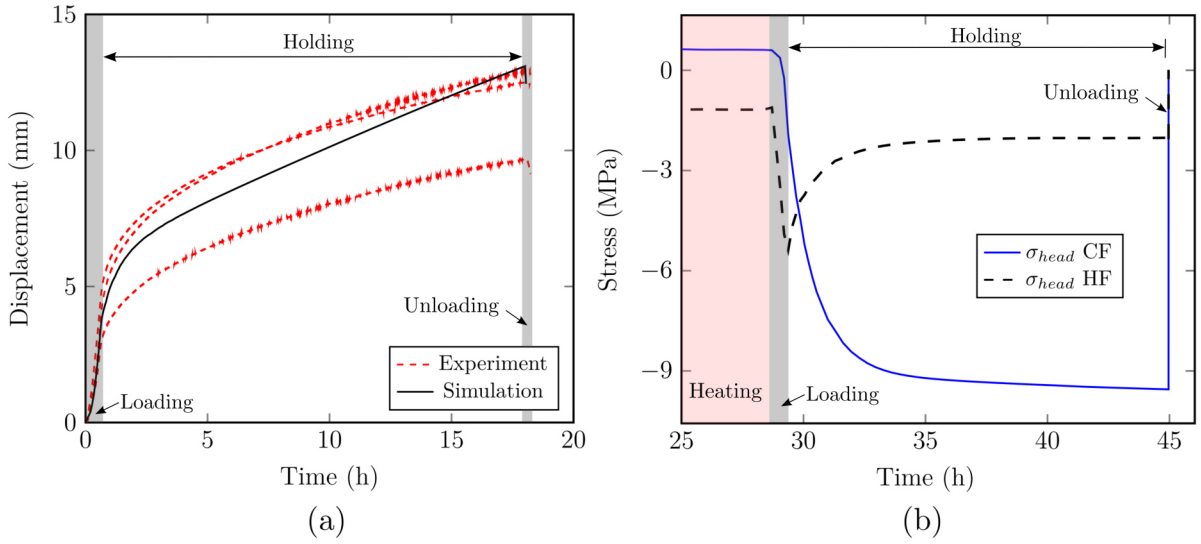

Figure 4.24: Test series S08: time variations of (a) displacements and (b) stresses in the masonry wall subjected to uniaxial creep load at 1500 °C in the direction normal to head joints.

4.1.8 S09: biaxial creep behavior

In this test series, two refractory masonry walls with 1100 × 1125 × 140 mm^3 dimensions were tested at high temperature. The modeling technique of S09 is similar to that of S07 and S08. Transient heat transfer analysis have been carried out to compute the temperature fields during heating and testing. Then, the temperature fields are employed as thermal loads in the transient

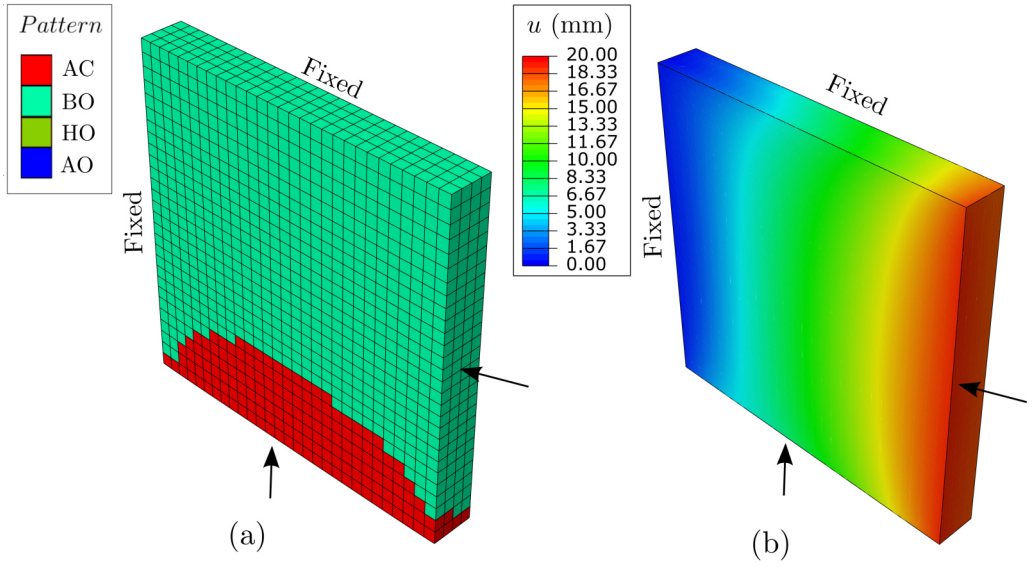

Figure 4.25: Test series S08: (a) joints patterns and (b) displacement fields in the direction normal to head joints (horizontal direction in this image) in a masonry wall subjected to uniaxial compression creep load at 1500 °C by the end of the holding step.

thermomechanical analysis. The physical model of the thermomechanical analysis is the same as that reported in Fig. 4.11. During heating, load application, load holding and unloading steps, the boundary conditions of two fixed rigid plates and the ground are set to fully fixed. During heating, the two moving rigid plates were free to move then, during load application, load holding and unloading steps, the measured experimental reaction forces, in both directions, were applied as concentrated loads to the moving rigid plates.

Comparisons between the experimental and numerical displacement – time diagrams in the directions normal to bed and head joints during loading, holding and unloading steps are shown in Fig. 4.26-a. Good agreements between the experimental and numerical results can be observed. During load application step, and for both directions, an increase in the displacement due to the gradual closure of joints can be observed. The maximum displacement in the direction normal to bed joints is higher as compared to that in the direction normal to head joints due to the difference between the number of bed and head joints in the wall.

An example of the time variations of the stresses (from the end of heating step to the end of unloading step) in the CF and HF in the direction normal to bed and head joints (σ_{bed} and σ_{head}) are reported in Fig. 4.26-b. As compared to S07 and S08, similar trends of σ_{bed} CF, HF and σ_{head} CF, HF can be observed. These trends can be explained in a similar way to that of series S07 (more details are reported above, section 4.1.6). The displacement in the loading directions and the joints patterns in the wall by the end of the holding step are shown in Figs. 4.27 and 4.28, respectively. In the HF and CF, most of bed and head joints are closed (pattern AC). Some open bed and head joints near the fixed plungers can be seen.

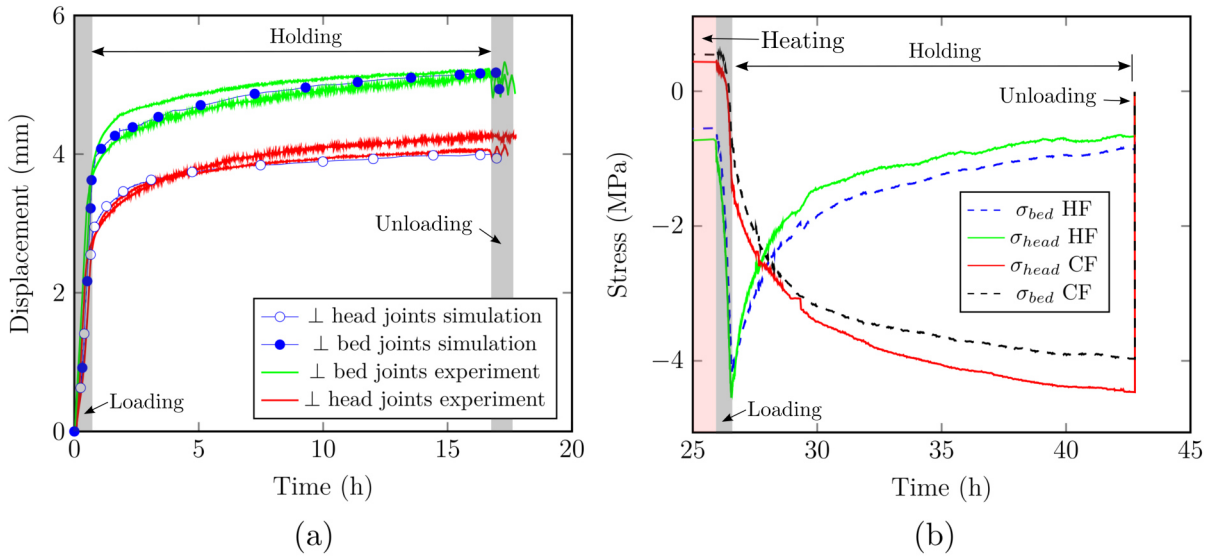

Figure 4.26: Test series S09: time variations of (a) the displacement and (b) the stresses in the masonry walls subjected to biaxial creep load at 1500 °C.

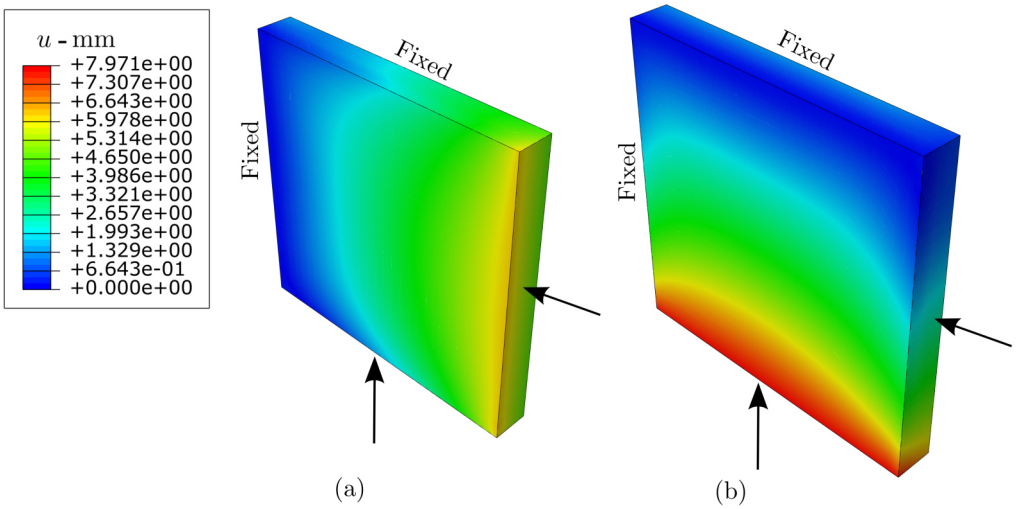

Figure 4.27: Test series S09: displacement fields in a masonry wall subjected to biaxial compression creep load: (a) in the direction normal to head joints (horizontal direction in this image) and (b) in the direction normal to bed joints (vertical direction in this image) by the end of the holding step.

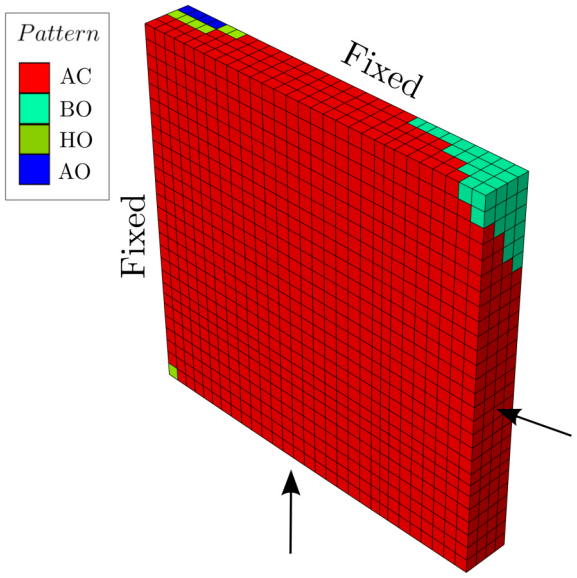

Figure 4.28: Test series S09: joints patterns in a masonry wall subjected to biaxial compression creep load at 1500 °C by the end of the holding step.

4.1.9 S10: biaxial relaxation behavior

The goal of test series S10 was to investigate the relaxation behavior of the wall (constant strain loading conditions). The modeling technique is similar to that of S07, S08 and S09 (transient heat transfer analysis then, transient thermomechanical analysis). The physical model of the thermomechanical analysis is the same as that reported in Fig. 4.11. During heating, the mechanical boundary conditions of the plungers and the ground are similar to those of S09. During loading, the boundary conditions are almost the same as S09 with only one difference, displacement boundary conditions were applied to the moving plungers and kept constant during the holding time.

Comparisons between the experimental and numerical time variations of the resulting reaction forces, in the directions normal to bed and head joints, during the two loading cycles are reported in Fig. 4.29. During loading (1^{st} cycle), the resulting reaction forces increased gradually to reach around 600 kN. Then, when the position of the plungers is locked, a decay in the resulting reaction forces was observed due to the relaxation behavior of the wall. In the beginning of the holding stage, a significant decrease in the reaction forces can be observed. Similar behavior was noticed for both loading cycles.

The joints patterns in the wall by the end of the holding step and after unloading of the two loading cycles are presented in Fig. 4.30. It can be seen that some joints reopen after unloading. In addition, the percentage of the closed joints in the second loading cycle (Fig. 4.30-c) is higher as compared to that of the first loading cycle (Fig. 4.30-a). This can be attributed to the higher load applied to the wall in the second loading cycle as compared to that of the first loading cycle.

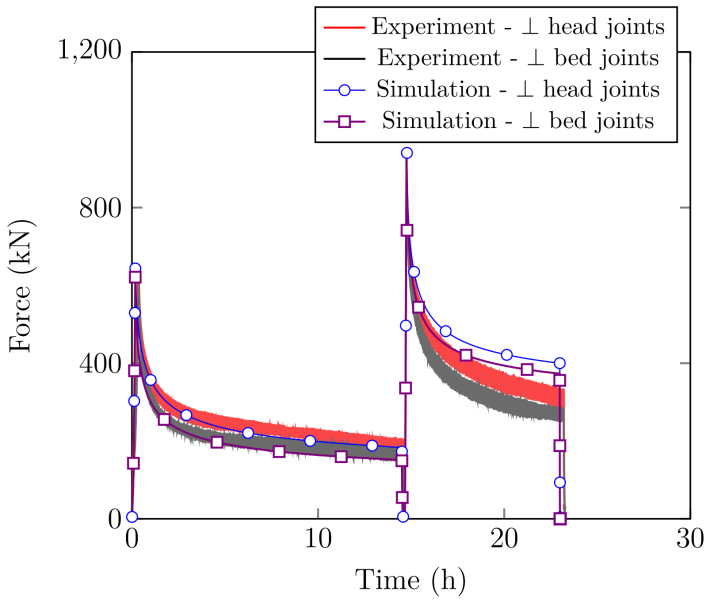

Figure 4.29: Test series S10: time variations of reaction forces, in the directions normal to bed and head joints, in a masonry wall subjected to a biaxial relaxation loading conditions at 1500 °C.

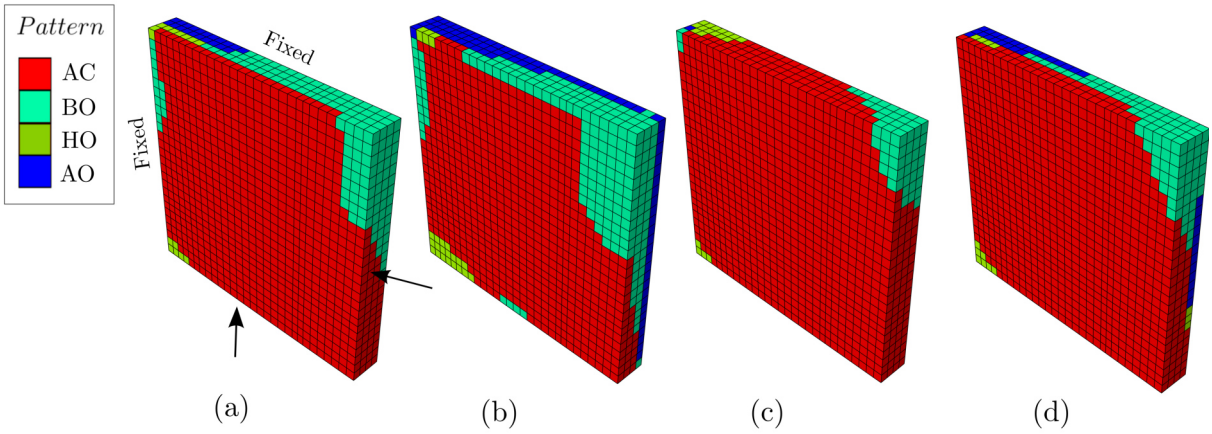

Figure 4.30: Test series S10: joints patterns in a masonry wall subjected to biaxial relaxation: (a) after first loading, (b) after first unloading, (c) after second loading and (d) after second unloading.

4.2 Masonry with mortar joints

In order to validate the current models, comparative studies with numerical and experimental results available in the literature were performed. Traditionally, the experimental results of two specific tests of masonry walls are widely used by the masonry community for the calibration of the numerical models. The two tests are: masonry subjected to in-plane shear performed by Raijmakers and Vermeltfoort [11] and masonry subjected to bending load (also called deep beam tests) carried out by Page [12]. Both experimental tests were carried out at room temperature.

Therefore, in the present multi scale model, the mechanical behavior of the base material of the bricks and the mortar is assumed elastic whereas, the behavior of the brick/mortar interface is damageable.

4.2.1 Masonry subjected to in-plane shear load

Schematic of the masonry wall with mortar joints subjected to combinations of uniaxial pre-compression and shear loading are depicted in Fig. 4.31 [11]. Solid clay bricks with length of 210 mm, height of 100 mm and depth of 52 mm were periodically arranged in a running bond texture. The thickness of the mortar joints was 10 mm. The size of the wall was $1000 \times 990 \times 52\ mm^3$ and it was made up of 18 courses, 16 of them were active and 2 were fixed to the stiff steel beams (the 2 courses in contact with the steel beams, the top and bottom ones, see Fig. 4.31). The mechanical parameters of the bricks, the mortar and the brick/mortar interface are reported in table 4.3. The testing procedures were as following: first, a pre-compression vertical load of 30 kN (0.3 MPa) was applied to the top steel beam. Then, it has been kept under displacement control and no vertical movements were allowed. Finally, a monotonically increasing horizontal displacement (u_h) was applied to the right surface of the top steel beam. The test was repeated 2 times and, for each test, the force-displacement relationship and the crack patterns were recorded.

Table 4.3: Shear test of masonry walls: mechanical parameters of the bricks, the mortar and the brick/mortar interface [100].

	Y (MPa)	ν	f_t (MPa)	C	$Tan\ \phi$
Brick	16000	0.15		———	
Mortar	800	0.15		———	
Interface	———		0.25	$1.4 \times f_t$	0.75

The finite element model has been developed using Abaqus and the wall has been meshed with 3D hexahedron elements (see Fig. 4.31). The two steel beams were replaced by rigid plates and no relative displacements between the contact surfaces of the rigid plates and the masonry were allowed. The masonry (bricks and mortar joints) was replaced by a homogeneous equivalent material model whose mechanical properties depend on the state of bed and head mortar joints (damaged or undamaged). The effective mechanical parameters of the four joint patterns were computed using the mechanical homogenization technique described in chapter 3 and are reported in table 4.4.

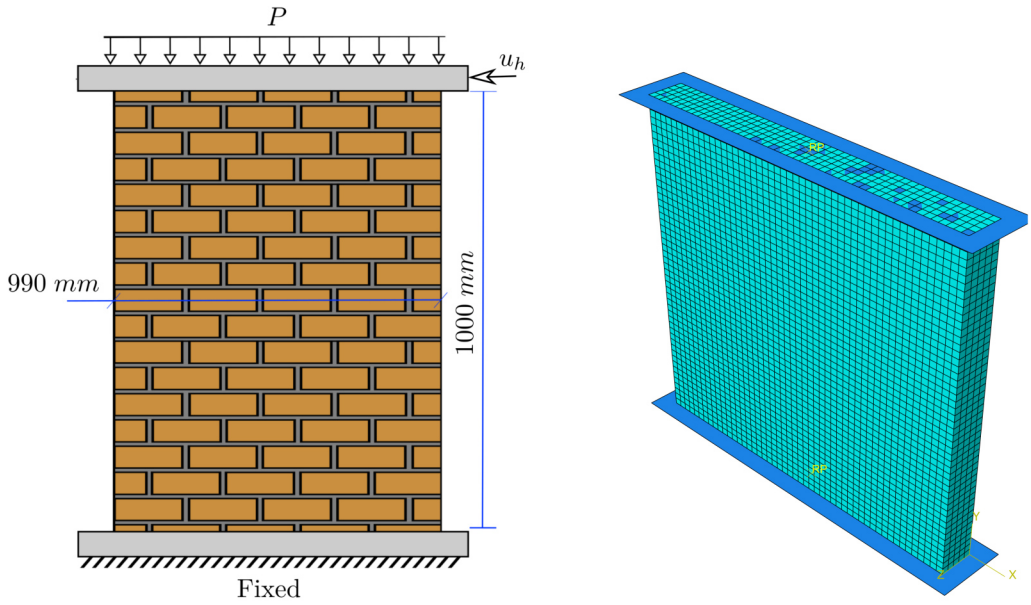

Figure 4.31: Schematic of masonry wall with mortar joints subjected to combination of compression and shear loading (left) [11] and the corresponding 3D FE model (right).

Table 4.4: Shear test of masonry walls: effective elastic parameters of the four joint patterns calculated using FE based homogenization technique.

Pattern	$\overline{\overline{\overline{\overline{C^e}}}}$ (MPa)					
AS	8593	503	1342	0	0	0
		3952	637	0	0	0
			13258	0	0	0
				1590	0	0
		Sym.			1723	0
						3975
BD	8593	0	1342	0	0	0
		1	0	0	0	0
			13258	0	0	0
				1	0	0
		Sym.			1723	0
						3975
HD	4220	358	677	0	0	0
		3856	602	0	0	0
			13226	0	0	0
				1353	0	0
		Sym.			1707	0
						3975
AD	1	0	0	0	0	0
		1	0	0	0	0
			13258	0	0	0
				1	0	0
		Sym.			1723	0
						3975

Comparisons between load displacement diagrams obtained using the present multi scale

model and those obtained by the micro numerical model of Lourenço et al. [159], multi scale numerical model of Marfia and Sacco [160] and experimental data of Raijmakers and Vermeltfoort [11] are reported in Fig. 4.32. It can be noticed that the present multi scale numerical model reproduced, with reasonable accuracy, the mechanical behavior of the masonry structure under combined compression and shear loading. The crack patterns of the two experimental tests and those obtained using the present multi-scale numerical model are presented in Fig. 4.33. Good agreements between the experimental and numerical results can be observed. Horizontal cracks (through bed joints) at the top and the bottom of the wall as well as a diagonal cracks through bed and head joints can be observed. The diagonal crack appears first at the middle of the wall and then grows in the directions of the steel beam supports. It should be noted that the percentage of damaged joints predicted by the numerical model is higher as compared to the experimental results. Because the experimental crack patterns were investigated using naked eye. That means in case of damaged joints with very small opening (damaged joint thickness), they might not be observed. However, in the numerical model, the damaged joints are captured automatically.

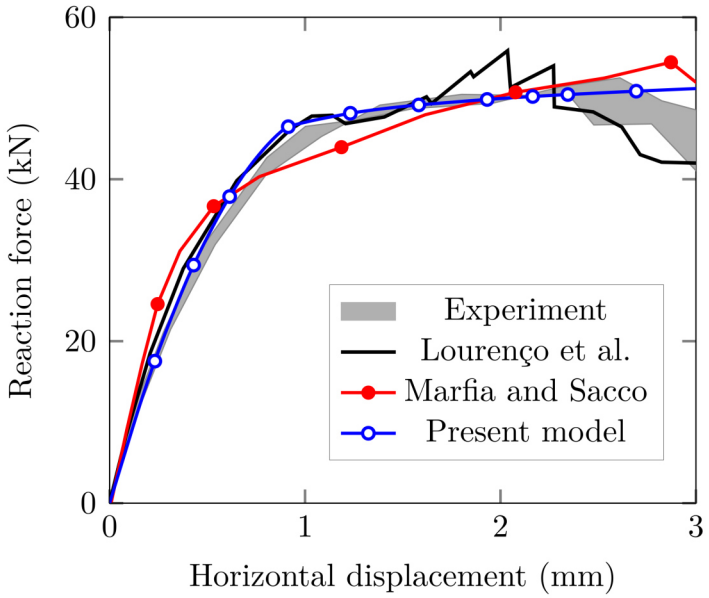

Figure 4.32: Masonry wall subjected to in-plane shear: variations of the horizontal reaction force with the horizontal displacement, experimental and numerical results.

4.2.2 Masonry subjected to bending load

In 1978, Page [12] performed bending tests of masonry walls with mortar joints as described in Fig. 4.34. Pressed solid clay bricks with length of 122 mm, height of 37 mm and depth of 54 mm were periodically arranged in a running bond texture. The thickness of the mortar joints was 5 mm. The mechanical parameters of the bricks, the mortar and the brick/mortar interface are reported in table 4.5. The values of G_{xy} and ν_{xy} of the bricks are 2890 MPa and

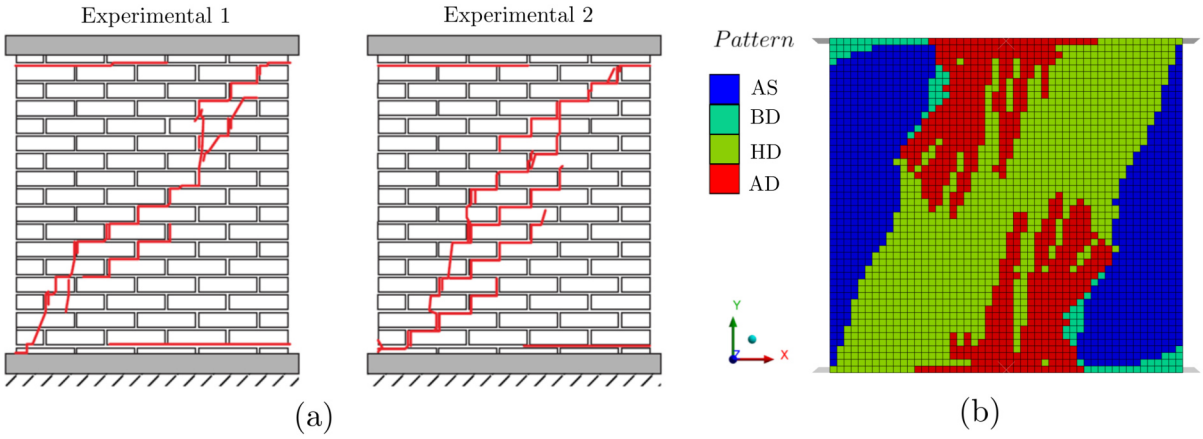

Figure 4.33: Crack patterns in the masonry walls with mortar joints subjected to combination of uniaxial compression and shear loading: (a) experimental [11] and (b) numerical results.

0.167, respectively [100]. $G_{xz} = 2536$ MPa, $G_{yz} = 2864$ MPa and $\nu_{xz} = \nu_{yz} = 0.167$ [100]. A vertical force (P) was applied to the top stiff beam. The experimental force - displacement diagrams were not reported by Page [12]. However, the calculated vertical stress distributions near mid height of the wall are available. In the finite element model, no relative displacements between the supports and the wall were allowed and the masonry wall was meshed with 3D hexahedron elements (see Fig. 4.34). The masonry (bricks and mortar joints) was replaced by a homogeneous equivalent material model whose mechanical properties depend on the state of bed and head mortar joints (damaged or undamaged). The effective mechanical parameters of the four joint patterns were computed using the mechanical homogenization technique described in chapter 3 and are reported in table 4.6.

Table 4.5: Deep beam test, mechanical parameters of the bricks, the mortar and the brick/mortar interface [100, 161].

	Y_x	Y_y	Y_z	ν	f_t	C	$Tan\,\phi$
Brick	5920	7550	5920	0.167		———	
Mortar	1200	1200	1200	0.21		———	
Interface			———		0.29	$1.4 \times f_t$	0.75

Vertical stress fields in masonry walls subjected to two levels of the vertical force (P) are shown in Fig. 4.35. As can be observed from the figure, two large compression stress arms are present between the two ends of the loading steel beam and the supports. The maximum values of compressive stresses are found near the ends of the loading beam and the supports. Comparisons between vertical stresses distribution obtained using the present numerical model and those obtained by the micro numerical model of Lourenço [100], homogenized model of Lopez et al. [161] and experimental data of Page [12] are reported in Fig. 4.36. Good predictions of the experimental behavior were obtained by the present multi-scale numerical model. The predicted crack patterns are reported in Fig. 4.37. The experimental crack patterns were not recorded. Tensile failure of head joints in the lower course of the masonry (between the two

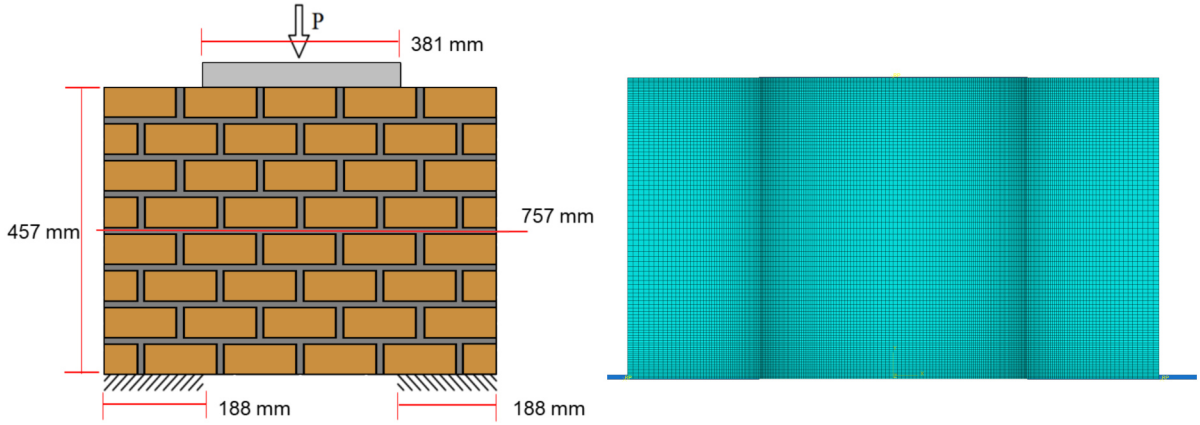

Figure 4.34: Schematic of masonry wall with mortar joints subjected to bending: geometry, boundary conditions [100] and finite element model.

Table 4.6: Deep beam test, effective elastic parameters of the four joint patterns.

Pattern	$\overline{\overline{C^e}}$ (MPa)					
AS	5095	954	999	0	0	0
		4938	862	0	0	0
			5485	0	0	0
		Sym.		1698	0	0
					1783	0
						2042
BD	4910	0	999	0	0	0
		1	0	0	0	0
			5485	0	0	0
				1	0	0
		Sym.			1783	0
						2042
HD	2805	589	511	0	0	0
		4803	768	0	0	0
			5339	0	0	0
				1367	0	0
		Sym.			1783	0
						2042
AD	1	0	0	0	0	0
		1	0	0	0	0
			5485	0	0	0
				1	0	0
		Sym.			1783	0
						2042

supports) can be observed. In addition, shear failure of head joints in the two compressive arms can be seen. With the increase of the vertical force (P), the number of damaged joints increases.

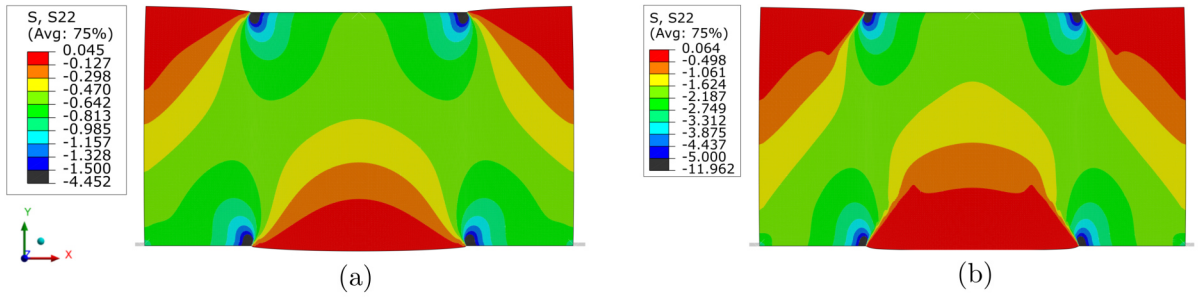

Figure 4.35: Vertical stress fields in a masonry wall subjected to bending load a) vertical force = 20 kN and b) vertical force = 60 kN.

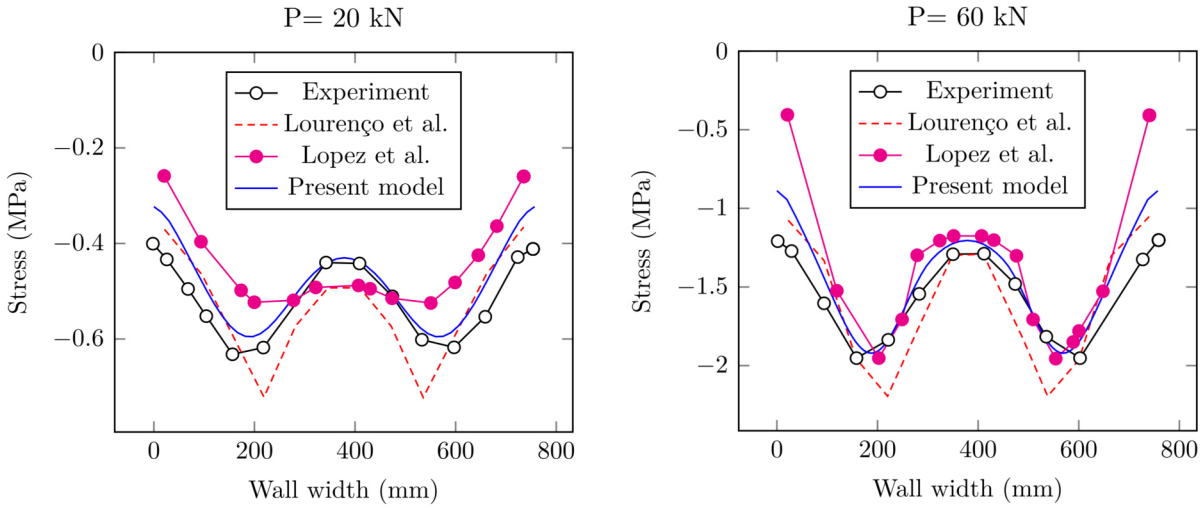

Figure 4.36: Distributions of vertical stresses in a masonry wall subjected to bending: experimental and numerical results.

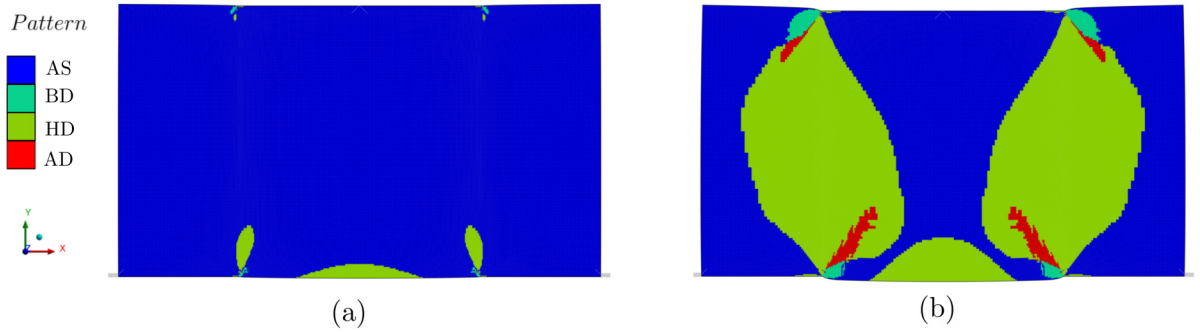

Figure 4.37: Crack patterns in a masonry wall subjected to bending load. (a) vertical force = 20 kN and (b) vertical force = 60 kN.

4.2.3 Masonry with elastic viscoplastic damageable behavior

The focus now is to model masonry structures with mortar joints subjected to bending and to take into account joints opening due to loading and their impact on the elastic viscoplastic behavior of masonry structures (i.e. masonry with elastic viscoplastic damageable behavior). Due to lack

of experimental data of masonry with mortar joints at high temperature, only numerical results are reported here. Schematic of the masonry structure subjected to bending in the y direction as well as the boundary conditions are presented in Fig. 4.34. Refractory bricks with length of 150 mm, height of 76 mm and depth of 50 mm are periodically arranged in a running bond texture. The thickness of the mortar joints is 2 mm. The base material of the bricks is Bauxite based refractories with material parameters reported in chapter 3 (table 3.1). The effective mechanical parameters (elastic and viscoplastic) of the four joint patterns are reported in chapter 3 (table 3.3). Two loading-holding conditions have been considered to predict the creep and stress relaxation behavior of the structure, namely constant displacement load (stress relaxation) and constant force load (creep). The loading and holding steps are as follows: first, displacement or concentrated force load has been applied to the loading beam then, kept constant for a specific time.

Time variations of vertical displacement of point A (see Fig. 4.38-a) in a masonry structure subjected to two levels of force (P), loading then holding, in the vertical direction are presented in Fig. 4.38-a. It can be observed that vertical displacement, in the loading direction, increases instantaneously due to load application, then increases at constant rate due to creep. In addition, the displacement increases with the increase of the applied force (P), because the viscoplastic strain rate increases with the increase of the stress (i.e. force). Time variations of vertical reaction forces in a masonry wall subjected to two levels of strain rate, loading then holding, in the vertical direction are presented in Fig. 4.38-b. It can be seen that the vertical reaction force increases to reach the peak by the end of loading step. Then, during the holding step, it decreases due to stress relaxation in the structure.

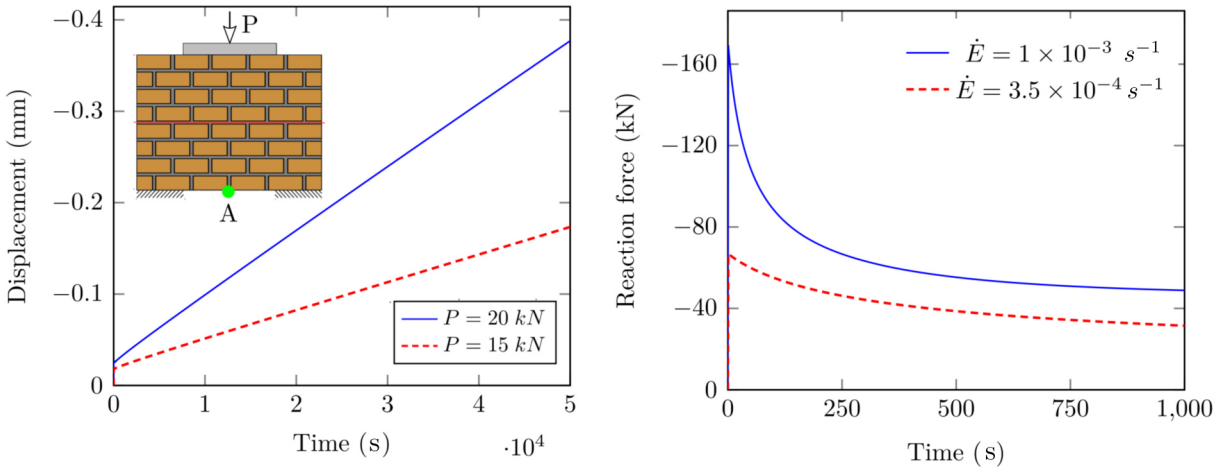

(a) Creep (b) Relaxation

Figure 4.38: Time variations of: (a) vertical displacement of point A in a masonry subjected to force loading and holding and (b) vertical reaction force of the loading beam in a masonry wall subjected to strain rate loading and holding.

Examples of the predicted crack patterns, by the end of the loading and holding steps, of the two simulated cases (creep and relaxation) are reported in Fig. 4.39. In both cases, tensile failure

of head joints in the lower course of the masonry (between the two supports) can be seen. In addition, shear failure of head joints (near the end of the two fixed supports) was observed. In the case of constant force loading (creep), a significant increase in the number of the damaged joints, by the end of the holding step (see Fig. 4.39-b), was observed as compared to the end of load application step (see Fig. 4.39-a) due to creep. On the other hand, a negligible increase was observed in the second loading case (relaxation) due to stress relaxation. It should by noted that, in the case of relaxation simulation and by the end of the loading stage, the number of open joints is higher as compared to the creep simulation, because the resulting reaction forces due to the applied strain rate (around 70 kN, see Fig. 4.38-b) was higher as compared to the applied load in the creep simulation (20 kN).

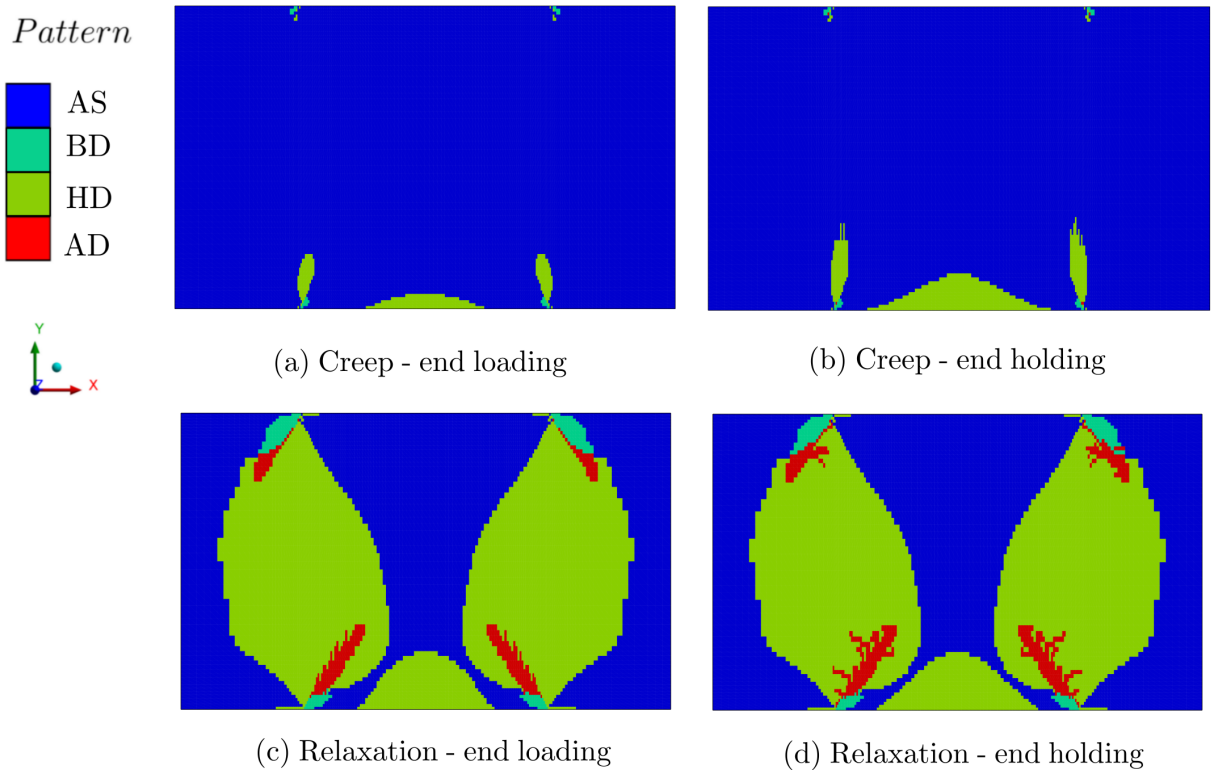

Figure 4.39: Crack patterns in a masonry subjected to: (a and b) constant force (20 kN) loading and holding in the vertical direction (y direction) and (c and d) constant strain rate ($\dot{E} = 3.5 \times 10^{-4}$) loading and holding in the vertical direction.

4.3 Conclusion

This chapter was devoted to the validation of the developed multi scale numerical models of masonry with dry or mortar joints presented previously in chapter 3. The multi scale numerical model of masonry with dry joints has been used to predict the mechanical behavior of alumina spinel refractory masonry subjected to a wide range of loading conditions including: uniaxial compression in the direction normal to bed joints at room and high temperature, uniaxial compression in the direction normal to head joints at room and high temperature and biaxial

compression at room and high temperature. It has been shown that the developed numerical model can reproduce with reasonable accuracy the nonlinear orthotropic elastic viscoplastic behavior of masonry with dry joints and accounts for gradual closure of joints and joints reopening. The multi scale model of masonry with mortar joints has been employed to simulate masonry walls subjected to in-plane shear and bending loads. With reasonable accuracy, the present model was able to predict the mechanical response of the studied cases. The validated models of masonry with dry and mortar joints will be employed later in chapter 5 to simulate and investigate the transient thermomechanical response of an industrial scale steel ladle.

CHAPTER 5

TRANSIENT NONLINEAR THERMO-MECHANICAL MODELING OF A STEEL LADLE

The present chapter is dedicated to transient nonlinear thermo-mechanical modeling of an industrial steel ladle. The constitutive material models of masonry with dry or mortar joints developed in chapter 3, validated in chapter 4 were used to represent the different masonry linings in the steel ladle. Details about the physical model of the studied ladle, materials and masonry type used for each linings are given in section 5.1. Descriptions of a typical thermal cycle of steel ladles and related cyclic thermal heating and cooling are presented in section 5.2. Details about the transient heat transfer analysis of the steel ladle and related thermal boundary conditions, governing equations and mechanical boundary conditions are described in section 5.3. The results and discussions of the transient heat transfer and thermomechanical analysis are presented in section 5.4. The conclusion of the present chapter is given in section 5.5.

5.1 Physical model and materials

Refractories are the best candidate materials for the steel ladle application due to their low thermal conductivity, thermal, chemical, and mechanical stability at high temperatures. To meet the mechanical, thermal and operational requirements, different refractory layers are used for the construction of the ladle. Each layer has a specific purpose and has unique thermo physical and mechanical properties. In the studied ladle, the different layers include a working lining, a safety lining (also called permanent lining), an insulation layer and a steel shell (see Fig. 5.1). The working lining is made of mortarless refractory masonry. The safety lining is built up with a dense refractory masonry with mortar joints with low thermal conductivity. The insulation layer (with 5 mm thickness) is made of a porous material with very low thermal conductivity.

The mechanical and thermo physical properties of each layer are reported in table 5.1, where ρ is the density, C_p is the specific heat, k is the thermal conductivity, Y is Young's modulus, and

CTE is the coefficient of thermal expansion. The thermo-physical and mechanical properties of the working lining and the bottom are reported in chapter 2 (alumina spinel). For the safety lining, the shear failure criteria of the brick/mortar interface were determined using slanted shear tests (similar to those performed by Brulin et al. [88]). The cohesion of the brick/mortar interface is equal to 0.73 MPa at 20 °C and 1.26 MPa at 600 °C. The internal friction angle is equal to 40° and Young's modulus of the mortar is equal to 1000 MPa (assumed due to lack of data).

Table 5.1: Thermo-physical and mechanical properties of the materials used for the different layers in the studied steel ladle.

Lining	Layer	Properties		References
Steel shell	Steel shell	ρ (kg/m^3)	7840	[129, 131, 138]
		k (W/m.K)	47.3 at 200 °C 42.3 at 350 37.3 at 500 °C	
		C_p (J/kg.K)	530 at 200 °C 666 at 500 °C	
		Y (GPa)	210 at 20 °C 170 at 400 °C	
		CTE (10^{-6}K^{-1})	12	
Safety lining	Bottom and wall bricks (dense layer)	ρ (kg/m^3)	2660	[129, 138]
		k (W/m.K)	2.6 at 400 °C 2.1 at 800 °C 2 at 1200 °C	
		C_p (J/kg.K)	8900 at 200 °C 1144 at 1200 °C	
		Y (GPa)	4.5 at 800 °C 3.5 at 1000 °C 1 at 1200 °C	
		CTE (10^{-6}K^{-1})	6	
Insulation	Bottom and wall insulation (porous layer)	ρ (kg/m^3)	510	[129, 131, 138]
		k (W/m.K)	0.15 at 250 °C 0.25 at 800 °C 0.34 at 1350 °C	
		C_p (J/kg.K)	1047	
		Y (GPa)	0.3	
		CTE (10^{-6} K^{-1})	9	

A typical industrial scale steel ladle has complex geometry and is composed of refractory linings, steel construction components, valves, purging plugs, lifting points, etc. In order to reduce the computational time and, as the main aim of the present work is to analyze the thermomechanical behavior of the refractory linings, some detailed features such as valves, nozzles, and purging plugs have been neglected. In addition, due to the symmetry of the studied ladle, only one quarter has been considered. The simplified physical model of the studied steel

ladle is presented in Fig. 5.1. The height and diameter of the ladle are 5 and 4.6 m, respectively. The thickness of each layer is given in mm and reported in Fig. 5.1 (except the insulation layer, 5 mm between the steel shell and the safety lining).

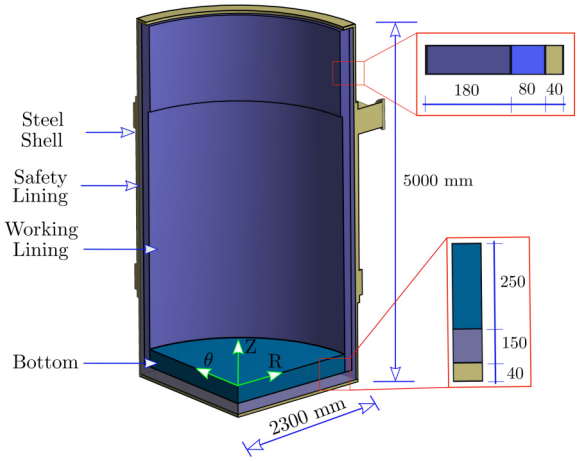

Figure 5.1: Schematic of a simplified steel ladle showing the different layers, all dimensions are in mm. The 5 mm thickness insulation layer is not represented.

5.2 Process description

In the steel industry, steel ladles are used to transport liquid steel from electric arc furnaces or converters to continuous casting machines. In addition, they are used as refining units. While holding liquid steel, other processes occur in parallel such as degassing and alloying. During these processes, the ladle is exposed to different thermal and mechanical operating conditions. A typical thermal cycle of steel ladle refractory linings includes:

- Step 1: preheating the working lining using natural gas burner (to around 1400 °C).
- Step 2: slight temperature decrease due to thermal losses while moving from the preheating device to the converter and waiting for liquid steel tapping.
- Step 3: sudden temperature increase due to tapping liquid steel into the ladle.
- Step 4: gradual temperature drop due to teeming liquid steel out of the ladle, thermal losses during linings check and, if required, linings repair.

Further details on the thermal modeling of the steel ladle thermal cycle, governing equations and boundary conditions of each step are given in section 5.3.

5.3 Thermal and mechanical modeling

During the previously described thermal cycle, the temperature distribution of the ladle varies with time and can be obtained by solving the transient form of the energy equation (equation 4.1). The initial temperature (T_i) of all material layers in the ladle is assumed to be the same as the

ambient temperature. Under this assumption, the initial boundary conditions can be expressed using equation 4.2.

During the first step, a natural gas burner is used to heat the inner surfaces of the ladle from the ambient temperature to around 1400 °C. The time period for this step is around 6.5 h [129]. The dominant heat transfer mode to the lining surfaces is radiation with only conduction occurring within the thickness of the different layers. Modeling radiative heat transfer between the burner and the lining surfaces requires solving the full Navier–Stokes and the energy conservation equations that govern the combustion process. This necessitates long computation time and lies outside the scope of the present work. A simple approach that can reasonably simulate the transient thermal response of the ladle during preheating is to consider convective heat transfer between a heat transfer fluid (HTF) and lining surfaces. The temperature of the HTF (T_{hf}) is assumed to be 1600 °C. The convective heat flux on the internal surfaces (q_{i1}) of the ladle can be expressed as [158]:

$$\begin{array}{c} q_{i1} = h_{i1}\left(T_{hf} - T\left(R,\theta,\ Z,t\right)\right), \\ \frac{\partial T_{i1}}{\partial \vec{n}} = h_{i1}\left(T_{hf} - T\left(R,\theta,\ Z,t\right)\right)\vec{\mathrm{n}}, \end{array} \tag{5.1}$$

where h_{i1} is the convective heat transfer coefficient during step 1 (its value is temperature dependent, see Fig. 5.2-a) and $\vec{n}$ is the outward normal to the surface. The radiative and convective thermal losses (q_e) from the outer surfaces of the steel shell to the ambient can be written as [158]:

$$q_e = h_e\left(T_{sh}\left(R,\theta,\ Z,t\right) - T_{amb}\right) + \epsilon S\left({T_{sh}}^4\left(R,\theta,\ Z,t\right) - {T_{amb}}^4\right), \tag{5.2}$$

where T_{amb}, ϵ, S, and T_{sh} are the ambient temperature (20 °C), emissivity (0.8), Stefan–Boltzmann constant, and steel shell outer surface temperature, respectively. h_e is the convective heat transfer coefficient between the steel shell outer surface and the ambient (10 W/m^{2}K). This boundary condition has been applied to the external surfaces during the whole steps of the thermal cycle of the ladle.

During step 2, the steel ladle is moved from the heating device to the converter or to the electric arc furnace and waits to receive the liquid steel. The duration of this step may reach 15 min. During this period, the inner and outer surfaces of the ladle exchange heat with the environment by convection and radiation mechanisms. Heat losses of the external surface are expressed by equation (5.2), whereas heat losses from the internal surfaces (q_{i2}) are written as:

$$q_{i2} = h_{i2}\left(T_i\left(R,\theta,\ Z,t\right) - T_{env.}\right) + \epsilon S\left(T_i^4\left(R,\theta,\ Z,t\right) - {T_{env}.}^4\right), \tag{5.3}$$

with h_{i2} (its value is temperature dependent, see Fig. 5.2-b), T_i, and $T_{env.}$ denoting the heat transfer coefficient during step 2, internal surfaces temperature, and environmental temperature (900 °C, the hot air inside the ladle), respectively.

After step 2, liquid steel (with $T_s = 1650$ °C) is poured inside the steel ladle, leading to a sudden increase in lining temperature (thermal shock). During this step, other processes may occur in parallel (degassing, alloying, etc.), and the total duration of this step is assumed to

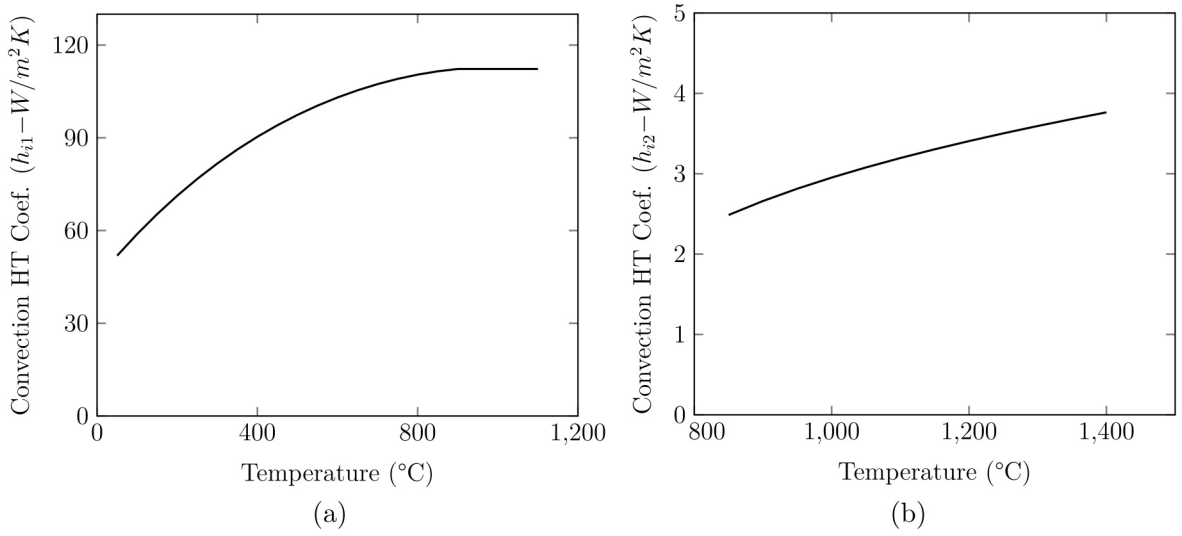

Figure 5.2: Temperature variations of the convection heat transfer cofficient used for (a) the first step and (b) the second step of the ladle thermal cycle.

be 2 h. During this period, heat is transferred from the liquid steel to the linings mainly by convection [127]. The convective heat flux on the internal surfaces (q_{i3}) can be expressed as:

$$q_{i3} = h_s \left(T_s - T_i \left(R, \theta,\ Z, t\right)\right). \tag{5.4}$$

Where h_s is the convective heat transfer coefficient between the liquid steel and the inner surfaces of the ladle. A very high value of h_s (2000 W/m^{2}K) was used in order to obtain the sudden temperature increase of the lining. This value is taken from [129].

Regarding the last step of the thermal cycle (step 4), liquid steel is drained out of the ladle. The temperatures of the ladle's internal and external surface decrease gradually due to thermal losses to the ambient. The heat losses during this step are considered similar to those of step 2. It should be noted that the heating and cooling rates during the four steps of the thermal cycle are different, as, according to Equations (3), (5) and (6), they are functions of the temperature of the internal surfaces. For example, in the beginning of the first preheating (1$^{\text{st}}$ step of 1$^{\text{st}}$ thermal cycle), the heating rate is very high as compared to the heating rate at the end of the same step.

The thermal model for steel ladle shown in Fig. 5.1 has been developed using Abaqus software. Then, weak thermomechanical coupling was used for the thermomechanical analysis. The computed temperature distributions have been used as a thermal load for the transient thermomechanical models.

Symmetry boundary conditions have been applied to the symmetric planes of the physical model of the ladle. The outer surface of the steel shell's bottom was assumed to be fixed in the vertical direction (z-direction in Fig. 5.1). The weight and hydro-static pressure of the liquid steel were neglected as their impacts on resulting stresses are very small (around 1 MPa) as compared to the impact of the thermal expansion of the bricks (around 100 MPa in some cases). The frictional interactions between the different layers of the ladle are considered in the numerical model using surface to surface contact in Abaqus (coefficient of friction 0.5). Several

constitutive material models were used for describing the mechanical behaviors of the working (masonry with dry joints) and the safety (masonry with mortar joints) linings. More details about the employed material models are given later in this chapter in section 5.4.3.

5.4 Results and discussion

5.4.1 Temperature fields

Time variations of the temperature of the working lining hot face (HF, surface in contact with liquid steel), cold face (CF, surface in contact with the safety lining) and the steel shell outer surfaces (bottom and wall) during the first three complete production cycles are shown in Fig. 5.3. Temperature distributions at the end of step 1, the end of step 2, the beginning of step 3, and the end of step 4 of the first thermal cycle are presented in Fig. 5.4 (see table 5.2 for full description of the three simulated thermal cycles and details about the four steps of each thermal cycle). As explained earlier, during the first step (a to b), heat is transferred by forced convection from a heat transfer fluid at 1600 °C to the working lining (initial temperature is about 20 °C). As a result, the temperature of the working lining increases gradually from room temperature to around 1400 °C. Then, the steel ladle is transported from the heating device to the converter or electric arc furnace while losing heat to the environment by convection and radiation mechanisms (b to c). This leads to a drop in the temperature to around 1200 °C. After that (c to d), liquid steel at around 1650 °C is tapped into the ladle, resulting in a sudden increase in the temperature. At the end of the thermal cycle (d to e), the working lining temperature decreases gradually. The observed decrease in temperature is due to the teeming of liquid steel and the heat losses (by convection and radiation mechanisms) from external and internal surfaces of the ladle to the ambient. Then, the first thermal cycle is repeated two times (except preheating from ambient temperature).

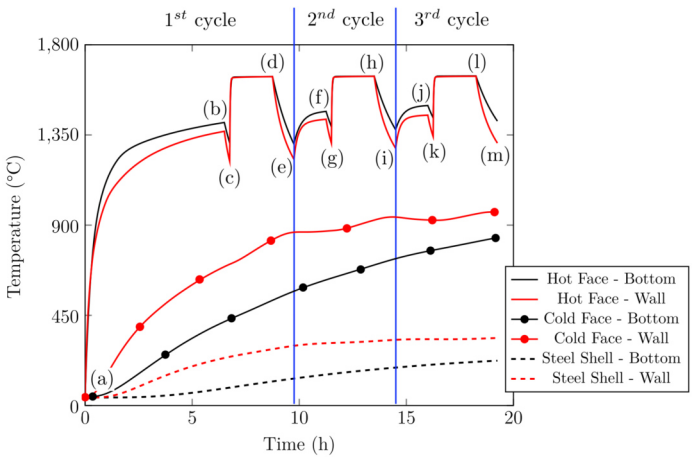

Figure 5.3: Temperature evolution of the working lining wall (mid. height), and bottom center (HF and CF) and outer surface of steel shell during the first three thermal cycles of the steel ladle.

Table 5.2: Summary of the three simulated thermal cycles of the steel ladle: time period of each step and corresponding points in Fig. 5.3.

	First cycle		Second cycle		Third cycle	
	Duration (h)	Points	Duration (h)	Points	Duration (h)	Points
Step 1	6.5	a to b	1.5	e to f	1.5	i to j
Step 2	0.25	b to c	0.25	f to g	0.25	j to k
Step 3	2	c to d	2	g to h	2	k to l
Step 4	1	d to e	1	h to i	1	l to m

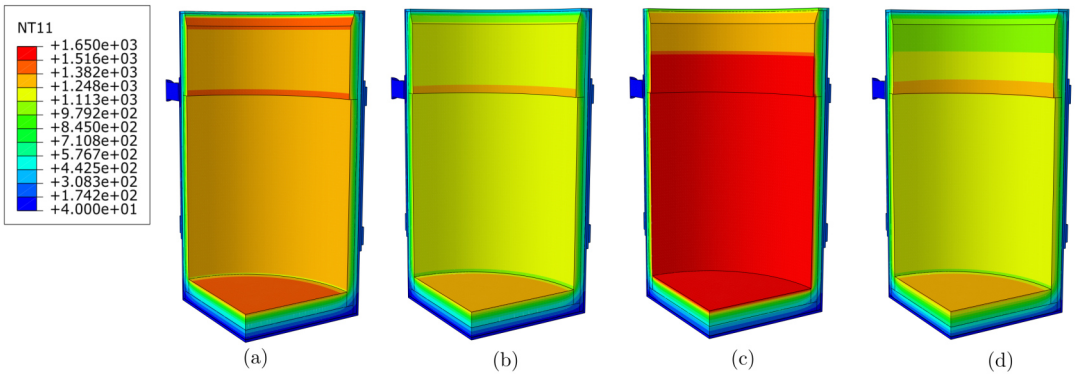

Figure 5.4: Temperature distributions (in °C) at the (a) end of step 1 (point b in Fig. 5.3), (b) end of step 2 (point c in Fig. 5.3), (c) end of step 3 (point d in Fig. 5.3), and (d) end of step 4 (point e in Fig. 5.3) of the first thermal cycle of the steel ladle.

Comparisons between temperature gradient through the thickness of the steel ladle's wall and bottom at the end of step 2 and end of step 4 of the first three full steel ladle's thermal cycles are shown in 5.5. For the second and third thermal cycles, after preheating, the temperature of the working lining is slightly higher when compared to the temperature at the end of the first preheating (points f and j as compared to point b in Fig. 5.3). Similarly, the working lining temperature at the end of step 2 (points g and k in Fig. 5.3) and 4 (points i and m in Fig. 5.3) of production cycles 2 and 3 is slightly higher than that of the first thermal cycle (point c at end of step 2 and point e at end of step 4 in Fig. 5.3). This behavior is caused by the overall temperature increase of the ladle after the first preheating cycle (see Fig. 5.5). It should be mentioned that during the first step of the three simulated production cycles, the inner surface temperature of the bottom is slightly higher than that of the wall. In addition, the steel shell bottom outer surface temperature is lower compared to that of the steel shell wall. This can be explained by the fact that the thickness of the working and safety lining at the bottom is higher than that at the wall.

5.4.2 Joints closure and reopening

An example of the gradual closure and reopening of the joints due to temperature fluctuations during the three thermal cycles of the steel ladle is shown in Fig. 5.6 (for a working lining without viscoplasticity - case B in table 5.3). Initially (at time = 0 s), bed and head joints are

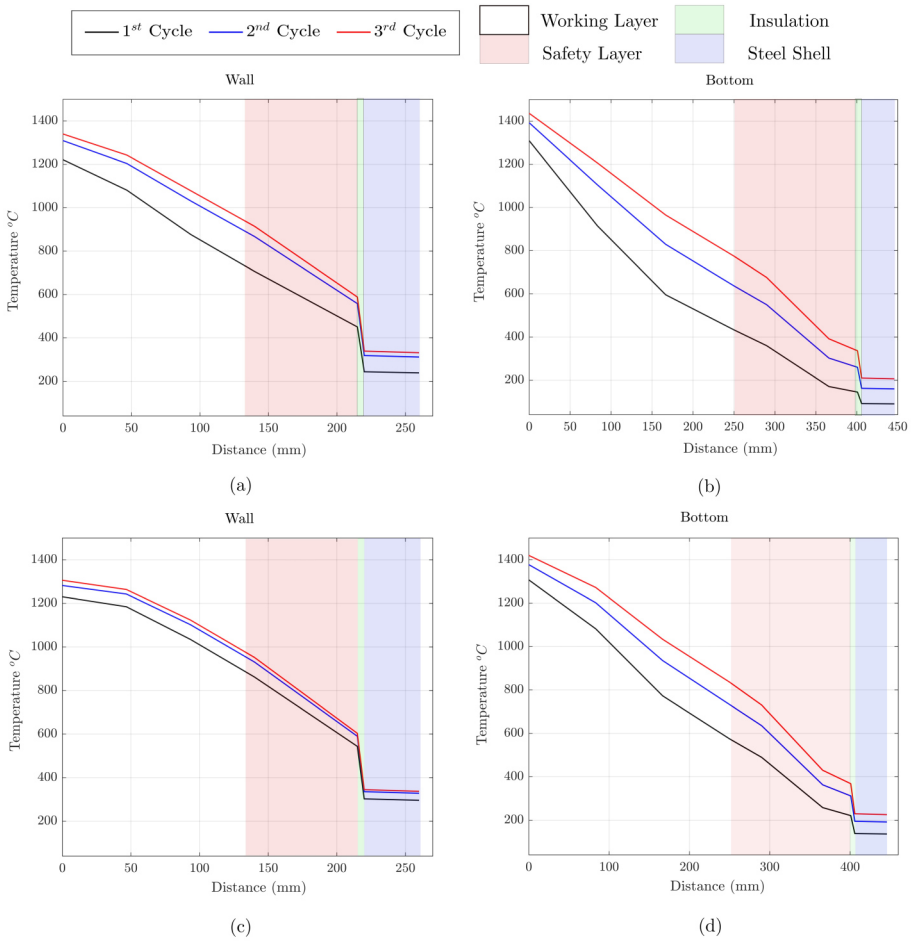

Figure 5.5: Temperature gradients through the thickness of the steel ladle's wall and bottom (a and b) at end of step 2 and (c and d) end of step 4 of three full ladle's thermal cycles (see table 5.2 for more details about each step of the three thermal cycles).

open and, therefore, the working lining (bottom and wall) is in pattern AO. With the increase of the temperature, joints close gradually due to the thermal expansion of the bricks. It has been noticed that joints at the working lining hot surface (internal surface of the ladle) usually close before joints at the cold surface (surface in contact with the permanent lining) (see Fig. 5.6-b). At almost 700 s, all joints in the hot face are closed and remain closed until the end of step 1. At the end of step 2, some joints at the outer top surface of the slag zone reopen (see Fig. 5.6-f). This can be attributed to thermal losses, the temperature drops of this region and, therefore, the change in stress from compression to tension. These open joints close again owing to liquid steel pouring inside the ladle and the sudden increase in temperature. As the temperature drop during step 4 is higher than that during step 2, one can notice that at the end of step 4, more joints are open as compared to the number of open joints at the end of step 2 (see Fig. 5.6-h). Therefore, waiting time (after preheating and before liquid steel tapping) is an important issue to consider when defining the time period of each step of the ladle thermal cycle. Long waiting time leads to high energy losses and may result in the opening of the joints at the wall and the bottom of the steel ladle just before tapping liquid steel in the ladle.

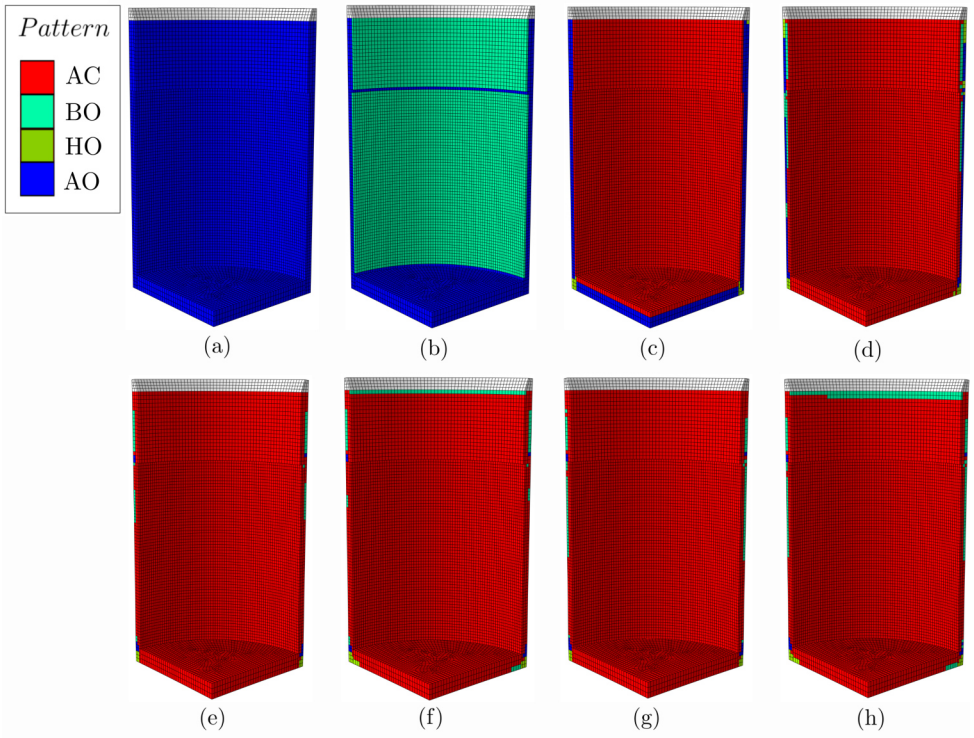

Figure 5.6: Gradual closure and reopening of joints due to temperature fluctuations during the first heating cycle for joint thickness of 0.1 mm (case B in table 5.3). (a) Time = 0 s (point a in Fig. 5.3), (b) time = 0.13 h, (c) time = 0.19 h, (d) time = 0.5 h ((b) to (d) corresponds to points after point a and before point b in Fig. 5.3), (e) time = 2.1 h (point b in Fig. 5.3), (f) time = 6.75 h (point c in Fig. 5.3), (g) time = 6.8 h (point d in Fig. 5.3) and (h) time = 9.25 h (point e in Fig. 5.3). The top zone in the working lining (in grey) is castable.

5.4.3 Stress fields

After computing the temperature distributions during the three complete thermal cycles of the ladle, some parametric studies have been carried out to investigate the impacts of dry joints thickness, joints behavior (natural or perfect) and the employed material behavior laws for the different layers of the ladle on the resulting thermomechanical response. Summary of the six simulated case studies are given in table 5.3. We start with the simplest case (A) and, then, add more complexities and details to the numerical model, trying to obtain reasonable values of thermomechanical stresses. For all the case studies, the temperature distributions presented in section 5.4.1 were used as thermal load in the thermomechanical analysis. Therefore, the resulting differences in the thermomechanical response are caused mainly by the different constitutive models employed in the thermomechanical analysis.

In previous work of the author [138], it has been shown that the linings are subjected to a biaxial stress state and the out of plane stresses are negligible as compared to the in-plane stresses. Therefore, the comparisons of the resulting thermomechanical stresses (for the six simulated cases) were carried out in terms of resulting in-plane stresses at mid height of the wall HF (2500 mm), the center of the bottom HF (R = 0 mm) and von Mises stresses in the steel shell outer surfaces (mid height of the wall and bottom center).

Table 5.3: Summary of the six simulated case studies of the ladle showing the considered joint behavior, joint thickness and employed constitutive material models for the working, safety linings and steel shell.

Case	Joint		Working lining	Safety lining	Steel shell
	Type	Thickness (mm)			
A	No Joint		Isotropic - Elastic	Isotropic - Elastic	Elastic
B	Perfect Joint	0.1	Orthotropic - Elastic		
C		0.3			
D		0.5			
E	Natural Joint	0.5			
F	Natural Joint	0.5	Orthotropic - Elastic - Viscoplastic	Orthotropic - Elastic - Damageable	Elastic - Plastic

5.4.3.1 Impacts of dry joints thickness

In the case A, the dry joints in the working lining and the mortar joints in the safety linings were neglected. All the layers of the ladle were modeled using simple isotropic linear elasticity. This case is considered as the reference case. To investigate the impacts of dry joints thickness on the resulting thermomechanical stresses, three cases were simulated (B, C and D). The joints behavior was considered as perfect (i.e. gradual closure of joints and increase of effective stiffness with joints closure were neglected). As mentioned in chapter 3, perfect joints with almost controlled thickness can be artificially generated by inserting cardboard spacers between the contact surfaces of the bricks and, in this case, joints can be considered as either open or closed. Therefore, the initial mechanical behavior of the working lining is orthotropic (due to the presence of open joints). To avoid the contribution of viscoplasticity, plasticity of the steel shell, the damage of mortar joints (in the safety linings) and for better understanding of the impact of joints thickness on resulting thermomechanical stresses, the mechanical behaviors of the other layers were considered as isotropic and purely elastic.

Time variations of the thermal stresses in the hot face of the wall (middle, $H = 2500$ mm) and bottom (center, $R = 0$ mm) of the working lining for different values of bed and head joint thickness (cases B, C and D), as well as the isotropic representation of the masonry (case A), during the first three thermal cycles are shown in Fig. 5.7. In general, it has been observed that the resulting thermal stresses increase with the increase in temperature, decrease with the increase of joint thickness, and their trends are similar to those of the temperature during the four steps of the ladle thermal cycle. In addition, the isotropic assumption of mortarless masonry leads to an overestimation of resulting thermal stresses.

During the first step, thermal stresses increase with the increase in temperature and thermal expansion of the bricks. Then (during step 2), they decrease slightly due to the temperature decrease and contraction of the bricks. The maximum value of thermal stresses is reached when liquid steel is tapped in the steel ladle. This is because of the sudden increase in temperature.

During step 4, they decrease again with the decrease in temperature. Finally, this trend is repeated. One can notice that the hot face is under high compressive stresses. This result may be explained by the fact that the temperature of the hot face is higher than the temperature of the other layers and it tends to expand faster than the safety, insulation layers, and the steel shell.

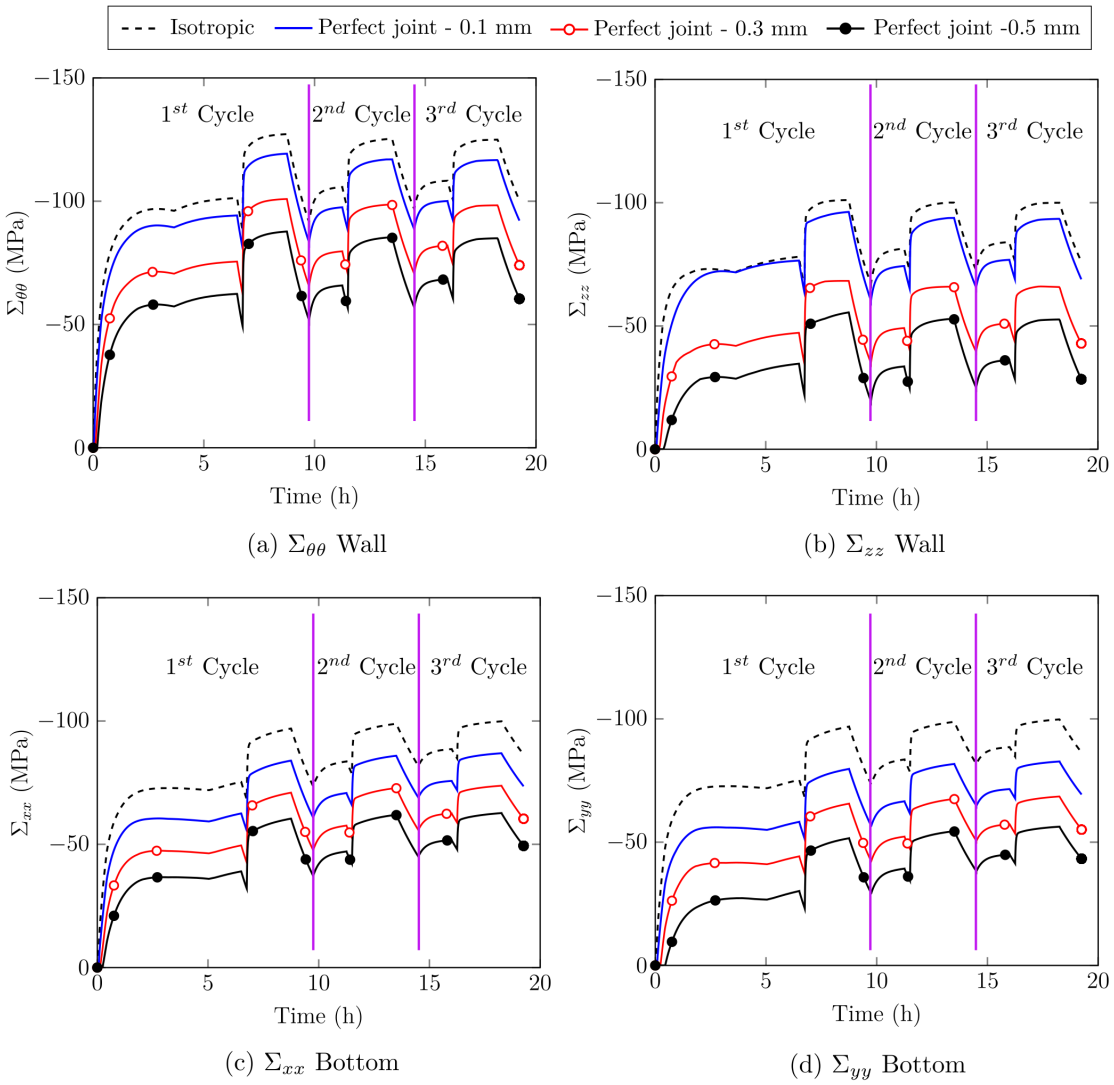

(a) $\Sigma_{\theta\theta}$ Wall (b) Σ_{zz} Wall

(c) Σ_{xx} Bottom (d) Σ_{yy} Bottom

Figure 5.7: (a and b) Time variations of the thermal stresses at the wall surface (HF) and (c and d) bottom surface (HF) of the working lining for different values of bed and head joint thickness during the first three thermal cycles of the steel ladle.

Time variations of the von Mises stresses in the steel shell (bottom and wall) for different values of bed and head joint thickness (cases B, C and D), as well as isotropic representation of the masonry (case A) are given in Fig. 5.8. Overall, it has been observed that the von Mises stresses increase with the increase in temperature, decrease with the increase of joint thickness, and their trends are similar to those of the temperature during the four steps of the ladle thermal cycle. Based on the above results, it can be concluded that increasing joint thickness leads to a decrease in the resulting thermal stresses in the bottom and the wall of the working lining, as well as the steel shell. Increasing joint thickness allows the bricks to expand freely (until closure of

joints), resulting in lower values of thermal stresses. After the closure of joints, thermal stresses increase at higher rates. This phenomenon can be noticed in Fig. 5.7 - b and d for joint thickness 0.5 mm. In the first 500 s, as joints thickness is higher than zero during this period (therefore, considered open), the values of the resulting thermal stresses are very small (almost zero).

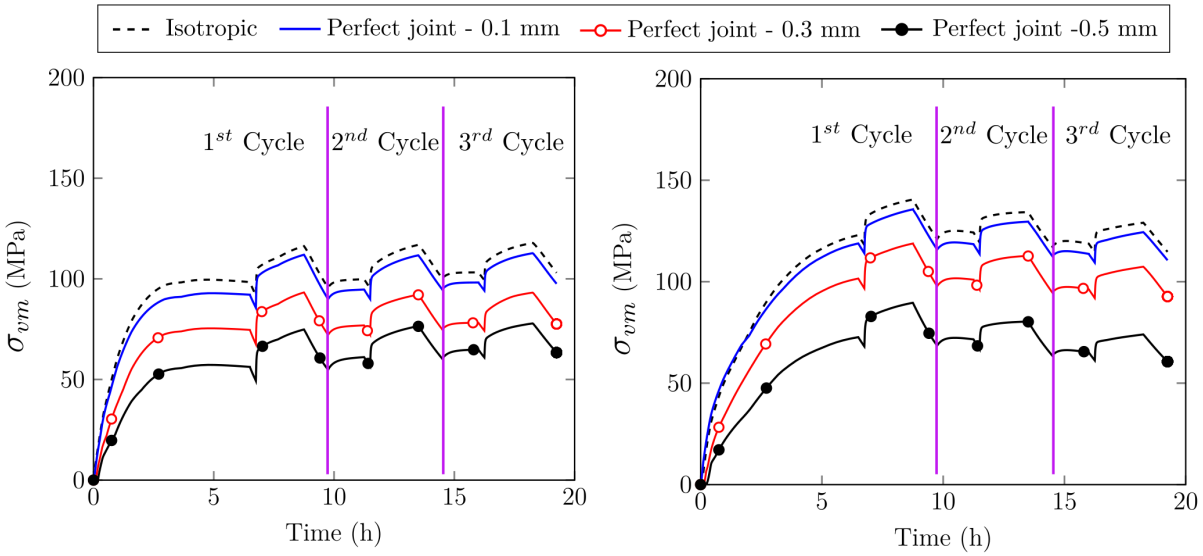

(a) Steel shell wall (b) Steel shell bottom

Figure 5.8: Time variations of the von Mises stresses in the (a) wall and (b) bottom of the steel shell for different values of bed and head joint thickness during the first three thermal cycles of the steel ladle.

5.4.3.2 Impacts of dry joints behavior

In most cases, cardboard spacers are not used while building the linings and natural joints are generated between the bricks by the dimensional, shape tolerances and surface roughness of the bricks. Therefore, a numerical simulation (case E) with natural joint behavior was carried out. For natural joints, as shown previously in chapters 2 to 4, the gradual closure of joints and the related gradual increase in the effective stiffness of the masonry with the closure of joints are considered. Case E may help in understanding the impacts of joint behavior on the resulting thermomechanical stresses. The considered joint behavior is similar to that presented in chapter 4. Indeed, the real joints behavior of the tapered shaped bricks (used for building the working lining) could be different from that of the cuboid bricks presented in this work. However, based on the available data, the assumption of similar joints behavior can be acceptable.

Time variations of the thermal stresses in the HF of the wall (middle, $H = 2500$ mm) and bottom (center, $R = 0$ mm) of the working lining for bed and head joints with natural behavior (cases E), as well as perfect joints behavior (cases C and D), during the first three heating cycles are shown in Fig. 5.9. Time variations of the von Mises stresses in the wall and the bottom of the steel shell for joints with perfect and natural behavior during the first three thermal cycles of the steel ladle are given in Fig. 5.10. In general, for masonry with natural joints behavior, similar

trends (as cases A, B, C and D) of the resulting thermal stresses in the working lining and the steel shell can be observed from the figures.

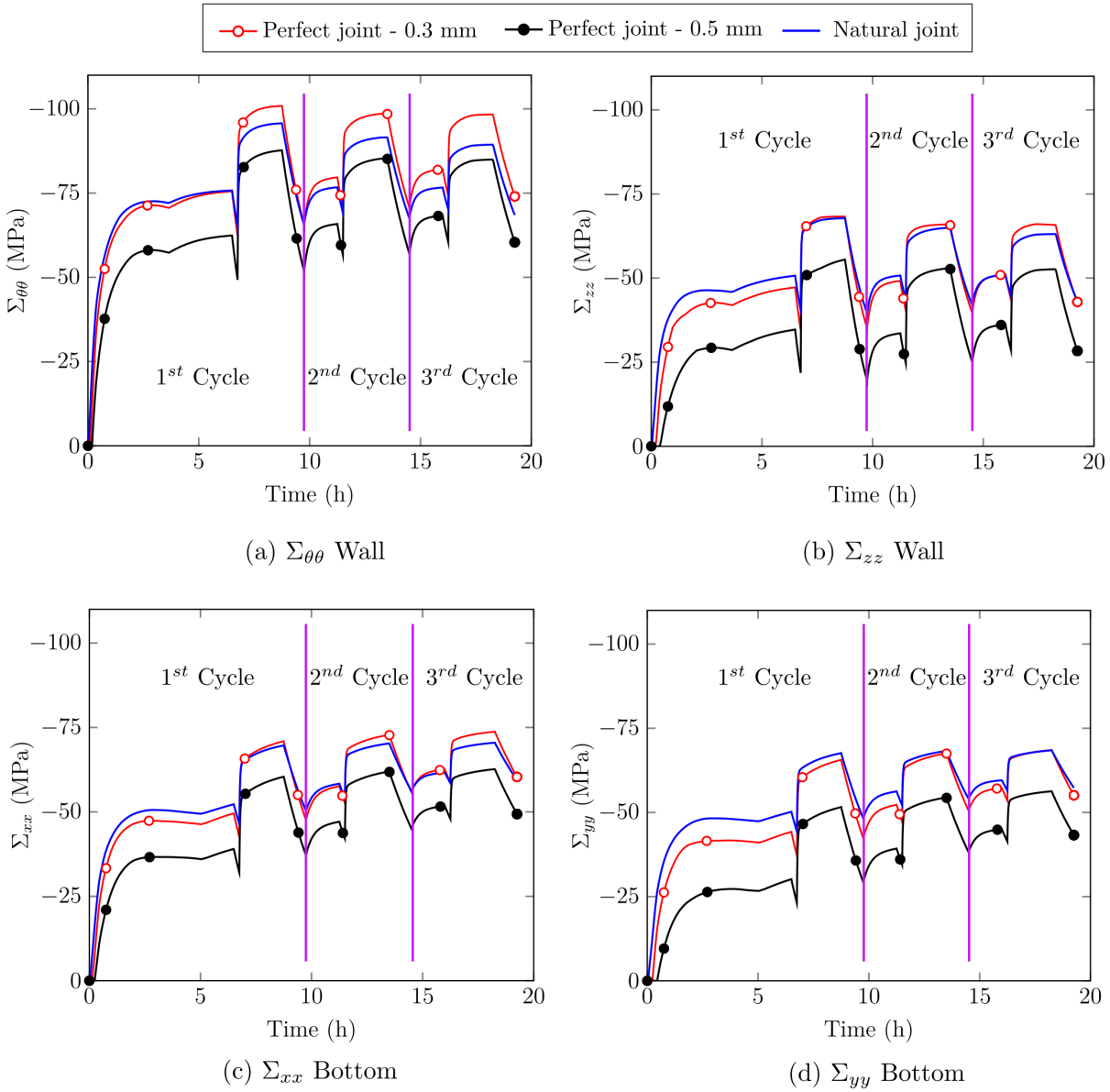

Figure 5.9: (a and b) Time variations of the thermal stresses in the wall HF and (c and d) bottom HF of the working lining for joints with perfect and natural behavior during the first three thermal cycles of the steel ladle.

For the same joint thickness (0.5 mm), using masonry with natural joints behavior results in higher values of resulting thermomechanical stresses. This can be attributed to that in the case of perfect joint, the in-plane effective stiffness of the masonry is almost zero and remains very small until full closure of joints (i.e. there is a sudden jump in the effective stiffness when full closure happens and the values of resulting stresses are almost zero before full closure of joints). On the other hand, for natural joints, the in-plane effective stiffness increases gradually with the gradual closure of joints and reaches the maximum value (same as that of the brick) when joints are fully closed. Based on these results, it can be recommended that decreasing the dimension

errors of the bricks and generating artificial joints using cardboard spacers could be better in terms of resulting thermomechanical stresses. Moreover, as presented in chapter 2, natural joints (caused mainly by the dimension errors of the bricks) leads to stress concentrations at the middle of the bricks and a significant reduction in the load bearing capacity of the masonry.

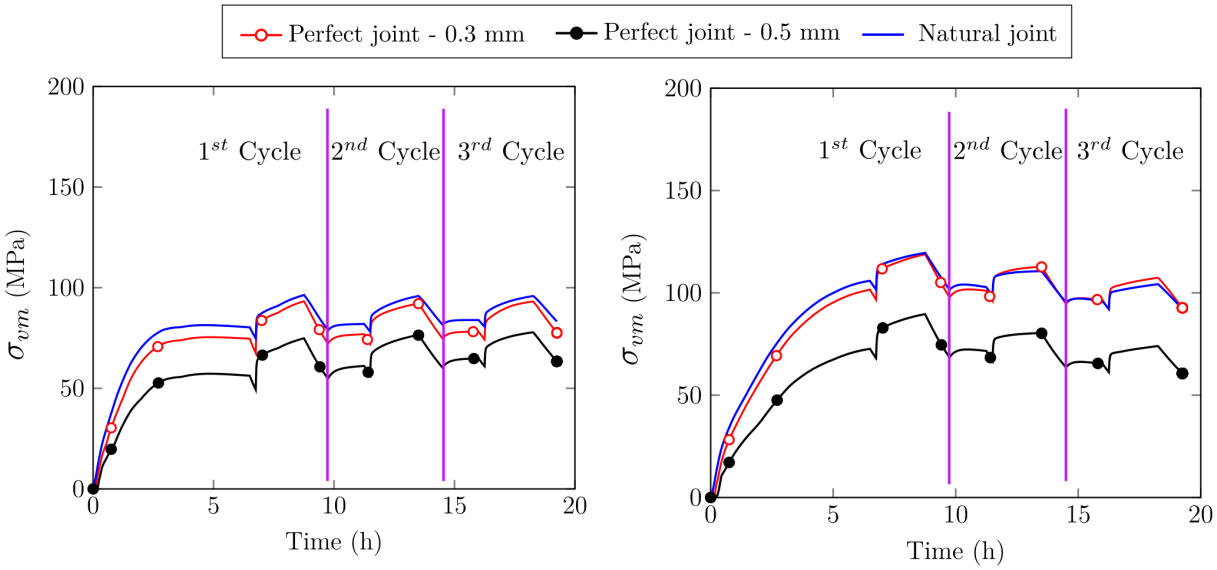

(a) Steel shell wall

(b) Steel shell bottom

Figure 5.10: Time variations of the von Mises stresses in the (a) wall and (b) bottom of the steel shell for joints with perfect and natural behavior during the first three thermal cycles of the steel ladle.

5.4.3.3 Linings with elastic-viscoplastic behavior

In the last case study (case F), the working and safety linings of the steel ladle are modeled using more accurate behavior laws. The orthotropic elastic viscoplastic behavior of refractory masonry with dry joints is considered. The von Mises plasticity theory was used to model the plastic behavior of the steel shell. One of the main challenges in this simulation is related to the lack of important data to define the temperature and corresponding yield stress at which the behavior of the masonry changes from elastic to elastic viscoplastic (creep starting temperature and corresponding yield stress). These data should be determined experimentally and should be available to build a realistic and accurate numerical model. In the case of refractories and for temperatures above or equal to 1000 °C, it has been usually assumed that the yield stress is equal to zero [139, 162, 163] (i.e. creep starts at any value of stress). In the case of alumina spinel, no creep parameters, creep starting temperature and corresponding yield stress data are available for temperatures below 1300 °C. It has been shown that, in chapter 2, at 1200 °C and under 6 MPa compressive load, the creep strain was insignificant as compared to higher temperatures. However, this conclusion was based on lower value of applied compressive stress as compared to the values of stresses observed here (steel ladle simulation) and the ultimate compressive stress of the material (25 MPa). Therefore, due to the lack of the required data, it has been assumed

that the creep starting temperature is 1200 °C (same creep parameters as 1300 °C) and the yield stress was set to zero.

Time variations of the thermal stresses in the hot face of the wall (middle, $H = 2500$ mm) and bottom (center, $R = 0$ mm) of the working lining for case E and F, as well as the isotropic elastic representation of the masonry (case A), during the first three thermal cycles of the ladle are shown in Fig. 5.11. In general, it has been observed that, in the first four hours, the resulting compressive thermal stresses in the case F are similar to that in the case E. Next, in the case F, the stresses decreased sharply (when the temperature reached the set value of creep starting temperature) to around -5 MPa due to stress relaxation. Then, they remained at this value till the end of the preheating stage. During the second step of the first thermal cycle and with the decrease of the temperature, the stresses changed from compressive to tensile. This can be attributed to the contraction of the bricks with the decrease in the temperature. By the start of the third step (liquid steel tapping), the stresses changed the sign again from tensile to compressive stresses due to the sudden increase in the temperature. During the same step, a decay in the stresses was observed due to stress relaxation. Finally, during the fourth step, the stresses changed from compressive to tensile due to heat losses and contraction of the bricks. The same trends have been observed for the second and third thermal cycles of the ladle. Similar results were obtained using the micro modeling technique developed within the framework of ATHOR project at University of Leoben.

The stress levels obtained here are still unrealistic, because they are higher than the ultimate compressive strength of the material (25 MPa at 1000 °C). Future numerical studies to optimize some geometrical parameters of the ladle, considering the real geometry of the ladle and materials (ramming mix, different materials used for the slag zone, the bottom and the working lining) are required. For the studied ladle, it has been assumed that the material of the slag zone, the bottom and the working lining is the same (due to lack of thermo-physical and mechanical properties of other materials). However, in reality, they are different. Moreover, the creep starting temperature and corresponding yield stress used in the model are another important factors that impacts the resulting thermomechanical stresses during the first four hours. For example, lowering the creep initiation temperature to 800 °C and having the corresponding creep parameters and yield stress would result in a reduction in the thermomechanical stresses. Moreover, the sudden decrease of stresses (once reaching the creep temperature set value) may not occur in reality. Including the creep impacts at lower temperatures would lead to gradual decrease of stresses instead of the sudden decrease noticed here. However, this requires experimental characterization and inverse identification of the creep parameters of the material at lower temperatures. Future experimental studies to investigate the creep behavior at lower temperatures and include its effects on the numerical model are planned.

The change of stress sign from compressive to tensile leads to reopening of dry joints in the HF of the wall and the bottom. On the other hand, the change of its sign from tensile to compressive leads to re-closure of the reopened joints. More explanations and insights are

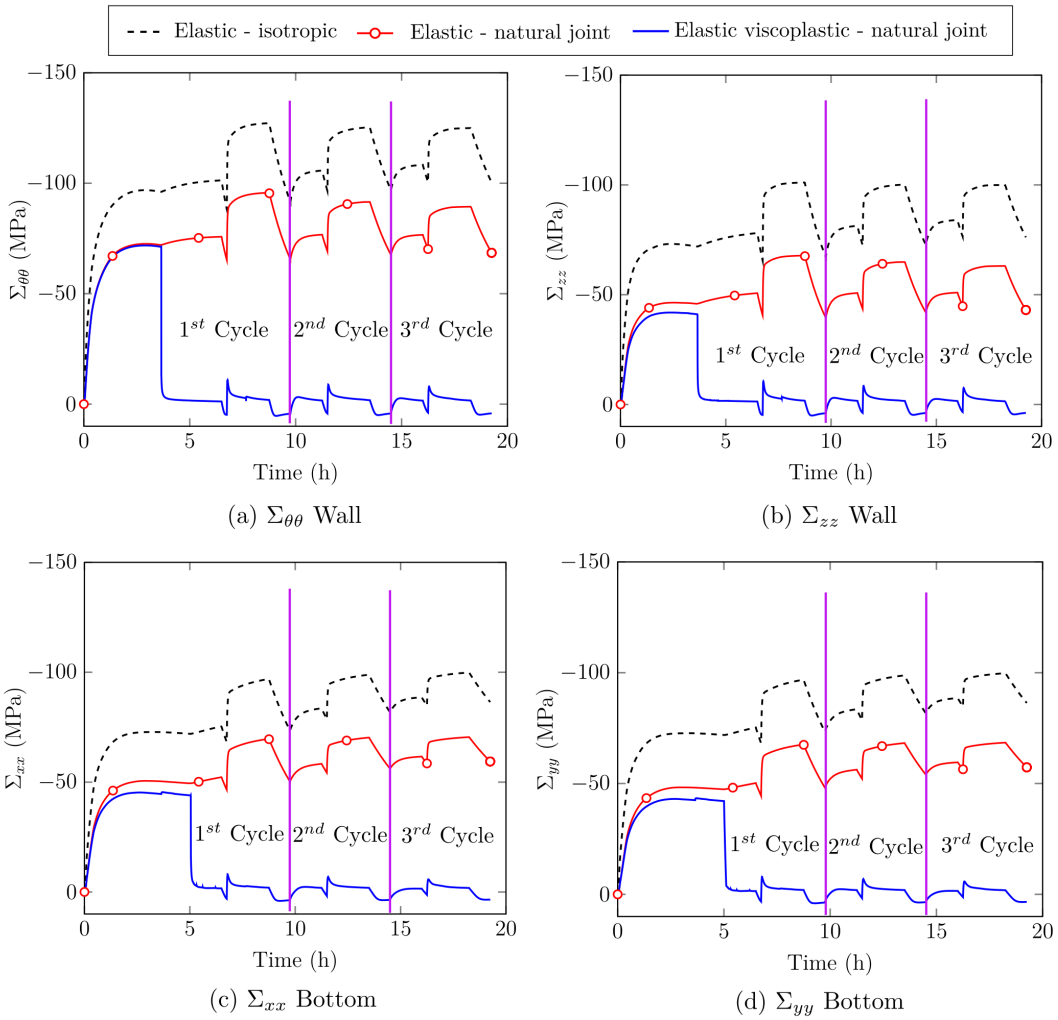

Figure 5.11: variations of the stresses (in the HF of the wall and the bottom) and comparisons of different constitutive material models including viscoplasticity.

given for the first and second changes of stress sign reported in Fig. 5.11 as following. Figure 5.12 shows the joint patterns in the working lining and the bottom at the end of step 2 (first temperature drop after first preheating), 500 seconds from the beginning of step 3 (first liquid steel tapping into the ladle - sudden temperature increase) and end of step 4 (temperature drop due to teeming liquid steel out of the ladle and waiting time for linings check and repair). It can be seen that with the temperature drop and change of stress sign, almost all joints in the HF of the bottom and the wall reopened (see Fig. 5.12-a). Then, the reopened joints close again when liquid steel is tapped into the ladle (see Fig. 5.12-b). Finally, with the second temperature decrease and the change of stress from compression to tension, joints in the HF reopen (see Fig. 5.12-c). These described openings and closures of joints during the first and second changes of stress sign were noticed for each change of stress sign shown in Fig. 5.11. Similar results were obtained using the micro modeling technique developed within the framework of ATHOR project at University of Leoben. In the safety lining, damage of bed or head or both mortar joints was observed. The damaged joints were mainly located in the top and the bottom zones of the wall

of the safety linings (see Fig. 5.13). The re-closure of damaged mortar joints under compressive loads was not included in the numerical model, because this requires further experimental studies of the mortar joints behavior during re-closure and further developments of the numerical model that are planned to be carried out in the future.

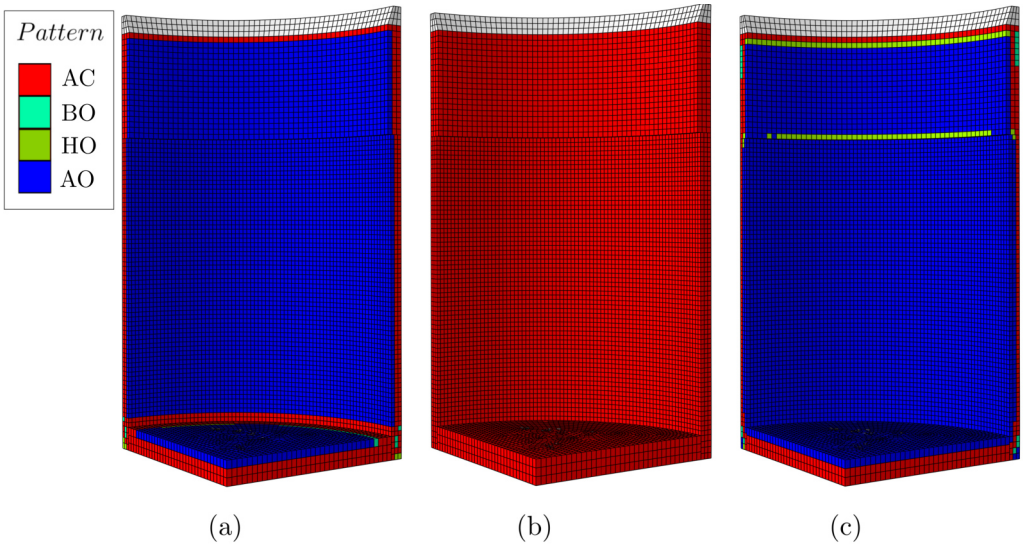

Figure 5.12: Joints reopening and closure in the wall and the bottom (working lining) of the steel ladle due to temperature fluctuations and the change of stress sign (from compressive to tensile and vice versa) at (a) the end of the second step, (b) the beginning of the third step and (c) the end of the fourth step of the first thermal cycle of the steel ladle.

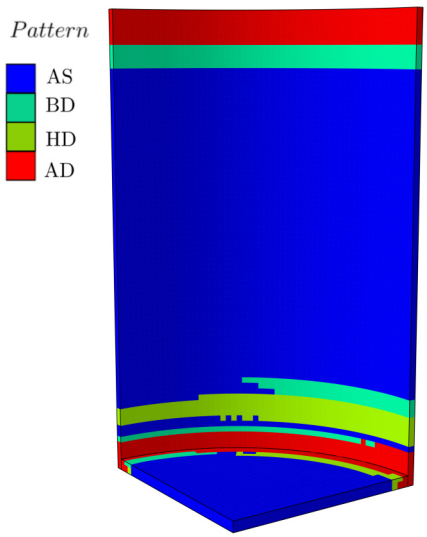

Figure 5.13: Damage of mortar joints in the safety lining wall.

The in-plane viscoplastic strains, in the case F, in the wall (in $\theta\theta$ and zz directions) and the bottom (in xx and yy directions) of the working lining of the steel ladle by the end of the three simulated thermal cycles are presented in Fig. 5.14. It can be seen that the highest values of viscoplastic strains are located in the HF of the wall in the $\theta\theta$ direction. Because, as presented in Fig. 5.11, the highest values of the computed thermomechanical stresses are normally in the

same direction. Moreover, the viscoplastic strains in the CF of the wall and the bottom are almost zero. This can be attributed to that the calculated temperatures of the CF of the bottom and the wall (presented in Fig. 5.3) were always below the set value of creep initiation temperature (1200 °C). No viscoplasticity was noticed in the safety lining because its temperature, again, was below the set value of creep initiation temperature.

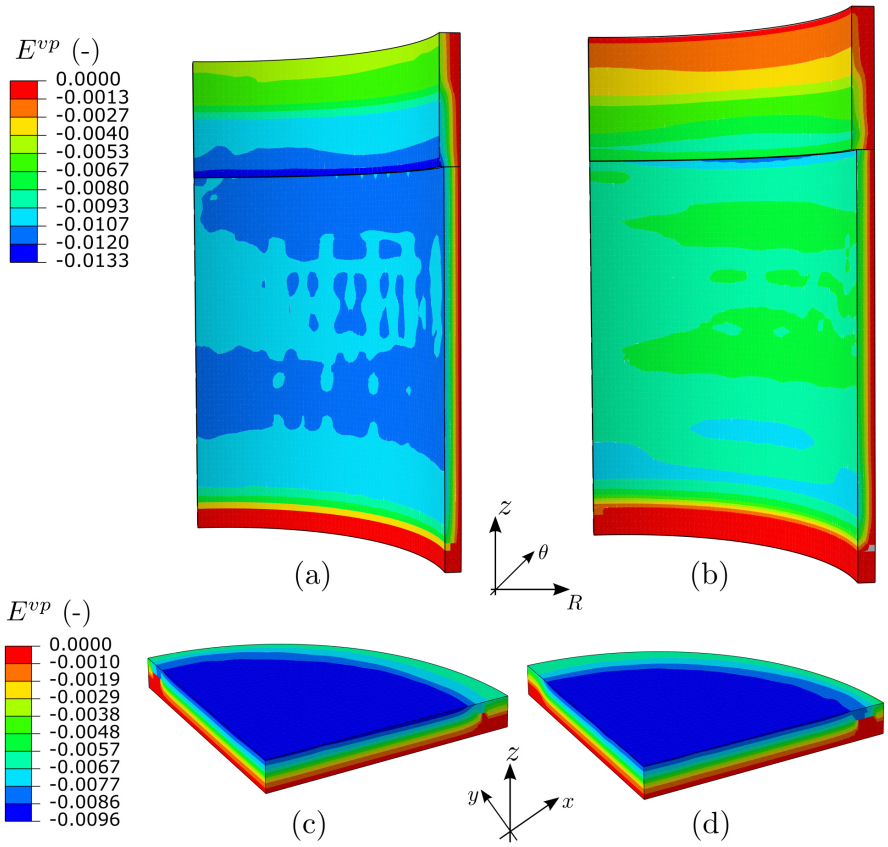

Figure 5.14: Viscoplastic strains fields in the wall (a and b) and the bottom (c and d) in directions (a) $\theta\theta$, (b) zz , (c) xx and (d) yy by the end of the three simulated thermal cycles of the steel ladle.

Time variations of von Mises stresses in the steel shell wall (middle, $H = 2500$ mm) and bottom (center, $R = 0$ mm) for cases E and F, as well as the isotropic elastic representation of the masonry (case A), during the first three heating cycles are shown in Fig. 5.15. Significant reductions of von Mises stresses were noticed four hours after the first preheating (corresponds to the sharp reduction in the stresses of the HF of the bottom and the wall).

It should be noted that changing the constitutive material models of the different layers of the ladle and the steel shell leads to a change in the von Mises stress distribution. Therefore, comparing the von Mises stress variations with time of a specific point may result in less accurate conclusion. A judicious comparison could be made in terms of the maximum value of von Mises stress in the entire steel shell. The maximum value of von Mises stresses in the steel shell, obtained numerically, was always located in the barrel zone (top zone of the steel shell wall) of the steel ladle. In real steel ladles, damage and high deformation of this zone were also observed

(see Fig. 5.16). A comparison between the maximum value of von Mises stresses for the six studied cases is presented in Fig. 5.17. The yield and ultimate tensile strength of steel are 250 and 400 to 550 MPa, respectively. The highest value of von Mises stress was obtained using the isotropic representation of the working linings (case A). On the other hand, the lowest value was obtained when more accurate material models of the working, the safety linings and the steel shell were employed. In addition, it can be seen that increasing the dry joints thickness leads to a decrease in the maximum value of Mises stress in the barrel zone.

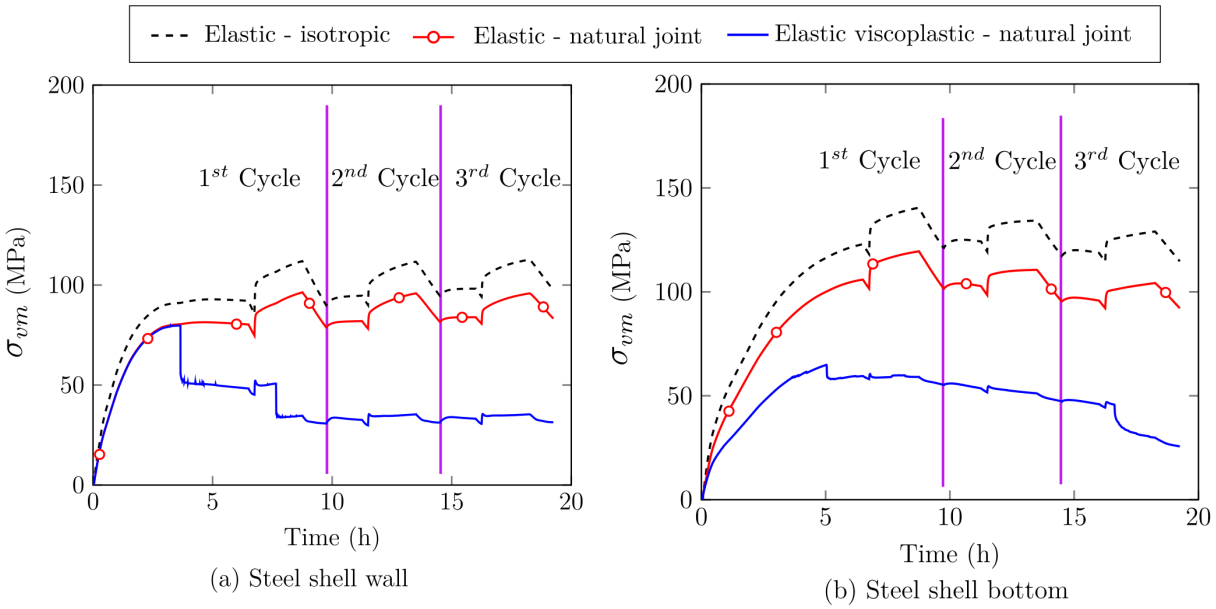

Figure 5.15: Time variations of von Mises stresses in the hot face of the steel shell wall and bottom for cases E, F and A during the first three thermal cycles of the steel ladle.

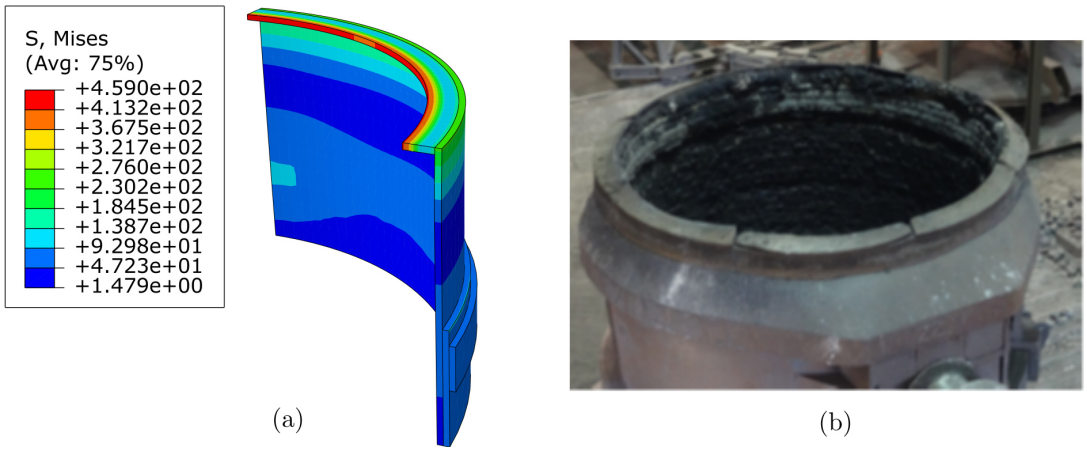

Figure 5.16: (a) Example of von Mises stress (in MPa, case A) in the barrel zone of the steel shell and (b) damage and permanent deformation of the top flange of a real steel ladle.

Based on the above results, it can be concluded that either the isotropic assumption of mortarless masonry or orthotropic elastic assumption leads to overestimation of resulting thermal stresses. In addition, it can be concluded that the most critical stage of the ladle thermal cycle

is the first preheating. Using a material with lower values of coefficient of thermal expansion could help in reducing the resulting thermomechanical stresses of the ladle. Further parametric studies to investigate the usage of perfect joints with an optimum thickness (combined with viscoplasticity at lower temperatures, below 1200 °C) on the resulting thermal stresses are planned to be carried out in the future. Indeed, the impacts of creep at lower temperatures, corrosion, damage, wear and thermal shock could change these conclusion and add more insights on the thermomechanical response of the ladle.

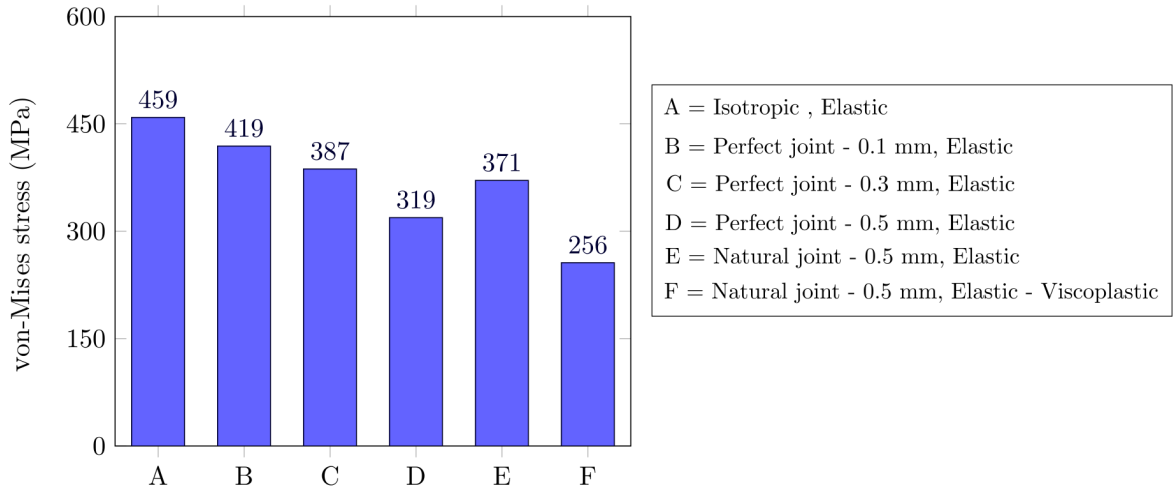

Figure 5.17: Maximum values of von Mises stress in the steel shell obtained from the six simulated case studies.

5.5 Conclusion

In the present work, three-dimensional coupled sequential thermomechanical analysis of a steel ladle has been carried out. The working lining and the bottom of the ladle have been replaced by an equivalent material model that takes into account the closure and reopening of joints due to cyclic thermal or mechanical loading/unloading. The temperature distribution of the steel ladle has been computed and used as a thermal load for the thermomechanical analysis. The thermomechanical model enables the visualization of the gradual closure and reopening of joints during the complete thermal cycle of the ladle. The impacts of joint thickness, joint behavior, constitutive material models used for the different linings of the ladle and the steel shell on the resulting thermomechanical stresses have been studied. The following conclusions can be drawn:

- With the increase in temperature, dry joints close gradually due to the thermal expansion of the bricks. Joints at the working lining hot surface close faster than joints at the cold surface.
- The temperature drop during the waiting time results in the opening of some joints at the outer top surface of the slag zone. Moreover, waiting time is an important issue to consider when defining the time period of each step of the ladle thermal cycle. Long waiting time

leads to high energy losses and may result in the opening of joints at the wall and the bottom of the steel ladle just before tapping liquid steel in the ladle.

- Resulting thermal stresses in the hot face increase with the increase in temperature, and their trends are similar to those of the temperature during the four steps of the thermal ladle heating cycle.
- Increasing joint thickness leads to a decrease in the resulting thermal stresses in the bottom and the wall of the working lining, as well as in the steel shell.
- For the same joint thickness, using masonry with natural joint behavior results in higher values of resulting thermomechanical stresses as compared to perfect joint.
- Either the isotropic assumption of mortarless masonry or orthotropic elastic assumption leads to overestimation of resulting thermal stresses.
- The inclusion of the viscoplasticity to the numerical model has a significant impact on the resulting thermomechanical stresses. A change of stress sign from compression to tension and opening/closure of dry joints in the HF of the working linings was observed. Moreover, lower values of the thermomechanical stresses were obtained when using more accurate behavior laws for the different layers in the steel ladle.

CHAPTER 6

CONCLUSIONS AND PERSPECTIVES

6.1 Summary and main contributions

The principal goals of this research were: firstly, the characterization of the mechanical and thermomechanical behavior of refractory masonry with dry joints and secondly, the development of constitutive material models to accurately describe the orthotropic elastic-viscoplastic behavior of masonry with dry or mortar joints. The experimental techniques, experimental results and the developed numerical models presented in this work could help in understanding the complex mechanical behavior of refractory linings and assist in their design and optimization.

The literature survey on the experimental work of masonry with dry joints (chapter 1) has shown that there is very limited available experimental data on the thermomechanical behavior of refractory masonry (only two tests) and our understanding of their mechanical behavior was limited. Therefore, for better understanding of the mechanical and thermomechanical behavior of these structures and for developing accurate numerical models that can capture the real phenomena, two large scale experimental campaigns have been carried out within the framework of ATHOR project (chapter 2). To gather more information from the tests, full field displacement measurement techniques (DIC) have been used when possible. In total, ten large scale test series (compromising 20 tests) have been performed. Each test series aimed at investigating some important features.

Uniaxial compression tests at room temperature and up to the rupture point of the walls were carried out to understand the impacts of the dimensional and shape tolerances of the bricks on the mechanical response and load bearing capacity of the wall. It has been shown that these tolerances lead to highly nonuniform displacement fields (obtained using DIC), limited contact and stress concentrations at the middle of the bricks. Therefore, the experimental values of the tangent Young's modulus of the wall and the ultimate compressive strength were smaller as compared to those of the constitutive material of the bricks.

To understand the mechanical behavior of the masonry at room temperature under cyclic

mechanical loading and unloading and to investigate the impacts of joints closure and reopening on the mechanical behavior, cyclic in-plane uniaxial and biaxial compression tests have been performed. The results indicated that the masonry has orthotropic mechanical behavior and the effective stiffness in the direction normal to head joints is higher than that in the direction normal to bed joints (for the studied walls, the number of head joints was smaller than the number of bed joints). In addition, it has been shown that the stress strain relationship of the masonry is highly nonlinear (strain stiffening behavior) due to the gradual closure of joints and the increase of the effective stiffness with joints closure. Moreover, it has been clearly demonstrated that after unloading there was usually permanent deformation and the walls did not recover their initial configuration. This behavior was attributed to that the final joints thickness after unloading is usually small as compared to the initial one (before load application).

The refractory linings normally operate at high temperature (around 1500 °C) and, at this temperature, the impacts of creep and stress relaxation are significant. Therefore, it was important to test refractory masonry at temperatures similar to those in-service. The in-plane uniaxial, biaxial creep and biaxial stress relaxation behaviors were investigated at 1500 °C. It was observed that during load application, the masonry has strain stiffening nonlinear orthotropic behavior due to the gradual closure of joints. However, during the holding time and after joints closure, the behavior was isotropic (the increase in the creep strain during the holding time was almost similar in the directions normal to bed and head joints). After unloading, the experimental results indicated that the recovered strain was very small as compared to the strain due to load application. This was attributed to that, during unloading, only few joints reopen and their final thickness is very small as compared to the initial joint thickness. Secondly, the permanent deformation caused by the viscoplastic behavior of the structure at high temperature. At high temperature, perfect closure of bed or head or both joints was achieved and some bricks were fused together.

As presented in chapter 1, two modeling techniques of masonry with dry joints were developed in the literature, namely: micro modeling and multi scale modeling. The multi scale modeling approach was chosen in the present work as it has a fair compromise between accuracy and computational cost. The main difficulties in developing multi scale models of masonry with dry joints are related to the heterogeneous micro structure of the material, which makes masonry global response strongly affected by shape, sizes and arrangement of bricks. However, as emphasized in chapters 1 and 2, some important features can be identified in the case of regular running bond masonry, such as the strongly nonlinear stress-strain relationship due to gradual closure of joints and the markedly orthotropic behavior (caused by the difference between the number of bed and head joints and the fact that they can be closed in one direction and open in the other direction).

To numerically capture such nonlinear phenomena and consider the impacts of gradual joints closure/reopening on the homogenized mechanical response, four periodic joint patterns were defined (chapter 3). Each pattern is associated with a specific state of bed and head joints (open

or closed). Then, the homogenized elastic viscoplastic behavior of each pattern was determined using FE based nonlinear homogenization technique. To consider the gradual increase in the effective stiffness with the gradual closure of joints and reproduce the strain stiffening behavior, the joints were reduced to an interface with small thickness (at the RVE level, micro modeling) where the constitutive normal and shear behaviors of the joints have been implemented. Suitable joints closure, reopening and pattern transition criteria were developed and implemented. The multi scale model was used to predict the mechanical response of masonry under a wide rang of thermomechanical loading conditions (experimental results presented in chapter 2). It has been shown that the developed numerical model can reproduce with reasonable accuracy the nonlinear orthotropic elastic viscoplastic behavior of masonry with dry joints and account for gradual closure of joints and joints reopening (chapter 4).

Regarding masonry with mortar joints, a homogenized elastic-viscoplastic multi scale model was developed (chapter 3). Both the bricks and mortar joints were considered to exhibit linear elasticity as well as rate-dependent plasticity (creep). Four joint patterns have been predefined based on the state of bed and head mortar joints (damaged/undamaged). The transition criterion between the four patterns was defined by tension cut-off associated with Mohr-Coulomb criterion. The homogenized elastic-viscoplastic behavior of each joint pattern has been determined using finite element based nonlinear homogenization approach.

Verification of the developed multi scale model of masonry with mortar has been carried out by comparing the numerical results of detailed micro models (brick and joints are considered) with the homogeneous equivalent material models (bricks and joints were replaced by a homogeneous material). Then, the developed model has been employed to predict the mechanical response of masonry walls subjected to in-plane shear and bending loads. With reasonable accuracy, the present model was able to predict the mechanical response of the studied cases and the crack patterns. The model was able to simulate the orthotropic, compressible, rate-dependent homogenized behavior of refractory masonry structures with mortar joints, and accounts for joints opening (chapter 4).

The multi scale constitutive material models of masonry with dry joints developed in chapter 3, calibrated and validated in chapter 4 were used to represent the different masonry linings in a simplified steel ladle (chapter 5). Then, three-dimensional coupled sequential transient thermomechanical analysis have been carried out. The temperature distributions of the steel ladle have been computed and used as a thermal load for the thermomechanical analysis. The transient thermomechanical model enables the visualisation of the gradual closure and reopening of joints during a complete thermal cycle of the ladle. The impacts of joints thickness, joints behavior, constitutive material models of the different linings of the ladle and the steel shell on the resulting thermal stresses have been studied. It has been shown that increasing joint thickness leads to a decrease in the resulting thermal stresses in the bottom and the wall of the working lining, as well as in the steel shell. In addition, for the same joint thickness, using masonry with natural joints behavior results in higher values of resulting thermomechanical stresses as compared to perfect

joint. The inclusion of the viscoplasticity to the numerical model has a significant impact on the resulting thermomechanical stresses. A change of stress sign from compression to tension and opening/closure of dry joints in the HF of the working linings were observed. Moreover, lower values of thermomechanical stresses were obtained when more accurate and complex behavior laws were used to describe the mechanical behavior of the different layers of the steel ladle.

6.2 Suggests for future work

On the overall, the proposed constitutive models showed to be rather accurate in predicting masonry nonlinear elastic viscoplastic behavior. Obviously, there is still room for improvements, present and future developments are listed below:

1. Extension of the presented homogenization technique to take into account the asymmetric creep behavior of refractories and the primary creep stage.
2. The presented homogenization technique have been applied to rectangular coordinate systems, further research is required to deal with cylindrical coordinates and defining periodic boundary conditions (in cylindrical coordinates).
3. Extension of the presented constitutive models to consider the damage of the bricks. This could help in predicting realistic stress levels in the case of steel ladle internal linings.
4. Extension of the multi scale model of masonry with mortar joints to take into account the re-closure of the damaged mortar joints under compressive loads. This would require some experimental investigations of the damaged joint behavior under compression (joints closure tests of masonry with damaged mortar joints).
5. More parametric studies to investigate the impact of ladle's bottom design and material properties on resulting thermomechanical stresses.
6. Numerical studies to optimize some geometrical parameters of the ladle, considering the real geometry of the ladle and materials and taking into account the creep impacts at lower temperatures are required.

In addition, further experimental studies are still required, some recommendations of future experimental work are given below:

1. Investigating the thermomechanical behavior of refractory masonry with mortar joints under a wide range of loading conditions, similar to those presented in chapter 2.
2. Joints closure tests of running bond masonry at different temperatures would be helpful in understanding the joints closure phenomena at different temperatures and accurately calculating the homogenized mechanical constants at higher temperatures.
3. Experimental studies to investigate the creep behavior of alumina spinel at lower temperatures and include its effects on the numerical model of the steel ladle. Because, at higher stress levels (up to the ultimate compressive stress of the material) compared to those presented in chapter 2 (6 MPa), creep and stress relaxation can start at lower temperatures.

Including the creep impacts at lower temperatures would lead to gradual decrease of the stresses in the ladle instead of the sudden decrease noticed in chapter 5.

4. In-situ measurement at an industrial scale steel ladle. This could be helpful for knowing the real stress and strain values in the ladle linings and verification of the numerical models.

Bibliography

[1] "ATHOR Refractory Linings - ETN ATHOR, available at: https://www.etn-athor.eu/."

[2] E. Blond, A. K. Nguyen, E. de Bilbao, T. Sayet, and A. Batakis, "Thermo-chemo-mechanical modeling of refractory behavior in service: Key points and new developments," *Int. J. Appl. Ceram. Technol.*, pp. 1–8, 2020.

[3] J. J. Coz Díaz, F. R. Mazón, P. J. García Nieto, and F. J. Suárez Domínguez, "Design and finite element analysis of a wet cycle cement rotary kiln," *Finite Elem. Anal. Des.*, vol. 39, no. 1, pp. 17–42, 2002.

[4] J. Qi, W. Yan, Z. Chen, S. Schafföner, W. Zhou, G. Li, and Q. Wang, "Preparation and characterization of microporous mullite-corundum refractory aggregates with high strength and closed porosity," *Ceram. Int.*, vol. 46, pp. 8274–8280, apr 2020.

[5] S. Smets, S. Parada, J. Weytjens, G. Heylen, P. T. Jones, M. Guo, B. Blanpain, and P. Wollants, "Behaviour of magnesia-carbon refractories in vacuum-oxygen decarburisation ladle linings," *Ironmak. Steelmak.*, vol. 30, no. 4, pp. 293–300, 2003.

[6] G. Wu, W. Yan, S. Schafföner, Y. Dai, B. Han, T. Li, S. Ma, N. Li, and G. Li, "A comparative study on the microstructures and mechanical properties of a dense and a lightweight magnesia refractories," *J. Alloys Compd.*, vol. 796, pp. 131–137, aug 2019.

[7] A. Buhr, R. Bruckhausen, and R. Fahndrich, "The steel industry in Germany–trends in clean steel technology and refractory engineering," *Refract. WORLDFORUM*, vol. 8, no. 1, pp. 57–63, 2016.

[8] Andus Buhr et al., "Dream Ladle Lining," in *VDEh Proceedings, 9th Int. Symp. Refract. Technol. Steel Ladle Lining*, (Mönchengladbach, Germany), pp. 13–15, VDEh Proceedings, 2016.

[9] E. Blond, N. Schmitt, F. Hild, P. Blumenfeld, and J. Poirier, "Effect of slag impregnation on thermal degradations in refractories," *J. Am. Ceram. Soc.*, vol. 90, no. 1, pp. 154–162, 2007.

[10] S. Samadi, S. Jin, D. Gruber, H. Harmuth, and S. Schachner, "Statistical study of compressive creep parameters of an alumina spinel refractory," *Ceram. Int.*, vol. 46, no. 10, pp. 14662–14668, 2020.

[11] T. M. J. Raijmakers and A. T. Vermeltfoort, "Deformation controlled tests in masonry shear walls," *Rep. TUE/BKO/93.08, Eindhoven Univ. Technol. Eindhoven, Netherlands.*, 1992.

[12] A. W. Page, "Finite element model for masonry," *J. Struct. Div.*, vol. 104, no. 8, pp. 1267–1285, 1978.

[13] D. J. Griffiths and D. F. Schroeter, *Introduction to quantum mechanics*. Cambridge University Press, 2018.

[14] R. Shankar, *Principles of quantum mechanics*. Springer Science & Business Media, 2012.

[15] N. Yu and A. A. Polycarpou, "Adhesive contact based on the Lennard–Jones potential: a correction to the value of the equilibrium distance as used in the potential," *J. Colloid Interface Sci.*, vol. 278, no. 2, pp. 428–435, 2004.

[16] G. M. Odegard, "6.2 Computational Multiscale Modeling – Nanoscale to Macroscale," in *Compr. Compos. Mater. II*, pp. 28–51, Elsevier, 2018.

[17] H. Yao, L. Ouyang, and W.-Y. Ching, "Ab Initio Calculation of Elastic Constants of Ceramic Crystals," *J. Am. Ceram. Soc.*, vol. 90, pp. 3194–3204, oct 2007.

[18] G. Cao, C. Deng, Y. Chen, X. Wang, C. Yu, J. Ding, H. Zhu, and N. Peng, "Influence of sintering process and interfacial bonding mechanism on the mechanical properties of MgO–C refractories," *Ceram. Int.*, vol. 46, no. 10, pp. 16860–16866, 2020.

[19] J. Zhao, H. Shang, Z. Zhu, G. Zhang, L. Duan, and X. Sun, "Simulation of meso-damage of refractory based on cohesion model and molecular dynamics method," in *AIP Conf. Proc.*, vol. 1971, p. 050008, 2018.

[20] R. Hill, "Elastic properties of reinforced solids: Some theoretical principles," *J. Mech. Phys. Solids*, vol. 11, no. 5, pp. 357–372, 1963.

[21] Z. Hashin, "Analysis of Composite Materials—A Survey," *J. Appl. Mech.*, vol. 50, no. 3, pp. 481–505, 1983.

[22] J. Espadas-Escalante, N. van Dijk, and P. Isaksson, "A study on the influence of boundary conditions in computational homogenization of periodic structures with application to woven composites," *Compos. Struct.*, vol. 160, pp. 529–537, 2017.

[23] Z. Xia, Y. Zhang, and F. Ellyin, "A unified periodical boundary conditions for representative volume elements of composites and applications," *Int. J. Solids Struct.*, vol. 40, no. 8, pp. 1907–1921, 2003.

[24] G. M. Odegard, "Multiscale modeling of nanocomposite materials," in *Virtual Test. Predict. Model. Fatigue Fract. Mech. Allow.*, pp. 221–245, Springer US, 2009.

[25] M. Hori and S. Nemat-Nasser, "On two micromechanics theories for determining micro-macro relations in heterogeneous solids," *Mech. Mater.*, vol. 31, no. 10, pp. 667–682, 1999.

[26] N. Tessier-Doyen, *Etude expérimentale et numérique du comportement thermomécanique de matériaux réfractaires modèles - in French*. PhD thesis, University of Limoges - France, 2003.

[27] J. D. Eshelby, "The elastic field outside an ellipsoidal inclusion," *Proc. R. Soc. London. Ser. A. Math. Phys. Sci.*, vol. 252, no. 1271, pp. 561–569, 1959.

[28] J. D. Eshelby, "The determination of the elastic field of an ellipsoidal inclusion, and related problems," *Proc. R. Soc. London. Ser. A. Math. Phys. Sci.*, vol. 241, no. 1226, pp. 376–396, 1957.

[29] O. Pierard, J. LLorca, J. Segurado, and I. Doghri, "Micromechanics of particle-reinforced elasto-viscoplastic composites: Finite element simulations versus affine homogenization," *Int. J. Plast.*, vol. 23, no. 6, pp. 1041–1060, 2007.

[30] J. Chaboche, P. Kanoute, and A. Roos, "On the capabilities of mean-field approaches for the description of plasticity in metal matrix composites," *Int. J. Plast.*, vol. 21, no. 7, pp. 1409–1434, 2005.

[31] P. P. Castañeda and P. Suquet, "Nonlinear Composites," in *Adv. Appl. Mech.*, pp. 171–302, Elsevier, 1997.

[32] A. Reuss, "Calculation of the flow limits of mixed crystals on the basis of the plasticity of monocrystals," *Z. Angew. Math. Mech*, vol. 9, pp. 49–58, 1929.

[33] W. Voigt, "Ueber die Beziehung zwischen den beiden Elasticitätsconstanten isotroper Körper," *Ann. Phys.*, vol. 274, no. 12, pp. 573–587, 1889.

[34] Z. Hashin, "The Elastic Moduli of Heterogeneous Materials," *J. Appl. Mech.*, vol. 29, no. 1, pp. 143–150, 1962.

[35] Z. Hashin and S. Shtrikman, "A variational approach to the theory of the elastic behaviour of multiphase materials," *J. Mech. Phys. Solids*, vol. 11, no. 2, pp. 127–140, 1963.

[36] T. Mori and K. Tanaka, "Average stress in matrix and average elastic energy of materials with misfitting inclusions," *Acta Metall.*, vol. 21, no. 5, pp. 571–574, 1973.

[37] E. Kröner, "Bounds for effective elastic moduli of disordered materials," *J. Mech. Phys. Solids*, vol. 25, no. 2, pp. 137–155, 1977.

[38] L. Walpole, "On the overall elastic moduli of composite materials," *J. Mech. Phys. Solids*, vol. 17, no. 4, pp. 235–251, 1969.

[39] J. C. Gerdeen and R. A. L. Rorrer, *Engineering design with polymers and composites*, vol. 30. CRC Press, 2011.

[40] Aboudi, Jacob, Steven M. Arnold and B. A. Bednarcyk, *Micromechanics of Composite Materials*. Elsevier, 2013.

[41] Y. Benveniste, "A new approach to the application of Mori-Tanaka's theory in composite materials," *Mech. Mater.*, vol. 6, no. 2, pp. 147–157, 1987.

[42] D. C. Lagoudas, A. C. Gavazzi, and H. Nigam, "Elastoplastic behavior of metal matrix composites based on incremental plasticity and the Mori-Tanaka averaging scheme," *Comput. Mech.*, vol. 8, no. 3, pp. 193–203, 1991.

[43] F. Desrumaux, F. Meraghni, and M. L. Benzeggagh, "Generalised Mori-Tanaka Scheme to Model Anisotropic Damage Using Numerical Eshelby Tensor," *J. Compos. Mater.*, vol. 35, no. 7, pp. 603–624, 2001.

[44] S. Mercier and A. Molinari, "Homogenization of elastic–viscoplastic heterogeneous materials: Self-consistent and Mori-Tanaka schemes," *Int. J. Plast.*, vol. 25, no. 6, pp. 1024–1048, 2009.

[45] M. Barral, G. Chatzigeorgiou, F. Meraghni, and R. Léon, "Homogenization using modified Mori-Tanaka and TFA framework for elastoplastic-viscoelastic-viscoplastic composites: Theory and numerical validation," *Int. J. Plast.*, vol. 127, no. November 2019, p. 102632, 2020.

[46] J. Qu and M. Cherkaoui, *Fundamentals of Micromechanics of Solids*. Hoboken, NJ, USA: John Wiley & Sons, Inc., 2006.

[47] Y.-c. Fung, P. Tong, and X. Chen, *Classical and computational solid mechanics*, vol. 2. World Scientific Publishing Company, 2017.

[48] M. Tsuda, E. Takemura, T. Asada, N. Ohno, and T. Igari, "Homogenized elastic-viscoplastic behavior of plate-fin structures at high temperatures: Numerical analysis and macroscopic constitutive modeling," *Int. J. Mech. Sci.*, vol. 52, no. 5, pp. 648–656, 2010.

[49] A. Iltchev, V. Marcadon, S. Kruch, and S. Forest, "Computational homogenisation of periodic cellular materials: Application to structural modelling," *Int. J. Mech. Sci.*, vol. 93, pp. 240–255, 2015.

[50] R. Hill, "The essential structure of constitutive laws for metal composites and polycrystals," *J. Mech. Phys. Solids*, vol. 15, no. 2, pp. 79–95, 1967.

[51] F. Fritzen, S. Forest, T. Böhlke, D. Kondo, and T. Kanit, "Computational homogenization of elasto-plastic porous metals," *Int. J. Plast.*, vol. 29, no. 1, pp. 102–119, 2012.

[52] T. Matsuda, N. Ohno, H. Tanaka, and T. Shimizu, "Effects of fiber distribution on elastic-viscoplastic behavior of long fiber-reinforced laminates," *Int. J. Mech. Sci.*, vol. 45, no. 10, pp. 1583–1598, 2003.

[53] T. T. Molla, K. Kwok, and H. L. Frandsen, "Efficient modeling of metallic interconnects for thermo-mechanical simulation of SOFC stacks: Homogenized behaviors and effect of contact," *Int. J. Hydrogen Energy*, vol. 41, no. 15, pp. 6433–6444, 2016.

[54] N. Ohno, K. Narita, and D. Okumura, "Homogenized elastic-viscoplastic behavior of plate-fin structures with two pore pressures," *Int. J. Mech. Sci.*, vol. 86, pp. 18–25, 2014.

[55] P. Henyš, L. Čapek, and J. Březina, "Comparison of current methods for implementing periodic boundary conditions in multi-scale homogenisation," *Eur. J. Mech. A/Solids*, vol. 78, no. July, p. 103825, 2019.

[56] S. L. Omairey, P. D. Dunning, and S. Sriramula, "Development of an ABAQUS plugin tool for periodic RVE homogenisation," *Eng. Comput.*, vol. 35, no. 2, pp. 567–577, 2019.

[57] T. Zahra and M. Dhanasekar, "Characterisation and strategies for mitigation of the contact surface unevenness in dry-stack masonry," *Constr. Build. Mater.*, vol. 169, pp. 612–628, 2018.

[58] T. Bui, A. Limam, V. Sarhosis, and M. Hjiaj, "Discrete element modelling of the in-plane and out-of-plane behaviour of dry-joint masonry wall constructions," *Eng. Struct.*, vol. 136, pp. 277–294, 2017.

[59] G. G. Chewe Ngapeya and D. Waldmann, "Overcome of bed-joint imperfections and improvement of actual contact in dry-stacked masonry," *Constr. Build. Mater.*, vol. 233, p. 117173, 2020.

[60] N. A. Nodargi, C. Intrigila, and P. Bisegna, "A variational-based fixed-point algorithm for the limit analysis of dry-masonry block structures with non-associative Coulomb friction," *Int. J. Mech. Sci.*, vol. 161-162, p. 105078, 2019.

[61] P. B. Lourenço, D. V. Oliveira, P. Roca, and A. Orduña, "Dry joint stone masonry walls subjected to in-plane combined loading," *J. Struct. Eng.*, vol. 131, no. 11, pp. 1665–1673, 2005.

[62] J. A. Thamboo, T. Zahra, and R. Dhanasekar, "Development of design methodology for mortarless masonry system: Case study – a resettlement housing colony," *J. Build. Eng.*, vol. 27, p. 100973, 2020.

[63] M. Martínez and S. Atamturktur, "Experimental and numerical evaluation of reinforced dry-stacked concrete masonry walls," *J. Build. Eng.*, vol. 22, pp. 181–191, 2019.

[64] H. Smoljanović, Ž. Nikolić, and N. Živaljić, "A finite-discrete element model for dry stone masonry structures strengthened with steel clamps and bolts," *Eng. Struct.*, vol. 90, pp. 117–129, 2015.

[65] G. Tempesta and S. Galassi, "Safety evaluation of masonry arches. A numerical procedure based on the thrust line closest to the geometrical axis," *Int. J. Mech. Sci.*, vol. 155, pp. 206–221, 2019.

[66] K. Andreev, S. Sinnema, A. Rekik, S. Allaoui, E. Blond, and A. Gasser, "Compressive behaviour of dry joints in refractory ceramic masonry," *Constr. Build. Mater.*, vol. 34, pp. 402–408, 2012.

[67] A. Gasser, K. Terny-Rebeyrotte, and P. Boisse, "Modelling of joint effects on refractory lining behaviour," *Proc. Inst. Mech. Eng. Part L J. Mater. Des. Appl.*, vol. 218, no. 1, pp. 19–28, 2004.

[68] S. Allaoui, A. Rekik, A. Gasser, E. Blond, and K. Andreev, "Digital image correlation measurements of mortarless joint closure in refractory masonries," *Constr. Build. Mater.*, vol. 162, pp. 334–344, 2018.

[69] G. G. Chewe Ngapeya and D. Waldmann, "Experimental and analytical analysis of the load-bearing capacity Pu of improved dry-stacked masonry," *J. Build. Eng.*, vol. 27, p. 100927, 2020.

[70] H. Ben Ayed, O. Limam, M. Aidi, and A. Jelidi, "Experimental and numerical study of Interlocking Stabilized Earth Blocks mechanical behavior," *J. Build. Eng.*, vol. 7, pp. 207–216, 2016.

[71] T. Zahra, *Strategies for Improving the Response of Drystack Masonry to Compression*. PhD thesis, Queensland University of Technology - Australia, 2017.

[72] R. A. Silva, E. Soares, D. V. Oliveira, T. Miranda, N. M. Cristelo, and D. Leitão, "Mechanical characterisation of dry-stack masonry made of CEBs stabilised with alkaline activation," *Constr. Build. Mater.*, vol. 75, pp. 349–358, 2015.

[73] T. Prietl, *Determination of material-specific parameters of refractory materials and linings under uniaxial and biaxial load conditions for the non-ferrous metal industry - in German*. PhD thesis, Montanuniversität Leoben - Austria, 2006.

[74] T. Prietl, H. Antrekowitsch, A. Triessnig, H. Studnicka, and A. Filzwieser, "The evaluation of refractory linings thermo-mechanical properties," *Proc. - Eur. Metall. Conf. EMC 2005*, vol. 3, pp. 1099–1112, 2005.

[75] A. Triessnig, H. Studnicka, and T. Prietl, "Determination of Thermo-Mechanical Properties at the RHI Refractories Technology Center Leoben," *RHI Bull.*, no. 1, pp. 33–37, 2006.

[76] T. M. Nguyen, E. Blond, A. Gasser, and T. Prietl, "Mechanical homogenisation of masonry wall without mortar," *Eur. J. Mech. A/Solids*, vol. 28, no. 3, pp. 535–544, 2009.

[77] W. A. Thanoon, A. H. Alwathaf, J. Noorzaei, M. S. Jaafar, and M. R. Abdulkadir, "Nonlinear finite element analysis of grouted and ungrouted hollow interlocking mortarless block masonry system," *Eng. Struct.*, vol. 30, no. 6, pp. 1560–1572, 2008.

[78] W. A. Thanoon, A. H. Alwathaf, J. Noorzaei, M. S. Jaafar, and M. R. Abdulkadir, "Finite element analysis of interlocking mortarless hollow block masonry prism," *Comput. Struct.*, vol. 86, no. 6, pp. 520–528, 2008.

[79] G. G. Chewe Ngapeya, D. Waldmann, and F. Scholzen, "Impact of the height imperfections of masonry blocks on the load bearing capacity of dry-stack masonry walls," *Constr. Build. Mater.*, vol. 165, pp. 898–913, 2018.

[80] D. Foti, V. Vacca, and I. Facchini, "DEM modeling and experimental analysis of the static behavior of a dry-joints masonry cross vaults," *Constr. Build. Mater.*, vol. 170, pp. 111–120, 2018.

[81] H. Smoljanović, N. Živaljić, Ž. Nikolić, and A. Munjiza, "Numerical analysis of 3D dry-stone masonry structures by combined finite-discrete element method," *Int. J. Solids Struct.*, vol. 136-137, pp. 150–167, 2018.

[82] C. Casapulla and L. U. Argiento, "In-plane frictional resistances in dry block masonry walls and rocking-sliding failure modes revisited and experimentally validated," *Compos. Part B Eng.*, vol. 132, pp. 197–213, 2018.

[83] F. Portioli and L. Cascini, "Large displacement analysis of dry-jointed masonry structures subjected to settlements using rigid block modelling," *Eng. Struct.*, vol. 148, pp. 485–496, 2017.

[84] A. Rekik, S. Allaoui, A. Gasser, E. Blond, K. Andreev, and S. Sinnema, "Experiments and nonlinear homogenization sustaining mean-field theories for refractory mortarless

masonry: The classical secant procedure and its improved variants," *Eur. J. Mech. A/Solids*, vol. 49, pp. 67–81, 2015.

[85] *Abaqus Documentation, ABAQUS/standard: User's Manual*. 1998.

[86] R. Van der Pluijm, "Non-linear behaviour of masonry under tension," *HERON-ENGLISH Ed.*, vol. 42, pp. 25–54, 1997.

[87] R. Van der Pluijm, "Shear behaviour of bed joints," in *Proc. 6th North Am. Mason. Conf. Drexel Univ. Philadelphia, Pennsylvania, USA*, pp. 125–136, 1993.

[88] J. Brulin, E. Blond, E. de Bilbao, A. Rekik, M. Landreau, A. Gasser, and Y. Colleville, "Methodology for brick/mortar interface strength characterization at high temperature," *Constr. Build. Mater.*, vol. 265, p. 120565, 2020.

[89] R. H. Atkinson, B. P. Amadei, S. Saeb, and S. Sture, "Response of Masonry Bed Joints in Direct Shear," *J. Struct. Eng.*, vol. 115, no. 9, pp. 2276–2296, 1989.

[90] G. van Zijl, "Modeling Masonry Shear-Compression: Role of Dilatancy Highlighted," *J. Eng. Mech.*, vol. 130, no. 11, pp. 1289–1296, 2004.

[91] F. Fouchal, F. Lebon, and I. Titeux, "Contribution to the modelling of interfaces in masonry construction," *Constr. Build. Mater.*, vol. 23, no. 6, pp. 2428–2441, 2009.

[92] P. Lourenço, J. Barros, and J. Oliveira, "Shear testing of stack bonded masonry," *Constr. Build. Mater.*, vol. 18, no. 2, pp. 125–132, 2004.

[93] V. Alecci, M. Fagone, T. Rotunno, and M. De Stefano, "Shear strength of brick masonry walls assembled with different types of mortar," *Constr. Build. Mater.*, vol. 40, pp. 1038–1045, 2013.

[94] R. G. Drysdale, A. C. Heidebrecht, and A. A. Hamid, "Tensile Strength of Concrete Masonry," *J. Struct. Div.*, vol. 105, no. 7, pp. 1261–1276, 1979.

[95] H. P. Backes, "Tensile strength of masonry," in *Proc. 7th Int. brick Mason. Conf.*, pp. 779–790, 1985.

[96] A. W. Page, "The strength of brick masonry under biaxial tension-compression," *Int. J. Mason. Constr.*, vol. 3, no. 1, pp. 26–31, 1983.

[97] A. W. Page, "The biaxial compressive strength of brick masonry.," *Proc. Inst. Civ. Eng.*, vol. 71, no. 3, pp. 893–906, 1981.

[98] H. B. Kaushik, D. C. Rai, and S. K. Jain, "Stress-Strain Characteristics of Clay Brick Masonry under Uniaxial Compression," *J. Mater. Civ. Eng.*, vol. 19, no. 9, pp. 728–739, 2007.

[99] L. Binda, G. M. Roberti, and C. Tiraboschi, "Problemi di misura dei parametri meccanici della muratura e dei suoi componenti," *Atti del Convegno Naz. La Mecc. delle Murature tra Teor. e Progett. Messin.*, 1996.

[100] P. B. Lourenço, *Computational strategies for masonry structures*. PhD thesis, TU Delft - the Netherlands, 1996.

[101] D. V. Oliveira and P. B. Lourenço, "Implementation and validation of a constitutive model for the cyclic behaviour of interface elements," in *Comput. Struct.*, vol. 82, pp. 1451–1461, Pergamon, 2004.

[102] P. B. Lourenço and J. G. Rots, "Multisurface Interface Model for Analysis of Masonry Structures," *J. Eng. Mech.*, vol. 123, no. 7, pp. 660–668, 1997.

[103] L. C. Silva, P. B. Lourenço, and G. Milani, "Derivation of the out-of-plane behaviour of masonry through homogenization strategies: Micro-scale level," *Comput. Struct.*, vol. 209, pp. 30–43, 2018.

[104] E. Minga, L. Macorini, and B. A. Izzuddin, "A 3D mesoscale damage-plasticity approach for masonry structures under cyclic loading," *Meccanica*, vol. 53, no. 7, pp. 1591–1611, 2018.

[105] M. Shadlou, E. Ahmadi, and M. M. Kashani, "Micromechanical modelling of mortar joints and brick-mortar interfaces in masonry Structures: A review of recent developments," *Structures*, vol. 23, pp. 831–844, feb 2020.

[106] M. Deng and S. Yang, "Experimental and numerical evaluation of confined masonry walls retrofitted with engineered cementitious composites," *Eng. Struct.*, vol. 207, p. 110249, 2020.

[107] N. Kumar and M. Barbato, "New Constitutive Model for Interface Elements in Finite-Element Modeling of Masonry," *J. Eng. Mech.*, vol. 145, no. 5, pp. 1–15, 2019.

[108] G. van Zijl, *Computational Modelling of Masonry Creep and Shrinkage*. PhD thesis, TU Delft - the Netherlands, 1999.

[109] A. J. Aref and K. M. Dolatshahi, "A three-dimensional cyclic meso-scale numerical procedure for simulation of unreinforced masonry structures," *Comput. Struct.*, vol. 120, pp. 9–23, 2013.

[110] D. Addessi, S. Marfia, and E. Sacco, "A plastic nonlocal damage model," *Comput. Methods Appl. Mech. Eng.*, vol. 191, no. 13-14, pp. 1291–1310, 2002.

[111] D. Addessi and E. Sacco, "A kinematic enriched plane state formulation for the analysis of masonry panels," *Eur. J. Mech. - A/Solids*, vol. 44, pp. 188–200, 2014.

[112] L. Pelà, M. Cervera, and P. Roca, "An orthotropic damage model for the analysis of masonry structures," *Constr. Build. Mater.*, vol. 41, pp. 957–967, 2013.

[113] J. Toti, V. Gattulli, and E. Sacco, "Nonlocal damage propagation in the dynamics of masonry elements," *Comput. Struct.*, vol. 152, pp. 215–227, 2015.

[114] C. Tesei and G. Ventura, "A unilateral nonlocal tensile damage model for masonry structures," *Procedia Struct. Integr.*, vol. 2, pp. 2690–2697, 2016.

[115] M. Valente and G. Milani, "Non-linear dynamic and static analyses on eight historical masonry towers in the North-East of Italy," *Eng. Struct.*, vol. 114, pp. 241–270, 2016.

[116] J. Lubliner, J. Oliver, S. Oller, and E. Oñate, "A plastic-damage model for concrete," *Int. J. Solids Struct.*, vol. 25, no. 3, pp. 299–326, 1989.

[117] J. Lee and G. L. Fenves, "Plastic-Damage Model for Cyclic Loading of Concrete Structures," *J. Eng. Mech.*, vol. 124, no. 8, pp. 892–900, 1998.

[118] R. Luciano and E. Sacco, "Homogenization technique and damage model for old masonry material," *Int. J. Solids Struct.*, vol. 34, no. 24, pp. 3191–3208, 1997.

[119] R. Luciano and E. Sacco, "A damage model for masonry structures," *Eur. J. Mech. A/Solids*, vol. 17, no. 2, pp. 285–303, 1998.

[120] M. Landreau, *Modélisation thermomécanique d'un piédroit de four à coke - in French*. PhD thesis, University of Orléans - France, 2009.

[121] J. Brulin, *Modélisation thermomécanique d'un creuset de haut fourneau - in French*. PhD thesis, University of Orléans - France, 2010.

[122] J. Fruhstorfer, L. Schöttler, S. Dudczig, G. Schmidt, P. Gehre, and C. G. Aneziris, "Erosion and corrosion of alumina refractory by ingot casting steels," *J. Eur. Ceram. Soc.*, vol. 36, no. 5, pp. 1299–1306, 2016.

[123] K. Andreev, B. Luchini, M. Rodrigues, and J. L. Alves, "Role of fatigue in damage development of refractories under thermal shock loads of different intensity," *Ceram. Int.*, vol. 46, no. 13, pp. 20707–20716, 2020.

[124] J. Chen, L. Chen, Y. Wei, N. Li, and S. Zhang, "Corrosion and penetration behaviors of slag/steel on the corroded interfaces of Al2O3-C refractories: Role of Ti3AlC2," *Corros. Sci.*, vol. 143, pp. 166–176, 2018.

[125] Y. Dai, J. Li, W. Yan, and C. Shi, "Corrosion mechanism and protection of BOF refractory for high silicon hot metal steelmaking process," *J. Mater. Res. Technol.*, vol. 9, no. 3, pp. 4292–4308, 2020.

[126] Y. Zou, A. Huang, R. Wang, L. Fu, H. Gu, and G. Li, "Slag corrosion-resistance mechanism of lightweight magnesia-based refractories under a static magnetic field," *Corros. Sci.*, vol. 167, p. 108517, 2020.

[127] J. L. Xia and T. Ahokainen, "Transient flow and heat transfer in a Steelmaking ladle during the holding period," *Metall. Mater. Trans. B Process Metall. Mater. Process. Sci.*, vol. 32, no. 4, pp. 733–741, 2001.

[128] A. Gasser, L. Chen, F. Genty, J. L. Daniel, E. Blond, K. Andreev, and S. Sinnema, "Influence of different masonry designs of bottom linings," in *Proc. Unified Int. Tech. Conf. Refract. UNITECR 2013*, (Victoria, Canada), pp. 851–856, 2013.

[129] M. F. Santos, M. H. Moreira, M. G. Campos, P. I. Pelissari, R. A. Angélico, E. Y. Sako, S. Sinnema, and V. C. Pandolfelli, "Enhanced numerical tool to evaluate steel ladle thermal losses," *Ceram. Int.*, vol. 44, no. 11, pp. 12831–12840, 2018.

[130] S. Yilmaz, "Thermomechanical Modelling for Refractory Lining of a Steel Ladle Lifted by Crane," *Steel Res. Int.*, vol. 74, no. 8, pp. 485–490, 2003.

[131] A. Hou, S. Jin, H. Harmuth, and D. Gruber, "A Method for Steel Ladle Lining Optimization Applying Thermomechanical Modeling and Taguchi Approaches," *Jom*, vol. 70, no. 11, pp. 2449–2456, 2018.

[132] A. Gasser, E. Blond, N. Yahmi, L. B. Teixeira, and S. Sinnema, "Thermomechanical Modelling of a Steel Ladle Using Periodical Homogenisation for the Refractory Masonries," *Refract. worldforum*, vol. 9, pp. 76 – 82, 2017.

[133] D. Vitiello, *Thermo-physical properties of insulating refractory materials*. PhD thesis, University of Limoges - France, 2021.

[134] R. Kaczmarek, *Mechanical characterization of refractory materials*. PhD thesis, University of Limoges - France, 2021.

[135] R. L. Oliveira, J. P. C. Rodrigues, J. M. Pereira, P. B. Lourenço, and H. U. Marschall, "Thermomechanical behaviour of refractory dry-stacked masonry walls under uniaxial compression," *Eng. Struct.*, vol. 240, p. 112361, 2021.

[136] L. Teixeira, S. Samadi, J. Gillibert, S. Jin, T. Sayet, D. Gruber, and E. Blond, "Experimental Investigation of the Tension and Compression Creep Behavior of Alumina-Spinel Refractories at High Temperatures," *Ceramics*, vol. 3, no. 3, pp. 372–383, 2020.

[137] J. Blaber, B. Adair, and A. Antoniou, "Ncorr: Open-Source 2D Digital Image Correlation Matlab Software," *Exp. Mech.*, vol. 55, no. 6, pp. 1105–1122, 2015.

[138] M. Ali, T. Sayet, A. Gasser, and E. Blond, "Transient thermo-mechanical analysis of steel ladle refractory linings using mechanical homogenization approach," *Ceramics*, vol. 3, no. 2, pp. 171–189, 2020.

[139] E. Blond, N. Schmitt, F. Hild, P. Blumenfeld, and J. Poirier, "Modelling of high temperature asymmetric creep behavior of ceramics," *J. Eur. Ceram. Soc.*, vol. 25, no. 11, pp. 1819–1827, 2005.

[140] J. Lemaitre and J.-L. Chaboche, *Mechanics of Solid Materials*. Cambridge University Press, 1990.

[141] M. Ali, T. Sayet, A. Gasser, and E. Blond, "Thermomechanical modelling of refractory mortarless masonry wall subjected to biaxial compression," in *UNITECR19*, (Yokohama, Japan), 2019.

[142] A. Rekik and A. Gasser, "Numerical homogenization model for effective creep properties of microcracked masonry," *Int. J. Solids Struct.*, vol. 102-103, pp. 297–320, 2016.

[143] M. Tsuda and N. Ohno, "Duplex model for homogenized elastic-viscoplastic behavior of plate-fin structures at high temperatures," *Int. J. Plast.*, vol. 27, no. 10, pp. 1560–1576, 2011.

[144] K. Goto, M. Arai, T. Matsuda, and G. Kubo, "Elasto-viscoplastic analysis for negative through-the-thickness Poisson's ratio of woven laminate composites based on homogenization theory," *Int. J. Mech. Sci.*, vol. 146-147, pp. 455–461, 2018.

[145] E. Tikarrouchine, G. Chatzigeorgiou, Y. Chemisky, and F. Meraghni, "Fully coupled thermo-viscoplastic analysis of composite structures by means of multi-scale three-dimensional finite element computations," *Int. J. Solids Struct.*, vol. 164, pp. 120–140, 2019.

[146] M. Ali, T. Sayet, A. Gasser, and E. Blond, "Computational homogenization of elastic-viscoplastic refractory masonry with dry joints," *Int. J. Mech. Sci.*, vol. 196, p. 106275, 2021.

[147] M. Ali, T. Sayet, A. Gasser, and E. Blond, "A Multiscale Model for Numerical Modelling of Homogenized Elastic-Viscoplastic Behavior of Mortarless Refractory Masonry Structures," in *14th World Congr. Comput. Mech. (WCCM), ECCOMAS Congr. 2020*, (Paris), 2021.

[148] J. N. Reddy, *Mechanics of laminated composite plates and shells: theory and analysis*. CRC press, 2003.

[149] N. Ohno, K. Ikenoya, D. Okumura, and T. Matsuda, "Homogenized elastic-viscoplastic behavior of anisotropic open-porous bodies with pore pressure," *Int. J. Solids Struct.*, vol. 49, no. 19-20, pp. 2799–2806, 2012.

[150] Z. Xue and J. W. Hutchinson, "Constitutive model for quasi-static deformation of metallic sandwich cores," *Int. J. Numer. Methods Eng.*, vol. 61, no. 13, pp. 2205–2238, 2004.

[151] R. L. Oliveira, J. P. C. Rodrigues, J. M. Pereira, P. B. Lourenço, and H. Ulrich Marschall, "Normal and tangential behaviour of dry joints in refractory masonry," *Eng. Struct.*, vol. 243, p. 112600, 2021.

[152] B. P. Sinha, "A simplified ultimate load analysis of laterally loaded model orthotropic brickwork panels of low tensile strength," *Struct Eng Part B*, vol. 56 B, no. 4, pp. 81–84, 1978.

[153] D. M. Herbert, D. R. Gardner, M. Harbottle, and T. G. Hughes, "Uniform lateral load capacity of small-scale masonry wall panels," *Mater. Struct. Constr.*, vol. 47, no. 5, pp. 805–818, 2014.

[154] B. Torres, F. B. Varona, F. J. Baeza, D. Bru, and S. Ivorra, "Study on retrofitted masonry elements under shear using digital image correlation," *Sensors (Switzerland)*, vol. 20, no. 7, p. 2122, 2020.

[155] L. C. Silva, P. B. Lourenço, and G. Milani, "Numerical homogenization-based seismic assessment of an English-bond masonry prototype: Structural level application," *Earthq. Eng. Struct. Dyn.*, vol. 49, no. 9, pp. 841–862, 2020.

[156] P. Lourenço, J. Rots, and J. Blaauwendraad, "Two approaches for the analysis of masonry structures: micro and macro-modeling," *Heron*, vol. 40, pp. 313–340, 1995.

[157] A. Orduña, "Non-linear static analysis of rigid block models for structural assessment of ancient masonry constructions," *Int. J. Solids Struct.*, vol. 128, pp. 23–35, 2017.

[158] Y. A. Cengel and A. J. Ghajar, *Heat and mass transfer: fundamentals and applications*. McGraw-Hill Education, 2007.

[159] P. Lourenço, J. Rots, and J. Blaauwendraad, "Two approaches for the analysis of masonry structures: micro and macro-modeling," *Heron (Delft)*, vol. 40, no. 4, pp. 313–340, 1995.

[160] S. Marfia and E. Sacco, "Multiscale damage contact-friction model for periodic masonry walls," *Comput. Methods Appl. Mech. Eng.*, vol. 205-208, no. 1, pp. 189–203, 2012.

[161] J. Lopez, S. Oller, E. Oñate, and J. Lubliner, "A homogeneous constitutive model for masonry," *Int. J. Numer. Methods Eng.*, vol. 46, no. 10, pp. 1651–1671, 1999.

[162] S. Jin, H. Harmuth, and D. Gruber, “Compressive creep testing of refractories at elevated loads-Device, material law and evaluation techniques,” *J. Eur. Ceram. Soc.*, vol. 34, no. 15, pp. 4037–4042, 2014.

[163] L. Teixeira, J. Gillibert, T. Sayet, and E. Blond, “A creep model with different properties under tension and compression — Applications to refractory materials,” *Int. J. Mech. Sci.*, vol. 212, p. 106810, 2021.

MAHMOUD Alaaeldeen Ahmed ALI

Modélisation thermomécanique non linéaire de maçonneries réfractaires

Cette thèse s'inscrit dans le cadre d'un projet de recherche Marie Curie financé par l'Union Européenne et consacré à "Advanced THermomechanical multiscale mOdelling of Refractory linings (ATHOR)". Les principaux objectifs de cette étude sont premièrement, la caractérisation du comportement mécanique et thermomécanique des maçonneries réfractaires sous une large gamme de conditions de chargement thermomécanique. Deuxièmement, développer des modèles numériques rigoureux et efficaces, en termes de calcul, pour les maçonneries réfractaires avec ou sans mortier. Le comportement mécanique et thermomécanique d'une maçonnerie réfractaire avec des joints sans mortier a été étudié pour une large gamme de conditions de chargement à température ambiante et à hautes températures (jusqu'à 1500 °C). Des essais de compression uniaxiale, dans les directions normales aux joints horizontaux ou verticaux, et des essais de compression biaxiale à température ambiante ont été réalisés. Des essais de fluage uniaxial, biaxial et de relaxation biaxiale ont été également réalisés à hautes températures. Les résultats de ces essais aident à comprendre le comportement thermomécanique complexe des revêtements réfractaires. L'impact des joints, leur fermeture et ouverture, des erreurs dimensionnelles et de forme des briques sont expliqués. Ensuite, des modèles numériques multi-échelles de maçonnerie ont été développés en se basent sur de l'homogénéisation non linéaire. Les modèles considèrent le comportement élasto-viscoplastique orthotrope de la maçonnerie réfractaire et tiennent compte de la fermeture et/ou de l'ouverture des joints. Les modèles développés ont été calibrés et validés en comparant les résultats expérimentaux et numériques de maçonneries soumises à une large gamme de conditions de chargement thermomécanique. Les résultats numériques donnent des précisions sur la réponse thermomécanique des revêtements réfractaires et aident à comprendre leur comportement mécanique complexe. Les modèles validés ont été utilisés pour prédire la réponse thermomécanique transitoire d'une poche à acier à l'échelle industrielle. Les méthodes expérimentales, les résultats et les modèles multi-échelles développés et présentés dans cette étude ouvrent de nouvelles perspectives intéressantes pour la conception et l'optimisation des revêtements réfractaires utilisés dans différentes structures industrielles.

Mots clés : Réfractaires, Maçonnerie, Modélisation thermomécanique, Homogénéisation non linéaire, Joints, Fluage

Nonlinear thermomechanical modeling of refractory masonry linings

This thesis is a part of a European funded Marie Curie research project dedicated to "Advanced THermomechanical multi scale mOdelling of Refractory linings (ATHOR)". The main goals of this study are firstly, characterizing the mechanical and thermomechanical behavior of refractory masonries with dry joints under a wide range of thermomechanical loading conditions. Secondly, developing rigorous and computationally efficient numerical models for the design and optimization of refractory masonry linings with and without mortar. The mechanical and thermomechanical behavior of refractory masonry with dry joints have been investigated. Uniaxial compression tests, in the directions normal to bed and head joints, and biaxial compression tests at room temperature were performed. Uniaxial and biaxial creep tests as well as biaxial relaxation tests at high temperature were carried out. The results of these tests help in understanding the complex thermomechanical behavior of refractory linings. The impacts of joints, joints closure and reopening, dimensional and shape errors of the bricks on the thermomechanical behavior were investigated. Then, multi-scale numerical models of masonry, with or without mortar, were developed. The models consider the orthotropic, nonlinear, elastic viscoplastic behavior of refractory masonry and account for joints closure or opening. The developed models, based on nonlinear homogenization technique, were calibrated and validated by comparing the experimental and numerical results of masonries subjected to a wide range of thermomechanical loading conditions. The numerical results provide more insights on the thermomechanical response of refractory linings and assist in understanding their complex mechanical and thermomechanical behaviors. The validated models were employed to predict the transient thermomechanical response of an industrial scale steel ladle. The experimental methods, results and the developed multi scale models presented in this study open very interesting ways and provide new insights that could be helpful for the design and optimization of refractory linings used in several high temperature industries.

Keywords : Refractories, Masonry, Thermomechanical modeling, Nonlinear Homogenization, Joints, Creep.

ATHOR EU MSCA ETN Refractory linings

LaMé Laboratoire de Mécanique Gabriel Lamé

MARIE CURIE ACTIONS